

"Structure-Property Relationships in Pnictide and Chalcogenide Thermoelectric Materials"

Dissertation

zur Erlangung des Grades
"Doktor der Naturwissenschaften"
im Promotionsfach Chemie

im Fachbereich Chemie, Pharmazie und Geowissenschaften der
Johannes Gutenberg-Universität Mainz

JOHANNES GUTENBERG
UNIVERSITÄT MAINZ



vorgelegt von

Christophe Paul Heinrich

geboren in Berlin

Mainz, den 31. März 2014

Dekan:

[REDACTED]

1. Berichtserstatter:

[REDACTED]

2. Berichtserstatter:

[REDACTED]

3. Berichtserstatter:

[REDACTED]

Tag der mündlichen Prüfung:

23/05/2014



Die vorliegende Arbeit wurde von Januar 2011 bis März 2014 unter der Leitung von [REDACTED] und [REDACTED] am Institut für Anorganische Chemie und Analytische Chemie der Johannes Gutenberg-Universität Mainz durchgeführt.

The work for this thesis was carried out in the period between January 2011 and March 2014 under the guidance of [REDACTED] and [REDACTED] at the Institute of Inorganic Chemistry and Analytical Chemistry of the Johannes Gutenberg-University Mainz.

Publications

- [1] T. I. Baiz, **C. P. Heinrich**, N. A. Banek, B. L. Vivekens, and C. Lind, "In-situ non-ambient X-ray diffraction studies of indium tungstate." *J. Solid State Chem.* **2012**, *187*, 195-199.
- [2] **C. P. Heinrich**, M. Panthöfer, and W. Tremel, "Ta₄FeTe₄: A new material for metallic single molecular wires?" *Eur. Phys. J. B*, **2012**, *85*, 221-227.
- [3] W. G. Zeier, A. LaLonde, Z. M. Gibbs, **C. P. Heinrich**, M. Panthöfer, G. J. Snyder, and W. Tremel, "Influence of a nano phase segregation on the thermoelectric properties of the *p*-type doped stannite compound Cu_{2+x}Zn_{1-x}GeSe₄." *J. Am. Chem. Soc.* **2012**, *134*, 7147-7154.
- [4] G. Kieslich, I. Veremchuk, I. Antonyshyn, W. G. Zeier, C. S. Birkel, K. Weldert, **C. P. Heinrich**, E. Visnow, M. Panthöfer, U. Burkhardt, Y. Grin, and W. Tremel, "Using crystallographic shear to reduce lattice thermal conductivity: high temperature thermoelectric characterization of the spark plasma sintered Magnéli phases WO_{2.90} and WO_{2.722}." *Phys. Chem. Chem. Phys.* **2013**, *15*, 15399-15403.
- [5] W. G. Zeier, Y. Pei, G. Pomrehn, T. Day, N. Heinz, **C. P. Heinrich**, G. J. Snyder, and W. Tremel, "Phonon scattering through a local anisotropic structural disorder in the thermoelectric solid solution Cu₂Zn_{1-x}Fe_xGeSe₄." *J. Am. Chem. Soc.* **2013**, *135*, 726-732.
- [6] **C. P. Heinrich**, T. W. Day, W. G. Zeier, G. J. Snyder, and W. Tremel, "Effect of Isovalent Substitution on the Thermoelectric Properties of the Cu₂ZnGeSe_{4-x}S_x Series of Solid Solutions." *J. Am. Chem. Soc.* **2014**, *136*, 442-448.
- [7] **C. P. Heinrich**, W. G. Zeier, T. Day, C. Panithipongwut, G. Kieslich, G. Brunklaus, G. J. Snyder, and W. Tremel, "Bond strength dependent superionic phase transformation in the solid solution series Cu₂ZnGeSe_{4-x}S_x." *J. Mater. Chem. A* **2014**, *2*, 1790-1794.

Publications

- [8] X. Zhou, **C. P. Heinrich**, M. Kluecker, S. Dolique, D. L. Mull, and C. Lind, "Non-hydrolytic sol-gel synthesis of tantalum sulfides." *J. Sol-Gel Sci. Technol.* **2014**, *69*, 596-604.
- [9] **C. P. Heinrich**, E. Visnow, A. Schmitz, P. Leidig, E. Müller, W. Tremel "Fast Two-step Synthesis of High Quality In-filled Skutterudites for Thermoelectric Applications" **2014** *in preparation*.
- [10] **C. P. Heinrich***, E. Visnow*, A. Schmitz, E. Müller, W. Tremel "Facile Top-Down Approach towards Nano-Bulk filled Skutterudite Materials" **2014** *in preparation*.
- [11] **C. P. Heinrich**, M. Schrade, I. Lieberwith, H. Fjeld, T. E. Norby, W. Tremel "Thermoelectric Properties and Optimization Strategies for *n*-type Tetragonal Tungsten Bronzes $\text{Nb}_{8-x}\text{W}_{9+x}\text{O}_{47-\delta}$ " **2014** *in preparation*.
- [12] **C. P. Heinrich**, Q. Guo, H. Kleinke, W. Tremel "Thermoelectric Properties of Olivine-type Ternary Fe_2GeS_4 " **2014** *in preparation*.

Acknowledgment

First of all, I want to thank my supervisor [REDACTED] for giving me the opportunity to work on this interesting research topic and the freedom to focus on whatever project I was most interested in. Beyond that, he was a very helpful advisor, supporting me and my ideas, and was always there to give useful advice whenever needed. I also want to thank my second advisor [REDACTED] for the great collaboration and especially for all the fruitful discussions. I never left a meeting at the DLR without having gained new perspectives, ideas and motivation.

I want to acknowledge the Graduate School of Excellence in Mainz (MAINZ) for the financial support throughout my doctoral thesis. Without this, I would not have been able to travel around the world, participate in summer schools, or attend to conferences, where I was able to establish the collaborations needed to conduct my research.

I would like to thank [REDACTED], [REDACTED], [REDACTED], [REDACTED] and the [REDACTED] at CalTech for the collaboration on the quaternary chalcogenide project. I learned so much from you. Thank you!

I want to express my gratitude to [REDACTED], [REDACTED], and [REDACTED] at the DLR for the great collaboration and the helpful discussions on the skutterudite project. Many thanks to [REDACTED] for helping me with the time consuming bulk synthesis and the characterizations, while I was abroad, and to [REDACTED] and [REDACTED] from the Research Center Jülich for the Mößbauer measurements. Thank you!

Further, I am indebted to [REDACTED] and [REDACTED] from the Group of [REDACTED] at the University of Oslo for the fruitful collaboration and many discussions on the oxide project. Without your input and technical advice the project would not have worked out so well. Many thanks as well to [REDACTED] for the HR-TEM Images. Thank you!

Moreover, I would like to thank [REDACTED] at the University of Waterloo, Ontario for inviting me and giving me the opportunity to conduct my research in his group. Many thanks as well to the group members for the hands-on training and help with the thermoelectric transport measurements. Thank you!

Thank you [REDACTED] and [REDACTED] for your help and the patience during all SEM/EDX sessions.

For helpful discussions and/or meticulous proof reading of my thesis I am thankful to (in alphabetical order): [REDACTED], [REDACTED], [REDACTED], [REDACTED], [REDACTED], [REDACTED], [REDACTED] and the

Acknowledgment

whole thermoelectric subgroup of the Tremel research group.

Furthermore, I want to thank the whole Tremel research group for a pleasant work climate, interesting scientific discussions and fun time during coffee breaks, group outings, BBQ's, parties, ...

At last, I want to express my gratitude to my family and especially to my wonderful wife [REDACTED] for the great support during my studies and my thesis. I know it was not always easy. Thank you!!!

Abstract

The goal of this work was to gain a deeper understanding of the structural chemistry of selected pnictide and chalcogenide thermoelectric materials. In the ongoing search for new materials for thermoelectric energy conversion, materials composed of inexpensive and earth abundant elements need to be explored and their thermoelectric efficiencies have to be improved. Different material classes provide diverse chemical optimization opportunities to enhance the thermoelectric properties. However, a profound knowledge of the underlying chemistry and the structure-property relationships is needed to seize these opportunities. This work focuses on three different material classes, that have been investigated with regard to their structural chemistry and their thermoelectric properties.

First, inspired by the thermoelectric properties of adamantine-like chalcogenides, the substitution series $\text{Cu}_2\text{ZnGeSe}_{4-x}\text{S}_x$ was investigated as a model system for isovalent anion substitutions. Throughout the substitution series, the induced changes of bonding character and structure, had a significant effect on several material properties. Thereby, the size of the band gap, the speed of sound, the phase transition temperature and the thermoelectric transport properties can be tuned. A phase transition was discovered throughout the complete solid solution series. Using variable temperature X-Ray diffraction and ^{63}Cu MAS-NMR we revealed that this phase transition is correlated to a superionic transition of Cu^+ ions, which get mobile at elevated temperatures. A detailed analysis of the thermal conductivity exhibited a 42% reduction of the room temperature lattice thermal conductivity due to disorder scattering. Further, the Callaway model was used to calculate the lattice thermal conductivity and revealed mass contrast to have a greater influence than strain contrast on these materials. Although no significant improvement of the thermoelectric figure of merit was obtained, important aspects of the structure-property relationships in adamantine-like materials were obtained, which will be of great use for future investigations.

Secondly, filled Skutterudites were investigated, which are a very promising and deeply investigated class of thermoelectric materials. To overcome the hitherto existing problems of long reaction times and material inhomogeneities, an easy two-step synthesis for indium-filled skutterudites was developed. By separating the kiefite host formation from the topotactic filler insertion, the reaction time was dramatically reduced and the formation of side phases was effectively circumvented. Thereby, an unadulterated investigation of the influence of the indium-filling degree on the structure and the thermoelectric properties was made possible. To this end,

Abstract

a series of indium-filled skutterudites $\text{In}_x\text{Co}_4\text{Sb}_{12}$ with nominal composition $x = 0.12, 0.15, 0.18$ and 0.20 were synthesized in bulk quantities. The structural and microstructural aspects of the obtained powders and short-time sintered pellets were investigated in addition to their thermal stability. The excellent sample homogeneity of the obtained materials were demonstrated via SEM/EDX, PSM measurements, ^{121}Sb Mößbauer spectroscopy, and powder X-Ray diffraction of standard laboratory and synchrotron data. Rietveld refinements revealed a marginal volume fraction of InSb in few samples, and allowed to determine the actual indium-filling degree. This enabled us to correlate the obtained transport data to the actual indium-filling degree and showed that the indium-filling has a positive effect on both, the electronic and thermal properties. The thermoelectric figure of merit was consequently enhanced up to a value close to unity at 420°C . Although a marginal presence of an InSb side phase ($\approx 0.1 \text{ vol}\%$) was revealed in some samples, this had no significant influence on the transport properties. Nevertheless, the resulting lower actual indium-filling degree had a dramatic effect on the thermoelectric properties, and resulted in a 18% reduction of the thermoelectric figure of merit. The detailed investigation of the thermoelectric properties revealed that a reduction of the lattice thermal conductivity by enhanced phonon scattering provides a very large optimization potential. For this reason, an easy, top-down approach towards indium-filled skutterudite nanoparticles has been developed. This enables the prospective investigation of nano-bulk skutterudite composite materials with electronically and phononically tailored properties.

Finally, the search for new, cheap and non-toxic, n -type thermoelectric materials has led us to the investigation of tetragonal tungsten bronzes. In this work, a first assessment of the potential of tetragonal tungsten bronzes for thermoelectric energy conversion was conducted. These compounds of general composition $\text{Nb}_{8-x}\text{W}_{9+x}\text{O}_{47-\delta}$ can be characterized by their infinitely adaptive structure. We chose this class of materials, due to their structural complexity, and high potential for electronic optimization by cation substitution (x) and controlled oxygen deficiency (δ). To this end, a series of compounds with low substitution degree $x = 0, 0.075, 0.1,$ and $1,$ was synthesized and structurally characterized by X-ray diffraction and high-resolution transmission electron microscopy. Further, the thermal stability and oxygen deficiency was analyzed using elaborated thermogravimetric analyses. Thermoelectric transport measurements revealed that both the cation substitution and the controlled oxygen defect concentration leads to enhanced electronic properties. Due to the complex structure, low, glass-like thermal conductivities were obtained, which resulted in an unoptimized figure of merit of 0.035 at 973 K in $\text{Nb}_7\text{W}_{10}\text{O}_{47}$. Although the obtained figure of merit was lower than in state of the art optimized n -type oxides,

the high Seebeck coefficient paired with the low, glass-like thermal conductivity and the yet to be exploited electronic optimization strategies demonstrates the potential of tetragonal tungsten bronzes for thermoelectric applications.

Zusammenfassung

Ziel dieser Arbeit war es ein tiefergehendes Verständnis der Strukturchemie von ausgewählten pnictogenen und chalkogenen thermoelektrischen Materialien zu gewinnen. Auf der Suche nach neuen thermoelektrischen Materialien gilt es, preiswerte und nachhaltige Verbindungen mit guten thermoelektrischen Eigenschaften zu entwickeln. Unterschiedliche Materialklassen bieten dabei verschiedene chemische Optimierungsmöglichkeiten, um die thermoelektrischen Eigenschaften zu verbessern. Um dieses Optimierungspotential nutzen zu können ist die genaue Kenntnis der zugrunde liegenden Chemie und der Struktur-Eigenschafts-Beziehungen unabdingbar. In dieser Arbeit wurden daher drei verschiedene Materialklassen hinsichtlich ihrer Strukturchemie und im Hinblick auf ihre thermoelektrischen Eigenschaften hin untersucht.

Angesichts der vielfältigen Substitutionsmöglichkeiten adamantanartiger quaternärer Chalkogenide, wurde zunächst die Mischkristallreihe $\text{Cu}_2\text{ZnGeSe}_{4-x}\text{S}_x$ als Modellsystem für isovalente Anionsubstitution untersucht. Die Substitution führte dabei sowohl zu einer Änderung des chemischen Bindungscharakters als auch zu strukturellen Veränderungen und ermöglichte es somit unterschiedliche Materialeigenschaften zu beeinflussen. So konnten sowohl die Größe der Bandlücke, die Schallgeschwindigkeit, die Temperatur des vorliegenden Phasenübergangs als auch die thermoelektrischen Eigenschaften beeinflusst werden. Bei allen Verbindungen der Mischkristallreihe konnte eine Phasenumwandlung detektiert werden. Mittels temperaturabhängiger Röntgendiffraktions- und ^{63}Cu MAS-NMR Messungen war es möglich diesen Phasenübergang mit einem Schmelzen des Cu-Untergitters zu korrelieren, was auf einen superionischen Phasenübergang schließen lässt. Eine detaillierte Analyse der bei Raumtemperatur gemessenen Wärmeleitfähigkeit ergab des Weiteren, dass je nach Substitutionsgrad eine Verringerung der Gitterwärmeleitfähigkeit von bis zu 42% möglich ist. Die für die Erniedrigung der Gitterwärmeleitfähigkeit ursächlichen Faktoren wurden mit Hilfe des Callaway Modells untersucht. Es konnte gezeigt werden, dass 34% der Erniedrigung auf den, durch die Substitution bedingten Massenkontrast und 8% auf den entstehenden Strainkontrast zurückzuführen sind. Zusammenfassend konnte keine Verbesserung der thermoelektrischen Gütezahl durch die Substitution von Selen durch Schwefel erzielt werden. Es wurden jedoch wichtige Struktur-Eigenschafts-Beziehungen aufgedeckt, die bei der zukünftigen Optimierung adamantanartiger Verbindungen von großem Nutzen sein werden.

Des Weiteren wurden gefüllte Skutterudite, eine viel erforschte und sehr erfolgsversprechende thermoelektrische Materialklasse, untersucht. Angesichts der

bisherigen Problematik von langen Reaktionszeiten und unreiner Materialsynthese, wurde in der vorliegenden Arbeit erstmals eine alternative zweistufige Synthese erarbeitet. Durch die effektive Trennung der Synthese des Kieftit-Gerüsts von der im Anschluss durchgeführten topotaktischen Insertion des Füllers, konnte sowohl die Reaktionszeit drastisch reduziert als auch die Entstehung von Nebenphasen effektiv umgangen werden. Damit wurde eine unverfälschte Untersuchung des Einflusses des Indium-Füllungsgrades auf die Struktur und die thermoelektrischen Eigenschaften erst ermöglicht. Es wurde eine Reihe von Indium gefüllten Skutteruditen $\text{In}_x\text{Co}_4\text{Sb}_{12}$ mit nomineller Zusammensetzung $x = 0,12, 0,15, 0,18$ und $0,20$ dargestellt. Die hergestellten Pulver wurden ebenso wie die gesinterten Pellets hinsichtlich ihrer Struktur, des Gefüges und der Temperaturstabilität untersucht. Dabei konnte die herausragende Homogenität der hergestellten Materialien mittels SEM/EDX, PSM, ^{121}Sb Mößbauer und Synchrotron-Röntgendiffraktion belegt werden. Zudem konnte durch die Verfeinerung der Indium-Lage ein Rückschluss auf den effektiven Indium-Füllungsgrad gewonnen werden. Es konnte gezeigt werden, dass sich ein erhöhter Indium-Füllungsgrad sowohl positiv auf die elektronischen als auch auf die thermischen Eigenschaften auswirkt, was folglich zu einer thermoelektrische Gütezahl von nahezu 1 bei 420°C führte. Mit Hilfe der Synchrotron Daten konnten sehr geringe Mengen an InSb in wenigen Proben nachgewiesen werden. Obwohl InSb als Nebenphase mit nur $\approx 0,1$ vol% Gesamtanteil keinen signifikanten Einfluss auf die Transporteigenschaften hat, konnte gezeigt werden, dass der hieraus resultierende niedrigere effektive Füllungsgrad eine um 18% erniedrigte Gütezahl zur Folge hatte. Eine detaillierte Untersuchung der Wärmeleitfähigkeit ergab schließlich, dass die Erniedrigung der Gitterwärmeleitfähigkeit ein sehr großes Optimierungspotential bietet. Aus diesem Grund wurde eine einfache top-down Methode entwickelt, um Nanopartikel von Indium gefüllten Skutteruditen in größerem Maßstab darzustellen.

Zudem wurden tetragonale Wolframbronzen als neuartige *n*-typ oxydische Thermoelektrika untersucht. Die Verbindungen mit der allgemeinen Zusammensetzung $\text{Nb}_{8-x}\text{W}_{9+x}\text{O}_{47-\delta}$ zeichnen sich durch ihre komplexe, aber einander ähnliche Struktur aus. Aufgrund ihrer strukturellen Komplexität und der Möglichkeit sowohl durch Substitution (x) als auch durch Kontrolle des Sauerstoffdefizites (δ) einen Einfluss auf die elektronischen Eigenschaften zu nehmen, bieten die tetragonalen Wolframbronzen gute Voraussetzungen als Thermoelektrika. Ziel der Arbeit war es zu ermitteln, ob tetragonalen Wolframbronzen brauchbare thermoelektrische Eigenschaften besitzen und mögliche Optimierungsstrategien zu evaluieren. Hierzu wurde eine Reihe von Verbindungen mit niedrigem Substitutionsgrad $x = 0, 0,075, 0,1$ und 1 , synthetisiert und mittels Röntgenbeugung und hochauflösender Elektronenmikroskopie strukturell

Zusammenfassung

analysiert. Weiterhin wurden mittels thermogravimetrischen Messungen die thermische Stabilität und der Einfluss des Sauerstoffpartialdruckes auf die Anzahl der Sauerstoffdefekte untersucht. Thermoelektrische Transportmessungen zeigten, dass sowohl durch Kationensubstitution als auch durch Kontrolle des Sauerstoffdefizites eine Verbesserung der elektronischen Eigenschaften erzielt werden konnte. Die komplexe Struktur dieser Materialien resultierte in niedrigen glas-artigen Werten der Wärmeleitfähigkeit. Daher konnte bereits initial eine thermoelektrische Gütezahl von 0,035 mit der Verbindung $\text{Nb}_7\text{W}_{10}\text{O}_{47}$ bei 973 K erzielt werden. Zwar lag der erhaltene zT Wert noch deutlich unter dem anderer etablierter n -typ Oxide, so ist doch für optimierte tetragonale Wolframbronzen ein deutlich höherer zT Wert zu erwarten.

Contents

Publications	V
Acknowledgment	VII
Abstract	IX
Zusammenfassung	XII
Table of Contents	XV
List of Figures	XIX
List of Tables	XXV
Nomenclature	XXVII
1. Introduction	1
1.1. Basic Thermoelectric Phenomena	2
1.2. Transport in Solids	5
1.2.1. Electronic Transport	5
1.2.2. Thermal Transport	7
1.3. Thermoelectric Figure of Merit	13
1.4. Thermoelectric Optimization Strategies	15
1.4.1. Optimization of the Seebeck Coefficient	16
1.4.2. Thermal Optimization	19
1.5. Pertinent Materials	20
1.5.1. Quaternary Chalcogenides $\text{Cu}_2\text{ZnGeSe}_{4-x}\text{S}_x$	20
1.5.2. Indium-filled Skutterudites $\text{In}_x\text{Co}_4\text{Sb}_{12}$	23
1.5.3. Tetragonal Tungsten Bronzes $\text{Nb}_{8-x}\text{W}_{9+x}\text{O}_{47}$	26

2. Quaternary Chalcogenides	31
2.1. Motivation	31
2.2. Experimental Details and Methods	32
2.3. Results and Discussion	34
2.3.1. Chemical Characterization	34
2.3.2. Electronic Transport Properties	38
2.3.3. Thermal Transport Properties	41
2.3.4. Superionic Phase Transition	44
2.4. Conclusions and Outlook	47
3. Indium-filled Skutterudites	49
3.1. Motivation	49
3.2. Experimental Details and Methods	50
3.3. Results and Discussion	53
3.3.1. Two-step Synthesis of Indium-filled Skutterudites	53
3.3.2. Structural Characterization of Bulk Indium-filled Skutterudites	56
3.3.3. Thermoelectric Properties of Bulk Indium-filled Skutterudites	65
3.3.4. Top-down Approach towards Indium-filled Skutterudite Nanoparticles	72
3.4. Conclusions and Outlook	77
4. Tetragonal Tungsten Bronzes	81
4.1. Motivation	81
4.2. Experimental Details and Methods	82
4.3. Results and Discussion	84
4.3.1. Synthesis and Chemical Characterization	84
4.3.2. Thermal Stability and Oxygen Deficiency	88
4.3.3. Thermoelectric Transport Properties and Optimization Strategies	91
4.4. Conclusions and Outlook	96

Supporting Information	99
A. Quaternary Chalcogenides	99
A.1. Refined X-ray Diffraction Data	100
A.2. Differential Scanning Calorimetry	102
A.3. UV-Vis Data	104
A.4. Thermal Conductivity Data	106
B. Indium-filled Skutterudites	109
B.1. EDX & PSM	109
B.2. Refined Synchrotron Data	110
B.3. ¹²¹ Sb-Möbbaauer Spectra	115
B.4. Thermoelectric Transport Data	117
B.5. Nanoparticle Synthesis	121
C. Tetragonal Tungsten Bronzes	123
C.1. Refined X-ray Diffraction Data	124
C.2. SEM and HR-TEM Images	125
C.3. Thermal Stability and TE Properties	128
Bibliography	129
Curriculum Vitae	141

List of Figures

1.1. Schematic of the thermovoltage arising due to the Seebeck effect and a simple thermopile.	3
1.2. Illustration of the monatomic chain model.	8
1.3. Phonon dispersion curves for monatomic (N=1) and multiaatomic (N>1) 1-dim. lattices.	9
1.4. Overview of the zT values of some state of the art <i>n</i> -type and <i>p</i> -type thermoelectric materials.	14
1.5. Influence of the charge carrier concentration on the thermoelectric properties.	16
1.6. Influence of multiple bands and resonant impurities on the density of states.	17
1.7. Example for band engineering of PbTe.	18
1.8. Influence of the size of the band gap on the figure of merit.	18
1.9. Spectral thermal conductivity.	19
1.10. Structure relationships in the adamantine structure family.	21
1.11. Illustration of the filled skutterudite crystal structure.	24
1.12. Figure of merit of state of the art oxide thermoelectric materials.	26
1.13. Threefold supercell of the tetragonal tungsten bronze structure.	28
2.1. Powder X-ray data of the solid solution series $\text{Cu}_2\text{ZnGeSe}_{4-x}\text{S}_x$	35
2.2. Refined atomic coordinates of the chalcogen position in the solid solution series $\text{Cu}_2\text{ZnGeSe}_{4-x}\text{S}_x$	36
2.3. Metal-chalcogen-metal bond angles in the solid solution series $\text{Cu}_2\text{ZnGeSe}_{4-x}\text{S}_x$	37
2.4. Kubelka-Munk band gap estimation of the solid solution series $\text{Cu}_2\text{ZnGeSe}_{4-x}\text{S}_x$	38

List of Figures

2.5. Temperature dependent electrical resistivity ρ of the solid solution series $\text{Cu}_2\text{ZnGeSe}_{4-x}\text{S}_x$	39
2.6. Temperature dependent Seebeck coefficient S of the solid solution series $\text{Cu}_2\text{ZnGeSe}_{4-x}\text{S}_x$	40
2.7. Temperature dependent thermal conductivity κ of the solid solution series $\text{Cu}_2\text{ZnGeSe}_{4-x}\text{S}_x$	41
2.8. Measured and modeled room temperature lattice thermal conductivity κ_{lat} of the solid solution series $\text{Cu}_2\text{ZnGeSe}_{4-x}\text{S}_x$	42
2.9. Longitudinal, transversal, and calculated mean sound velocity of the solid solution series $\text{Cu}_2\text{ZnGeSe}_{4-x}\text{S}_x$	43
2.10. Refined lattice parameters a and c of $\text{Cu}_2\text{ZnGeSe}_{4-x}\text{S}_x$ as a function of temperature.	45
2.11. Temperature dependent ^{63}Cu magic angle spinning nuclear magnetic resonance of the stannite type $\text{Cu}_2\text{ZnGeSe}_4$	46
3.1. Phase diagram of the binary Co-Sb system.	53
3.2. Refined powder diffraction data of CoSb_3	55
3.3. Scanning electron microscopy image of synthesized $\text{In}_x\text{Co}_4\text{Sb}_{12}$ bulk powder and pellet.	57
3.4. PSM measurement of $\text{In}_{0.18}\text{Co}_4\text{Sb}_{12}$	58
3.5. Refined powder diffraction data of $\text{In}_{0.12}\text{Co}_4\text{Sb}_{12}$ and $\text{In}_{0.20}\text{Co}_4\text{Sb}_{12}$	60
3.6. Refined indium-filling degree vs lattice parameter and refined lattice parameter vs measurement cycle.	62
3.7. ^{121}Sb Mößbauer spectrum of $\text{In}_{0.20}\text{Co}_4\text{Sb}_{12}$	63
3.8. Temperature dependence of the electrical conductivity from indium-filled skutterudites $\text{In}_x\text{Co}_4\text{Sb}_{12}$	65
3.9. Temperature dependence of the Seebeck coefficient from indium-filled skutterudites $\text{In}_x\text{Co}_4\text{Sb}_{12}$	66
3.10. Temperature dependence of the power factor of indium-filled skutterudites $\text{In}_x\text{Co}_4\text{Sb}_{12}$	68

3.11. Temperature dependence of the total thermal conductivity of indium-filled skutterudites $\text{In}_x\text{Co}_4\text{Sb}_{12}$	69
3.12. Dependence of the electronic and lattice thermal conductivity on the indium-filling degree of skutterudites $\text{In}_x\text{Co}_4\text{Sb}_{12}$	70
3.13. Temperature dependence of the thermoelectric figure of merit from indium-filled skutterudites $\text{In}_x\text{Co}_4\text{Sb}_{12}$	71
3.14. CoSb_3 nanoparticles obtained by ultra fine colloidal grinding.	75
3.15. Refined powder diffraction data for bulk and nano $\text{In}_{0.18}\text{Co}_4\text{Sb}_{12}$	76
3.16. $\text{In}_{0.18}\text{Co}_4\text{Sb}_{12}$ nanoparticles obtained by ultra fine colloidal grinding.	76
4.1. Leball fit for the powder diffraction data of $\text{Nb}_8\text{W}_9\text{O}_{47}$	85
4.2. Scanning electron microscopy images of the as-synthesized powder (left) and the consolidated pellet (right).	86
4.3. HR TEM images of $\text{Nb}_{8-x}\text{W}_{9+x}\text{O}_{47-\delta}$	87
4.4. Thermal stability of $\text{Nb}_8\text{W}_9\text{O}_{47}$ under different $p\text{O}_2$	89
4.5. Redox reaction of $\text{Nb}_8\text{W}_9\text{O}_{47-\delta}$ monitored by thermogravimetric analysis.	90
4.6. Temperature dependence of the electronic transport properties from the substitution degree in TTB.	92
4.7. Temperature dependence of the thermal diffusivity and conductivity from the substitution degree in TTB.	93
4.8. Temperature dependence of the power factor and the thermoelectric figure of merit from the substitution degree in TTB.	94
4.9. Electronic transport properties after controlled oxidization and reduction cycles.	95
A.1. Crystal structure of the stannite type $\text{Cu}_2\text{ZnGeSe}_{4-x}\text{S}_x$	99
A.2. Refined powder diffraction data of $\text{Cu}_2\text{ZnGeSe}_3\text{S}$	100
A.3. Refined powder diffraction data of $\text{Cu}_2\text{ZnGeSe}_2\text{S}_2$	100
A.4. Refined powder diffraction data of $\text{Cu}_2\text{ZnGeSeS}_3$	101
A.5. Refined powder diffraction data of $\text{Cu}_2\text{ZnGeS}_4$	101
A.6. DSC/TG measurement of $\text{Cu}_2\text{ZnGeSe}_3\text{S}$	102
A.7. DSC/TG measurement of $\text{Cu}_2\text{ZnGeSe}_2\text{S}_2$	102

List of Figures

A.8. DSC/TG measurement of $\text{Cu}_2\text{ZnGeSeS}_3$	103
A.9. DSC/TG measurement of $\text{Cu}_2\text{ZnGeS}_4$	103
A.10. Superionic phase transition temperatures in dependence of the substitution degree.	104
A.11. Kubelka-Munk band gap estimation of $\text{Cu}_2\text{ZnGeSe}_3\text{S}$	104
A.12. Kubelka-Munk band gap estimation of $\text{Cu}_2\text{ZnGeSe}_2\text{S}_2$	105
A.13. Kubelka-Munk band gap estimation of $\text{Cu}_2\text{ZnGeSeS}_3$	105
A.14. Kubelka-Munk band gap estimation of $\text{Cu}_2\text{ZnGeS}_4$	106
A.15. Thermal conductivity data of $\text{Cu}_2\text{ZnGeSe}_3\text{S}$	106
A.16. Thermal conductivity data of $\text{Cu}_2\text{ZnGeSe}_2\text{S}_2$	107
A.17. Thermal conductivity data of $\text{Cu}_2\text{ZnGeSeS}_3$	107
A.18. Thermal conductivity data of $\text{Cu}_2\text{ZnGeS}_4$	108
A.19. Refined metal-chalcogen bond distances of the solid solution series $\text{Cu}_2\text{ZnGeSe}_{4-x}\text{S}_x$	108
B.1. EDX measurement of $\text{In}_x\text{Co}_4\text{Sb}_{12}$ powder.	109
B.2. PSM Histogram of measured Seebeck coefficients.	110
B.3. Refined powder diffraction data of $\text{In}_{0.12}\text{Co}_4\text{Sb}_{12}$	110
B.4. Refined powder diffraction data of sintered $\text{In}_{0.12}\text{Co}_4\text{Sb}_{12}$	111
B.5. Refined powder diffraction data of $\text{In}_{0.12}\text{Co}_4\text{Sb}_{12}$ after the first thermoelectric characterization cycle.	111
B.6. Refined powder diffraction data of $\text{In}_{0.12}\text{Co}_4\text{Sb}_{12}$ after the second thermoelectric characterization cycle.	112
B.7. Refined powder diffraction data of $\text{In}_{0.12}\text{Co}_4\text{Sb}_{12}$ after the third thermoelectric characterization cycle.	112
B.8. Refined powder diffraction data of $\text{In}_{0.15}\text{Co}_4\text{Sb}_{12}$	113
B.9. Refined powder diffraction data of $\text{In}_{0.18}\text{Co}_4\text{Sb}_{12}$	113
B.10. Refined powder diffraction data of $\text{In}_{0.20}\text{Co}_4\text{Sb}_{12}$	114
B.11. ^{121}Sb Mößbauer spectrum of $\text{In}_{0.12}\text{Co}_4\text{Sb}_{12}$ powder.	115
B.12. ^{121}Sb Mößbauer spectrum of the $\text{In}_{0.12}\text{Co}_4\text{Sb}_{12}$ pellet.	115
B.13. ^{121}Sb Mößbauer spectrum of $\text{In}_{0.20}\text{Co}_4\text{Sb}_{12}$ powder.	116

B.14. ^{121}Sb Mößbauer spectrum of CoSb_3	116
B.15. Cycling behavior of the electronic conductivity of $\text{In}_{0.12}\text{Co}_4\text{Sb}_{12}$	117
B.16. Cycling behavior of the electronic conductivity of $\text{In}_{0.15}\text{Co}_4\text{Sb}_{12}$	117
B.17. Cycling behavior of the electronic conductivity of $\text{In}_{0.18}\text{Co}_4\text{Sb}_{12}$	118
B.18. Cycling behavior of the electronic conductivity of $\text{In}_{0.20}\text{Co}_4\text{Sb}_{12}$	118
B.19. Cycling behavior of the Seebeck coefficient of $\text{In}_{0.12}\text{Co}_4\text{Sb}_{12}$	119
B.20. Cycling behavior of the Seebeck coefficient of $\text{In}_{0.15}\text{Co}_4\text{Sb}_{12}$	119
B.21. Cycling behavior of the Seebeck coefficient of $\text{In}_{0.18}\text{Co}_4\text{Sb}_{12}$	120
B.22. Cycling behavior of the Seebeck coefficient of $\text{In}_{0.20}\text{Co}_4\text{Sb}_{12}$	120
B.23. Refined crystallite size distribution in dependence of the milling time.	121
C.1. Pseudo-binary phase diagram of Nb_2O_5 and WO_3	123
C.2. Lebail fit for the powder diffraction data of $\text{Nb}_{7.925}\text{W}_{9.075}\text{O}_{47}$	124
C.3. Lebail fit for the powder diffraction data of $\text{Nb}_{7.9}\text{W}_{9.1}\text{O}_{47}$	124
C.4. Lebail fit for the powder diffraction data of $\text{Nb}_7\text{W}_{10}\text{O}_{47}$	125
C.5. Zoomed-in SEM image of cavities in consolidated TTB pellets.	125
C.6. HR TEM images of $\text{Nb}_{8-x}\text{W}_{9+x}\text{O}_{47-\delta}$	126
C.7. HR TEM images of $\text{Nb}_{8-x}\text{W}_{9+x}\text{O}_{47-\delta}$	127
C.9. Temperature dependent heat capacity of $\text{Nb}_{8-x}\text{W}_{9+x}\text{O}_{47}$	128
C.8. Thermal stability of $\text{Nb}_8\text{W}_9\text{O}_{47}$	128

List of Tables

1.1. Crystallographic data of stannite-type $\text{Cu}_2\text{M}^{\text{II}}\text{M}^{\text{IV}}\text{X}_4$	22
1.2. Crystallographic data of kesterite-type $\text{Cu}_2\text{M}^{\text{II}}\text{M}^{\text{IV}}\text{X}_4$	22
2.1. Refined lattice parameters, c/a ratio, cell volume, and respective R_{wp} -value of the solid solution series $\text{Cu}_2\text{ZnGeSe}_{4-x}\text{S}_x$	36
3.1. Refined weighted profile residual, goodness of fit, lattice parameter a , y - and z - coordinates of the Sb site and vol% of InSb side phase.	61
3.2. Refined site occupancies and isotropic atomic temperature factor of In, Co and Sb.	61
3.3. Refined ^{121}Sb Mößbauer parameters of CoSb_3 , $\text{In}_{0.12}\text{Co}_4\text{Sb}_{12}$, and $\text{In}_{0.20}\text{Co}_4\text{Sb}_{12}$	64

Nomenclature

α_T	isothermal expansion coefficient
χ	molar fraction
ϵ	fitting parameter
ϵ_F	fermi energy
$\frac{\Delta a}{a}$	local change in lattice parameter
$\frac{\Delta M}{M}$	relative change of atomic mass
Γ	disorder scattering parameter
γ	Grüneisen parameter
κ	thermal conductivity
$\kappa^{bipolar}$	bipolar contribution to the thermal conductivity
κ_{el}	electronic contribution to the thermal conductivity
κ_{lat}	lattice thermal conductivity
κ_{lat}^{pure}	lattice thermal conductivity of a non-disordered crystal
κ_{tot}	total thermal conductivity
μ	mobility
μ_T	Thomson coefficient
∇T	temperature gradient
ν_m	average sound velocity
Ω	average volume per atom
ω	frequency
$\pi_{a,b}$	Peltier coefficient
ρ	electrical resistivity
σ	electric conductivity
τ	scattering relaxation time
Θ_D	Debye-Temperature
a	lattice parameter a
a_0	lattice parameter a in equilibrium condition
<i>ANL</i>	Argonne National Laboratory
<i>APS</i>	Advanced Photon Source
B	quality factor
b	lattice parameter b
B_T	isothermal bulk modulus
C	heat capacity

Nomenclature

c	lattice parameter c
<i>CalTech</i>	California Institute of Technology
<i>DLR</i>	Deutsches Zentrum für Luft- und Raumfahrt e.V.
<i>DOS</i>	density of states
dq_P	Peltier heat
dq_T	Thomson heat
<i>DSC</i>	differential scanning calorimetry
E	electric field
e	charge of a charge carrier
<i>EDX</i>	energy dispersive X-ray spectroscopy
<i>ETD</i>	Everhard-Thornley detector
f	distribution function
h	Planck constant
<i>HT – S – σ2</i>	High Temperature Seebeck- and Sigma-measuring system
i^+	strength of current
k	wave vector
k_B	Boltzmann constant
K_s	spring constant
L	Lorenz number
l	mean free path
m^*	effective mass
m_b^*	band effective mass
<i>MAS – NMR</i>	magic angle spinning nuclear magnetic resonance
n	charge carrier concentration
N_V	band degeneracy
p	momentum
<i>PSM</i>	Potential-Seebeck-Microprobe
q	heat flow
q_j	joule heat
R	diffuse reflectance
R_{wp}	weighted profile residual value
<i>RTG</i>	radioisotope thermoelectric generator
S	Seebeck coefficient
<i>SoS</i>	speed of sound
T	absolute temperature
<i>TEG</i>	thermoelectric generator
<i>TGA</i>	thermogravimetric analysis

u	disorder scaling parameter
V	voltage
v_d	drift velocity
vCD	low voltage high contrast detector
W	power
zT	figure of merit

1

Introduction

The research area of thermoelectrics is a vast and interdisciplinary field of material science dealing with the conversion of energy through the thermoelectric transport phenomena. Although the basic principles have been known for over a century, physicists, chemists, and engineers still find challenges in this diverse research area. With the steadily receding supply of fossil fuels and the associated increasing costs, renewable energy technologies have experienced an increased interest in the last 20 years. Thermoelectric generators (TEG), which are capable to convert heat energy directly into electrical energy, have the potential to improve the efficiency of every waste heat producing process. [1–4] Furthermore, the high reliability of a TEG, due to the absence of any moving parts has been proven in spacecraft, where RTGs (radioisotope thermoelectric generators) have been used since 1961. [5] However, large scale commercial use has been limited so far by the low efficiency of the materials used in TEG. Therefore, a profound knowledge of thermoelectric materials and the establishment of structure property relationships are needed to design new and optimize known thermoelectric materials with higher efficiencies.

This thesis comprises both, the investigation of known thermoelectric materials to obtain a deeper understanding of the respective structure-property relationships and the investigation of a new thermoelectric material to gauge its potential use for thermoelectric application. The comprehensive goal in all materials investigated for this thesis was to control and lower their thermal conductivity and to design materials with inherently low thermal conductivities.

Introduction

In Chapter 1, the basic theory and concepts of the thermoelectric phenomena, the transport in solids, and their use for thermoelectric energy conversion are introduced. Furthermore, different strategies for material optimization are established, and the challenges in developing new highly efficient thermoelectric materials are illustrated. The Chapters 2-4 can be read independently, and are divided into the three material classes investigated for this thesis. The Chapters 2 and 3 deal with the two already established thermoelectric material classes, whereas chapter 4 comprises the work on the "new" material not investigated for thermoelectric application so far. In the 2nd Chapter, the synthesis and characterization of the anion substituted solid solution series $\text{Cu}_2\text{ZnGeSe}_{4-x}\text{S}_x$ is reported. The influence of the substitution on the structure, the thermoelectric properties and the newly discovered superionic phase transformation are discussed. Chapter 3 covers the investigation of In-filled skutterudites $\text{In}_x\text{Co}_4\text{Sb}_{12}$. A fast two-step synthesis of bulk quantity, phase pure filled skutterudite material and a top down approach to filled skutterudite nanoparticles has been elaborated. In this chapter the synthesis, processing and characterization of In-filled bulk and nano-bulk composite materials are treated, with a focus on the thermal stability and the influence of the indium-filling degree on the structure and thermoelectric properties. Chapter 4 comprises the evaluation of tetragonal tungsten bronzes (TTB) $\text{Nb}_{8-x}\text{W}_{9+x}\text{O}_{47}$ as a thermoelectric material. The synthesis, processing and structural characterization of TTB compounds are discussed. Further the thermal stability and controlled oxygen deficiency are investigated. To conclude, the influence of the cation substitution and the oxygen deficiency, on the thermoelectric transport properties were analyzed to gauge the thermoelectric potential of the tetragonal tungsten bronzes.

1.1. Basic Thermoelectric Phenomena

In principle, there are two basic ways to investigate the properties of an electrical conductor or semiconductor: with an electric field, with a temperature gradient, or with both. Applying an electric field E to a conductor will result in an electric current. The current density J_e will be proportional to the applied electric field. When no temperature gradient is present, the proportionality factor is the electrical conductivity σ . [6]

$$J_e = \sigma E \tag{1.1}$$

Analogous to this, if a temperature gradient ∇T is applied, a flow of heat q results.

When no electrical current is allowed, the heat flow per unit area is proportional to the temperature gradient, with the thermal conductivity κ as proportionality factor. [6]

$$q = \kappa \nabla T \tag{1.2}$$

In addition to the electric and thermal conductivity, there is a third phenomenon, which causes an electric flow in response to a temperature gradient. This effect was first demonstrated in 1821 by Thomas Johann Seebeck. He discovered that a compass needle deflects, when a temperature gradient is applied to a conductor loop of dissimilar metals. [7–11] However, Seebeck did not realize that the magnetic field was induced by a thermo current and, therefore, named the effect thermomagnetic effect. H. C. Oersted corrected his mistake and introduced the term *thermoelectricity*. In honor of Seebeck, the phenomenon of an arising potential in a conductor after the application of a temperature gradient was named the Seebeck effect. The occurrence of the Seebeck effect can be explained by thermodiffusion. Analogous to gas in a

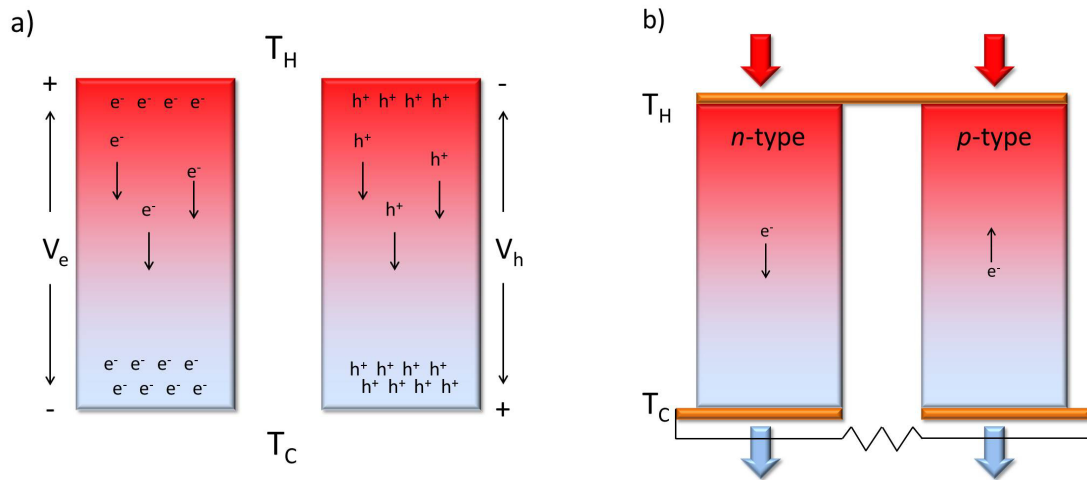


Figure (1.1) – a) Schematic of the thermovoltage arising due to the Seebeck effect. In response to a temperature gradient, charge carriers diffuse from the hot end to the cold end until the resulting thermoelectric voltage is canceled by the heat flux. b) Schematic of a simple thermopile in a TEG, consisting of one n- and p-type leg.

closed tube, charge carriers (electrons or holes) are enclosed in a conductive material. If a temperature gradient is applied, the gas molecules on the hot end side will have a higher velocity than those on the cold end side. Thus, the hot gas expands, and the cold gas contracts, resulting in a net flow of gas molecules from the hot to the cold side.

Figure 1.1 a displays this analogy of charge carriers to gas molecules. The diffusion of charge carriers from the hot end to the cold end causes a thermoelectric voltage

Introduction

to be built. The flow of charge carriers will occur until the heat flux is canceled by the resulting voltage V . The thermoelectric voltage is found to be proportional to the temperature difference ΔT , with the Seebeck coefficient S (or thermopower) as the proportionality factor.

$$V = S \cdot \Delta T \quad (1.3)$$

More accurately, the Seebeck coefficient is temperature dependent, and therefore the linear expression of equation 1.3 is only valid for small temperature differences:

$$V = \int_{T_1}^{T_2} S(T) dT \quad (1.4)$$

The Seebeck coefficient is positive when the majority of the charge carriers are holes (p -type) and is negative when the dominating charge carrier type are electrons (n -type). Like the electric and thermal conductivity, the Seebeck coefficient is an intrinsic, material-specific property. Because it can only be measured in contact with another material (i.e. under closed circuit conditions) a common misconception is that a junction between two materials is necessary for a thermoelectric voltage to occur. The voltage arising in one piece (or leg) of an n - or p -type material is usually rather low. However, by combining p - and n -type materials electrically in series and thermally in parallel, the voltages of every single leg sum up to a voltage large enough to use. Figure 1.1 b) illustrates the coupling of n - and p -type legs to a thermoelectric generator.

Considering the situation where an electric current flows from a substance A to a substance B, heat may either be emitted or be absorbed at the junction, depending on the direction of the current. [6] This effect was reported in 1834 by the French physicist Jean Charles Athanase Peltier. [12] He passed a current through a bismuth-antimony thermocouple and found that the transported heat (Peltier heat) dq_P was proportional to the magnitude i^+ and the duration of the external current. The proportionality factor is called the Peltier coefficient $\pi_{a,b}$. [8]

$$dq_P = \pi_{a,b} i^+ \quad (1.5)$$

In contrast to the irreversible joule heating q_j , which occurs when a current is passed across a conductor with the resistivity ρ ($q_j = J_e \rho$), the Peltier effect and the Seebeck effect are reversible processes. However, the Peltier effect is not the reverse of the Seebeck effect, which is a common misconception. The Peltier effect only occurs under flowing current; in contrast, the Seebeck effect is only responsible

for building up a potential, independent of whether the potential is used to drive a current, or not. [6] The thermodynamic connection between the Seebeck and the Peltier effect was established by William Thomson (later *Lord Kelvin*) in 1854. [13] He tried to derive a connection between the two effects using the first and second laws of thermodynamics and found that a third thermoelectric phenomenon was needed to bring the experimental results and theory into conformity. The third thermoelectric effect, the Thomson effect, states that heat is absorbed or emitted (dq_T) if a current passes across a conductor when a temperature gradient ∇T is present. [6] The Thomson coefficient μ_T is temperature dependent and has a positive sign if heat is absorbed.

$$dq_T = \mu_T J_e \nabla T \quad (1.6)$$

1.2. Transport in Solids

1.2.1. Electronic Transport

In the Drude model, electrons are described as a gas moving through the lattice of a solid. The electric conductivity is dependent of the concentration of charge carriers n moving with a drift velocity v_d in the direction of an applied electric field E . The drift velocity can be written as: [14]

$$v_d = \frac{e\tau E}{m^*} \quad (1.7)$$

with the carried charge e , the scattering relaxation time τ , and the effective carrier mass m^* . With this, the current density J_e (charge per area per time) can be described as the multiplication of the charge carrier concentration n , the transported charge per carrier e and the drift velocity v_d : [14]

$$J_e = nev_d \quad (1.8)$$

with Ohm's law (equation 1.1), an expression for the electrical conductivity is found. [14]

$$\sigma = \frac{ne^2\tau}{m^*} = en\mu \quad (1.9)$$

Equation 1.9 shows the dependences of the electrical conductivity, which rises with charge carrier concentration and scattering relaxation time, but decreases with the

Introduction

effective mass. Using the definition of the carrier mobility μ : [14]

$$\mu = \frac{e\tau}{m^*} \quad (1.10)$$

the electrical conductivity can be rewritten in the more common expression:

$$\sigma = en\mu \quad (1.11)$$

In general, not all charge carriers in a band contribute to the electronic transport. Usually, only carriers within a few $k_B T$ (Boltzmann constant $k_B = 1,3806 \times 10^{-23} JK^{-1}$) of the electrochemical potential are able to contribute significantly. Electronic transport is usually described by the solutions of the Boltzmann transport equations (BTE) under the relaxation time approximation. [14] The non equilibrium electron distribution is approximated by a Fermi-Dirac distribution function f : [15]

$$f = \frac{1}{(1 + \exp[\epsilon - \eta])} \quad (1.12)$$

with the reduced energy ($\epsilon = \frac{E}{k_B T}$) and the reduced electrochemical potential η . At 0 K the highest occupied energy level represents the Fermi energy ϵ_F , and the electrochemical potential is the energy (for $T > 0$ K) at which half of the states are occupied ($f = 1/2$). [16] Within the single parabolic band model (SPB), the carrier energies can be described by an isotropic, periodic dispersion relation. [17] In band theory, free delocalized electrons are described as waves in the periodic lattice potential. The superposition of the possible wave functions (Bloch functions) leads to the band structure. A band gap arises from the energy difference of either non-interacting atomic orbitals or from bonding and antibonding interactions. The energy of the bands can be plotted as a function of the wave vector k , which gives the band dispersion. The wave vector is related to the momentum p of an electron via: [17]

$$k = \hbar p \quad (1.13)$$

Conduction arises when a band is partially filled, enabling electrons to move from an occupied to an unoccupied state of similar energy. The energy dispersion of a band is given by the dispersion relation: [17]

$$E(k) = V_0 + \frac{\hbar^2 k^2}{2m^*} \quad (1.14)$$

The density of states $N(E)$ for a parabolic dispersion relation is given by:

$$N(E) = \frac{(2m^*)^{3/2}}{2\pi^2\hbar^3} \sqrt{E} \quad (1.15)$$

while the effective mass of an electron in a parabolic band is defined by: [17]

$$1/m^* = \frac{1}{\hbar^2} \frac{\partial^2 E(k)}{\partial k^2} \quad (1.16)$$

Following equation 1.16, the effective mass is dependent on the curvature of the energy dispersion, hence the effective mass decreases with increasing band dispersion. In a wide band, the electrons are free, delocalized particles. A narrow band, however, has more localized electrons, due to the higher effective mass. [17] For details on the solutions of the Boltzmann transport equations within the single parabolic band approximation, the reader is referred to more comprehensive reviews. [16, 18]

1.2.2. Thermal Transport

The total thermal conductivity κ_{tot} of a solid arises due to different phenomena and can be written as the sum of the electronic contribution κ_{el} , the bipolar contribution $\kappa_{bipolar}$ and the lattice contribution κ_{lat} to the thermal conductivity. [19]

$$\kappa_{tot} = \kappa_{el} + \kappa_{lat} + \kappa_{bipolar} \quad (1.17)$$

Charge carriers, moving across a material, transport some amount of heat and are responsible for the electronic and bipolar contribution to the thermal conductivity. The bipolar contribution is often insignificant and is usually omitted. The electronic contribution to the thermal conductivity depends directly on the electrical conductivity, which is expressed by the Wiedemann-Franz law: [3, 20, 21]

$$\kappa_{el} = L\sigma T = Lne\mu T \quad (1.18)$$

with the Lorenz number L (for free electrons $L = \frac{\pi^2 k_B^2}{3e^2} = 2,44 \times 10^{-8} W\Omega K^{-2}$ [22]), the charge carrier concentration n , the electron charge e , and the electron mobility μ . If the temperature dependent electronic conductivity is known, the lattice contribution to the thermal conductivity can be calculated directly by subtracting the electronic contribution from the total thermal conductivity ($\kappa_{lat} = \kappa_{tot} - \kappa_{el}$). An upturn in the lattice thermal conductivity at higher temperatures can usually be attributed

Introduction

to the unaccounted for bipolar contribution. For a more detailed description of the electronic and bipolar contribution to the thermal conductivity, the reader is referred to comprehensive reviews. [14, 23, 24]

In contrast to the electronic contribution, the lattice thermal conductivity can be altered independently of other transport mechanisms and, therefore, plays a major role in optimizing thermoelectric materials. The lattice contribution to the thermal conductivity arises from coupled vibrational motions of atoms or molecules in the solid, called phonons. Ideally, a material should behave like a glass for phonons and a well ordered crystal for electrons. This concept of a Phonon-Glass-Electron-Crystal (PGEC) was introduced by Slack in 1995. [25] In analogy to the kinetic gas theory, the lattice thermal conductivity can be described by the group velocity v_g of the phonons, the phonon mean free path length l (distance between two scattering events) and the heat capacity C . [26]

$$\kappa_{lat} = \frac{1}{3} C v_g l \quad (1.19)$$

Taking the frequency dependences and the scattering relaxation time $\tau = \frac{l}{v_g}$ into account yields:

$$\kappa_{lat} = \frac{1}{3} \int_0^{\omega_{max}} C(\omega) v_g(\omega) l(\omega) d\omega = \frac{1}{3} \int_0^{\omega_{max}} C(\omega) v_g^2(\omega) \tau(\omega) d\omega \quad (1.20)$$

This shows that the lattice thermal conductivity can be controlled by changing the group velocity, the heat capacity or the phonon mean free path.

Phonon dispersion and group velocity The simplest model for thermal transport in a solid is the monoatomic chain. In figure 1.2, a simple periodic chain of atoms is shown. Each atom has the mass M and is connected to its neighboring atom

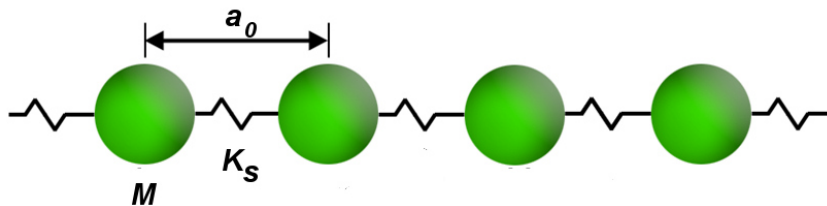


Figure (1.2) – Illustration of the monoatomic chain model. Each primitive unit cell of length a_0 consists of one atom with mass M . Atoms are connected via springs with the spring constant K_s .

via springs with the spring constant K_s . The spring constants (bond strength) are equal, and the interatomic spacing corresponds to the unit cell length in equilibrium a_0 . At temperatures above 0 K, the atoms vibrate around their equilibrium position. Assuming periodic boundary conditions, the solution of Newton's law provides the allowed phonon frequencies ω_k : [24]

$$\omega_k = 2\sqrt{\frac{K_s}{M}} \sin\left(\frac{ka_0}{2}\right) \quad k = n\pi/a_0 \quad (1.21)$$

with the vibrational frequencies ω , the spring constant K_s , the atomic mass M , the phonon wave vector k and the unit cell length a_0 . The maximum phonon frequency ω_k^{max} can easily be derived from equation 1.21 as:

$$\omega_k^{max} = 2\sqrt{\frac{K_s}{M}}, \quad (1.22)$$

and it can be seen that the phonon frequencies are a periodic functions with a reciprocal lattice periodicity of $2\pi/a_0$. Therefore, it is common to plot the phonon dispersion curves (phonon frequency ω plotted against the wave vector k) from 0 to π/a . In figure 1.3, typical images of phonon dispersion curves are illustrated with dependence on the number of atoms N in the unit cell. The monatomic lattice ($N=1$)

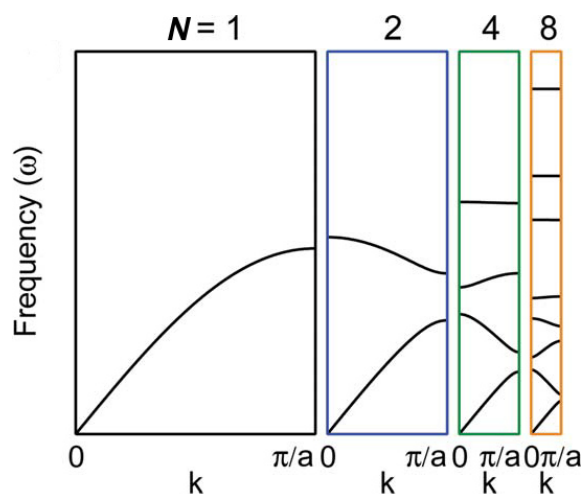


Figure (1.3) – Phonon dispersion curves for monoatomic and multiatomic 1-dimensional lattices. [26]

shows only one branch, called the acoustic branch ($\omega(k) = 0$ for $k = 0$). In the acoustic branch, atoms move in harmonic vibrations. Doubling the unit cell length (bisecting the reciprocal lattice vector) leads to a second branch, the so-called optical branch (see figure 1.3 $N=2$, diatomic chain). This can be visualized by "back-folding"

Introduction

of the monatomic dispersion curve to the new unit cell length ($a' = 2a$). [17, 27] The high frequency optical branches represent anharmonic vibrations. The group velocity v_g can be defined as the slope of the phonon branches. [24]

$$v_g = \frac{\delta\omega}{\delta k} = a_0 \sqrt{\frac{K_s}{M}} \cos(ka_0/2) \quad (1.23)$$

In conclusion, a low spring constant (soft bond) and a high atom mass result in a low phonon group velocity. Remembering equation 1.20, we can see that the thermal conductivity depends on the phonon group velocity, which is difficult to access due to the broad phonon dispersion. However, high frequency optical phonons have a lower group velocity and usually contribute little to the transport of heat through the lattice. This is especially true for materials with high mass contrast and different chemical bonds, which promote a large phonon band gap, and a poor interaction between optical and acoustic phonons. Hence, the acoustic phonons are the main heat carriers, and materials that have a low phonon group velocity in the acoustic branch should exhibit a low thermal conductivity. From the example with the 1-dimensional chain, the dispersion relation for a 3-dimensional lattice can easily be derived. The total number of branches in a 3-dimensional lattice is equal to $3N$. Because there are 3 translation axes, there will be 3 acoustic modes, and the remaining $3N-3$ modes can be attributed to the optical branches. [10, 17, 27]

Heat Capacity In the solid state, heat is stored in vibrational motion. With increasing temperature, more and more vibrational states become occupied. The energy difference between the vibrational states is given by:

$$\Delta E = \hbar\omega \quad (1.24)$$

for the vibrational density of states (DOS) follows: [15]

$$g(\omega)d(\omega) = \frac{4\pi\omega^2 V}{v_m^3} d\omega \quad (1.25)$$

with the vibrational frequency ω , the average Volume per atom V , and the average sound velocity v_m . Because of the maximum of $3N$ possible vibrational modes, there has to be a threshold for the maximum frequency as well. This frequency is called the Debye-frequency ω_D . Thus, integrating the vibrational DOS over all possible

frequencies gives the total amount $3N$ of vibrational modes: [15]

$$3N = \int_0^{\omega_D} g(\omega) d(\omega) \quad (1.26)$$

The heat capacity can be derived thermodynamically, considering the total energy U of the phonon modes: [15]

$$C \propto \int_0^{\Theta_D/T} \frac{x^4 e^x}{(e^x - 1)^2} \left(\frac{T}{\Theta_D} \right)^3 dx \quad (1.27)$$

with the Debye-Temperature $\Theta_D = \frac{\hbar \omega_d}{k_B}$. At temperatures above the Debye temperature ($T \gg \Theta_D$), all vibrational modes are occupied and the heat capacity reaches its upper limit of $3R$ (Dulong-Petit law). [15] An approximation of the Debye temperature can be made using the mean speed of sound v_m and the average volume per atom Ω :

$$\Theta_D = \sqrt[3]{\frac{6\pi^2 v_m \hbar}{\Omega k_B}}. \quad (1.28)$$

The average speed of sound can be calculated from measured longitudinal v_l and transverse v_t sound velocities:

$$v_m^3 = \frac{3}{v_l^{-3} + 2v_t^{-3}}. \quad (1.29)$$

In conclusion, to obtain a material with a low thermal conductivity κ , a low heat capacity C is needed. Materials composed of a small number of heavy atoms, weakly bound in a large unit cell, have a low Debye frequency, and thus, a low Debye temperature, which leads to a low heat capacity.

Phonon mean free path The phonon mean free path describes the mean distance traveled by phonons between two scattering processes. There are several mechanisms to scatter phonons: normal phonon scattering (N), Umklapp scattering (U), impurity or point defect scattering (PD), boundary scattering (B) and electron-phonon scattering (EP). Each scattering mechanism can be characterized by a relaxation rate $1/\tau$, which is the inverse of the corresponding relaxation time τ . Following Matthiessen's rule, a combined scattering relaxation rate can be calculated: [28]

$$\tau^{-1} = \tau_N^{-1} + \tau_U^{-1} + \tau_{PD}^{-1} + \tau_B^{-1} + \tau_{EP}^{-1} \quad (1.30)$$

Introduction

Electron-phonon scattering will not be discussed here, since its contribution is small in comparison to other scattering mechanisms. Normal and Umklapp processes are both phonon-phonon processes. However, normal processes scale linear with ω , preserve the phonon wave vector and are usually ignored next to Umklapp processes (U-processes), which vary with ω^2 . Umklapp processes are 3 phonon processes, which occur when two phonons in the first Brillouin zone collide to generate a third phonon outside the first Brillouin zone. Hence, the crystal momentum changes during the scattering process. [28] The temperature dependence of the lattice thermal conductivity for Umklapp processes follows a $1/T$ dependence. [26]

$$\kappa_{lat} = \frac{(6\pi^2)^{2/3}}{4\pi^2} \frac{\bar{M}v_m^3}{T\Omega^{2/3}\gamma^2} \quad (1.31)$$

with \bar{M} the average mass, v_m the mean sound velocity, Ω the volume per atom and γ the Grüneisen parameter. The Grüneisen parameter is used to describe the change in vibrational properties due to volume changes of the lattice. The Grüneisen parameter is defined as: [29]

$$\gamma = - \left(\frac{d \ln \omega_D}{d \ln V} \right)_T = \frac{3\alpha_T B_T V}{C}, \quad (1.32)$$

and can be derived with the linear coefficient of expansion α_T and the isothermal bulk modulus B_T .

For nanostructured or nanosized thermoelectric materials, grain boundary scattering is a very effective way to reduce the lattice thermal conductivity. In the ideal case, crystalline interfaces are introduced on different length scales, which can act as scattering centers and have a direct influence on τ_{GB} . Prominent examples for the beneficial influence of grain boundary scattering are superlattices of $\text{Bi}_2\text{Te}_3\text{-Sb}_2\text{Te}_3$, $\text{AgPb}_m\text{SbTe}_{2+m}$ and PbTe . [30–32] Although grain boundary scattering can still be effective, when the dimensions of the crystal are some orders of magnitude greater than the phonon mean free path, [33] nanostructured materials are usually hard to synthesize in a reproducible way. [34] Additionally, the interfaces have to withstand the severe thermal cycling of a thermoelectric device without losing their beneficial structure.

Another powerful method is the introduction of impurities, or point defects. This is usually achieved by isoelectronic alloying of Heusler compounds, [35] skutterudites, [36, 37] lead telluride, [38] SiGe , [28, 39] and quaternary copper selenides. [40] Point defect scattering arises from both, a mass difference (mass field fluctuation) and a strain field fluctuation. [41] The latter results from different bonding interactions and size differences between the host and the impurity and has an influence on the

lattice parameters. Following Callaway's expression to model the effect of point defect scattering at high temperatures [42] and combining it with the approaches of Alekseeva *et al.* [38] and Yang *et al.* [35] leads to a simple model for the reduction of the lattice thermal conductivity. Assuming only Umklapp and point defect scattering, the ratio between the lattice thermal conductivity of the crystal with disorder κ_{lat} and the perfect crystal without defects κ_{lat}^{pure} is: [40]

$$\frac{\kappa_{lattice}^{mod}}{\kappa_{lattice}^{pure}} = \frac{\tan^{-1}(u)}{u}, \quad u^2 = \frac{\pi^2 \Theta_D \Omega}{h \nu_m^2} \kappa_{lattice}^{pure} \Gamma \quad (1.33)$$

where u , Θ , h , ν_m , and Γ are the disorder scaling parameter, the average volume per atom, the Planck constant, the average sound velocity, and the disorder scattering parameter, respectively. For the simple cubic case, the disorder scattering parameter Γ can be written as:

$$\Gamma = \chi (1 - \chi) \left[\left(\frac{\Delta M}{M} \right)^2 + \epsilon \left(\frac{\Delta a}{a} \right)^2 \right] \quad (1.34)$$

where χ , $\frac{\Delta M}{M}$, ϵ , and $\frac{\Delta a}{a}$ are the molar fraction of the impurity, the relative change of atomic mass due to the impurity, the fitting parameter representing the elastic properties matrix, and the local change in lattice parameters resulting from the substitution, respectively.

A lower limit for the lattice thermal conductivity, called the glassy limit, was first derived by Cahill *et al.* in 1992. [43] The model is derived from the Einstein's model for amorphous materials and assumes a phonon mean free path of one half of its wavelength. Within the high temperature limit, an estimation of the minimal lattice thermal conductivity is possible using the average volume per atom and measured longitudinal and transversal sound velocities: [26]

$$\kappa_{min} = \frac{1}{2} \left(\frac{\pi}{6} \right)^{1/3} k_B \Omega^{-2/3} (2v_t + v_l) \quad (1.35)$$

1.3. Thermoelectric Figure of Merit

The first discussions on the efficiency of thermoelectric applications were conducted by Altenkirch in 1909 and 1911 [44, 45]. Taking all thermoelectric effects and transport phenomena into account, three conditions must be met to have a good thermoelectric material. First, the material should have a large thermoelectric effect (Seebeck

Introduction

coefficient S or Peltier coefficient $\Pi_{a,b}$ for a TEG or a thermoelectric heat pump). Second, to be able to maintain a stable temperature gradient within the material, the heat flow, and thus the thermal conductivity, must be low. And third, to keep irreversible energy losses due to Joule heating to a minimum, the resistivity of the material should be as low as possible. However, the combination of these three properties has proven to be hard to achieve, since they are highly correlated. A high Seebeck coefficient S is usually paired with a low electrical conductivity σ and vice versa. The quality of a thermoelectric material, thus, can be expressed in its dimensionless figure of merit zT : [21]

$$zT = \frac{S^2 \sigma}{\kappa} \cdot T \quad (1.36)$$

Figure 1.4 gives an overview of the published figure of merit for some state of the art thermoelectric materials. Due to the different structures and sizes of the band gap,

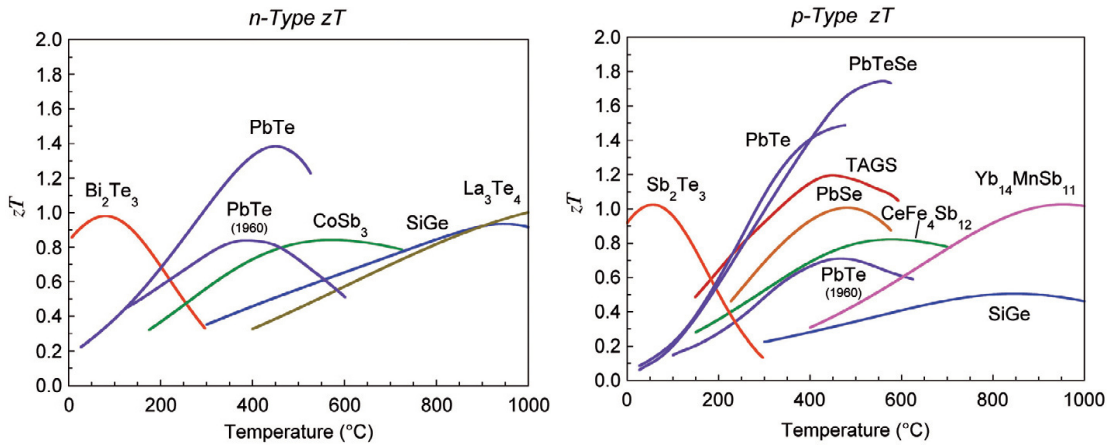


Figure (1.4) – Overview of the zT values of some state of the art n -type and p -type thermoelectric materials. TAGS stands for $(GeTe)_{1-x}(AgSbTe_2)_x$. Due to the different structures and sizes of the band gap, the zT value also has a maximum at a varying temperature. [46]

the maximum zT values of varying materials can be found at different temperatures. The working temperature of a TEG is usually determined by the heat source, hence, the choice of the material plays an important role in the efficiency of the TEG. Like every other heat engine, thermoelectric generators are limited by the Carnot efficiency ($\eta_C = \frac{\Delta T}{T_H}$): [10, 21, 47]

$$\eta = \frac{W}{q} = \eta_C \cdot \eta_{TE} = \eta_C \cdot \frac{\sqrt{1 + ZT} - 1}{\sqrt{1 + ZT} + \frac{T_C}{T_H}}, \quad (1.37)$$

with W , q , η_c , η_{TE} , ZT , T_H , and T_C representing the power generated, the heat flow, the Carnot efficiency, the thermoelectric efficiency, the device figure of merit, and the temperatures on the hot and cold end side, respectively. To obtain a combined efficiency in the order of the Carnot efficiency, the thermoelectric efficiency has to be 1, which translates to an infinite zT value. However, as can be seen in Figure 1.4, the zT of state of the art materials is around and above 1. Designing new high zT materials and increasing the figure of merit of known materials to enhance the device efficiency have been the ongoing challenges in the field of thermoelectrics.

1.4. Thermoelectric Optimization Strategies

There are several ways to optimize the thermoelectric figure of merit in a material. The challenge lies in the complexity of and the correlations between the properties of interest. To obtain a high zT value (see equation 1.36), a high Seebeck coefficient, high electric conductivity and a low thermal conductivity are needed. According to equation 1.17, the thermal conductivity can be divided into an electronic and a lattice contribution. While the lattice contribution to the thermal conductivity can usually be altered independently, the electronic contribution is correlated with the electric conductivity over the Wiedemann-Franz law (see equation 1.18). Thus, a high electric conductivity, inevitably results in a high electronic contribution to the thermal conductivity. This makes both properties dependent on the carrier concentration as well as on the carrier mobility (see equation 1.11). The Seebeck coefficient is also strongly dependent on the charge carrier concentration. For a material with a high carrier concentration (degenerate semiconductor), the Seebeck coefficient is given by: [3, 48]

$$S = \frac{8\pi^2 k_B^2}{3eh^2} m_d^* T \left(\frac{\pi}{3n} \right)^{2/3} \quad (1.38)$$

with the density of states effective mass m_d^* and the charge carrier concentration n . At lower carrier concentrations (non degenerate semiconductor) the Seebeck coefficient is proportional to $\ln\left(\frac{1}{n}\right)$. [9, 10] Figure 1.5 illustrates the dependencies of the thermoelectric properties on the charge carrier concentration. The maximum zT and power factor can be found around a charge carrier concentration of about 10^{19} to 10^{21} per cm^3 . The control of the charge carrier concentration n is, therefore, a crucial aspect in the optimization of a thermoelectric material. However, other optimization strategies, which can vaguely be divided into the optimization of the Seebeck coefficient and thermal optimization, have been developed as well.

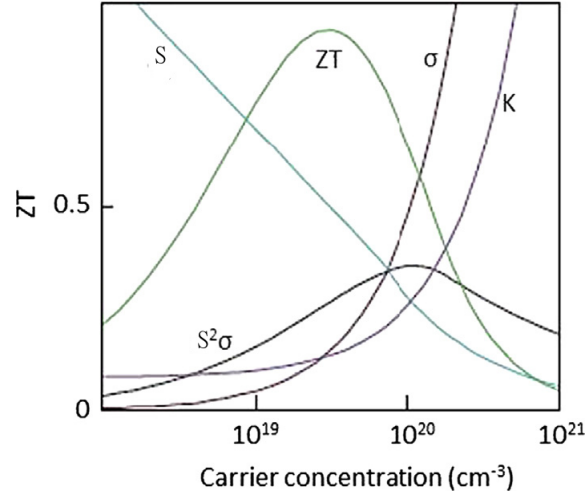


Figure (1.5) – Influence of the charge carrier concentration on the electric conductivity σ , the thermal conductivity κ , the Seebeck coefficient S , the power factor $S^2\sigma$, and the figure of merit zT . [49]

1.4.1. Optimization of the Seebeck Coefficient

The last section showed that a large Seebeck coefficient is necessary to obtain a high figure of merit. Taking equation 1.38 into consideration, the Seebeck coefficient of a material with optimized charge carrier concentration can still be enhanced by increasing the density of states effective mass m_d^* at the Fermi level. [48, 50–55] The density of states effective mass at the Fermi level can either be increased by the contribution of a larger number of conducting bands N_V (higher band degeneracy) to the density of states or by the introduction of resonant impurities, creating flat bands with a high band effective mass at the Fermi level. The dependence of the density of states effective mass on the band degeneracy N_V and the band effective mass m_b^* is given as: [10, 54, 56]

$$m_d^* = N_V^{2/3} \cdot m_b^* \quad (1.39)$$

The concept of resonant impurity doping has been introduced by Heremans *et al.* in 2008 and was demonstrated by doping bulk PbTe with Tl. [56] The influence of multiple bands and resonant states on the total density of states in PbTe is illustrated in Figure 1.6. However, increasing the band effective mass also has an influence on the carrier mobility ($m_b^* \approx 1/\mu$). A high band effective mass will lead to a low carrier mobility and, in consequence, to a low electric conductivity. It can be seen that an over all optimization is hard to achieve. A measure for the zT of materials with

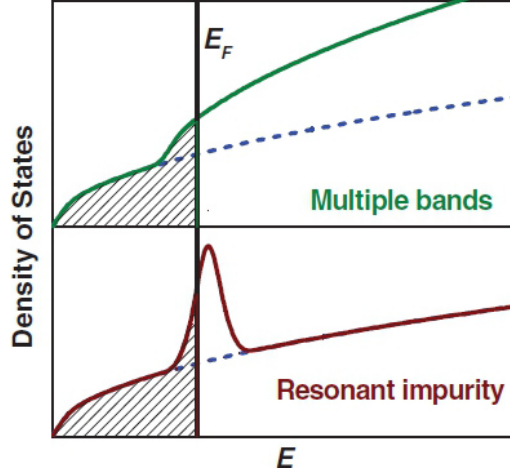


Figure (1.6) – Influence of multiple bands and resonant impurities on the density of states. Dashed lines represent the principal valence band of PbTe without the contribution of multiple bands or resonant doping. Both methods can be used to enhance the Seebeck coefficient, either by increasing the number of bands or through increasing the density of states effective mass. [57]

optimized carrier concentrations is the quality factor B , which is defined as:

$$B \propto \frac{\mu N_V m_b^{*3/2}}{\kappa_{lat}} \quad (1.40)$$

with the mobility μ , the band degeneracy N_V , the band effective mass m_b^* and the lattice contribution to the thermal conductivity κ_{lat} .

A larger band degeneracy N_V is beneficial for the thermoelectric figure of merit, since every carrier pocket contributes to the Seebeck effect. In general, it is not possible to change the band degeneracy, since this would imply a change in symmetry and crystal structure. However, due to the different temperature dependence of different bands, a convergence of those bands, to obtain a larger combined N_V , is possible. This was demonstrated by Pei in 2011. [58] PbTe has a light valence band at the L point, with a degeneracy of 4 and a heavier valence band at the Γ point, with a degeneracy of 12. Figure 1.7 shows an image of the first Brillouin zone, illustrating the different carrier pockets and the temperature dependence of the two degenerate bands. A combined band degeneracy of 12-16 could be obtained around 500 K, resulting in a $zT = 1.8$ at 850 K. According to equation 1.38, the Seebeck coefficient increases with increasing temperature. However, the zT curves plotted against temperature (see Figure 1.4) are not constantly rising, but have a maximum at a certain temperature. This behavior can be attributed to bipolar conduction. If the band gap of a thermoelectric material is small, carrier excitations over the

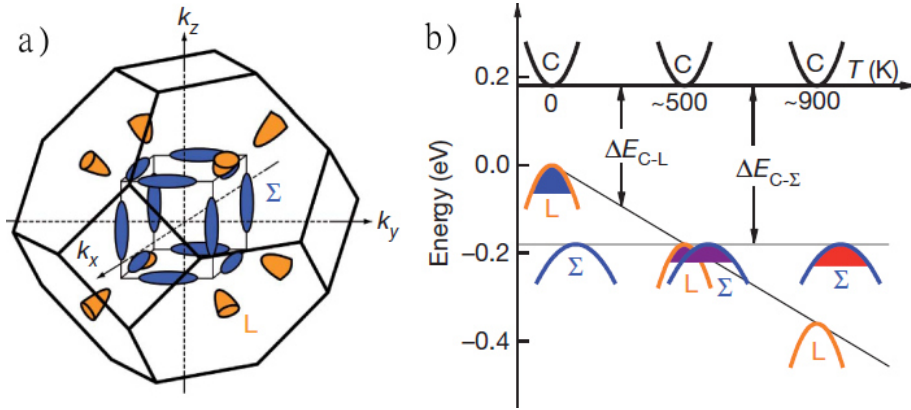


Figure (1.7) – Example for band engineering of PbTe: a) First Brillouin Zone of PbTe illustrating the carrier pockets for the L-point and \$\Gamma\$-point. b) Temperature dependence of the two valence bands leading to a combined band degeneracy of 12-16 at the convergence temperature. [58]

band gap (roll over) can occur, causing bipolar conduction. The resulting Seebeck coefficient can be derived as the sum over the hole and electron contributions (see equation 1.41). Due to their opposing signs, the resulting Seebeck coefficient is substantially lowered, which forces the \$zT\$ value to decrease as well.

$$S = \frac{S_p \sigma_p + S_n \sigma_n}{\sigma_p + \sigma_n} \quad (1.41)$$

Increasing the band gap of a material (e.g. by isovalent substitution) enables the delay of this roll over to higher temperatures, which also results in a higher \$zT\$ value, as illustrated in Figure 1.8.

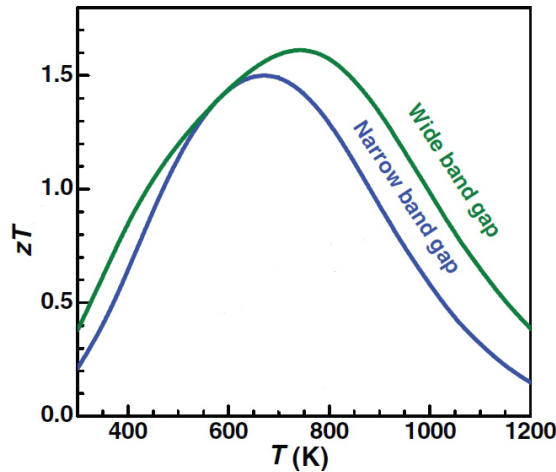


Figure (1.8) – Illustration of the influence of the band gap size on the figure of merit. With a larger band gap size, the carrier activation across the band gap is shifted to higher temperatures, which leads to higher peak \$zT\$ values before the influence of the minority carriers decreases the thermopower. [57]

1.4.2. Thermal Optimization

The thermal conductivity of a material is, to a large extent, an inherent material specific property. The type of bonding, the bond strength, the mass contrast, the number of heavy atoms, the number of atoms per primitive unit cell, and the size of the unit cell are, for example, a few parameters that influence the heat capacity and the group velocity and, therefore, influence the thermal conductivity. Thus, the initial choice of thermoelectric material is crucial to obtain a material with an inherently low thermal conductivity. However, the thermal conductivity depends strongly on the phonon mean free path, which enables many different strategies to be used to lower the thermal conductivity by phonon scattering (see section 1.2.2). [59] Common to all these strategies is the creation of additional scattering centers, such as grain boundaries (nanostructuring) [60] or point defects. [41] Figure 1.9 shows the spectral thermal conductivity. The thermal conductivity can be calculated by

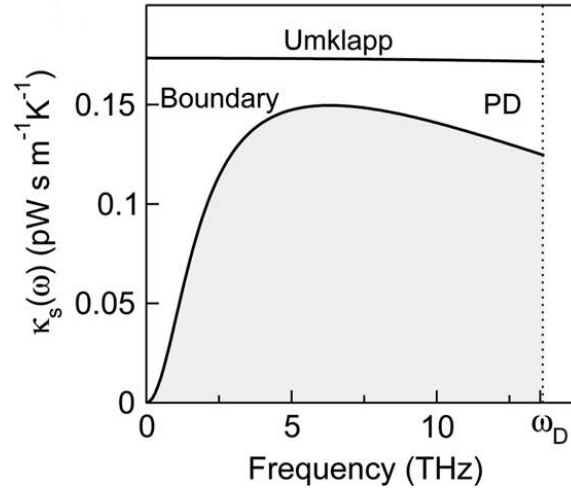


Figure (1.9) – Plot of the spectral thermal conductivity illustrating the influence and frequency dependence of different scattering mechanisms. If only Umklapp scattering is the dominant scattering mechanism, the top constant curve applies. The bottom curve arises, if boundary and point defect scattering are predominant as well. [26]

integrating the spectral thermal conductivity over the complete frequency range. If only Umklapp scattering dominates the thermal transport, the spectral thermal conductivity is a constant function of the frequency, and the top curve applies. When boundary and point defect scattering are also predominant, the spectral thermal conductivity is represented by the lower curve. [26, 33] It can be seen that grain boundary scattering is more effective at lower frequencies, whereas point defect scattering plays a major role at higher frequencies. Therefore, the best approach is to use different scattering mechanisms on several length scales to effectively lower the lattice thermal conductivity. [32]

1.5. Pertinent Materials

In the following section, pertinent material classes are briefly introduced. Focusing on the important structures and properties, fundamental information will be given, which are necessary to understand the research objectives of the following chapters. For more complementary information, the reader is referred to the cited literature.

1.5.1. Quaternary Chalcogenides $\text{Cu}_2\text{ZnGeSe}_{4-x}\text{S}_x$

This section is in part an adapted reproduction of *J. Am. Chem. Soc.* **2014**, *136*, 442-448 [40] and *J. Mater. Chem A* **2014**, *2*, 1790-1794. [61] Reproduced by permission of the American Chemical Society Copyright 2014 and the Royal Society of Chemistry Copyright 2014.

$\text{Cu}_2\text{ZnGeSe}_4$ belongs to the family of adamantane like structures, a large class of wide band gap semiconductors, which have been intensively studied for their electrical properties, [62,63], thermal properties, [64], magnetic properties, [65,66] and photovoltaic application, [67–70] exceeding 10% efficiency. [71] In spite of their large band gap and usually low carrier mobilities, these materials exhibit good thermoelectric performance upon doping and have a structurally conditioned low thermal conductivity. Due to this, these quaternary chalcogenides have recently been in the focus of thermoelectric research. [40,61,72–77]

Owing to their structural robustness, the family of tetrahedrally bonded quaternary chalcogenides is quite large ($\text{Cu}_2\text{-II-IV-X}_4$, with II = Mn, Fe, Co, Ni, Zn, Cd, Hg; IV = Si, Ge, Sn and X = S, Se, Te), and ideal for the investigation of structure-property relationships. The structure can be derived from the diamond structure, where each atom is coordinated by its four nearest neighbors, forming a tetrahedral network. In Figure 1.10 the structural relationship between the adamantane-like structures is illustrated. All compounds with structures derived from diamond are said to be “adamantine”. In multinary compounds (binary, ternary and quaternary compounds), the two substructures are populated with cations and anions, respectively. In the binary case (e.g. ZnS), the cubic sphalerite-type structure (space group $F4\bar{3}m$) is obtained. For ternary compounds, the ordered substitution of the divalent metal into mono and trivalent metals doubles the identity period of the initial cubic unit cell, leading to a tetragonal symmetry of the chalcopyrite-type (structure type $I\bar{4}2d$, e.g. CuFeS_2). Due to the different bonding conditions between the metal cations and the chalcogen anions, and the resulting slightly different bond angles and lengths, a tetragonal distortion takes place, leading to a $c/(2a) < 1$. Lowering the symmetry further and doubling the amount of formula units per unit cell, leads

from the chalcopyrite-type to the stannite-type structure (space group $I\bar{4}2m$), where the trivalent cation is replaced by a di- and a tetravalent cation (e.g. Cu_2FeSnS_4). A characteristic for the stannite structure type are layers of corner sharing Cu-X tetrahedra at $\frac{1}{4}$ and $\frac{3}{4}$ of the c-axis(see figure 1.10). A symmetry decrease, however,

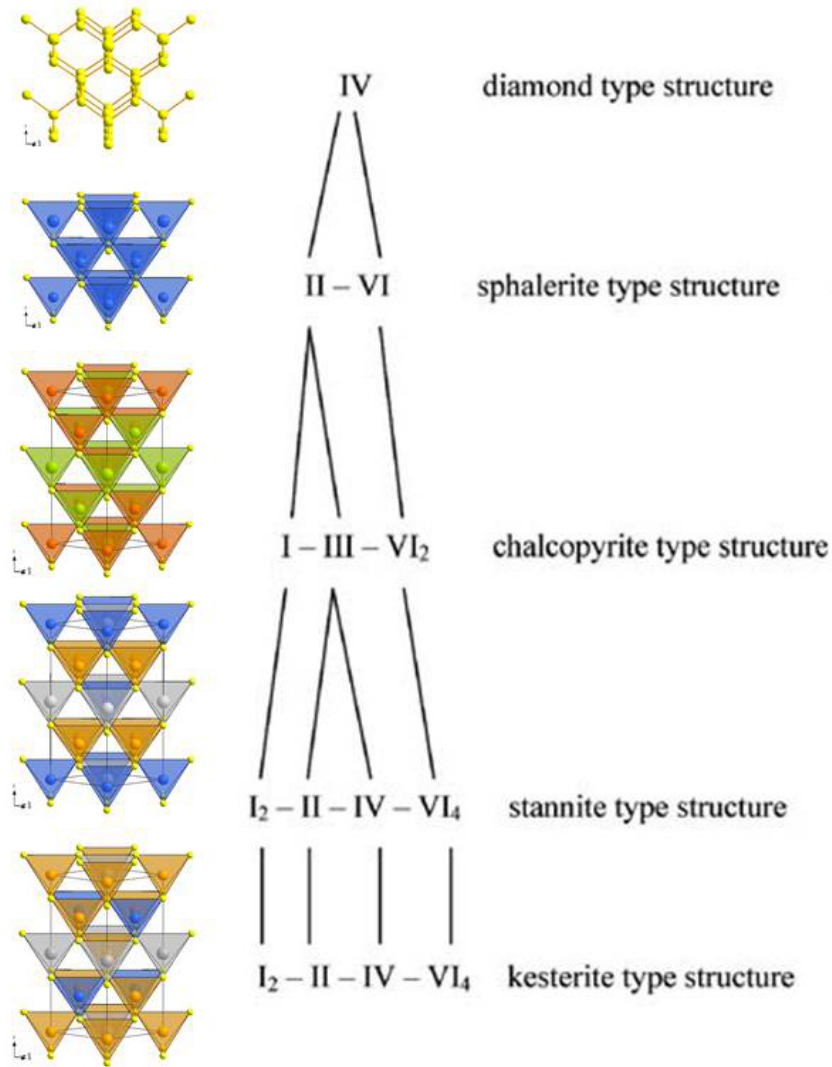


Figure (1.10) – *Structure relationships in the adamantine structure family.*

can not only be achieved by ordered substitution of the metal cations, but also by changing the metal ordering (the arrangement of the cations in the structural sites of the unit cell). By doing so, the kesterite-type structure (space group $I\bar{4}$) can be derived from the stannite-type structure. Although the structures of the adamantine family can be easily derived by doubling of the unit cell and cation substitutions, a direct group-subgroup relation does not exist in every case. The sphalerite structure, indeed, is a hettotype of the diamond structure with a translational equivalent

Introduction

transition of index 2. This means that the translational lattice stays invariant and other symmetry elements are omitted. The index of two illustrates that half of the symmetry elements, here all inversion centers in between the C-C bonds, are omitted. The sphalerite structure, however, is not a "direct" aristotype of the chalcopyrite structure and is only a non-maximal subgroup of sphalerite structure. In respect to the group-subgroup relations, the chalcopyrite structure is not even related to the stannite structure type. However, the kesterite structure type is a hettotype to both, the chalcopyrite and the stannite structure type. In both cases the relation can be described by a translational equivalent transition of index 2. Thus, the group of symmetry elements of the chalcopyrite and stannite structure type have a subgroup, in which all symmetry elements of the kesterite structure are present. In this work, only quaternary chalcogenides were investigated, and therefore the direct aristotype-hettotype relation of stannite and kesterite is of interest. In tables 1.1 and 1.2 the different "decorations" of the lattice site in stannite and kesterite are presented.

Table (1.1) – Crystallographic data of stannite-type $Cu_2M^{II}M^{IV}X_4$. [78]

Atoms	Wyckoff	Position	Point Symmetry	Occupation
M^{II}	2a	(0, 0, 0)	$\bar{4}2m$	1.0
Cu	4d	$(0, \frac{1}{2}, \frac{1}{4})$	$\bar{4}..$	1.0
M^{IV}	2b	$(0, 0, \frac{1}{2})$	$\bar{4}2m$	1.0
X	8i	(0.2449, 0.2449, 0.1298)	$..m$	1.0

Table (1.2) – Crystallographic data of kesterite-type $Cu_2M^{II}M^{IV}X_4$. [79]

Atoms	Wyckoff	Position	Point Symmetry	Occupation
M^{II}	2d	$(\frac{1}{2}, 0, \frac{1}{4})$	$\bar{4}$	1.0
Cu1	2a	(0, 0, 0)	$\bar{4}$	1.0
Cu2	2c	$(0, \frac{1}{2}, \frac{1}{4})$	$\bar{4}$	1.0
M^{IV}	2b	$(\frac{1}{2}, \frac{1}{2}, 0)$	$\bar{4}$	1.0
X	8i	(0.756, 0.756, 0.8722)	1	1.0

Due to their high tolerance towards structural variations, a variety of earth abundant quaternary adamantine compounds have been synthesized, and the effects of cation substitution and doping on the structure [80] and thermoelectric properties have been investigated. [62, 72–77, 81–85] Furthermore, solution based syntheses of

quaternary chalcogenide nanoparticles [86–89] enabled the thermoelectric investigation of nanoscaled chalcogenides. [90–92] Aside from this, copper selenide based materials have recently attracted interest in the field of thermoelectric materials for their superionic conduction and very low resulting thermal conductivities. Above the phase transition temperature, mobile copper cations result in a "phonon-liquid electron-crystal" type behavior, which leads to low heat capacities. [84, 93] Coupled with an inherent structural disorder, low thermal conductivities and reasonably high zT values can be found in compounds such as $\text{Cu}_2\text{Zn}(\text{Sn}/\text{Ge})\text{Se}_4$ [72–77] and $\text{CuGa}(\text{Se}/\text{Te})_2$. [81, 85] These properties are a direct result of the structure and bonding environment, which could be further optimized by cation substitution. [76, 77]

In this thesis, the hitherto neglected influence of anion substitution on the structure and the chemical and physical properties has been investigated. To this end the complete solid solution series $\text{Cu}_2\text{ZnGeSe}_{4-x}\text{S}_x$ has been synthesized, and the influence on the structure, thermoelectric properties and superionic phase transition has been investigated. The experimental details, results and discussions can be found in Chapter 2.

1.5.2. Indium-filled Skutterudites $\text{In}_x\text{Co}_4\text{Sb}_{12}$

Skutterudites are a deeply investigated class of materials with highly promising thermoelectric properties. The material family is named after the Norwegian town Skutterud, where the mineral CoAs_3 was first discovered. The general formula is MPn_3 , with M a transition metal (Co, Rh, Ir) and Pn a pnictide (P, As, Sb). The for thermoelectric application more interesting Sb containing materials can be derived from the isostructural mineral kieftite (CoSb_3). The cubic crystal structure (space group $\text{Im}\bar{3}$; $Z=8$) is composed of eight corner sharing MPn_6 octahedra, similar to the ReO_3 structure type, but severely distorted. The special Wyckoff positions 8c-site ($\frac{1}{4}, \frac{1}{4}, \frac{1}{4}$) and the 24g-site (0, y, z) are occupied by the transition metals and the pnictides, respectively, forming a large icosahedral void in the unit cell center (see figure 1.11). Short M-Pn and Pn-Pn bond distances indicate a strong covalent bonding character, which is even more strengthened by the $[\text{Pn}_4]^{-4}$ four membered rings, connecting the corner shared octahedra. This rigid character is responsible for the high thermal conductivity in skutterudites.

In 1977 Jeitschko et al. showed that the icosahedral void (Wyckoff position 2a), in the center of the unit cell, can be filled with different filler atoms, depending on the size- and the electronegativity-match to the unfilled kieftite host. [94] Possible filler atoms are lanthanides, actinides, alkaline earth, and certain triel or tetrel elements.

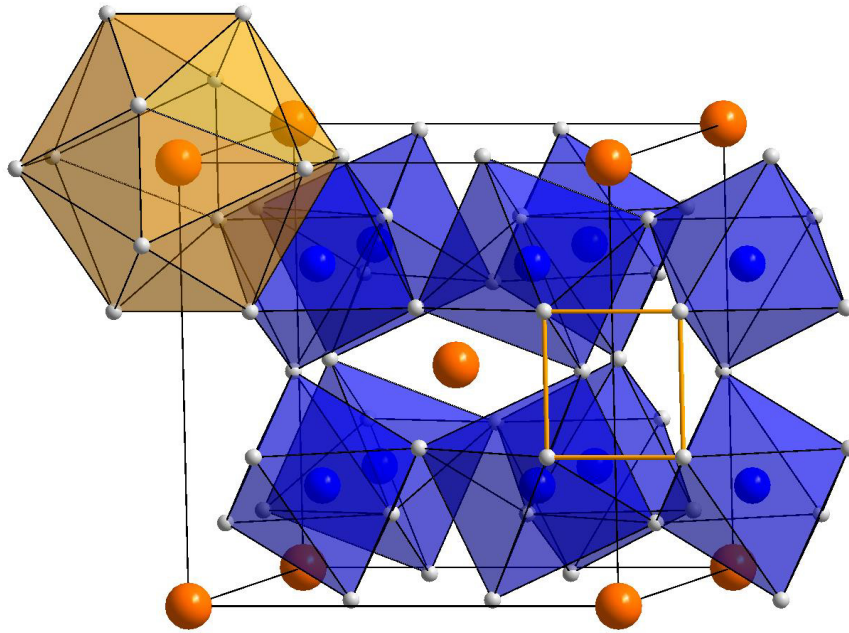


Figure (1.11) – *Illustration of the filled skutterudite crystal structure. Transition metals M are represented by blue spheres, pnictides Pn by gray spheres, and the filling atoms by orange spheres, respectively. The octahedral coordination of the transition metals and the icosahedral coordination of the filler atom are depicted by blue and orange polyhedra. One example of the $[Pn_4]^{-4}$ squares connecting neighboring MPn_6 octahedra is highlighted by yellow bonds.*

The original mineral kiefertite $CoSb_3$ has a very high power factor, but its large lattice thermal conductivity (approx. $11 \text{ W K}^{-1}\text{m}^{-1}$) prevents a high thermoelectric figure of merit. Encouraged by the phonon-glass-electron-crystal (PGEC) concept of Slack in 1995, [25] new thermoelectric materials with large voids (e.g. skutterudites, clathrates) were investigated for their thermoelectric performance. By filling these voids with small atoms, which might vibrate without coupling to the matrix, a decrease in lattice thermal conductivity was expected. Indeed, due to the filling of the void and the resulting heterodesmic bonding the thermal conductivity could be drastically reduced, leading to a room temperature zT of 0.125 in $CeFe_4Sb_{12}$, [95] and a zT reaching almost unity at 800 K. [96] These positive results have caused high research interest in other possible filler atoms and the understanding of structure property relationships in the skutterudite material. [36, 95–108] Experiments on materials with a low filling fraction, compared to highly filled skutterudites, showed that the influence on the thermal conductivity can be understood, if these materials are thought of as solid solution of fully filled and unfilled skutterudites. [36] In contrast to the PGEC concept, the reduction in the lattice thermal conductivity is

not caused due to a random rattling of the filler atoms. Inelastic neutron scattering experiments on thallium filled skutterudites gave clear evidence of a sharp peak in the phonon density of states at low temperatures. [109] Koza et al. showed, that the reduction in thermal conductivity is mainly due to low energy eigenmodes of the filler coupled to the host lattice dynamics. These eigenmodes are characterized by a small or zero phonon group velocity, which makes them ineffective for heat transfer. [97] In addition to the reduction in lattice thermal conductivity, the filling atom acts like an electron donor (eg. $\text{In} \rightarrow \text{In}^+ + \text{e}^-$; $\text{Ce} \rightarrow \text{Ce}^{3+} + 3\text{e}^-$), and thus can be used to tailor the electronic properties. Filled kiefitites, therefore are *n*-type thermoelectric materials. To obtain *p*-type materials either a substitution of the transition metal (e.g. with Fe) or the pnictide (e.g. with Ge) is possible.

Further successful attempts to lower the lattice thermal conductivity were conducted by Toprak et al in 2004. [110] A hydrochemical coprecipitation method was used to synthesize nanosized kiefitite, which was subsequently annealed to obtain a set of samples with different particle sizes. The beneficial impact of nanostructuring (higher grain boundary concentration) was confirmed with CoSb_3 nanocomposites as well. [111] Further techniques to synthesize nanostructured materials with enhanced thermal properties are melt spinning [112–114] or high pressure torsion of a compacted pellet. [115] However, these techniques require nonstandard laboratory equipment, and therefore are not so common.

The investigation of single filled $\text{In}_x\text{Co}_4\text{Sb}_{12}$ by He et al. [101] showed very promising thermoelectric properties. The maximal void filling fraction of indium was found to be 0.22. However, the maximum zT of 1.2 was found at 575 K in the compound $\text{In}_{0.25}\text{Co}_4\text{Sb}_{12}$, possibly due to a side phase of InSb . The beneficial presence of nanostructured InSb could be demonstrated by Li et al. in 2009. [116] Next to InSb side phases, other binary side phases as CoSb_2 and CoSb occur. These additional phases have significant effects on the thermoelectric transport properties, which makes an unadulterated investigation of the filled skutterudite very hard. As a consequence, reported zT values from In-filled skutterudites vary significantly, depending on the phase composition. [101, 108, 116–122] In spite of all effort spend to understand the phase relations in the In-Co-Sb system, [121, 123] several structural questions are still under investigation. For a detailed structural characterization a phase pure synthesis is crucial. To this end, an alternative two-step synthesis was developed to obtain high quality bulk indium-filled skutterudites. With these, the influence of indium as filler was investigated in detail. Further, an easy top-down approach towards indium-filled skutterudites was developed. The experimental details, results and discussions can be found in Chapter 3.

1.5.3. Tetragonal Tungsten Bronzes $\text{Nb}_{8-x}\text{W}_{9+x}\text{O}_{47}$

Due to their inherent chemical and physical stability, low toxicity and usually cheap and earth abundant chemical composition, oxide materials already exhibit many highly wanted properties for the thermoelectric energy conversion. However, oxide thermoelectric materials in general exhibit lower zT values than the competing non-oxide materials. Up to now, only few p -type materials are known with a figure of merit exceeding unity. [124] An overview of the figure of merit of different state of the art p - and n -type oxide materials is given in Figure 1.12. [125]

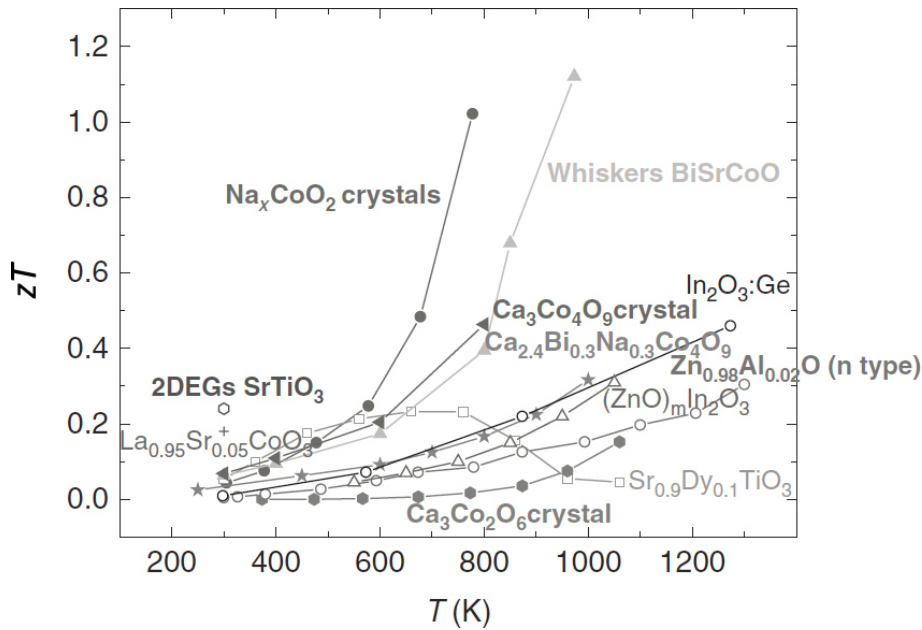


Figure (1.12) – *Figure of merit of state of the art oxide thermoelectric materials. [125]*
Note, only p -type materials achieve zT values above unity. In comparison, the best n -type materials exhibit a maximum zT of up to 0.4 above 1200 K

Sodium or lithium doped CoO_2 have been thoroughly investigated as anode materials due to their layered structure and rich intercalation chemistry. However, these can be valuable characteristics for thermoelectric materials as well. Indeed, doped cobaltates, the structurally related misfit layered oxides $[\text{Ca}_2\text{CoO}_{3-\delta}]_q[\text{CoO}_2]$, and the BiSrCoO Whiskers all are good p -type thermoelectric materials. [126–129] The complex layered oxyselenide BiCuSeO composed of ionic layers of $(\text{Bi}_2\text{O}_2)^{2+}$ and covalent layers of $(\text{Cu}_2\text{Se}_2)^{2-}$ can be considered similar in respect to the layered, heterodesmic bonding context. By doping on the Bi site a zT value of up to 0.8 have been obtained at 773 K. [130] In comparison, the best n -type materials (e.g. doped ZnO or In_2O_3) achieve only zT values about 0.4 at temperatures above 1200 K, a fact that can be explained by their simple crystal structure and the consequently higher thermal conductivity. [131, 132]

The trend towards lower thermal conductivities via nanoscaling or nanostructuring is exemplified in the newly emerging interest for Magnéli phases as n -type thermoelectric materials. [133] This large class of materials was first investigated by A. Magnéli in 1949 and can be described as mixed valence early transition metal oxides of Ti, V, Nb or W. [134–140] The typical structure motive of Magnéli phases are crystallographic shear planes (CS planes), which emerge from extended Wadley defects. Due to the reduction, oxygen defects form. These tend to diffuse to certain crystallographic planes and induce crystallographic shearing from previously corner-shared to edge-shared metal-oxygen octahedra. Certain defect concentrations give rise to specific CS planes, which is the driving force to form different Magnéli phases with specific oxygen non-stoichiometry. The crystal structure is altered on the nanoscale from a simple structure (e.g. ReO_3 -type) to a large unit cell with well defined CS planes. These CS planes can be used to effectively reduce the lattice thermal conductivity, as we could show with the tungsten Magnéli phases $\text{WO}_{2.9}$ and $\text{WO}_{2.722}$. [141] Although the thermal conductivity can be dramatically reduced due to the larger unit cell and CS planes, only certain compositions or reduction degrees are stable. Therefore, an optimization of the electronic transport properties is not easily achievable. In an attempt to combine the structurally complex character of the Magnéli phases with the potential to continuously vary the electronic properties, we considered the structurally similar tetragonal tungsten bronzes (TTB).

Several different tungsten bronzes are known in the literature. However, in this work the term TTB will only be used for compounds of composition $\text{Nb}_{8-x}\text{W}_{9+x}\text{O}_{47}$, on which we are focusing in this investigation. The tetragonal tungsten bronzes belong to the group of infinitely adaptive structures [142], crystallizing in the orthogonal space group Pbam . The structure of the complete series and the oxidation behavior of the highly reduced end members were previously investigated via HR-TEM and electron diffraction by F. Krumeich. [143–146] In the pseudo-binary phase diagram of Nb_2O_5 and WO_3 [147] (see supporting information C.1) the tetragonal tungsten bronzes can be found in between the tungsten-rich and niobium-rich phases, which are characterized by parallel and orthogonal CS planes, respectively. [148, 149] The so called 4:9 phase ($\text{Nb}_8\text{W}_9\text{O}_{47} = 4x \text{Nb}_2\text{O}_5 + 9x \text{WO}_3$) and the complete series of $\text{Nb}_{8-x}\text{W}_{9+x}\text{O}_{47}$, with x ranging from 0 to 5, crystallizes in a threefold superstructure (lattice parameters $a = 36.570 \text{ \AA}$; $b = 36.690 \text{ \AA}$, $c = 3.945 \text{ \AA}$), shown in Figure 1.13, of the TTB structure. [150, 151] The complex crystal structure is composed of corner sharing octahedra with pentagonal tunnels. In the superstructure, 12 out of 36 pentagonal tunnels are filled with metal-oxygen chains running through the short crystallographic c axis. The resulting pentagonal dipyrramids (represented by

turquoise polyhedra in Figure 1.13) are ordered systematically and connected by common corners in c direction and edge-sharing with neighboring octahedra in the ab plane. Starting from the most oxidized compound $\text{Nb}_8\text{W}_9\text{O}_{47}$ an ordered substitution

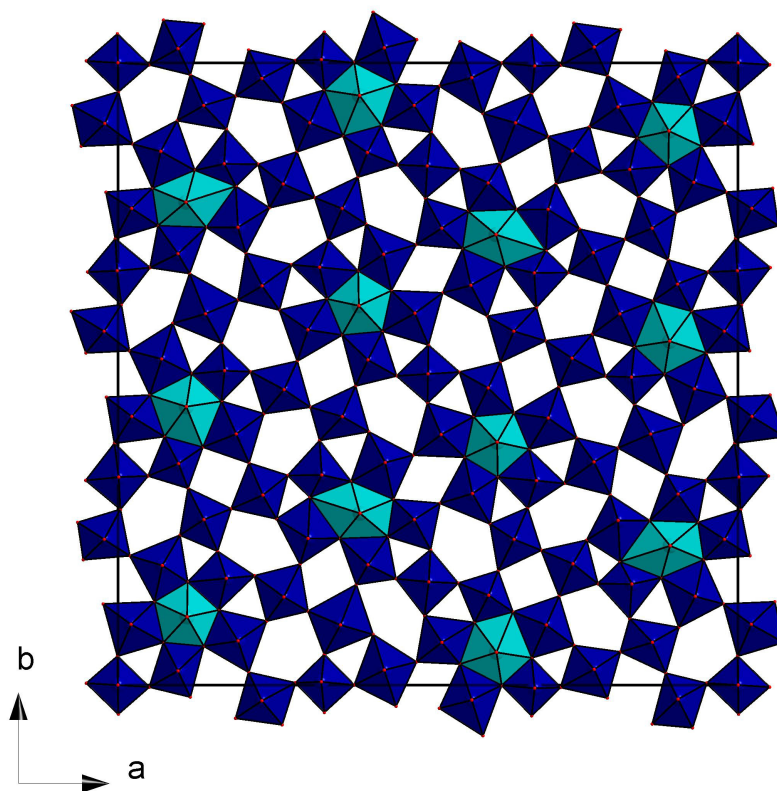


Figure (1.13) – *Threefold supercell of the tetragonal tungsten bronze structure used to describe the complete series of $\text{Nb}_{8-x}\text{W}_{9+x}\text{O}_{47}$ with x ranging from 0 to 5. The complex crystal structure is composed of distorted, corner sharing octahedra with pentagonal tunnels. 12 out of 36 pentagonal tunnels are filled with metal-oxygen chains running through the short crystallographic c axis. The resulting pentagonal dipyramids (here turquoise) are ordered systematically and connected by common corners in c direction and edge sharing in the ab plane.*

of 2 Nb^{5+} by either Nb^{4+} and W^{6+} or W^{4+} and W^{6+} is possible. This leads to the theoretical series of $\text{Nb}^{4+}_n\text{Nb}^{5+}_{8-2n}\text{W}^{6+}_{9+n}\text{O}_{47}$ or $\text{W}^{4+}_m\text{Nb}^{5+}_{8-2m}\text{W}^{6+}_{9+m}\text{O}_{47}$, respectively. In combination, the substitution series $\text{Nb}_{8-x}\text{W}_{9+x}\text{O}_{47}$ is obtained and a substitution up to $\text{Nb}_3\text{W}_{14}\text{O}_{47}$ ($x = 5$) is possible. With increasing substitution degree the amount of transition metals in the oxidation state +4 increases. This corroborates with a reduction consequently an increase in the charge carrier concentration.

Due to the very large unit cell ($Z=6$; $\approx 5300 \text{ \AA}^3$) and the complex crystal structure, low values of the lattice thermal conductivity are to be expected. The name bronzes

and the reported dark blue color of the cation substituted members might indicate, that with increasing substitution the system can be tuned from the highly oxidized, isolating $\text{Nb}_8\text{W}_9\text{O}_{47}$ to a highly reduced, metal-like $\text{Nb}_3\text{W}_{14}\text{O}_{47}$ with itinerant electrons. The electronic properties, hence, should be easily tunable by a reduction via cation substitution. A controlled oxygen deficiency leading to crystallographic shear planes similar to the Magnéli phases might be possible as well. This would also allow to tune the electronic and thermal properties. Up to now, the tetragonal tungsten bronzes $\text{Nb}_{8-x}\text{W}_{9+x}\text{O}_{47}$ have not yet been investigated for their thermoelectric transport properties. Therefore, we decided to conduct initial investigations on the thermoelectric properties and the possible optimization by cation substitution or controlled oxygen deficiency. The experimental details, results and discussions can be found in Chapter 4.

2

Quaternary Chalcogenides

This chapter contains partially adapted reproductions from *J. Am. Chem. Soc.* **2014**, *136*, 442-448 [40] and *J. Mater. Chem A* **2014**, *2*, 1790-1794. [61] Reproduced by permission of the American Chemical Society Copyright 2014 and the Royal Society of Chemistry Copyright 2014. This project was done in collaboration with [REDACTED] from the California Institute of Technology (CalTech). Project design, material synthesis and processing, chemical characterization and data analysis were conducted at the Johannes Gutenberg-University of Mainz. Powder consolidation and thermoelectric characterization were done at CalTech.

2.1. Motivation

Initial results from our group on cation substitutions in the quaternary chalcogenide system $\text{Cu}_2\text{ZnGeSe}_4$ showed that significant changes in the structure and phase composition can be obtained by controlled cation substitution. Aliovalent cation substitution ($\text{Cu}_{2+x}\text{Zn}_{1-x}\text{GeSe}_4$) has led to nanophase segregations located on the grain boundaries [76] and isovalent cation substitution ($\text{Cu}_2\text{Zn}_{1-x}\text{Fe}_x\text{GeSe}_4$) induced local anisotropic structural disorder. [77] These structural and compositional changes are mirrored by a significant reduction in the thermal transport, and thus can be used to optimize the thermoelectric figure of merit of these materials. Inspired by these results, we decided to further investigate the influence of substitutions on the structure and properties of the $\text{Cu}_2\text{ZnGeSe}_4$ system. The just recently observed

insulator-to-metal transition in $\text{Cu}_2\text{ZnGeSe}_4$ illustrates that these systems are not yet entirely understood. To this end, the effect of anion substitution in $\text{Cu}_2\text{ZnGeSe}_{4-x}\text{S}_x$ was investigated. As the nature of the chemical bonding changes with the degree of substitution, an influence on the structure, the thermoelectric transport properties and the newly discovered phase transition is to be expected. With this work we aim to broaden our knowledge of the influence of substitution effects in $\text{Cu}_2\text{ZnGeSe}_4$, towards a more comprehensive understanding of the structure-property relationships in adamantane-like systems.

2.2. Experimental Details and Methods

Synthesis Bulk samples of polycrystalline $\text{Cu}_2\text{ZnGeSe}_{4-x}\text{S}_x$ with compositions of $x = 0, \dots, 4$ were prepared by solid state reaction using elemental powders of Cu (Alfa Aesar, 99.999 %), Zn (Sigma Aldrich, 99.995 %), Ge (Chempur, 99.99 %), Se (Alfa Aesar, 99.999 %) and S pieces (Alfa Aesar, 99.999 %). The phase purity of all starting materials was verified by powder X-ray diffraction, and all synthetic procedures were carried out under controlled atmosphere in a N_2 dry box. S was carefully resublimed twice under dynamic vacuum to ensure dry and phase pure conditions. Annealing was performed in evacuated quartz ampoules, which were preheated at 1073 K under dynamic vacuum for 5 hours to ensure dry conditions. The absence of water was found to be crucial to obtain phase pure reaction products, since the presence of water resulted in the formation of the respective hydrogen chalcogenides, which are able to act as an unwanted transport agent. [152] The starting elements were thoroughly ground, sealed in quartz ampoules, and annealed in the first step at 923 K for 48 hours ($x = 0$) or for 96 hours ($x \geq 1$). In the second step, the harvested powders were ground again, re-sealed and re-annealed for 96 hours at 1073 K and 973 K, respectively. Heating and cooling rates for all procedures in the horizontal tube furnaces were 5 K/min. The different synthetic temperatures were chosen due to a structural phase transformation at 1063 K, which occurs in the sulfur containing members of this series. [153] It was found that the second annealing step was necessary to prevent the formation of the binary and ternary side phases. The quartz ampoules were 10-12 cm in length and 11 mm in inner diameter with a maximum of 1.5 g of starting materials per ampoule. This ampoule geometry was found to prevent a significant loss of selenium at higher temperatures, indicated by red selenium precipitation present in longer ampoules. The obtained powders of $\text{Cu}_2\text{ZnGeSe}_{4-x}\text{S}_x$ were hand ground, and phase purity was verified via powder X-ray diffraction prior to consolidation. Due to the good crystallinity of the binary

and ternary side products, impurity levels as low as 0.25 vol% could be detected via quantitative Rietveld refinements. Impure samples were discarded. To ensure sample homogeneity and reproducibility of all measurements, multiple samples of each compound were synthesized and merged to form a large batch after the phase purity was confirmed by powder X-ray diffraction and Rietveld refinement.

Powder Processing Clean batches of powders were used for consolidation into 1-1.5 mm thick, 12 mm diameter disks at 873 K for 5 hours ($x = 0$), 1073 K for 6 hours ($x = 1$), and 973 K for 6 hours ($x \geq 2$) under a pressure of 40 MPa by induction hot pressing in high density graphite dies. [154] The resulting sample density was determined from the mass and geometry of the consolidated disks.

Characterization Details Room temperature powder X-ray diffraction measurements were performed on a Siemens D5000 powder diffractometer with a Braun M50 position sensitive detector, Ge (220) monochromator and CuK_α radiation (step size of 0.0078° in 2Θ). Variable temperature X-ray diffraction for $\text{Cu}_2\text{ZnGeSe}_4$ was performed on a Philips PANalytical X'Pert Pro with CuK_α radiation (step size of 0.0084° in 2Θ), and a Seifert XRD 3000 P with CuK_α radiation (step size of 0.02° in 2Θ) was used for the sulfur containing compounds. Pawley and Rietveld refinements were performed with TOPAS Academic V4.1 [155], applying the fundamental parameter approach using the crystallographic data from Schäfer and Nitsche as structure model. [78] The instrumental measurement uncertainty for the determination of the lattice parameters at room temperature is approximated to be 0.003 \AA .

Coupled DSC/TG analysis were carried out using a Netzsch STA 449 F3 Jupiter device. About 10 mg of the sample were heated in an alumina crucible under flowing argon atmosphere with a heating rate of 5 or 10 K/min.

Optical reflectance spectra of the fine powdered samples were measured at room temperature on a Varian Cary 5000 UV/VIS-NIR spectrometer equipped with an integrating Ulbricht Sphere and BaSO_4 as standard. Optical band gap energies were calculated applying the Kubelka-Munk approximation. [156]

Thermal diffusivity was measured using a Netzsch laser flash diffusivity instrument (LFA 457). Prior to thermal diffusivity measurements, samples were spray coated with a thin layer of graphite to minimize errors in the emissivity and measured under flowing argon atmosphere. The data was analyzed using a Cowan model with pulse correction. Heat capacity (C_p) was estimated using the Dulong-Petit approximation ($C_p = 3k_B$ per atom) and theoretical densities were calculated from the molar mass and the refined lattice parameters for each composition.

The speed of sound was measured in the laboratory of Professor W. L. Johnson (CalTech) using a Panametrics NDT 5800 pulser/receiver and 5 and 25 MHz shear and longitudinal transducers from Ultrasonics. Honey was used as couplant. The data were recorded on a Tektronix TDS 1012 digital oscilloscope. The speed of sound was estimated by the time between pulse and responses as well as the sample thickness.

The Seebeck coefficient was calculated from the slope of the voltage vs. temperature gradient measurements from Chromel–Nb thermocouples under dynamic vacuum, applying a temperature gradient of 10 K. [157]

Electrical resistivity was measured using the van der Pauw technique under a current of 20 mA and pressure-assisted contacts. [158] The high resistivity values of some samples resulted in high contact resistances in the van der Pauw measurement system, leading to untrustworthy data at lower temperatures. Therefore, data-points with large contact resistances and high Van der Pauw ratios were discarded. All thermoelectric measurements were performed under dynamic vacuum and on multiple samples for each composition. The measurement data presented include data collected during heating and cooling.

The ^{63}Cu MAS-NMR spectra were recorded with a Bruker Avance 500 spectrometer using a special high-temperature Bruker WVT 4 mm double-resonance probe, operating at 132.64 MHz and a rotor frequency of 10 kHz while applying temperatures ranging from 300 K to 523 K (bearing gas nitrogen, ± 5 K). For each spectrum, 16384 transients were averaged with a relaxation delay of 0.2 s and a pulse length of 1.5 μs (B_1 -field: 83.3 kHz).

2.3. Results and Discussion

2.3.1. Chemical Characterization

To investigate the influence of isovalent anion substitution on $\text{Cu}_2\text{ZnGeSe}_4$, a substitution with tellurium or sulfur can be considered. Initial experimental results on the substitution of selenium with sulfur or tellurium showed, that the production of the complete solid solution series $\text{Cu}_2\text{ZnGeSe}_{4-x}\text{Te}_x$ in sufficient phase purity and quantity would be problematic. Impurity scattering of phonons on grain boundaries is known to strongly influence the thermal conductivity of a thermoelectric material. [76] Therefore, substitution with S was chosen and particular emphasis was placed on pure materials with no side phases. All samples were checked for phase purity prior to any measurement. Respective powder X-ray diffraction data of the solid solution series are shown in Figure 2.1. All reflections can be indexed to

the solid solution series limited by the quaternary chalcogenides $\text{Cu}_2\text{ZnGeSe}_4$ and $\text{Cu}_2\text{ZnGeS}_4$, and no secondary phases were observed.

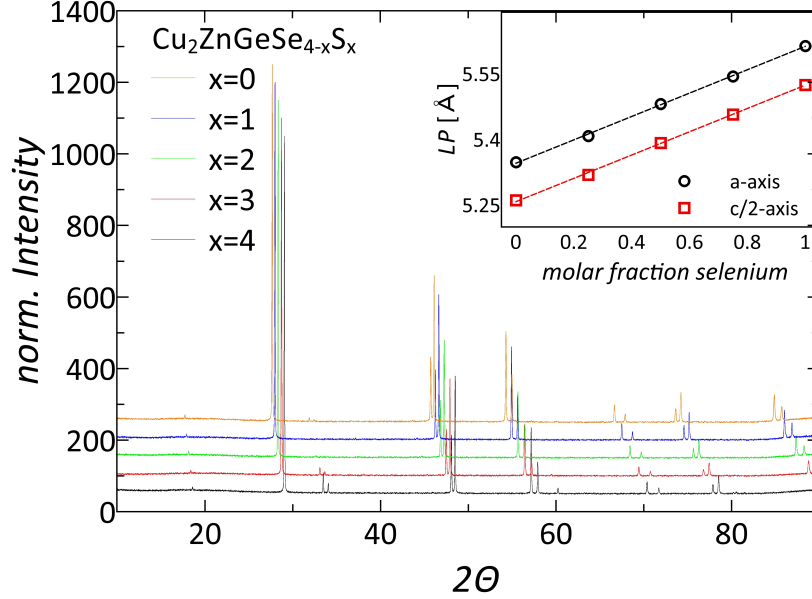


Figure (2.1) – Normalized powder X-ray data of the complete solid solution series $\text{Cu}_2\text{ZnGeSe}_{4-x}\text{S}_x$ with $x = 0-4$ (plots are shifted in intensity for better visibility). The inset shows the refined lattice parameters (LP) a and $c/2$ in Å. Corresponding to Vegard’s law, a linear trend of lattice parameters is seen.

Rietveld refinements of the room temperature diffraction data showed site occupancies of Cu^+ and Zn^{2+} significantly below 100%, with the missing electron density found on the interstitial sites. [76] However, due to the very similar scattering form factors for X-rays of Cu^+ and Zn^{2+} , a distinction via X-ray diffraction is not possible. The refinements of lattice parameters show an isotropic increase of the a - and c -axes, with increasing selenium content in accordance to Vegard’s law (see inset Figure 2.1). [159] The strict trend in lattice parameters and constant c/a ratio corroborates a homogeneous chalcogen distribution within each sample and the successful substitution of selenium by sulfur in $\text{Cu}_2\text{ZnGeSe}_{4-x}\text{S}_x$, consistent with the work of Wold *et al.* [153] Refined X-ray data obtained before hot pressing, as well as data obtained from consolidated samples, show no significant contribution of texture in these materials. Further, the consolidated pellets have more than 95% theoretical density, as determined from the mass and sample geometry. Disks of these polycrystalline materials, therefore, are considered suitable for thermoelectric characterization. The refined powder X-ray data, including profile fit, profile difference, and profile of the complete solid solution series, can be found in the supporting information (section A.1). Refined lattice parameters, c/a ratio, cell volume, and weighted profile R-factors of all refinements are summarized in Table

Table (2.1) – Refined lattice parameters, c/a ratio, cell volume, and respective R_{wp} -value of the solid solution series $Cu_2ZnGeSe_{4-x}S_x$.

x	a[Å]	c[Å]	c/a	V[Å ³]	R_{wp} [%]
0	5.61333(2)	11.04886(5)	1.968	348.143763(6)	0.066
1	5.54397(3)	10.91399(7)	1.968	335.448068(8)	0.066
2	5.48101(3)	10.78398(7)	1.967	323.966618(8)	0.064
3	5.40804(2)	10.63897(6)	1.967	311.156856(7)	0.061
4	5.34808(2)	10.52225(7)	1.967	300.95697(8)	0.064

2.1. Refinements of the non-special chalcogen position (Wyckoff position 8i; Figure 2.2) show a constant increase in the x- and y-coordinates with increasing selenium content. The z-coordinate of the chalcogen position, however, does not change over

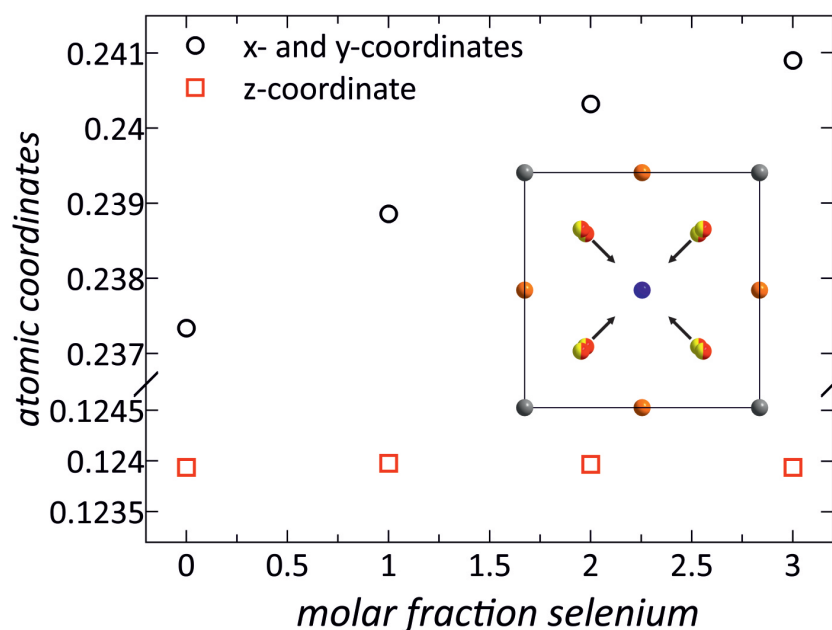


Figure (2.2) – Refined atomic coordinates of the chalcogen position (Wyckoff position 8i). With increasing selenium content the chalcogen position shifts towards the center of the unit cell. The inset shows a projection of the unit cell in the c -direction; the arrows indicate the shift of the split chalcogen position (yellow and red) with increasing selenium content.

the solid solution series. In other words, the average chalcogen position shifts with increasing selenium content toward the center of the unit cell (see inset Figure 2.2), which results in a partial change in the tetrahedral metal-chalcogen-metal bond angles (Figure 2.3). Metal-chalcogen bond distances increase linearly with increasing selenium content (see supporting information figure A.19). Bond angles between

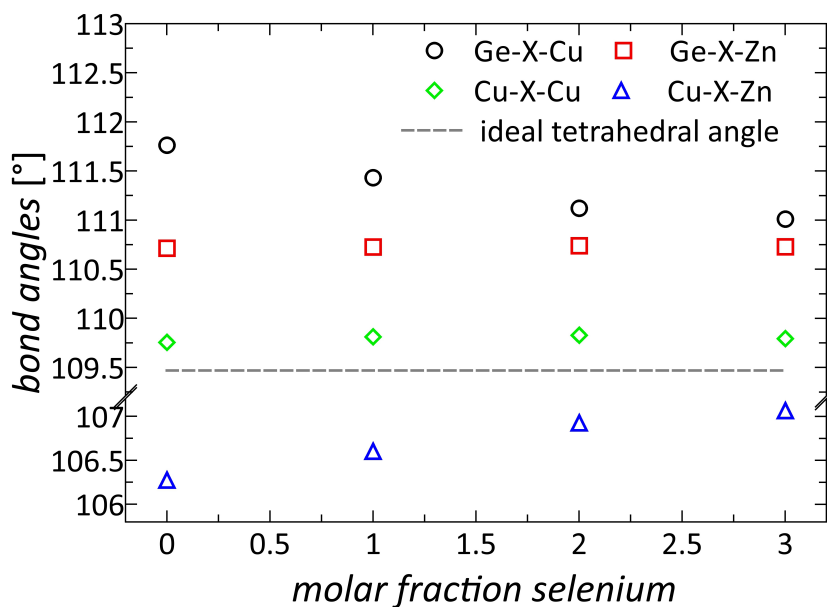


Figure (2.3) – Metal-chalcogen-metal bond angles in comparison to the ideal tetrahedral angle. Bond angles between metals with different z coordinates (Ge-X-Cu and Cu-X-Zn) change with composition, while angles between metals on the same z coordinate (Ge-X-Zn and Cu-X-Cu) are independent of the composition.

metals with different z coordinates are either increasing (Cu-X-Zn = 106.93° on average) or decreasing (Ge-X-Cu = 111.12° on average) with increasing selenium content. Angles between metals with the same z coordinate (Cu-X-Cu = 109.8° and Ge-X-Zn = 110.47° with X = chalcogen), however, are independent of the selenium content. Although the maximum change in the measured average bond angles is rather small (approximately 1°), local changes in bonding angles due to substitution leads to some amount of crystallographic strain, which affects the thermal transport properties (vide infra).

Combined DSC/TG measurements show the presence of a subtle exothermic event throughout the complete solid solution series (see supporting information section A.2), as reported previously for $\text{Cu}_2\text{ZnGeSe}_4$. [76] This indicates the occurrence of a phase transition which has been unobserved so far. [64, 160] The phase transition temperature is tunable by the sulfur content and shifts to higher temperatures with increasing amount of sulfur. Significant weight loss under flowing argon does not occur up to 973 K or 1123 K for selenium-rich or sulfur-rich samples, respectively. However, due to significant selenium evaporation under dynamic vacuum at temperatures above 723 K, thermoelectric transport measurements were conducted up to a maximum temperature of 673 K to ensure the thermal stability of the samples.

The optical band gap was calculated from the measured diffuse reflectance spectra R , using the Kubelka-Munk approximation. Figure 2.4 shows the absorption spectra plotted as $(\alpha h\nu)^2$ against photon energy. The estimated band gap energies (see inset Figure 2.4) range from 1.4 eV to 2.0 eV for $\text{Cu}_2\text{ZnGeSe}_4$ and $\text{Cu}_2\text{ZnGeS}_4$, respectively. Spectra used to extrapolate the band gap can be found in the supporting information A.3. The tunability of the band gap energies by anion substitution has been intensely investigated for photovoltaic applications in several of these wide band gap materials [70, 161, 162] and can easily be explained by the respective anionic radii. Because of a decrease in anion radius by substitution with sulfur, the orbital overlap is reduced; hence, the dispersion of the bands decreases, and the band gap grows energetically with respect to Se-rich samples.

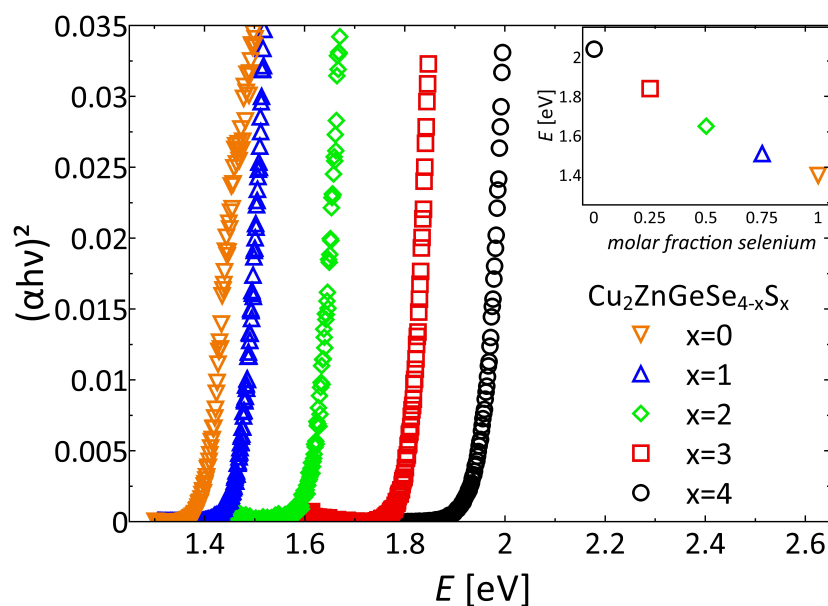


Figure (2.4) – Kubelka-Munk plot from the absorption spectra of the solid solution series $\text{Cu}_2\text{ZnGeSe}_{4-x}\text{S}_x$ with $x = 0-4$. The inset shows the corresponding extrapolated band gap energies ranging from 1.4 to 2.0 eV.

2.3.2. Electronic Transport Properties

The temperature-dependent electrical resistivity of the complete solid solution series $\text{Cu}_2\text{ZnGeSe}_{4-x}\text{S}_x$ is shown in Figure 2.5. As expected for undoped, semiconducting, wide band gap materials, the resistivity is rather large and decreases with increasing temperature. Note that, as all samples are valence precise, low charge carrier concentrations are expected, which consequently results in a high resistivity. It has been shown that a 10-fold decrease in the resistivity is possible by cation doping. [76]

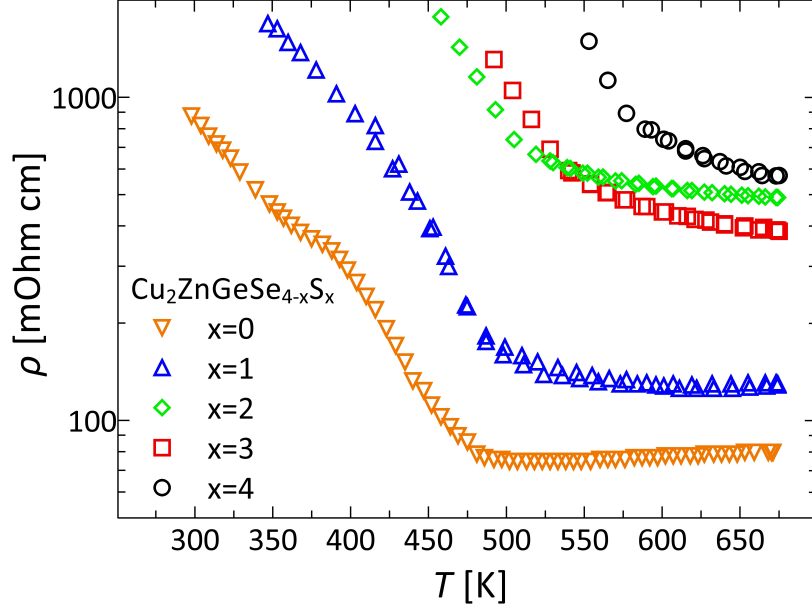


Figure (2.5) – Temperature dependence of the electrical resistivity ρ of the complete solid solution series $\text{Cu}_2\text{ZnGeSe}_{4-x}\text{S}_x$, with $x = 0-4$, illustrating the trend of higher resistivity with decreasing content of selenium.

Usually, no great change in the electronic band structure is expected by anion substitution. Nevertheless, the smaller size of the sulfide anions with respect to the selenide anions leads to a lower degree of covalency, owing to the difference in electronegativity compared to sulfur. The lower degree of covalency causes very low carrier mobilities, due to the localization of the charge carriers by the higher coulombic forces. As a result, the electrical resistivity scales with the sulfur content. The only exception to this trend is the sample with composition $\text{Cu}_2\text{ZnGeS}_2\text{Se}_2$. Above 540 K, higher resistivity values are observed in comparison to those for $\text{Cu}_2\text{ZnGeS}_3\text{Se}$. However, previous work showed that the control over the amount of anion defects, and hence, the charge carrier concentration is difficult to achieve. [77] Extrinsic carriers from intrinsic defects may, therefore, be the reason for the higher resistivity of $\text{Cu}_2\text{ZnGeS}_2\text{Se}_2$ at higher temperatures. To obtain lower resistivity values in the undoped quaternary copper chalcogenide $\text{Cu}_2\text{ZnGeSe}_4$, a substitution of selenium with tellurium could be envisaged. In addition to the chalcogenide composition, the phase transformation has a significant effect on the electrical resistivity. Around the phase transition temperature, all samples show a change in the temperature dependence of the resistivity (kink or change in slope). At temperatures below the phase transition temperature, the slope of the resistivity-temperature plot is rather steep, as expected from undoped semiconductors. At temperatures higher than the transition temperature, a constant or slightly increasing electrical resistivity can

be observed, which confirms the existence of a metal to insulator transition in the complete substitution series $\text{Cu}_2\text{ZnGeSe}_{4-x}\text{S}_x$.

The temperature dependence of the Seebeck coefficient is shown in Figure 2.6. The Seebeck coefficients range from $+300 \mu\text{V}/\text{K}$ to $+500 \mu\text{V}/\text{K}$, and the positive

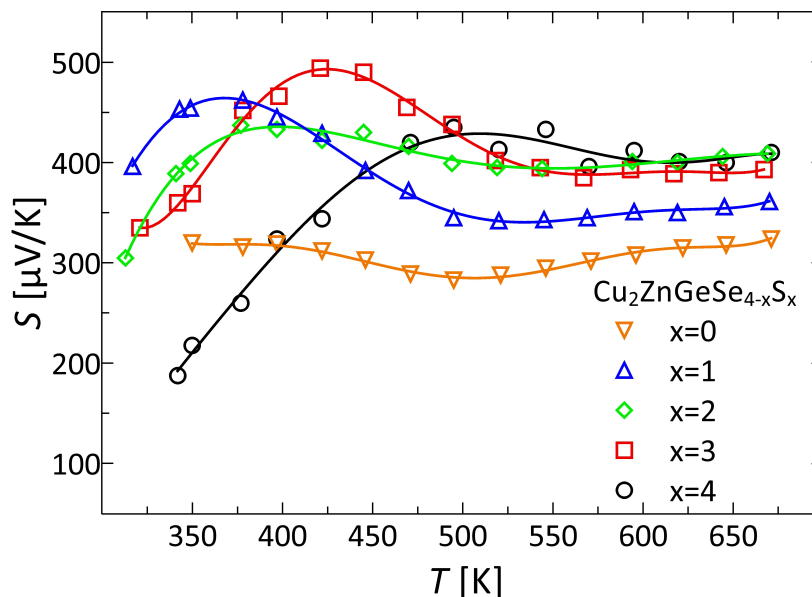


Figure (2.6) – Temperature dependence of the Seebeck coefficient S of the complete solid solution series $\text{Cu}_2\text{ZnGeSe}_{4-x}\text{S}_x$ with $x = 0-4$. Data points are shown with a line as a guide to the eye.

values indicate holes as majority charge carriers. Due to the large band gaps and the absence of doped states close to the band edges, no thermal excitation of charge carriers over the band gap, and hence, no contribution by bipolar conduction is to be expected. As a result, the temperature dependence of the Seebeck coefficient should be constant, which is in good agreement with the measured high-temperature data. The low-temperature trend of these intrinsic Seebeck compounds suggests that there may be characteristics of extrinsic semiconductor behavior below room temperature, even though the resistivity appears to be of intrinsic semiconductor type. The phase transition is visible as a vague minimum in the thermopower. The trend of the Seebeck values within the solid solution series is a result of a combination of the changing band gap and the intrinsic carriers from defects. [77] These results indicate that a single parabolic band model is not applicable in these materials, and a more involved model would have to be elaborated to explain the Seebeck data in detail, which is beyond the scope of this work.

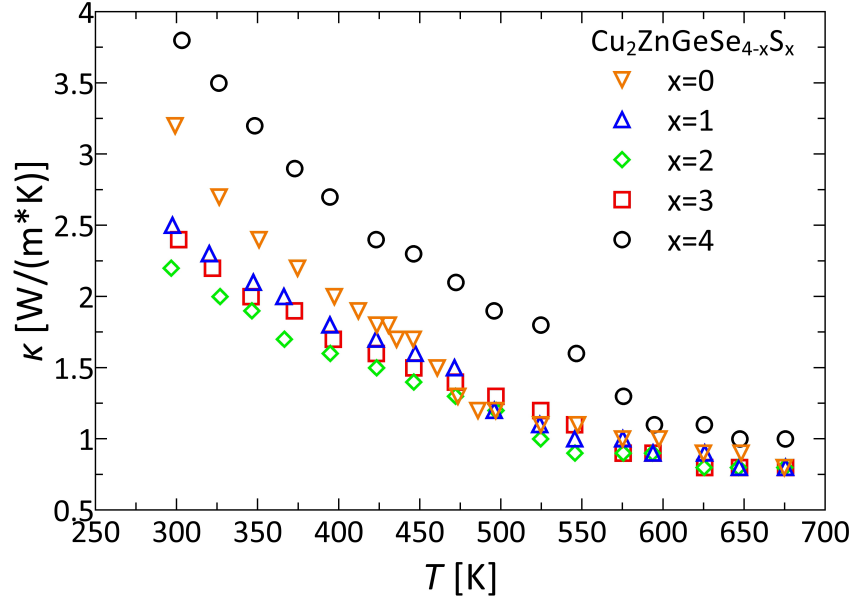


Figure (2.7) – Temperature dependence of the total thermal conductivity κ of the complete solid solution series $\text{Cu}_2\text{ZnGeSe}_{4-x}\text{S}_x$ with $x = 0-4$. Because of the low electrical conductivity, the lattice thermal conductivity equals the total thermal conductivity.

2.3.3. Thermal Transport Properties

The temperature-dependent thermal conductivity of the complete solid solution series $\text{Cu}_2\text{ZnGeSe}_{4-x}\text{S}_x$ is shown in Figure 2.7. Every sample exhibits an overall $1/T$ dependence of the thermal conductivity, which indicates Umklapp scattering to be responsible for the majority of phonon scattering processes. [26] At the aforementioned phase transition temperature, however, a significant drop in the thermal conductivity can be seen. Usually, the thermal conductivity can be interpreted as the sum of the electronic contribution κ_{el} and the lattice contribution κ_{lat} , where the electronic contribution is calculated by the Wiedemann-Franz law. Due to the overall high resistivity of the samples, the calculated electronic contributions to the thermal conductivity are close to 0 over the whole temperature range. Therefore, the measured total thermal conductivity κ_{tot} can be interpreted as the lattice thermal conductivity. Considering this, we believe that the chosen system is suitable to study the effect of anion substitution on the reduction of κ_{lat} . To avoid any influences of the phase transition on the lattice thermal conductivity, the influence of the anion substitution on the thermal conductivity was investigated at room temperature, which is considerably below the phase transition temperatures (see Figure 2.8). $\text{Cu}_2\text{ZnGeSe}_4$ exhibits overall lower thermal conductivity than $\text{Cu}_2\text{ZnGeS}_4$, which can be attributed to the larger atomic mass and the softer bonding character of the heavier homologue. [42] However, these are not the only parameters defining the

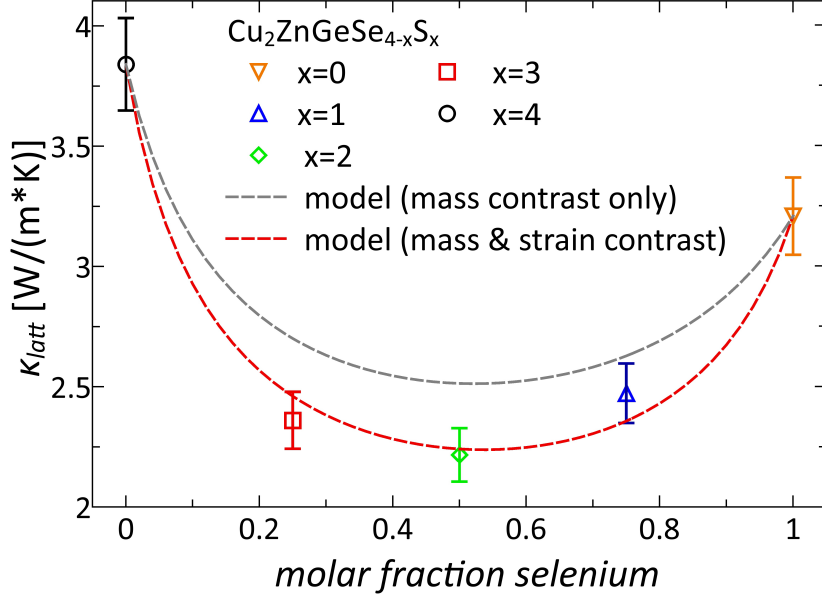


Figure (2.8) – Room temperature lattice thermal conductivities and modeled lattice thermal conductivities of the complete solid solution series $\text{Cu}_2\text{ZnGeSe}_{4-x}\text{S}_x$ with $x = 0 - 4$ (gray dashed line, mass contrast only [$\epsilon = 0$]; red dashed line, mass and strain contrast [$\epsilon = 36$]) plotted against the molar fraction of selenium.

thermal conductivity. In addition to the average anion molar mass, substitution leads to disorder, creating mass contrast and strain contrast in the anion lattice. Both effects are known to act as point scattering sites for phonons. [41] Taking this into account, we have to conclude that the lattice thermal conductivity decreases with increasing disorder at the anion site. Thus, the lowest lattice thermal conductivity is found in the compound $\text{Cu}_2\text{ZnGeS}_2\text{Se}_2$. A total reduction of 42% is obtained for κ_{lat} at room temperature.

Thermal Transport Modeling To be able to differentiate between the influence of the mass contrast and the strain contrast in the disordered crystal, we calculated κ_{lat} using the Callaway model. [35, 38, 41, 42] Assuming Umklapp and point defect scattering to be the main scattering mechanisms ($T > \Theta_D$), the ratio of the modeled lattice thermal conductivity of a disordered crystal, κ_{lat}^{mod} and the lattice thermal conductivity of the pure crystal without disorder κ_{lat}^{pure} is

$$\frac{\kappa_{lat}^{mod}}{\kappa_{lat}^{pure}} = \frac{\tan^{-1}(u)}{u}, \quad u^2 = \frac{\pi^2 \Theta_D \Omega}{h \nu_m^2} \cdot \kappa_{lat}^{pure} \cdot \Gamma \quad (2.1)$$

where u , Θ , h , ν_m , and Γ are the disorder scaling parameter, the average volume per atom, the Planck constant, the average sound velocity, and the disorder scattering parameter, respectively. The disorder scattering parameter Γ can be written as

$$\Gamma = \chi(1 - \chi) \left[\left(\frac{\Delta M}{M} \right)^2 + \epsilon \left(\frac{\Delta a}{a} \right)^2 \right] \quad (2.2)$$

where χ , $\frac{\Delta M}{M}$, ϵ , and $\frac{\Delta a}{a}$ are the molar fraction of selenium, the relative change of atomic mass due to the replacement of selenium by sulfur, the fitting parameter representing the elastic properties of the quaternary chalcogenide, and the local change in lattice parameters resulting from the substitution (pseudocubic approximation $a = \sqrt[3]{V}$), respectively. The disorder scattering parameter indicates mass and strain contrast to be the major contributions to point defect scattering. To calculate κ_{lat}^{mod} , the measured thermal conductivities of $\text{Cu}_2\text{ZnGeS}_4$ and $\text{Cu}_2\text{ZnGeSe}_4$ were used as κ_{lat}^{pure} , and the weighted average of both calculations was applied for κ_{lat}^{mod} . Furthermore, speed of sound measurements were conducted on the complete solid solution series (see Figure 2.9) to obtain the average speed of sound ν_m and the Debye temperature Θ_D . A linear trend was assumed to interpolate the average sound velocities and Debye temperatures of intermediate compositions, which is in good agreement with the speed of sound data obtained from samples with intermittent compositions. The calculated Debye temperatures range from 260 K to 340 K for $\text{Cu}_2\text{ZnGeSe}_4$ and $\text{Cu}_2\text{ZnGeS}_4$, respectively.

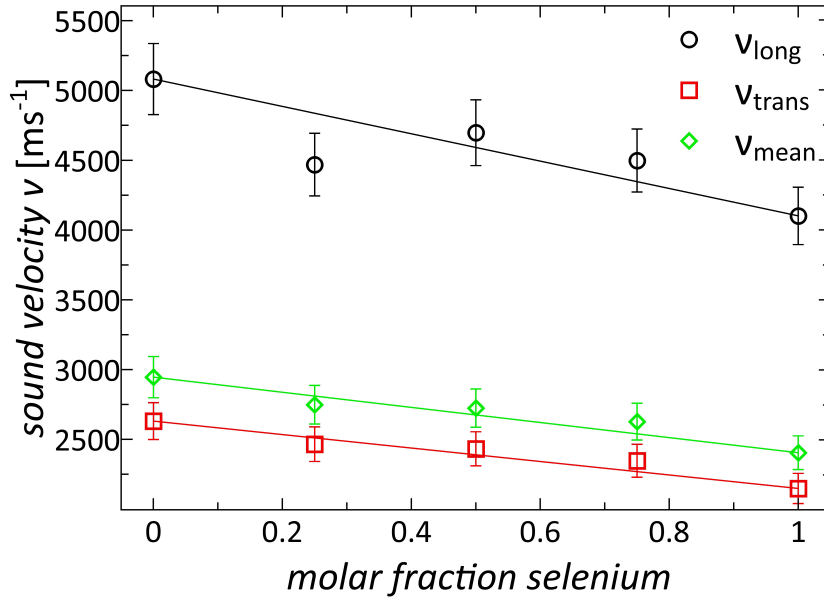


Figure (2.9) – Measured longitudinal, transversal, and calculated mean sound velocity, including the interpolated fit for thermal conductivity calculations, of the complete solid solution series $\text{Cu}_2\text{ZnGeSe}_{4-x}\text{S}_x$ with $x = 0-4$.

A comparison of the measured room temperature thermal conductivity data with the modeled thermal conductivities, calculated with the contribution of mass

fluctuation only (gray dashed line) and with the contribution of mass and strain contrast (red dashed line), can be seen in Figure 2.8. The best fit ($\epsilon = 36$) was obtained under consideration of mass and strain contrast. This is in good agreement with the value of $\epsilon = 40$ found by Steigmeier and Abeles for germanium-silicon alloys. [28] The calculated thermal conductivities, taking only mass contrast into account, show a reduction in thermal conductivity of 34%. Considering a total reduction in thermal conductivity of 42%, the remaining reduction of 8% can be attributed to strain contrast. The good agreement of the fit with the measured data indicates that the reduction of the lattice thermal conductivity within the anion substitution series can easily be calculated using only refined lattice parameters, sound velocities, and thermal conductivity data from the boundary phases. This underlines the importance of this modeling approach to predict a possible reduction of κ_{lat} in similar systems.

2.3.4. Superionic Phase Transition

Up to this point, the evidence of a phase transition within the complete solid solution series was given by differential scanning calorimetry measurements. Additionally, the influence of the phase transition on the electronic and thermal transport properties was identified, and the anion substitution was found to be an easy way to control the phase transition temperature. To further understand the nature of this phase transition, additional investigations are necessary. To address the question whether the phase transition is coupled to a structural change, temperature dependent X-ray diffraction measurements were used. The measurements were performed on the complete solid solution series. Figure 2.10 shows Pawley refined lattice parameters as a function of temperature. The substitution of Se by S results in a decrease of the lattice parameters a and c , following Vegard's law (a result of the smaller ionic radius of sulfur compared to selenium). Furthermore, the lattice parameters increase linearly with temperature, due to linear thermal expansion of the quaternary chalcogenides. Hence, no structural phase transformation can be observed, which would have been visible as a change of slope in the refined lattice parameters. This corroborates the hypothesis of a superionic phase transition, and a "melting" of the copper sublattice, where the average atom positions are conserved.

In Addition, ^{63}Cu magic angle spinning nuclear magnetic resonance measurements (MAS-NMR) of $\text{Cu}_2\text{ZnGeSe}_4$ were conducted at different temperatures (see Figure 2.11). The signal splitting below the phase transition temperature of 450 K indicates the presence of at least two distinct Cu cation sites. However, the second-order

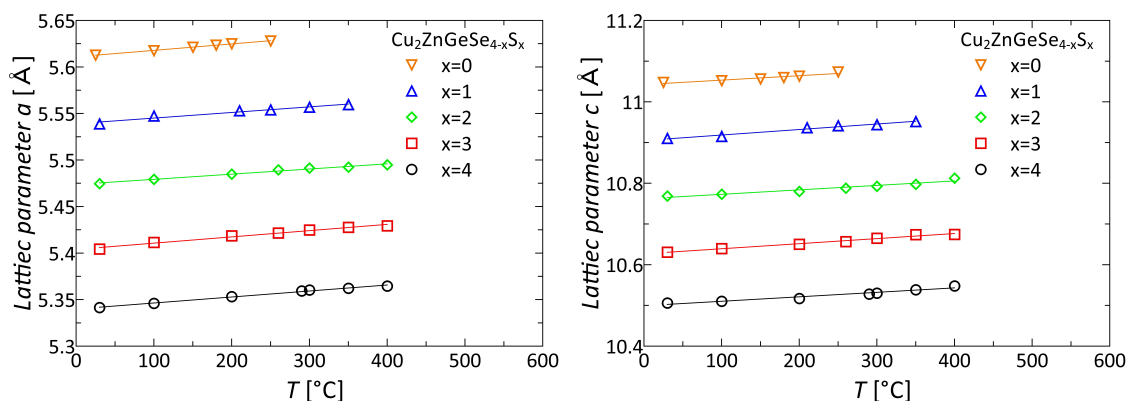


Figure (2.10) – Refined lattice parameters a and c of $\text{Cu}_2\text{ZnGeSe}_{4-x}\text{S}_x$ as a function of temperature. The lattice parameters increase linearly with temperature as a result of the thermal expansion of the lattice. A structural phase transformation would be visible as a change of slope (or kink) in the data.

quadrupolar line shapes cannot be deconvoluted unambiguously, owing to the conflicting demands of increased resolution (faster spinning) and high temperatures. Above 450 K, a broad featureless line shape was observed. In the stannite crystal structure type of $\text{Cu}_2\text{ZnGeSe}_4$ (see supporting information Figure A.1), Cu is merely located on a single crystallographic site, Wyckoff position $4d$ (0, 1/2, 1/4), forming slabs of CuX_4 -tetrahedra. Therefore, a combination of the significantly lower site occupancy of Cu and the ^{63}Cu MAS-NMR data strongly suggests interstitial Cu^+ occupation in this compound. With increasing temperature, all Cu cations become mobile, leading to a superionic phase transformation at 450 K. Above the superionic transition temperature, the cation mobility results in partially averaged local electric field gradients at the copper site, as reflected by the ^{63}Cu MAS-NMR line shape seen in Figure 2.11. Unfortunately, within the solid solution series only $\text{Cu}_2\text{ZnGeSe}_4$, the compound with the lowest phase transition temperature, could be investigated by ^{63}Cu MAS-NMR. The phase transition temperatures of the other compositions (see supporting information figure A.10) are not within the limited temperature range of the used instrument.

Considering the occurrence of a superionic phase transition, the initial interstitial site occupancy in the prepared samples can easily be explained. During synthesis, temperatures above the phase transition temperatures lead to mobile Cu^+ ions, populating the special Wyckoff position as well as interstitial sites. Due to the used intermediate cooling rate during synthesis, some amount of the copper ions are trapped at the interstitial site. Hence, changing the cooling rate around the phase transition temperature should have an influence on the amount of copper at the interstitial sites. A fast cooling rate (quenching) over the phase transition

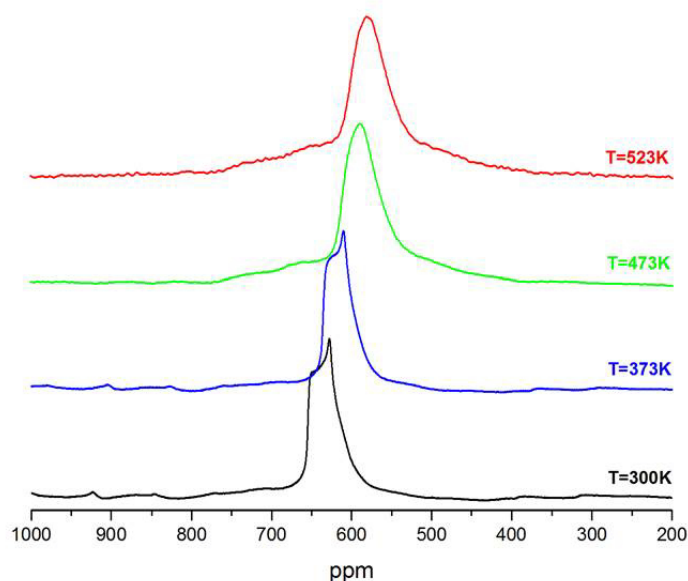


Figure (2.11) – ^{63}Cu magic angle spinning nuclear magnetic resonance of $\text{Cu}_2\text{ZnGeSe}_4$ at different temperatures below and above the phase transformation at 450 K. The signal at lower temperatures shows at least two distinct lattice sites (whose second order quadrupolar line shapes cannot be unambiguously extracted) that later merge into one (apparent) site for Cu, thus suggesting mobile Cu cations due to a superionic phase transformation.

temperature is more likely to produce samples with a higher amount of disorder and interstitial site occupancy.

A possible other method to obtain information on interstitial site occupancy and Cu-Zn antisite disorder is neutron diffraction. In contrast to X-ray diffraction, where the atom form factor depends on the electron density distribution, the wavelength and the scattering angle, the neutron scattering length varies from isotope to isotope, scaling with the strength of neutron-nucleus interaction. Due to different neutron scattering lengths of Cu (7.718 fm) and Zn (5.680 fm), the occupancy at the different lattice sites could be refined. Additionally, a differentiation between the ordered variants of stannite and kesterite should be feasible, which is also not possible with X-ray diffraction.

The influence of the phase transition on the transport properties may be understood by considering the possible interstitial occupancy of copper as well as the missing electron density at the specific lattice sites. Below the phase transition temperature, only holes from intrinsic defects contribute to the transport. At a certain temperature, the bonding attraction between the copper ions and the anions can be overcome by the thermal energy, and copper ions start to become mobile. This leads to an

increase in the resistivity with temperature and an increase of the Seebeck coefficient. While this mechanism cannot be detected by standard laboratory X-ray diffraction the exothermic effect in the differential scanning calorimetry supports the idea of a superionic phase transformation. [76, 93] The increase in the transition temperature with increasing sulfur content can be explained by the lower degree of covalent bonding character in sulfur-rich samples. With increasing ionicity, the copper is more strongly bonded to the lattice, and thus, higher temperatures are needed to overcome this energy barrier. This energy-activated behavior can be seen in many ionic conductors. [93]

Although high copper ion mobility has led to high zT values in few materials, those materials are not yet considered for device tests. In addition to a high zT value, a long thermal cycling stability under closed circuit conditions is also crucial for the application in a thermoelectric generator. Unfortunately, superionic materials usually exhibit poor cycling stability, due to enhanced ion migration. In this case, the change of bonding character, which is induced by isovalent anion substitution may be an effective way to control the phase transition temperature, and thus, control the ion migration in these materials.

2.4. Conclusions and Outlook

Inspired by the thermoelectric properties of adamantine-like chalcogenides, the substitution series $\text{Cu}_2\text{ZnGeSe}_{4-x}\text{S}_x$ has been synthesized as a model system for isovalent anion substitutions. Furthermore, structural, electronic and thermal properties have been investigated. Throughout the series, a Vegard-like behavior of lattice parameters is shown, which is reflected in a linear trend of bond distances, band gap energies, and speed of sound values. Within the substitution series, the special chalcogen position shifts towards the unit cell center, which induces a change of bonding angles away from the ideal tetrahedral angle. This structural change induces crystallographic strain, decreasing the thermal conductivity. The presence of a phase transformation could be confirmed throughout the complete solid solution series and was shown to have a significant influence on the transport properties. Around the phase transition temperature, the resistivity shows an insulator to metal transition, the Seebeck coefficient has a vague minimum and the thermal conductivity drops significantly. Control of the phase transition temperature can be obtained by substitution. This enables us to substantially change the phase transition temperature, and thus, the transport properties. The gradually changing covalent bonding character upon anion substitution, resulting in a higher localization of charge carriers, is reflected by an

overall increase in the electric resistivity. The investigation of the Seebeck coefficient showed large, positive Seebeck values, increasing upon substitution. The detailed analysis of the thermal conductivity revealed an overall $1/T$ dependence and a 42% reduction of the room temperature lattice thermal conductivity by disorder scattering due to the anion substitution. Further, the successful use of the Callaway model to calculate the lattice thermal conductivity has been demonstrated to be a powerful tool to predict the lattice contribution to the thermal conductivity. The calculations revealed mass contrast (reduction of 34%) to have a greater influence than strain contrast (reduction of 8%). The investigation of the phase transition by variable temperature X-ray diffraction and ^{63}Cu MAS-NMR supports the hypothesis of a superionic phase transition. VT-XRD measurements showed a linear increase in the lattice parameter with temperature, which indicates that the phase transition is not accompanied by a structural change. ^{63}Cu MAS-NMR measurements gave clear evidence of Cu^+ located at at least two distinct sites below the phase transition temperature. The signals coalesce above the transition temperature, in accordance with the image of a melting Cu-sublattice. Additionally, the effects of the phase transition on the transport properties can be understood within the image of a superionic phase transition. Although the investigated sulfur substitution series did not lead to an enhancement of the thermoelectric figure of merit, the established structure-property relationships are useful to further optimize other related adamantine materials with a higher potential for thermoelectric application. The structurally conditioned low thermal conductivity and the superionic phase transition can easily be controlled via isovalent anion substitution. The low thermoelectric figure of merit of the sulfur containing compounds are mainly due to the high electric resistivity. These, however, could be enhanced by substitution with the heavier homologue tellurium or by the use of adamantine-like structures with an inherently higher carrier mobility.

3

Indium-filled Skutterudites

This project was done in collaboration with [REDACTED] from the German Aerospace Center (Deutsches Zentrum für Luft- und Raumfahrt, DLR) in Cologne. Project design, material synthesis and processing, chemical characterization and data analysis were conducted at the Johannes Gutenberg-University of Mainz. Powder consolidation and thermoelectric characterization were done at the DLR.

3.1. Motivation

Skutterudite materials have been a focus of thermoelectric research for over two decades (see section 1.5.2). The indium-filled variants of CoSb_3 have especially proven to exhibit a high potential for thermoelectric energy conversion, due to their reduced thermal conductivity and exceptional electronic properties. Furthermore, indium atoms, filling the crystallographic void of the skutterudite structure, are able to donate electrons to the host structure, hence enabling the optimization of the charge carrier concentration. Another way to optimize the transport properties is to increase the amount of phonon scattering centers, for example, by grain boundary scattering via nanoscaling. Skutterudite materials do not have any intrinsic possibilities for nanostructuring, and therefore, the development of nanosized, filled skutterudite powders, which have been optimized in respect to their electronic properties, is an important step towards phonon and electron engineered materials. Different synthetic routes towards nanoscaled skutterudites with an increased grain boundary

concentration have been already investigated, including wet chemical approaches [110] and melt spinning [112]. However, these routes usually lead to phase mixtures with unwanted impurity phases comprised of InSb, Sb, CoSb, and CoSb₂. The influence of these side phases can be seen in the range of published thermoelectric properties of indium-filled skutterudites. [101, 117–120, 163] Although nanosized impurities of InSb have been reported to show a beneficial influence on the thermal properties, [116] phase pure samples will facilitate the understanding of structure-property relationships.

To this end, an alternative two-step synthesis for phase pure filled skutterudites with varying indium content was investigated. The obtained materials were analyzed with respect to phase composition, homogeneity, thermal stability and thermoelectric transport properties. Further, an easy top-down approach towards filled skutterudite nanoparticles starting from bulk skutterudite materials was developed. With this work we aim to broaden our knowledge of the influence of the indium-filling degree, the phase purity, and the grain size distribution in skutterudite materials on the thermoelectric properties.

3.2. Experimental Details and Methods

Synthesis Bulk samples of polycrystalline In_xCo₄Sb₁₂ with compositions of $x = 0, 0.12, 0.15, 0.18,$ and 0.20 were prepared by solid state reactions using elemental powders of In (Alfa Aesar, 99.999 %), Co (Alfa Aesar, 99.998 %), and Sb shots (Alfa aesar, 99.9999 %). The phase purity of all starting materials was verified by X-ray diffraction, and all synthetic procedures were carried out under controlled atmosphere in a N₂ glove box. Annealing was performed in evacuated quartz ampoules, which were preheated at 800 °C under dynamic vacuum for 5 hours to ensure dry conditions. The used synthesis method of filled skutterudite samples can be divided into two steps: first, the formation of the unfilled CoSb₃ kiefertite host, and second, the topotactic indium insertion. In the first step, the starting elements are thoroughly ground, sealed in quartz ampoules, and annealed at 700 °C for 12 hours. During this initial reaction, the CoSb₃ phase has formed. To eliminate small amounts of excess Sb, the powder compact is finely ground again and reannealed at 700 °C for 12 hours. During the second annealing step, excess Sb transports to the opposite side of the ampoule, driven by the inherent temperature gradient within the used horizontal tube furnaces. In the second step, phase pure CoSb₃ is thoroughly mixed with In, sealed again and reacted at 700 °C for 48 hours. Heating and cooling rates for all procedures in the horizontal tube furnaces were 5 °C/min. The quartz ampoules were 10 cm in length and 11 mm in inner diameter with a maximum of 5 g of starting

materials per ampoule. The obtained powders of $\text{In}_x\text{Co}_4\text{Sb}_{12}$ were hand ground, and phase purity was verified via standard X-ray diffraction prior to further processing. To ensure sample homogeneity and reproducibility of all measurements, multiple samples of each compound were synthesized and merged to form large batches after the phase purity was confirmed by powder X-ray diffraction and Rietveld refinement. These batches were used for the subsequent processing and all measurements.

Ball Milling High purity, bulk indium-filled skutterudite powder of nominal composition $\text{In}_{0.18}\text{Co}_4\text{Sb}_{12}$ was used to produce nanosized particles via ultra-fine colloidal grinding using a Retsch PM200 planetary ball mill. A 50 ml hardened steel grinding jar was loaded with 100 hardened steel grinding balls, each with a diameter of 3 mm, and 30 g of skutterudite bulk powder. Freshly dried, distilled and degassed n-hexane was used as liquid grinding medium. Loading of the grinding jar and the post-milling powder processing were carried out in a N_2 glove box to prevent sample oxidation. The total milling time of 25 hours was divided into alternating blocks of 10 min milling at 500 rpm and 15 min of cool down.

Powder Processing Batches of bulk powders with different In content were used for consolidation into 1-1.5 mm thick, 12.7 mm diameter disks at 590 °C under a pressure of 56 MPa by direct current-assisted short-time sintering utilizing a DSP ("Direktsinterpresse"). Boron nitride coated high density graphite was used as die material to sinter four pellets simultaneously in the same die. The heating rate was ≈ 60 K/min. Maximum temperature and pressure were applied for 10 min before the pressure was released and the sample cooled down in an uncontrolled way. The resulting pellets had more than 98% of theoretical density, as determined by the pellet mass and the Archimedes method.

Characterization Details Room temperature powder X-ray diffraction measurements were performed on a Siemens D5000 powder diffractometer in transmission geometry with a Braun M50 position sensitive detector, Ge (220) monochromator and CuK_α radiation, with a step size of 0.0078° in 2Θ . The samples were mounted between two strips of scotch tape.

High resolution synchrotron powder diffraction data were collected on beam line 11-BM at the Advanced Photon Source (APS) of the Argonne National Laboratory (ANL) with an average wavelength of 0.413721 \AA . Discrete detectors covering an angular range from -6 to 16° 2Θ were scanned over a 34° 2Θ range, with data points collected every $0.001^\circ\Theta$ and a scan speed of $0.01^\circ/\text{s}$. All samples were diluted with amorphous silica in a 1:1 molar ratio to reduce the X-Ray absorption and obtain

a total $\mu R \approx 1$. The samples were mounted in Kapton tubes with 0.4 mm radii. Rietveld refinements of all diffraction data were performed with TOPAS Academic V4.1 [155] applying the fundamental parameter approach.

The thermoelectric characterization was conducted at the German Aerospace Center (DLR). Temperature dependent Seebeck coefficients and electric conductivities were measured simultaneously on the HT-S- σ 2 measuring system (High Temperature Seebeck & electrical conductivity). [164] Thermal diffusivity was measured using a Netzsch laser flash diffusivity instrument (LFA 427). Heat capacity (C_p) was estimated using the Dulong-Petit approximation ($C_p = 3k_B$ per atom) and theoretical densities were calculated from the molar mass and the refined lattice parameters for each composition. The accuracy of measurements are estimated to be 5%, 7%, and 10% for the Seebeck coefficient, the electrical conductivity and the thermal conductivity, respectively.

Scanning electron microscopy (SEM) images and energy dispersive X-ray spectroscopy (EDX) measurements of the as-synthesized powders and the sintered pellets were recorded using a FEI Nova NanoSEM600 equipped with an Everhart-Thornley detector (ETD) and a low voltage high contrast detector (vCD) in high vacuum mode. The acceleration voltage was chosen to be between 15-30 kV. The samples were mounted on an aluminum stub using adhesive conductive carbon tape. For energy dispersive X-ray spectroscopy, a built-in EDAX-Genesis detector was used.

Transmission electron microscopy (TEM) images of nanosized particles were collected on a Phillips EM-420 equipped with a slow scan CCD detector (1 k x 1 k) and a LaB₆ electron gun operated with an acceleration voltage of 120 kV. TEM samples were prepared by dispersion of the sample in ethanol or hexane by use of an ultrasonic bath in full power mode and drop casting on 300 mesh carbon coated copper grids.

¹²¹Sb Mößbauer measurements were performed in standard transmission geometry using a ^{121m}Sn in CaSnO₃ source of nominal activity 0.3 mCi on a constant acceleration spectrometer. During the measurements, both source and absorber were held at 10 K to increase the fraction of recoil-free emission and absorption processes. The velocity calibration was performed with α -Fe at room temperature utilizing a ⁵⁷Co/Rh source. The extracted isomer shifts are reported in reference to InSb at 10 K ($\delta = -8.6$ mm/s relative to the Ca^{121m}SnO₃ source).

3.3. Results and Discussion

3.3.1. Two-step Synthesis of Indium-filled Skutterudites

A phase pure synthesis is the first, very important step to investigate a thermoelectric material. Impurities or inhomogeneities often cause significant changes in transport properties. Although a beneficial influence may sometimes be obtained, only an undisturbed, well-characterized system enables the proper investigation of structure-property relationships. In order to design a solid state synthesis, knowledge of the underlying phase-relations is crucial. Figure 3.1 shows the binary Co-Sb phase diagram, [165] and thus gives important information on the thermodynamic stability of the δ -phase CoSb_3 , as well as the other binary phases. CoSb_3 is incongruently melting

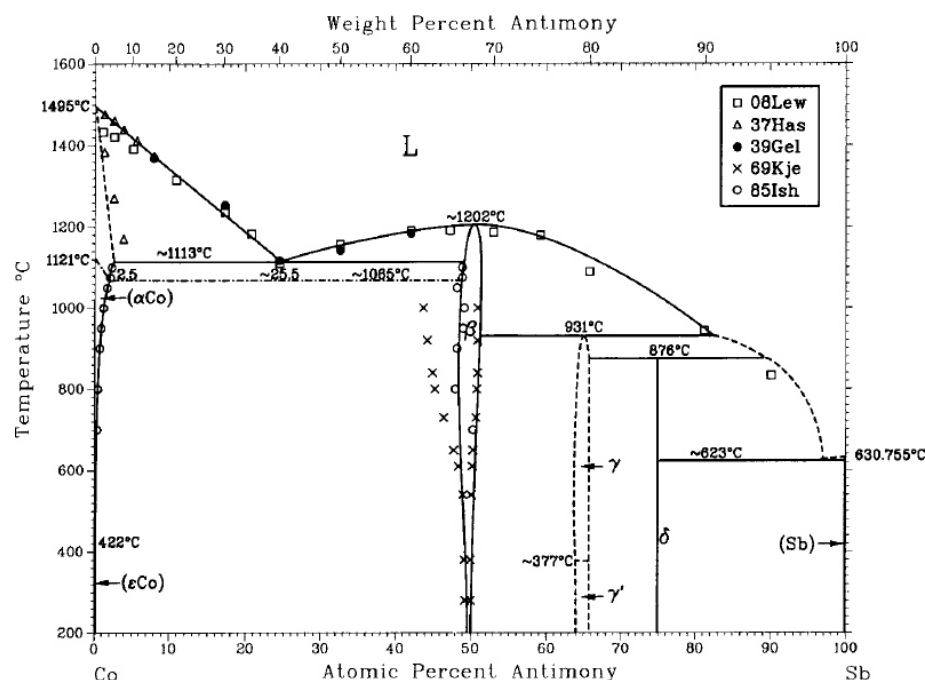


Figure (3.1) – Phase diagram of the binary Co-Sb system, illustrating the incongruent melting point of CoSb_3 at 876°C and CoSb_2 at 931°C , next to the congruent melting point of CoSb at 1202°C . [165]

and has the lowest decomposition temperature of all binary Co-Sb phases (876°C). The decomposition temperature of CoSb_2 is slightly higher at 931°C . CoSb melts congruently with a melting point of 1202°C . The commonly used solid state synthesis of filled or unfilled CoSb_3 materials is done using a melt-quench-anneal method. To obtain a good homogeneity, the powder mixture is heated to temperatures above the melting point (usually $> 1100^\circ\text{C}$). Subsequently, the liquid mixture is quenched to room temperature as fast as possible to minimize phase formation within the temperature range between the melting point and the decomposition temperature. By

quenching, the homogeneous atom distribution of the melt can usually be maintained. However, in order to obtain well crystallized and homogeneous materials, a long annealing step at temperatures below the decomposition temperature is necessary. The disadvantages of this method are the long annealing periods of up to a week, and the inability to prevent small quantities of CoSb_2 or CoSb to form during the quenching process. It should be considered that these impurities are more stable up to higher temperatures than CoSb_3 , and thus cannot be converted to kieftite by long time annealing below the melting point. The addition of a filler element to the synthesis facilitates the occurrence of side reactions and the formation of impurity phases during the quenching process (e.g. InSb). Further, the formation of binary phases with the filler atom will inevitably lead to a change in stoichiometry, which in turn will promote the formation of other impurity phases.

Besides the phase purity, the reaction time to obtain a material of a certain purity plays an important role in the commercialization of new materials. Hence, longtime annealing steps are rather unwanted and other methods with shorter reaction times were investigated. A very fast synthesis of filled skutterudite materials in only a few hours was reported by Biwas et al. in 2011 using a rapid microwave method. [166] However, the method has some disadvantages concerning the phase purity and scalability, which resulted in inferior thermoelectric properties. To overcome the difficulties of sample impurity and long reaction times an alternative two-step synthesis method was established during this work to obtain high quality powders of indium-filled skutterudites in bulk quantities and short reaction times.

To avoid the formation of side phases, the synthesis of indium-filled skutterudites was divided into two steps. First, CoSb_3 was synthesized as the host material, and then filled in the second step by a topotactic filler-insertion reaction. Due to this, the side reactions of In (as a filler) with elemental Sb can be avoided. In the first step, phase pure CoSb_3 was synthesized by the reaction of Co and Sb powder at 700°C for 12 hours. This reaction temperature is well below the decomposition temperature of CoSb_3 , but above the melting point of Sb . Although the reaction takes place above the melting point of Sb , a reaction of Co dissolved in an Sb -melt can be excluded. In this case, the formation of a molten bead would be expected. However, the obtained product consists of a powder compact that is only sintered together. Furthermore, the reaction duration of 12 hours is quite short for a classic solid-solid reaction, which could be an indication of the participation of Sb through the gas phase. However, besides the known high antimony partial pressure no experimental evidence is found to strengthen this assumption. The typical X-ray powder diffraction data obtained after the initial reaction shows phase pure and

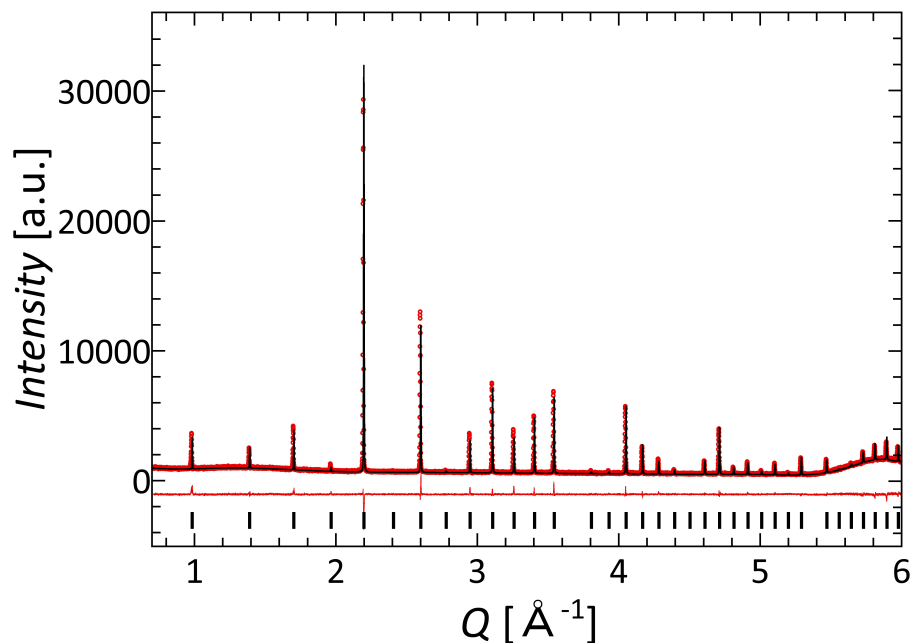


Figure (3.2) – Refined powder diffraction data of a CoSb_3 sample after the initial reaction at 700°C for 12 h (red dots), including profile fit (black solid line), and profile difference (red solid line). The refined peak positions are indicated by black tick marks. Even after the short reaction time of 12 hours well crystallized, phase pure kieftite is obtained.

well crystallized CoSb_3 (see Figure 3.2). Nevertheless, if the powder compact is ground again and annealed a second time at 700°C for 12 hours, a small amount of antimony transports to the colder side of the ampoule. The Sb transport probably is driven by a small inherent temperature gradient within the used horizontal tube furnaces. [152] During this second annealing, no further sintering takes place and fine powdered phase pure CoSb_3 is obtained. Unfortunately, it is uncertain whether the transported antimony arises from unreacted antimony, undetected within the resolution of standard laboratory diffraction (CuK_α radiation), or if the antimony leaks out of the already formed kieftite phase. A proper quantification either of the transported antimony or of the antimony defect concentration in the resulting CoSb_3 was not possible. In the second step, the kieftite powder is thoroughly mixed with indium, sealed again in an ampoule and reacted at 700°C for 48 hours. Although no optimization of the reaction time has been done so far, the total time for the two-step synthesis is significantly lower than the common melt-quench-anneal method. A set of bulk powder batches with different In content ($\text{In}_x\text{Co}_4\text{Sb}_{12}$ with $x = 0.12, 0.15, 0.18$ and 0.20) was produced in order to investigate the phase composition, homogeneity and the effect of the filling level on the thermal and electronic transport properties. Consolidated samples were obtained by short-time sintering via DSP. A

sinter program, previously elaborated at the DLR for filled skutterudite materials, was used to consolidate the samples. [119] The heating rate was $\approx 60^\circ\text{C}/\text{min}$. The maximum temperature of 590°C and pressure of 56 MPa were applied for 10 min, before the pressure was released and the sample cooled down in an uncontrolled way. The resulting pellet densities, determined pycnometrically, were all above 98% theoretical density. Disks of these polycrystalline materials, therefore, are considered suitable for thermoelectric characterization.

3.3.2. Structural Characterization of Bulk Indium-filled Skutterudites

The refined laboratory X-ray diffraction data, obtained from synthesized skutterudite powders as well as compacted pellets, are redundant with respect to the high quality synchrotron data shown below and will not be shown here. However, all reflections could be indexed to the skutterudite structure type and no secondary phases were observed within the resolution limit of the used diffractometer. During the sintering process and the thermoelectric characterizations, the materials are subjected to thermal cycling under varying conditions and may be inclined to compositional, structural or microstructural changes. Therefore, a detailed structural characterization was not only conducted on the synthesized powders, but also on thermally cycled pellets.

SEM/EDX analysis The microstructural and elemental analyses of all indium-filled skutterudite samples are very comparable. Exemplary scanning electron microscopy images of the synthesized powder and consolidated/measured pellet can be seen in Figure 3.3. Both images were taken from samples with nominal composition $\text{In}_{0.12}\text{Co}_4\text{Sb}_{12}$. Samples of varying indium content did not exhibit any differences with respect to the sample homogeneity, grain size distribution or grain growth during the sintering process. The surface of the powder (left image) and the polished surface of the pellet (top part right image) show no sign of contrast, corroborating with a homogeneous material. The two-step synthesis, therefore, seems to be better suited for the preparation of phase pure materials than the melt-quench-anneal method, which is known to lead to side phases of Sb and InSb at the grain boundaries. [119] The polished surface and the breaking edge of the pellet (bottom part of right image) show only a few cavities, confirming the high density obtained by short time sintering. The grain sizes before and after consolidation range from $2\text{-}5\ \mu\text{m}$, which demonstrates that no significant grain growth took place during the sintering process and several

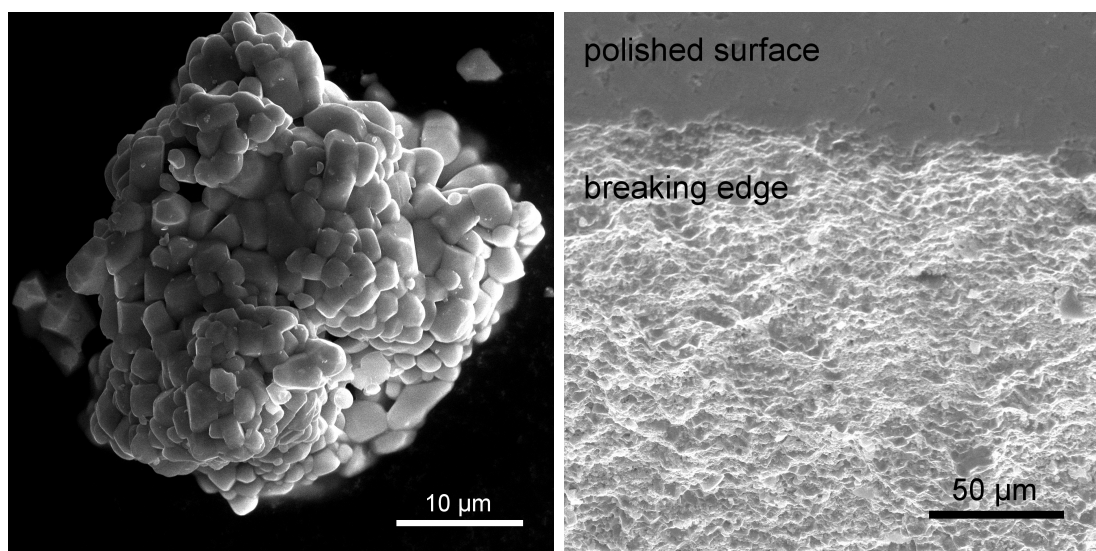


Figure (3.3) – Exemplary scanning electron microscopy image of synthesized $In_xCo_4Sb_{12}$ bulk powder (left) and a consolidated $In_xCo_4Sb_{12}$ pellet (right). In comparison to extended hot-pressing, no significant grain growth took place during the short-time sintering process and the thermal cycling due to thermoelectric characterization. Images shown here were taken from a sample of nominal composition $In_{0.12}Co_4Sb_{12}$

subsequent thermal cycles of thermoelectric characterization. Powder homogeneity was confirmed by energy dispersive X-ray spectroscopy, shown in the supporting information Figure B.1. However, it has to be noted that the measurement accuracy of the EDX is about 3 at% and, therefore, does not allow a proper quantification of the indium content and will not detect small compositional variations. Furthermore, neither conclusions about nor quantification of Sb deficiency could be attained by energy dispersive X-ray spectroscopy analysis due to the limited accuracy of the used method.

Potential-Seebeck-Microprobe An alternative measurement method to gain information on sample homogeneity is the Seebeck scanning microprobe. [167] The Seebeck coefficient is very sensitive for compositional changes, which affect the charge carrier concentration. An inhomogeneous distribution, either of indium as filler atom or of Sb defects, would result in a change of the Seebeck coefficient. Therefore, Potential-Seebeck-Microprobe (PSM) measurements were conducted on all sintered samples on each side. Figure 3.4 shows a typical plot of a PSM measurements obtained from the complete surface of a pellet. For this scan a sample of nominal composition $In_{0.18}Co_4Sb_{12}$ was used. The very good radial sample homogeneity is evident. The position-dependent Seebeck values can be summarized in a histogram, and thus, provide information on the range of obtained Seebeck values in a pellet. Figure

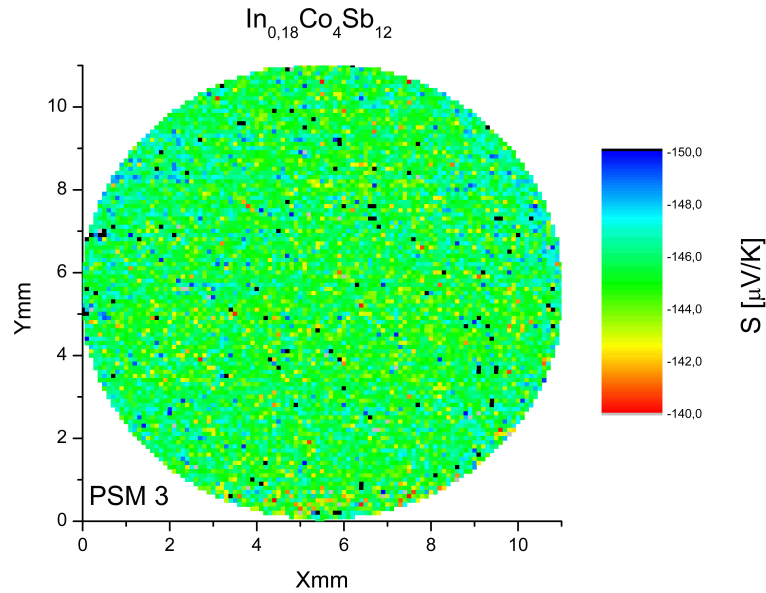


Figure (3.4) – Potential-Seebeck-Microprobe measurement of the complete surface of a consolidated pellet of nominal composition $\text{In}_{0.18}\text{Co}_4\text{Sb}_{12}$. Due to the very sensitive nature of the Seebeck coefficient, small compositional changes can be visualized. The very uniform and narrow distribution of Seebeck values demonstrates the outstanding sample homogeneity.

B.2 in the supporting information illustrates the obtained Seebeck distribution measured on all samples. The single measurements exhibit small distribution of Seebeck coefficients below $20 \mu\text{V}/\text{K}$, which corroborates with the good sample homogeneity. A very small difference can be seen between measurements operated on opposite sides of some of the pellets. This might be an indication of a slight compositional gradient along the pellet height, possibly resulting from a temperature gradient, due to the Peltier effect, during the sintering process. However, the small differences of only $5 \mu\text{V}/\text{K}$ are very subtle and will not significantly affect the thermoelectric figure of merit. In comparison to the Seebeck data obtained using the HT-S- σ 2 system, see section 3.3.3, the Seebeck values obtained from PSM measurements are slightly lower, which is a common systematic error of the PSM system.

X-ray powder diffraction All samples were analyzed via laboratory X-ray diffraction before and after powder consolidation. Nevertheless, some questions concerning the site occupancies or possible anti-site disorder could not be answered due to the limited resolution and weak, but significant, sample fluorescence. To this end, a set of 8 samples, comprising unprocessed powders of compositions $\text{In}_x\text{Co}_4\text{Sb}_{12}$, with $x = 0.12, 0.15, 0.18, 0.20$, and samples of composition $x = 0.12$ after consolidation, after the first complete thermoelectric characterization (denominated "Cycle #1"),

and after a second and third cycle of electronic transport measurements (denominated "Cycle #2" and "Cycle #3"), were sent to beamline 11-BM at the Advanced Photon Source (APS) of the Argonne National Laboratory (ANL) to collect high resolution synchrotron diffraction data. This set of samples was chosen in order to investigate the influence of the indium-filling degree on the structure, as well as to analyze possible changes induced by consolidation and thermal cycling during sample measurements. The data obtained from 11-BM generally has the advantage of high resolution ($<0.0002 \Delta Q/Q$), no sample fluorescence, and a low sample absorption. The energy of the Sb L edge is just below the energy of ≈ 30 KeV used at 11-BM, which would result in a total sample absorption of $\approx 2.8 \mu\text{R}$. Normally, measurements of samples up to a total absorption value of $5 \mu\text{R}$ are suitable, if the absorption is accounted for during the Rietveld refinement. However, to obtain data sets without significant contribution of absorption, the samples were diluted with amorphous silica in a 1:1 molar ratio. Unfortunately, the sample with composition $x = 0.15$ was contaminated during sample preparation. The contamination most likely is composed of scrubbing powder (main side phase consists of calcite), which was used to clean the mortar before mixing the powders with amorphous silica. The additional crystalline phases in this sample are partially overlapping with the skutterudite reflexes and, thus, prevent a proper refinement.

In-depth Rietfeld refinements of the room temperature synchrotron data were conducted with an elaborated refinement sequence, to prevent cross contributions of simultaneously refined parameters. To check for deviations from the ideal occupancies, the occupancy parameters were refined in separate least-squares cycles with a fixed scale factor in alternation with the thermal parameters until convergence. Several sets of refinements were conducted to implement possible anti-site disorder (In_{Sb} , Sb_{In}). However, the large obtained errors in site occupancies and temperature parameters ($B_{i_{so}}$) combined with too high or low $B_{i_{so}}$ -values are a good indication for an over parametrization. Because of this, the refinements were conducted under the assumption of normal site occupancy. For a more thorough investigation of possible anti-site disorder, neutron diffraction or combined neutron-synchrotron diffraction studies are under consideration. Data of samples with composition $\text{In}_{0.12}\text{Co}_4\text{Sb}_{12}$ and $\text{In}_{0.20}\text{Co}_4\text{Sb}_{12}$ are shown in Figure 3.5, including profile fits, profile differences, and profiles. The complete set of refined synchrotron data can be found in the supporting information in section B.2. Looking at the refined diffractograms, the high quality (phase purity and crystallinity) of the skutterudite materials, obtained by the two-step method, is conspicuous. Although the samples exhibit quite different thermoelectric properties (see section 3.3.3), the differences in the powder pattern are

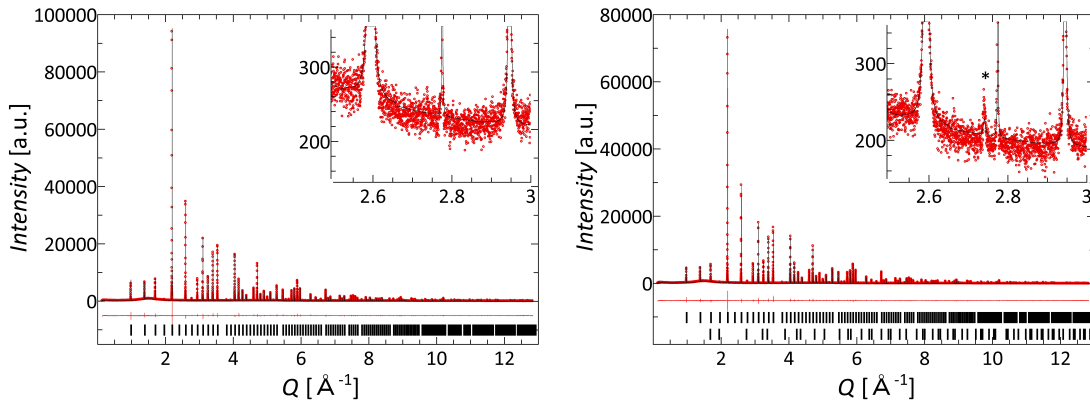


Figure (3.5) – Refined powder diffraction data for the samples of nominal composition $In_{0.12}Co_4Sb_{12}$ (left) and $In_{0.20}Co_4Sb_{12}$ (right), including profile fit (black solid line), and profile difference (red solid line). The refined peak positions are indicated by black tick marks. The zoomed-in plots illustrate the presence of InSb as side phase marked by an asterisk in $In_{0.20}Co_4Sb_{12}$. Note the large difference in peak intensities between the skutterudite phase and the InSb side phase.

difficult to determine at a glance. Only through extreme enlargement of the figures (see zoomed-in inlets) very subtle, additional Bragg intensities, marked by an asterisk, can be seen in the two samples of highest nominal In content, $In_{0.18}Co_4Sb_{12}$ (see supporting information Figure B.9) and $In_{0.20}Co_4Sb_{12}$ (right image Figure 3.5). This additional phase can be indexed to cubic InSb, indicated by the lower tick marks in the right image of Figure 3.5. It has to be noted that these additional reflexes could only be detected due to the high spatial resolution and beam flux obtained at 11-BM and could not be resolved by standard laboratory powder diffraction. The illustrated reflex of InSb at $Q \approx 2.75 \text{ \AA}^{-1}$ can be indexed to the second strongest (80%) Bragg intensity (220) in the InSb pattern. However, the absolute intensity after background subtraction is still below 100 counts. In comparison, the strongest skutterudite Bragg intensity has over 70000 counts, which shows that the impurity phase comprises only a very small volume fraction of the sample. However, due to the weak reflexes a proper quantitative analysis is not possible and the refined value of $\approx 0.1 \text{ vol}\%$ has to be seen as a crude estimation. In addition, two very broad features can be seen in every plot around Q values of 1.5 \AA^{-1} and 5 \AA^{-1} , which corroborate the contribution of the amorphous silica. In order to allow a proper background evaluation, these intensities were modeled via ‘dummy’ reflexes prior to the refinement.

For further evaluation, refined parameters such as the lattice parameter a , y - and z - coordinates of the 24g-Sb site, vol% of InSb side phase, site occupancies and isotropic atomic temperature factors (B_{iso}) of In, Co and Sb are listed in Table 3.1 and 3.2. The weighted profile residuals and goodness of fit for all refinements are below 6.7% and 1.1, respectively. The sample with an indium content of 0.15, which

has been contaminated, exhibits larger estimated standard deviation values. Within the refined lattice parameters, two trends can be depicted, as illustrated in Figure 3.6. In the left image, the refined indium site occupancy is plotted against the refined lattice parameter a . The linear trend illustrates the increase in lattice parameter

Table (3.1) – Refined weighted profile residual (R_{wp}), goodness of fit (GOF), lattice parameter a , y - and z - coordinate of the Sb site and vol% of InSb side phase. Numbers in parentheses indicate the estimated standard deviation determined by the refinement.

sample #	R_{wp} [%]	GOF	LP a [Å]	y -coord. (Sb)	z -coord. (Sb)	InSb [vol%]
In _{0.12} Co ₄ Sb ₁₂	0.05896	1.017	9.04603(0)	0.15801(2)	0.33529(2)	0
"In _{0.12} " sintered	0.05571	1.034	9.04606(0)	0.15796(2)	0.33517(2)	0
"In _{0.12} " Cycle #1	0.06111	1.097	9.04572(0)	0.15823(3)	0.33545(3)	0
"In _{0.12} " Cycle #2	0.05801	1.064	9.04557(0)	0.15772(2)	0.33548(3)	0
"In _{0.12} " Cycle #3	0.06380	1.005	9.04550(0)	0.15809(3)	0.33546(3)	0
In _{0.15} Co ₄ Sb ₁₂	0.09063	1.369	9.47050(0)	0.15824(5)	0.33530(5)	0
In _{0.18} Co ₄ Sb ₁₂	0.06574	1.027	9.05073(0)	0.15788(3)	0.33510(3)	0.087(18)
In _{0.20} Co ₄ Sb ₁₂	0.06627	1.039	9.04953(0)	0.15779(3)	0.33498(3)	0.116(20)

Table (3.2) – Refined site occupancies (Occ) and isotropic atomic temperature factor (B_{iso}) of In, Co and Sb. Numbers in parentheses indicate the estimated standard deviation determined by the refinement.

sample #	Occ_{In} [%]	Occ_{Co} [%]	Occ_{Sb} [%]	B_{iso} In [Å ²]	B_{iso} Co [Å ²]	B_{iso} Sb [Å ²]
In _{0.12} Co ₄ Sb ₁₂	0.1130(15)	1.0000(12)	1.0000(12)	1.82872(13121)	0.28426(650)	0.48163(226)
"In _{0.12} " sintered	0.1103(14)	1.0000(12)	1.0000(11)	1.77984(11965)	0.33794(662)	0.47870(223)
"In _{0.12} " Cycle #1	0.1130(18)	1.0000(14)	1.0000(14)	2.20400(17454)	0.35588(816)	0.47685(273)
"In _{0.12} " Cycle #2	0.1134(16)	1.0000(12)	1.0000(12)	2.97778(18221)	0.33687(722)	0.47364(243)
"In _{0.12} " Cycle #3	0.1005(18)	1.0000(14)	1.0000(14)	1.98971(19981)	0.34892(816)	0.44562(269)
In _{0.15} Co ₄ Sb ₁₂	0.1107(31)	1.0031(27)	0.9847(26)	1.78210(25659)	0.27523(1386)	0.47028(476)
In _{0.18} Co ₄ Sb ₁₂	0.1602(19)	1.0085(15)	1.0000(14)	2.99965(13304)	0.32601(802)	0.46256(267)
In _{0.20} Co ₄ Sb ₁₂	0.1446(18)	1.0047(14)	1.0000(14)	1.63439(11580)	0.27802(780)	0.44191(264)

due to the expansion of the unit cell, which is a direct consequence of filling the crystallographic void. The refined values are in very good agreement with results reported from other groups. [101, 121, 123, 163] However, it is important to note that the samples with nominal In content of $x = 0.18$ and 0.20 have a substantially lower actual indium-filling degree, due to the formation of very small amounts of InSb. The actual indium-filling degree of the sample of nominal composition In_{0.20}Co₄Sb₁₂ is reduced by almost 28% to a value of 0.145, which is even lower than the value of 0.160 found for the sample of nominal composition In_{0.18}Co₄Sb₁₂. The formation of InSb, therefore, plays a crucial role in the actual indium-filling level, which can easily be understood considering the very different indium contents in In_{0.20}Co₄Sb₁₂ (1.2 at%) and InSb (50 at%).

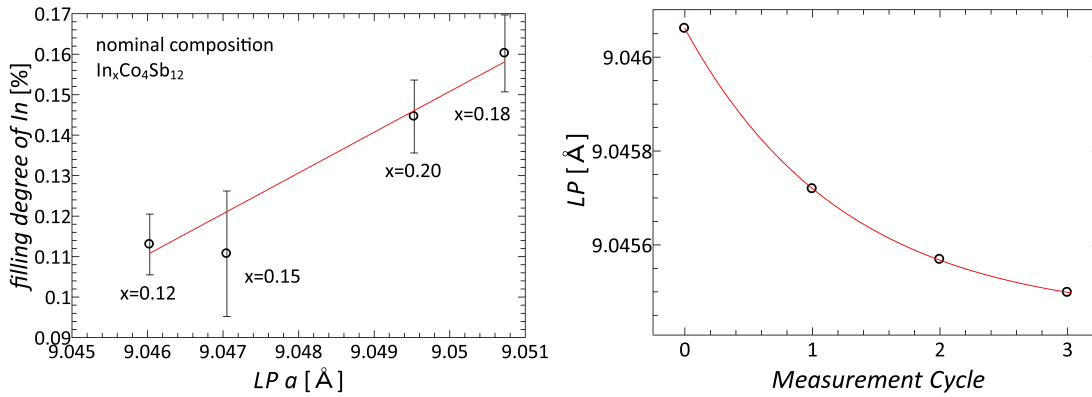


Figure (3.6) – *Left: Refined In site occupancy plotted against the lattice parameter a . Note, the sample of nominal composition $In_{0.20}Co_4Sb_{12}$ exhibits a lower indium-filling degree and a smaller lattice parameter than the sample of nominal composition $In_{0.18}Co_4Sb_{12}$, which can be explained by different InSb concentrations, reducing the amount of In inserting the void site. Right: Refined lattice parameter a plotted against the number of thermoelectric measurements cycles, illustrating a subtle decrease in LP with increasing number of thermal cycles.*

The image on the right side of Figure 3.6 shows the refined lattice parameters plotted against the measurement cycles. The lattice parameter of the sintered material corresponds to the lattice parameter of the unprocessed powder (denominated "Cycle #0"). With an increasing number of measurements, hence, an increasing number of thermal cycles up to 550 °C, the lattice parameter decreases slightly. However, no significant change in the site occupancies was detected by Rietveld refinements. The small decrease in lattice parameter could, for example, be correlated to a very small loss of antimony and/or indium, which could not be detected by SEM/EDX or the refinement of the high resolution synchrotron data. A loss of antimony would result in a higher defect concentration and, as a result, a higher intrinsic charge carrier concentration. In contrast, a loss of In would lead to a lower filling degree, which would result in a higher thermal conductivity and a lower extrinsic charge carrier concentration (see Subsection 3.3.3). The combination of both would lead to a complex change in the transport properties. The small changes after only three cycles, however, are too small to analyze in a quantitative or qualitative manner. An ongoing loss of antimony and/or indium at elevated temperatures will most certainly result in substantial material degradation. Therefore, further investigations have to be conducted to examine the source and starting temperature of degradation. Additionally, it has to be elucidated if the degradation saturates with increasing number of thermal cycles or not.

Other refined parameters showed no significant trend. The refinement of the non special Wyckoff position of antimony resulted in values of 0.158 and 0.335 for the y-

and z-coordinates, respectively. The calculated site occupancies of Co and Sb showed a full site occupation, and the refined isotropic atomic temperature factors for In, Co and Sb were in good agreement with comparable literature values [163,168]. The large calculated isotropic atomic temperature factors of In illustrates the rattling character of the filler atom and is typical for filled skutterudites.

^{121}Sb Mößbauer spectrometry To obtain more information on the structure of the synthesized materials, ^{121}Sb Mößbauer measurements were conducted at the Jülich Research Center. Mößbauer spectroscopy is usually a very sensitive method based on the recoil-free absorption and emission of gamma rays in solids. The method enables the detection of subtle changes in nuclear energy levels, which are triggered by the chemical environment of the nucleus (e.g. oxidation state, bonding properties, etc.). Because of the sensitive nature of the method, the presence of InSb as a side phase, Sb deficiencies or even In on the Sb lattice site were thought to make a detectable difference on the environment of Sb at the 24g site.

To this end, we measured a set of skutterudite samples with the compositions $\text{In}_{0.12}\text{Co}_4\text{Sb}_{12}$ and $\text{In}_{0.20}\text{Co}_4\text{Sb}_{12}$ before and after consolidation and thermal cycling and compared these spectra with data obtained on an unfilled kieftite sample. The

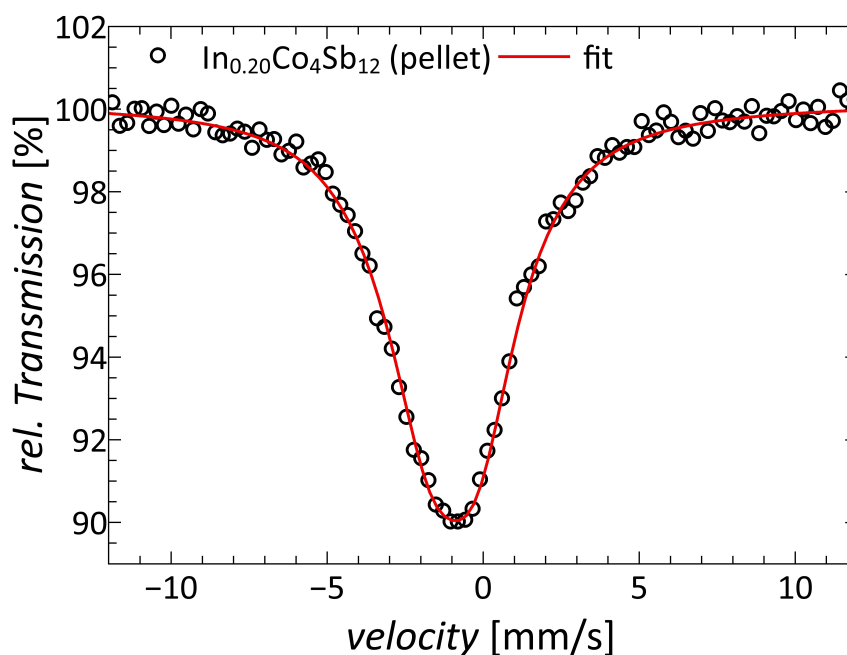


Figure (3.7) – ^{121}Sb Mößbauer spectra of the $\text{In}_{0.20}\text{Co}_4\text{Sb}_{12}$ sample after consolidation and thermal cycling due to thermoelectric characterization.

Mößbauer spectrum obtained from the the $\text{In}_{0.20}\text{Co}_4\text{Sb}_{12}$ sample after consolidation and thermal cycling is shown in Figure 3.7. All other Mößbauer spectra can be

found in supporting information B.3. The spectra are mainly characterized by the isomer shift (δ) and the quadrupole splitting (Δ). The isomer shift corresponds to the peak position on the spectrum and can be considered proportional to the Sb (5s) contribution to the valence band. The quadrupole splitting corresponds to the splitting of the nuclear sub-levels under the influence of the electric field gradient and is thus related to the distortion of the local environment. Refined Mößbauer parameters of all spectra are displayed in Table 3.3. The isomer shifts relative to InSb

Table (3.3) – ^{121}Sb Mößbauer data of CoSb_3 , $\text{In}_{0.12}\text{Co}_4\text{Sb}_{12}$, and $\text{In}_{0.20}\text{Co}_4\text{Sb}_{12}$ before (powder) and after (pellet) consolidation and thermal cycling, including isomer shift (δ) relative to InSb (-8.6 mm/s), quadrupole splitting (Δ), asymmetry parameter (η) and line width (Γ). Numbers in parentheses indicate the estimated standard deviation of the fit.

sample #	δ [mm/s]	Δ [mm/s]	η	Γ [mm/s]
CoSb ₃	-0.9(1)	9.6(6)	0.8(2)	3.8(3)
In _{0.12} Co ₄ Sb ₁₂ (powder)	-1.2(1)	11.6(7)	0.6(3)	3.5(4)
In _{0.12} Co ₄ Sb ₁₂ (pellet)	-1.0(1)	9.2(1)	0.8(1)	3.0(1)
In _{0.20} Co ₄ Sb ₁₂ (powder)	-1.0(1)	9.8(7)	1.0(2)	3.7(3)
In _{0.20} Co ₄ Sb ₁₂ (pellet)	-1.1(1)	9.0(3)	0.8(1)	3.1(1)

and quadrupole split correspond well to published CoSb₃ data [169–171]. The isomer shift of $\delta \approx -1.0\text{ mm/s}$ indicates a large covalent contribution to the Sb bonding, intermediate between the bonding in elemental Sb and InSb. [172] The presence of the small InSb side phase concentration in the In_{0.20}Co₄Sb₁₂ samples, demonstrated by high resolution synchrotron data, and the influence of thermal cycling (comparison between powder and pellet samples) seem to have no effect on the spectra. The hyperfine parameters (δ and Δ) of indium-filled CoSb₃ are not altered compared to the unfilled CoSb₃, which illustrates the topotactic nature of the indium insertion into the kieftite structure.

3.3.3. Thermoelectric Properties of Bulk Indium-filled Skutterudites

Electronic transport properties The temperature dependent electrical conductivity of the indium-filled skutterudite samples $\text{In}_x\text{Co}_4\text{Sb}_{12}$ with $x = 0.12, 0.15, 0.18$ and 0.20 between room temperature and 550°C are shown in Figure 3.8. Data

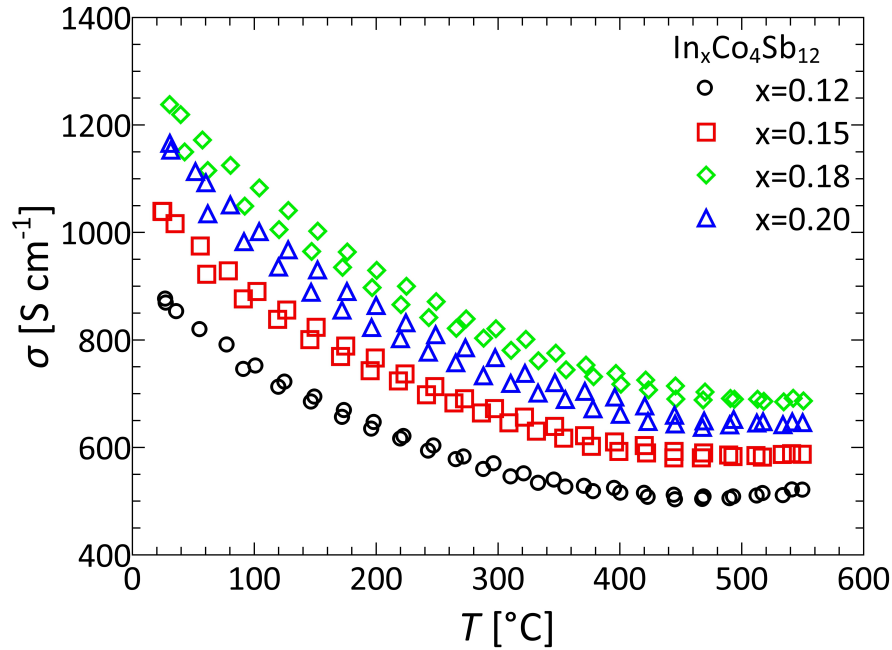


Figure (3.8) – Temperature dependence of the electrical conductivity from the indium-filled skutterudites $\text{In}_x\text{Co}_4\text{Sb}_{12}$ with $x = 0.12, 0.15, 0.18$ and 0.20 , illustrating the trend of a high conductivity with higher indium-filling degree. The heating and cooling data show a decrease of the electrical conductivity upon thermal cycling. Note, the nominal In content does not correspond to the actual indium-filling degree (see section 3.3.2)

collection was conducted during heating and cooling, after thermal equilibrium had been reached. The data collected during heating exhibits a slightly higher electrical conductivity than the data collected during cooling. However, above 500°C heating and cooling data converge, which could be a sign of sample degradation at elevated temperatures. All measured indium-filled skutterudites exhibit a high electrical conductivity above 500 S/cm within the complete temperature range. The electrical conductivity decreases slightly with increasing temperature, as expected for heavily doped semiconductors, and increases with the indium-filling degree. This can easily be explained by the electron donating nature of In as a filler atom. A higher filling level results in a higher charge carrier concentration and, thus, higher electrical conductivity. The sample of nominal composition $\text{In}_{0.18}\text{Co}_4\text{Sb}_{12}$ exhibits the highest electrical conductivity of 1250 S/cm at room temperature and 700 S/cm at 550°C .

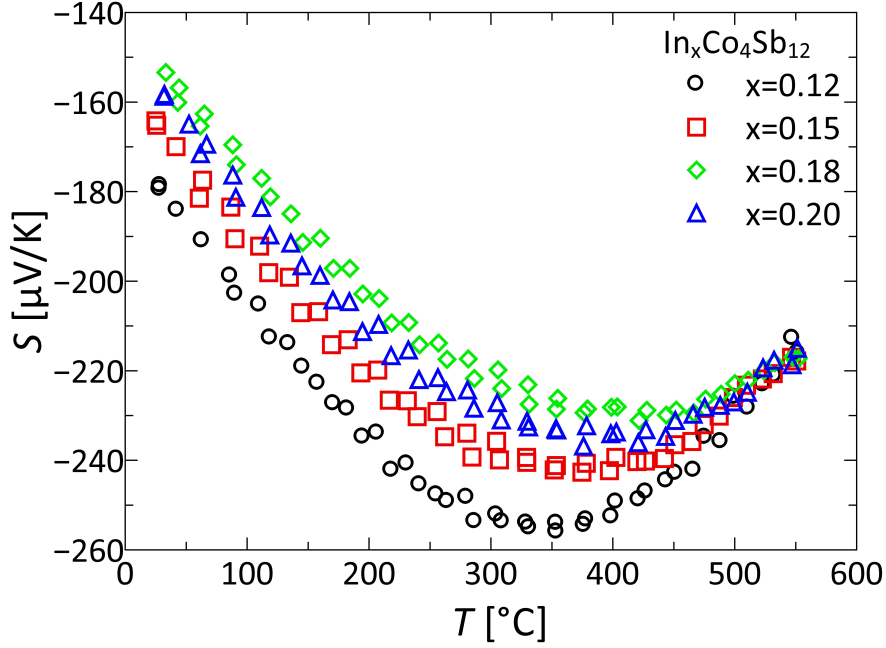


Figure (3.9) – Temperature dependence of the Seebeck coefficient from the indium-filled skutterudite samples $\text{In}_x\text{Co}_4\text{Sb}_{12}$ with $x = 0.12, 0.15, 0.18$ and 0.20 , illustrating the lowering of the Seebeck coefficient with a higher indium-filling degree. The heating and cooling data show an increase of the absolute value of the Seebeck coefficient upon thermal cycling. Note, the nominal In content does not correspond to the actual indium-filling degree (see section 3.3.2)

It is important to note that the nominal compositions do not mirror the actual indium-filling degree as determined by synchrotron diffraction. Considering this the controversial trend from the samples with nominal composition $\text{In}_{0.20}\text{Co}_4\text{Sb}_{12}$ (actual indium-filling degree of 14%) and $\text{In}_{0.18}\text{Co}_4\text{Sb}_{12}$ (actual indium-filling degree of 16%) can be understood. The minor InSb side phase and the resulting lower indium-filling degree, thus, have a very large influence on the electrical conductivity, which demonstrates the importance of a phase pure synthesis for skutterudite materials.

Further, it can be seen that the measured cooling and heating curves yield different values for the electric conductivity. In comparison to data collected during heating, data collected during cooling exhibit an up to 50 S/cm reduced electrical conductivity below $\approx 480^\circ\text{C}$, but are in good agreement above this temperature. This could be correlated to an equilibrium of the indium-filled skutterudite with liquid at 484°C , as described by Grytsiv et al. [121], or the reported Sb-rich eutectic point in the In-Sb phase diagram at 492.5°C . [173] To investigate the degradation of thermal cycling above 480°C , all samples were characterized at least two times. The electronic properties of the sample of nominal composition $\text{In}_{0.12}\text{Co}_4\text{Sb}_{12}$ were characterized three times. After each characterization, small pieces were cut from the pellet for

further structure analysis (synchrotron diffraction, Mößbauer spectroscopy, etc.), and the remaining pellets were used for the next characterization cycle. A comparison of the electrical conductivity data from different measurement cycles for all samples can be found in supporting information section B.4. With increased thermal cycling during measurements, the electronic conductivity is gradually lowered. However, aside from the decrease in refined lattice parameter, no structural or microstructural changes could be found by SEM/EDX or Mößbauer analysis. Hence, a more thorough analysis of the structural changes induced by thermal cycling above 480 °C has to be conducted to understand the changes in thermoelectric transport properties.

Figure 3.9 illustrates the temperature dependent Seebeck coefficients of the indium-filled skutterudite samples $\text{In}_x\text{Co}_4\text{Sb}_{12}$, with $x = 0.12, 0.15, 0.18$ and 0.20 , measured between room temperature and 550 °C. Like the electrical conductivity measurements, the data shown here represent data collected during heating and cooling, after thermal equilibrium had been reached. All indium-filled skutterudites exhibit a large negative Seebeck coefficient, which indicates electrons to be the majority charge carriers. The Seebeck values range from $-255 \mu\text{V}/\text{K}$ for the sample of nominal composition $\text{In}_{0.12}\text{Co}_4\text{Sb}_{12}$ at 350 °C to $-150 \mu\text{V}/\text{K}$ for the sample of nominal composition $\text{In}_{0.18}\text{Co}_4\text{Sb}_{12}$ at room temperature. With increasing temperature, the absolute values of the Seebeck coefficient maximize at temperatures between 350 °C and 425 °C for $\text{In}_{0.12}\text{Co}_4\text{Sb}_{12}$ and $\text{In}_{0.18}\text{Co}_4\text{Sb}_{12}$, respectively. This trend is common for heavily doped semiconductors. The decrease in Seebeck coefficient above a certain temperature can be explained by the contribution of bipolar conduction, resulting from thermal excitations of electrons over the band gap. Like the electrical conductivity, the Seebeck coefficient scales with the filling degree of indium. However, due to the increase in extrinsic charge carriers resulting from an increased indium-filling degree, the absolute value of the Seebeck coefficient is reduced. This trend can easily be seen under consideration of the actual indium-filling degree instead of the nominal composition, which is plotted in Figure 3.9. The sample of nominal composition $\text{In}_{0.18}\text{Co}_4\text{Sb}_{12}$ has the highest actual indium-filling degree, hence the lowest absolute Seebeck coefficient. At high temperatures, intrinsic charge carriers become dominant due to thermal excitations over the band gap, which results in similar Seebeck values above 500 °C. Analogous to the electrical conductivity, a small difference between data collected during heating and cooling can be seen in some samples. The comparison of the Seebeck data from different measurement cycles for all samples can be found in supporting information section B.4. However, the differences are not as pronounced as in the electrical conductivity, which could be an indication that the source for these changes in transport properties may not

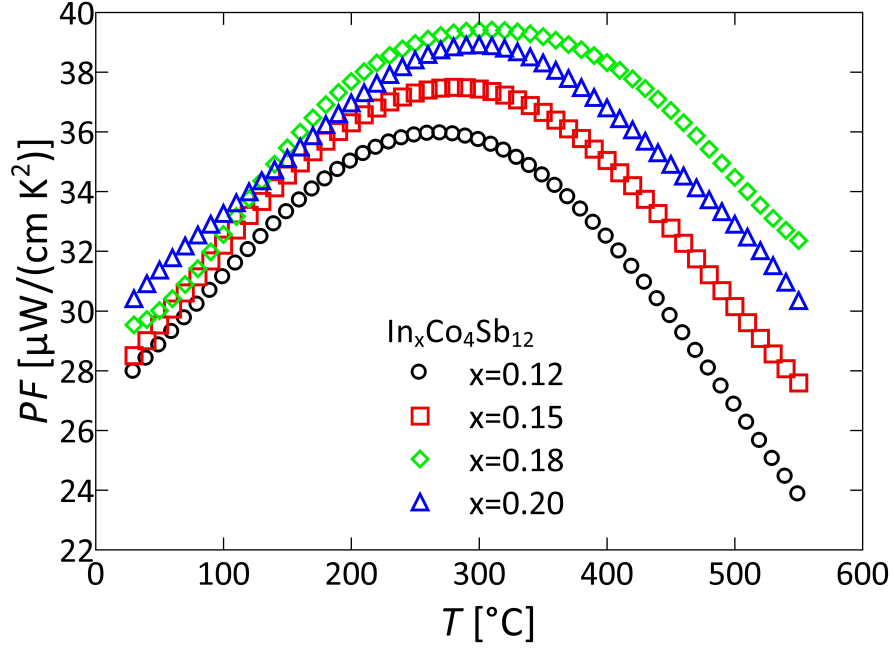


Figure (3.10) – Temperature dependence of the power factor of indium-filled skutterudite samples $\text{In}_x\text{Co}_4\text{Sb}_{12}$ with $x = 0.12, 0.15, 0.18$ and 0.20 , illustrating an enhanced power factor with increasing indium-filling degree. Note, the nominal In content does not correspond to the actual indium-filling degree (see section 3.3.2).

be related to a change in the charge carrier concentration, but rather a change in microstructure.

The high electrical conductivity and absolute Seebeck coefficient of the indium-filled skutterudite samples result in excellent values for the power factor $S^2\sigma$, which can be seen in Figure 3.10. With rising temperature, the power factor increases, due to the increase in absolute Seebeck coefficient, at lower temperatures and maximizes around 300°C , with values ranging from 35 to $39 \mu\text{Wcm}^{-1}\text{K}^{-2}$. The sample of nominal composition $\text{In}_{0.18}\text{Co}_4\text{Sb}_{12}$, which has the highest indium-filling degree, exhibits the highest power factor. Considering that the indium-filling degree corroborates with the charge carrier concentration, the optimal charge carrier concentration has not yet been reached, thus a material with a higher carrier concentration (higher filling level) is expected to exhibit an even higher power factor.

However, the indium-filling does not only have a beneficial influence on the electronic properties. The thermal conductivity is improved as well. Figure 3.11 shows the measured thermal conductivity for $\text{In}_x\text{Co}_4\text{Sb}_{12}$ samples with $x = 0.12, 0.15, 0.18, 0.20$ between room temperature and 550°C . Indium-filling leads to a dramatic reduction in the thermal conductivity in comparison to the binary kiefite, which possesses a room temperature thermal conductivity of $\approx 11 \text{WK}^{-1}\text{m}^{-1}$. Although the differences in thermal conductivity are not very large in the measured set of samples,

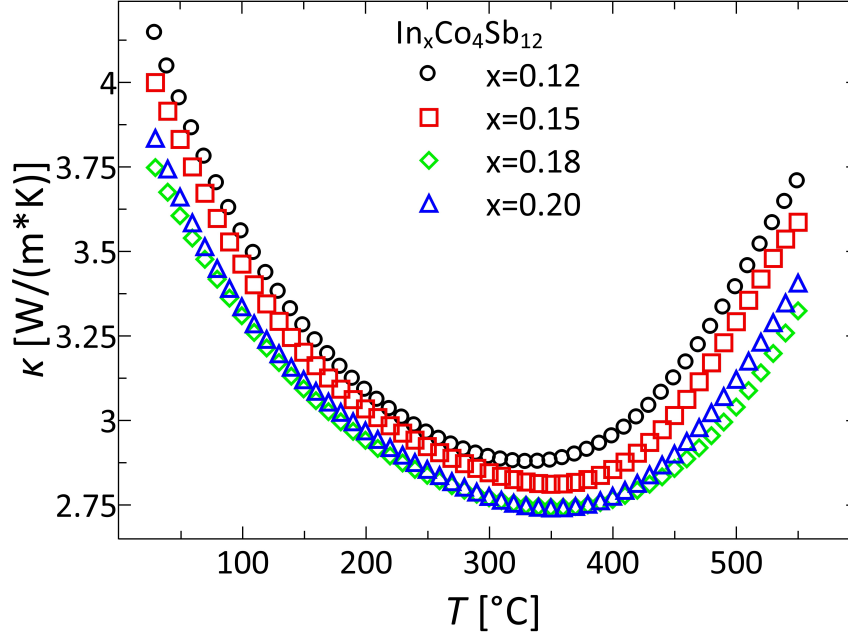


Figure (3.11) – Temperature dependence of the total thermal conductivity of indium-filled skutterudite samples $\text{In}_x\text{Co}_4\text{Sb}_{12}$ with $x = 0.12, 0.15, 0.18$ and 0.20 , illustrating a reduced thermal conductivity with increasing indium-filling degree. The increase of the thermal conductivity at elevated temperatures indicates the larger influence of bipolar conduction with rising temperature. Note, the nominal In content does not correspond to the actual indium-filling degree (see section 3.3.2).

the thermal conductivity is lowered to values between 3.75 and $4.15 \text{ WK}^{-1}\text{m}^{-1}$ at room temperature and is further decreased to minimum values ranging from 2.75 to $2.88 \text{ WK}^{-1}\text{m}^{-1}$ around 350°C , depending on the indium-filling degree. Above 350°C the thermal conductivity increases again, likely due to the increasing contribution of bipolar conduction. To further assess the influence of indium-filling on the thermal conductivity, a differentiation must be made between the electronic and lattice contributions to the thermal conductivity. To this end, the electronic contribution was calculated by use of the Wiedemann-Franz law (see equation 1.18). For exact calculations, the temperature dependence of the Lorenz number, which is a function of the chemical potential and the scattering mechanism, has to be considered. However, for a qualitative analysis, a constant, temperature independent Lorenz number was assumed. Because the metallic limit of the Lorenz number ($2.44 \times 10^{-8} \text{ V}^2\text{K}^{-2}$) usually overestimates the electronic contribution to the thermal conductivity, an intermediate value of $2.0 \times 10^{-8} \text{ V}^2\text{K}^{-2}$, often used for skutterudite materials, [174,175] was employed for the calculations. The resulting values for the electronic (κ_{el}) and lattice contribution (κ_{lat}) to the thermal conductivity can be seen in Figure 3.12. Although the temperature dependence might be inaccurate, due to the assumption

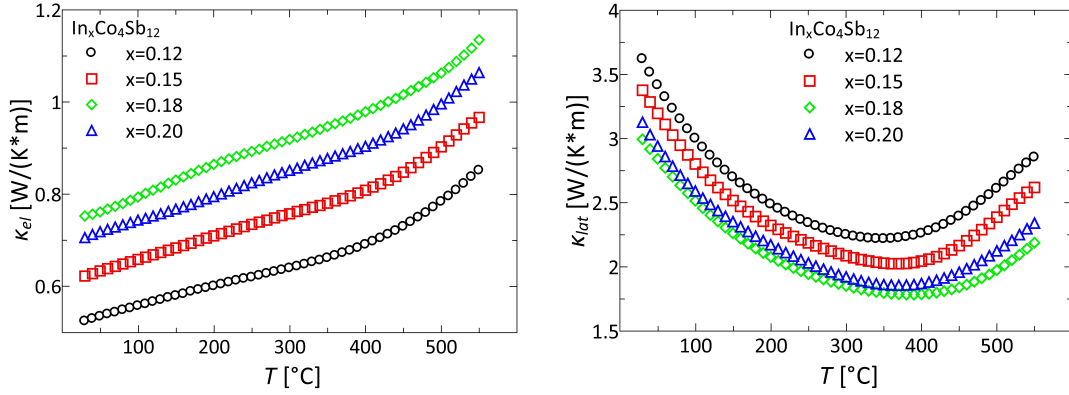


Figure (3.12) – Dependence of the electronic (left) and lattice (right) thermal conductivity on the indium-filling degree of skutterudite samples $In_xCo_4Sb_{12}$ with $x = 0.12, 0.15, 0.18$ and 0.20 . The upturn of the electronic and lattice thermal conductivity at elevated temperatures can be attributed to the unaccounted contribution of bipolar conduction. Note, the nominal In content does not correspond to the actual indium-filling degree (see section 3.3.2). With increasing actual indium-filling degree the electronic thermal conductivity is increased, whereas the lattice thermal conductivity is reduced.

of a temperature independent Lorenz number, a clear trend can be observed between samples of different indium content. The electronic thermal conductivity κ_{el} increases from 0.53 to $0.75 \text{ WK}^{-1}\text{m}^{-1}$ with increasing indium-filling degree at room temperature. In contrast, the room temperature lattice thermal conductivity κ_{lat} decreases from 3.62 to $3.00 \text{ WK}^{-1}\text{m}^{-1}$ with increasing actual filling level. This trend can easily be explained by the properties of In as a filling atom in skutterudites. If an indium atom occupies the crystallographic void of the skutterudite structure, the lattice thermal conductivity is lowered, due to the addition of low energy eigenmodes to the phonon dispersion of the host lattice. However, these indium atoms are also capable of donating electrons to the $CoSb_3$ host, which in result increases the charge carrier concentration, as well as the electrical conductivity, and thus leads to an increase in the electronic contribution to the thermal conductivity. The upturn in the lattice thermal conductivity above 350°C can be corroborated by the increasing contribution of bipolar conduction not accounted for by the Wiedemann-Franz law. The increasing amount of InSb in the samples of nominal composition $In_{0.18}Co_4Sb_{12}$ and $In_{0.20}Co_4Sb_{12}$ seems not to have any influence on the lattice thermal conductivity, which scales solely with the increasing indium-filling degree. This could be correlated to their marginal presence or might be an indication that InSb precipitates do not significantly reduce the lattice thermal conductivity as previously reported. [116,119] Generally, it can be seen that the lattice thermal conductivity is responsible for the major contribution to the total thermal conductivity. This shows the great potential of phonon engineering in skutterudite materials. A further reduction

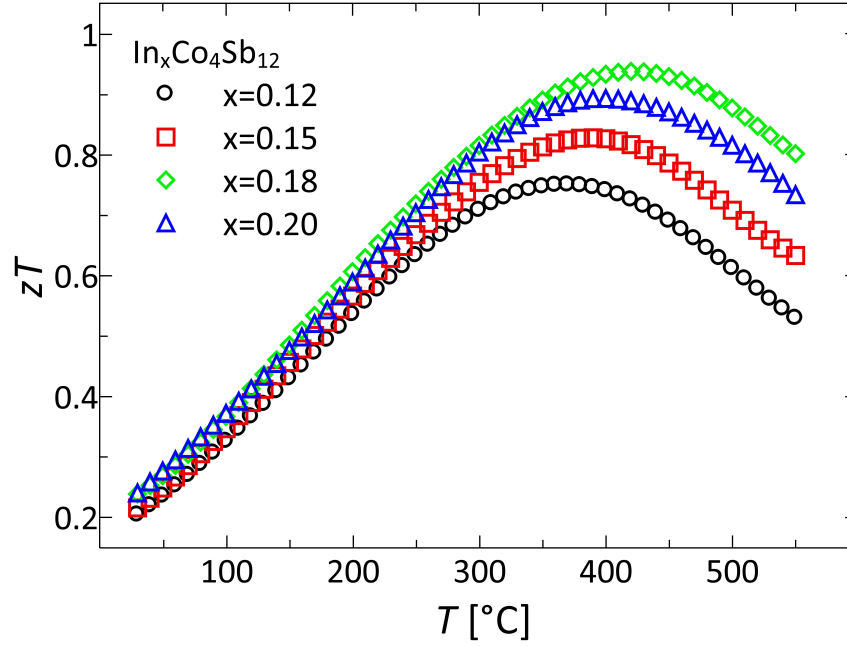


Figure (3.13) – Temperature dependence of the thermoelectric figure of merit from indium-filled skutterudites samples $\text{In}_x\text{Co}_4\text{Sb}_{12}$ with $x = 0.12, 0.15, 0.18$ and 0.20 . Note, the nominal In content does not correspond to the actual indium-filling degree (see section 3.3.2) The highest zT value of 0.94 at 420°C is obtained with the sample of nominal composition $\text{In}_{0.18}\text{Co}_4\text{Sb}_{12}$, which has a indium-filling degree of 16%.

of the lattice thermal conductivity, e.g. by multiple filler atoms, enhanced grain boundary scattering or point defect scattering, will thus have a great influence on the thermoelectric figure of merit zT .

Combining the electronic and thermal characterizations of the thermoelectric properties, the figure of merit was calculated for the series of indium-filled skutterudite samples $\text{In}_x\text{Co}_4\text{Sb}_{12}$ with $x=0.12, 0.15, 0.18$ and 0.20 . The results are summarized in Figure 3.13. The figure of merit of all bulk indium-filled skutterudite samples is above 0.2 at room temperature and further increases with rising temperature up to a maximum value zT_{max} ranging from 0.75 to 0.94 at 370°C and 420°C , respectively. At even higher temperatures the influence of bipolar conduction forces the zT value to decrease again. With increasing actual indium-filling degree the zT_{max} value and the temperature of the maximal figure of merit increase. A linear trend of zT_{max} values with indium-filling degree can be found, which demonstrates that the enhancement of the figure of merit can be solely attributed to a higher indium-filling degree of the skutterudite material and is independent of the InSb side phase. The mere presence of InSb , therefore, seems not to have a significant influence on the thermoelectric properties, like previously reported by Mallik et al. [176] However, we could show that InSb is usually correlated to a reduction in the actual indium-filling

degree, which influences the thermoelectric properties to a large extent. Therefore, the presence of InSb side phases is not considered beneficial to the thermoelectric properties. Assuming that the linear trend of zT_{max} values and indium-filling degree can be extrapolated to higher indium-filling degrees, a sample with a filling degree of 20% would have a zT_{max} value around 1.09. In comparison to the zT_{max} value of 0.89 found in the sample of nominal composition $\text{In}_{0.20}\text{Co}_4\text{Sb}_{12}$, the marginal amount of InSb is responsible for a large reduction about 18% in the figure of merit. To completely avoid the formation of InSb, an insertion reaction of indium into the kieffite host at temperatures below 480 °C is currently under investigation. Further, an improvement of the figure of merit by reducing the lattice thermal conductivity is to be expected. To this end, a top-down approach towards indium-filled skutterudite nanoparticles was explored.

3.3.4. Top-down Approach towards Indium-filled Skutterudite Nanoparticles

Nanosized particles are either produced in a top-down or a bottom-up approach. The bottom-up approach usually comprises wet chemical syntheses. [110, 177–180] Advantages of these methods are often a good control over the size and shape of the obtained nanoparticles. However, some disadvantages, like a poor sample homogeneity or phase purity, especially in ternary systems, scalability, and the use of surface functional agents, have to be overcome. Surface active agents, organic molecules with a functional group binding to specific surfaces of the nanoparticles, are used to control the size and shape, but are often a hindrance to further powder processing. A complete removal of those surface active agents is usually difficult. If surface active agents remain during the sintering process, these organics will decompose at the elevated temperatures, forming impurities. In contrast, the top-down approach starts with bulk material. The particle size is then subsequently reduced via grinding or milling, and the sample homogeneity and phase purity of the bulk material can often be conserved. In comparison to a bottom up approach, however, the size and shape control are inferior. Considering the subsequent compaction of the powdered material, which is usually accompanied with grain growth, the control of the nanoparticle shape is usually unnecessary. Further, a narrow size distribution, obtained by size-controlled bottom up methods, will result in a narrow grain size distribution in the compacted material. This, in return, will only affect phonons of certain frequencies and will lead to a less pronounced reduction of the thermal conductivity than a material with a broad particle size distribution, which is able to scatter phonons of

various frequencies. Therefore, a broad size distribution, which is inherently obtained by the grinding process, is considered to be beneficial for obtaining a low thermal conductivity.

To conserve the phase purity of skutterudite materials during the grain size reduction, ultra fine colloidal grinding is necessary. Similar to kiefite, filled skutterudites are incongruently melting, with a decomposition temperature around 876 °C. Although those temperatures are not reached during the milling process, the energy input per particle volume, induced by a collision with a grinding ball of a certain mass and velocity, can be comparable to thermal vibration at elevated temperatures. Therefore, the use of a liquid grinding medium is crucial for an enhanced dissipation of energy during the milling process. The energy input to the material can be controlled by the mass and velocity of the grinding balls. To obtain nanosized powders, many small grinding balls are usually used in order to increase the number of collisions between the grinding balls, the particles and the grinding jar itself. The mass of the grinding ball is, thus, fixed, and the rotation speed has to be adjusted to provide enough energy to enable size reduction up to the nanometer regime, but not enough energy to cause sample decomposition.

An exact analysis of the obtained particle size distribution, which usually ranges from a few micrometers (bulk) to a few nanometers (nano), is very difficult to attain. In the following discussion a distinction between crystallites or grains and particles will be made. Crystallites are coherently scattering domains within a particle and is confined by its grain boundaries. These are usually visible via electron microscopy due to a different contrast from defect sites on the grain boundary or due to the contrast from different crystallographic orientations of the grains. Several grains can be sintered/grown together to form a particle. In contrast to a multi-grain particle, in an agglomeration of grains the single grains are not intergrown and are only attached by weak attractive forces. In addition, the term "particle" is used as an umbrella term to describe a single distinguishable entity, whose size can be measured. Granulometric methods, based on particle diffusion, will lead to an "effective" size distribution of particles. However, a differentiation between single particles and agglomerates is not possible, thus the real particle size is usually overestimated. Another method is the crystallite size refinement of diffraction data, which gives information on the size of coherently scattering domains. The determined crystallite size does not necessarily have to be equal to the grain size and can easily be underestimated. A large particle will most probably consist of several crystallites, whereas nanoparticles often consist of only one crystallite. The correct determination of a distribution of crystallite sizes with diffraction techniques still remains problematic, because only a limited

number of different crystallite sizes can be refined. A third method is the direct evaluation of particle sizes via transmission electron microscopy. In comparison to granulometric methods and the evaluation of diffraction data, this method can be seen as a local probe. Only a small fraction of the particles can be analyzed, but the direct visualization of the particles and the distinction between crystallites in high resolution are very valuable. Further, it has to be considered that the existence of large particles might not be observed due to the selective nature of the sample preparation. However, TEM analysis is the only unadulterated measure of the nanoparticles and is, therefore, very important for a proper particle analysis.

To find the ideal milling parameter for indium-filled skutterudite materials, the milling process was tested on waste kiefite material and was conducted under air instead of a controlled atmosphere, which was assumed to have no influence on the milling results. To this end, 30 g of this bulk powder were loaded into a hardened steel grinding jar together with ≈ 100 hardened steel grinding balls of 3 mm diameter and covered in *n*-hexane. The rotational speed of the planetary ball mill was set to 550 rpm with an alternating milling and cooling time of 10 min. Small amounts of powder were removed after 1/6, 1/3, 1/2, 1, 2, 3, 4, 5, 7.5, 10, 12.5, 15, 17.5 and 20 h total milling time and were used to analyze the phase composition and grain size distribution via X-ray diffraction and transmission electron microscopy. TEM samples were prepared by drop casting out of a diluted suspension of particles in *n*-hexane. The suspension was sonicated in an ultrasonic bath for at least 10 min prior to drop casting in order to reduce particle agglomerations. A total milling time below one hour did not result in a sufficient reduction in grain size, which could be seen by a rapid sedimentation of the particles during sample preparation for TEM analysis. Samples milled for at least one hour showed significant peak broadening in the X-ray diffraction pattern due to the reduction of the coherent scattering domains. However, the existence of remaining large crystallites can also be seen in the diffraction pattern, indicated by sharp Bragg intensities, which are in superposition with the broad peaks from nanosized crystallites. Milling times longer than 15 h, yielded significant amounts of CoSb_2 as side phase, indicating sample decomposition.

Figure 3.14 shows typical particles obtained after 15 h of milling time. Due to the absence of any surface active agents, the particles prefer to be in contact with each other instead of being dispersed by solvent molecules. Hence, a strong particle agglomeration up to few 100 nm in size can be seen. Nevertheless, due to the contrast within an agglomerate, it is evident that these are built to a large extent by an accumulation of smaller, around 20 nm, particles. Measured particle sizes range from

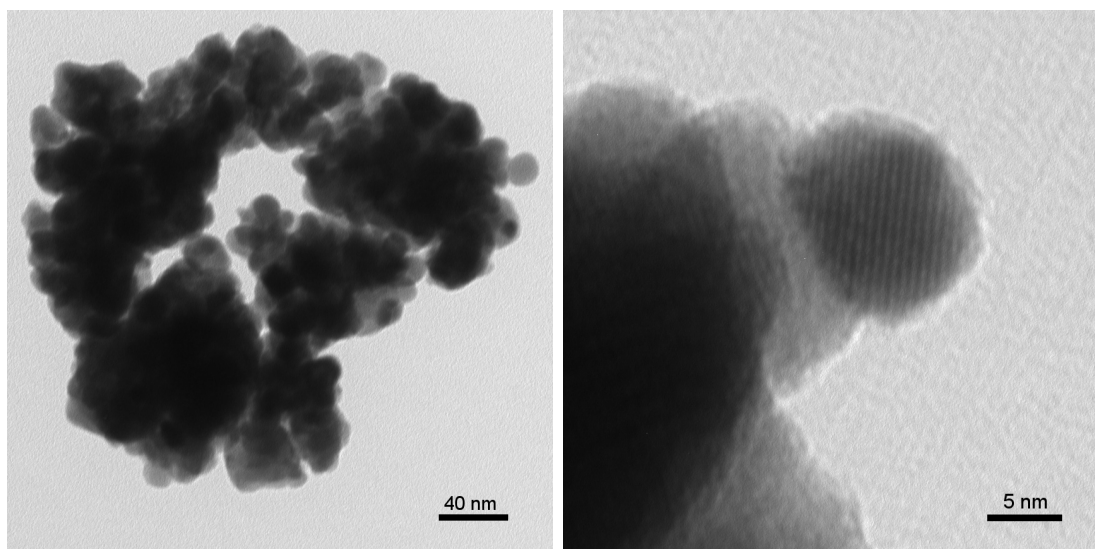


Figure (3.14) – *CoSb₃ nanoparticles obtained by ultra fine colloidal grinding in *n*-hexane for 15 h. A broad particle size distribution is obtained, with sizes ranging from 10 to 100 nm. The absence of any surface-active agents results in strong particle agglomeration. Lattice fringes, observed in the right image illustrate the good crystallinity, which could be retained from the bulk phase.*

10 nm to 100 nm. The lattice fringes, observed in the right image, illustrate the good crystallinity of the kiefite material, which could be retained from the bulk phase. Rietfeld refinements were conducted to assess information on the grain size distribution of samples milled for 1, 5 and 10 h. The refinements show that a good fit could be obtained with a combination of two crystallite sizes, which converged to values in the range of 20 nm and 60-80 nm. With longer milling time the fraction of 20 nm particles increases at the expense of the larger particles from 30% after 1 h to 80% after 10 h. The refined fractions of powders processed for 1, 5 and 10 h total milling time are shown in Figure B.23 in the supporting information.

Consequently, the following parameters were used to produce indium-filled nanoparticles. To avoid the oxidation of the nanoparticles, the grinding jar was loaded and sealed in a N₂ glove box and freshly dried, distilled and degassed *n*-hexane was used as grinding liquid. After the milling process, the obtained powders were dried and stored in the glove box under controlled atmosphere. A large batch of ≈ 60 g of bulk In_{0.18}Co₄Sb₁₂ powder was synthesized. Half of this batch (30 g) was further processed, in a planetary ball mill for 10 h at a rotation speed of 500 rpm, to nanosized powder. Along with the slightly reduced milling time and rotational speed, the intermittent cooling time was prolonged to 15 min in order to avoid sample decomposition. The obtained powder was analyzed by X-ray diffraction and TEM analysis. Powder X-ray diffraction data obtained from the bulk- and nano-powders can be seen in Figure 3.15.

Indium-filled Skutterudites

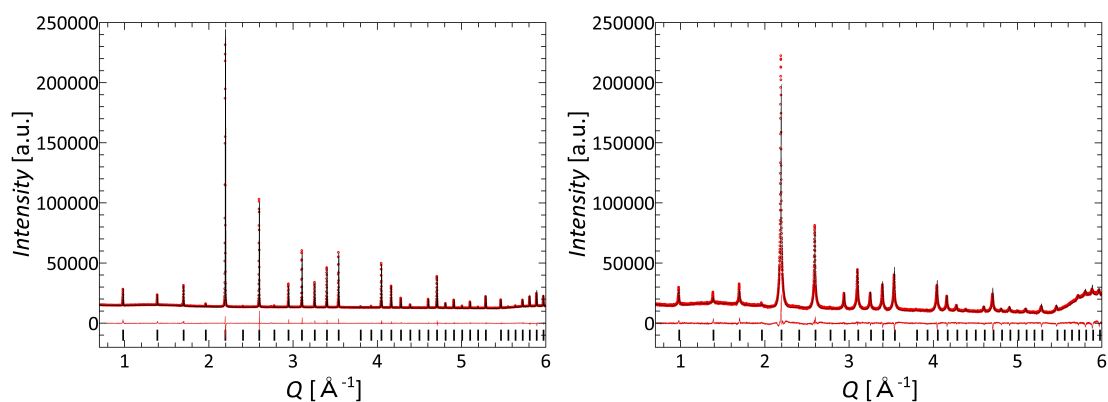


Figure (3.15) – Refined powder diffraction data for bulk- (left) and nano- (right) $\text{In}_{0.18}\text{Co}_4\text{Sb}_{12}$ (red dots), including profile fit (black solid line), and profile difference (red solid line). The refined peak positions are indicated by black tick marks.

In comparison to the diffraction pattern of the bulk powder, the pattern of the nano powder displays very obvious peak broadening due to small coherently scattering domains. Further, a superposition of narrow and broad diffraction peaks can be seen, which is a good indication of a broad particle size distribution. This corroborates the results of the crystallite size refinements, where the two used crystallite sizes converge to 20 and 100 nm. The quantitative analysis showed that the majority (60 vol%) of the nano powder consists of nanoparticles with a crystallite size around 20 nm. In contrast, the refinement of the bulk powder exhibits a crystallite size around 400 nm. TEM images of the $\text{In}_{0.18}\text{Co}_4\text{Sb}_{12}$ nanoparticles corroborate well with the results from the powder diffraction. In Figure 3.16 two transmission electron micrographs are

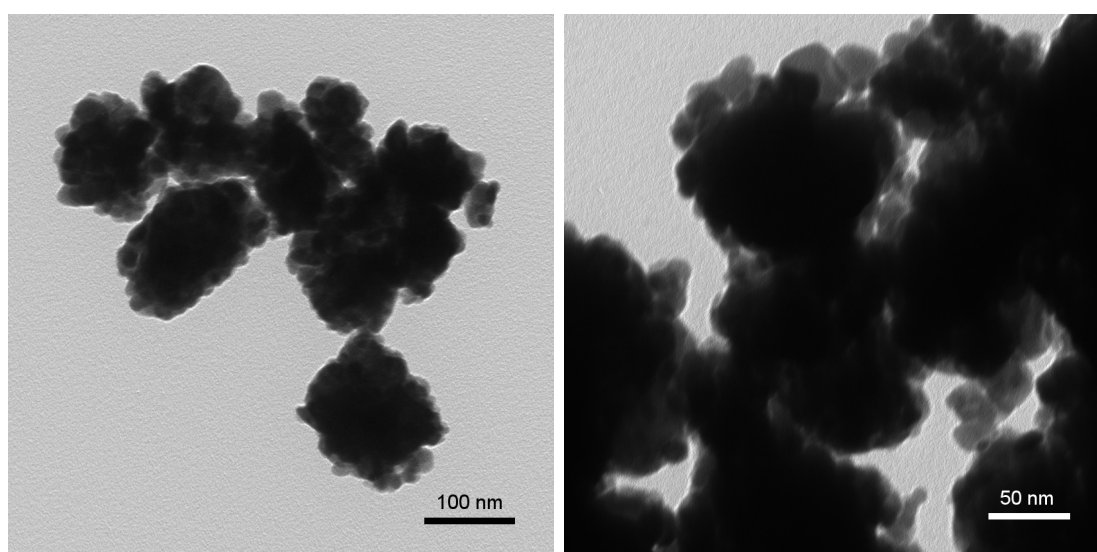


Figure (3.16) – CoSb_3 nanoparticles obtained by ultra fine colloidal grinding in *n*-hexane for 10 h. A broad particle size distribution is obtained, with sizes ranging from 20 to 100 nm.

shown. Although the obtained particles are strongly agglomerated, a weak contrast within the agglomerates reveal the accumulation of very polydisperse particles.

The ability to synthesize high quality bulk indium-filled skutterudite powders and to further process these powders to obtain a nanosized powder of the same material enables the unadulterated investigation of grain boundary scattering in skutterudite materials. By mixing bulk and nano powders it might be possible to control the amount of grain boundaries in the resulting consolidated pellet. To this end, the consolidation of nano-bulk powders to high density pellets and the correlated grain growth behavior during the short time sintering process are under investigation. Further, thermoelectric transport measurements on bulk-nano composite materials with varying grain sizes and grain size concentrations are envisaged.

3.4. Conclusions and Outlook

An easy two-step synthesis was developed to synthesize high quality phase pure bulk skutterudites to investigate the influence of the indium-filling degree on the structure and the thermoelectric properties. In comparison to the standard melt-quench-anneal synthesis, the developed two-step synthesis method separates the kiefite formation reaction from the topotactic filler insertion. This allows not only to conduct the reactions at lower temperatures with shorter reaction times, but also to effectively circumvent the formation of impurity phases by side reactions of the starting elements. The method was used to synthesize indium-filled skutterudites $\text{In}_x\text{Co}_4\text{Sb}_{12}$ with nominal composition $x = 0.12, 0.15, 0.18$ and 0.20 in bulk quantities. Current-assisted short-time sintering was used to consolidate the obtained powders into high density ($>98\%$) pellets for further thermoelectric characterization.

Structural and microstructural analysis of the obtained powders and consolidated pellets were conducted by SEM/EDX, standard X-ray diffraction, and ^{121}Sb Mößbauer spectroscopy, which showed homogeneous, single phase skutterudite materials with grain sizes in the order of $\approx 2 \mu\text{m}$. The very good sample homogeneity could be further demonstrated by Potential-Seebeck-Microprobe measurements of the pellet surfaces, illustrating a homogeneous and narrow distribution of measured Seebeck values. The fast current-assisted short-time sintering process of the powders and the subsequent thermal cycling during thermoelectric characterization of the consolidated pellets did not have a significant influence on the obtained microstructure and phase composition. Further, the topotactical indium insertion, the indium-filling degree, and repeated thermal cycling did not show an effect on the ^{121}Sb Mößbauer spectra. Although no secondary phases could be detected by SEM/EDX, ^{121}Sb Mößbauer spectroscopy

or standard X-ray diffraction (CuK_α radiation), high resolution synchrotron data obtained at beamline 11-BM (APS) of the Argonne National Laboratory revealed a marginal volume fraction ($\approx 0.1\%$) of InSb in the samples of nominal composition $\text{In}_{0.18}\text{Co}_4\text{Sb}_{12}$ and $\text{In}_{0.20}\text{Co}_4\text{Sb}_{12}$. Rietveld refinements of the high quality synchrotron data showed a linear trend between the indium-filling degree and the refined lattice parameter. A proper determination of the lattice parameter, thus, can be used to extrapolate the actual indium-filling degree in skutterudite materials, in case a proper refinement of the indium occupancy is not possible. Further, a slight decrease in the lattice parameter, correlated with a change in the electronic transport properties of samples with an increasing number of thermal cycles above 480°C , was found. This might be an indication of material deterioration above 480°C , which could limit future high temperature applications. However, no further change in the structure or microstructure was found, and in-depth investigations of long time thermal cycling experiments are needed to understand the underlying deterioration process.

Due to the high quality of the obtained materials, the influence of the actual indium-filling degree on the transport properties could be identified without significant disturbance from side phases. With increasing indium-filling degree, the electrical conductivity and thermal resistivity could be enhanced, which resulted in a figure of merit close to unity at 420°C for the sample of nominal composition $\text{In}_{0.18}\text{Co}_4\text{Sb}_{12}$. This remarkable improvement can be solely attributed to the insertion of indium into the kieftite structure. The resulting heterodesmic bonding within the filled skutterudite structure enables a dramatic decrease in the thermal conductivity. Further, calculations of the lattice contribution to the thermal conductivity showed a clear trend of decreased lattice thermal conductivity scaling with the indium-filling degree. In addition, due to the electron donating nature of the filling element, the charge carrier concentration also scales with the indium-filling degree, which results in an increased electrical conductivity and a decreased Seebeck coefficient. The presence of InSb side phases in marginal amounts were found to have no significant influence on the transport properties. However, the lower actual filling degree, which is a direct consequence of an InSb side phase, has a dramatic effect on the thermoelectric properties. This could be revealed with the sample of nominal composition $\text{In}_{0.20}\text{Co}_4\text{Sb}_{12}$. The InSb side phase of $\approx 0.1 \text{ vol}\%$ led to a substantially lowered actual filling degree, which can be attributed to the very different indium content in filled skutterudites and InSb. Due to this decreased indium-filling level, the figure of merit decreased by almost 18%, which demonstrates the importance of the indium-filling degree in skutterudite materials.

In addition to this, an easy top down approach towards phase pure nanosized

filled skutterudite particles was developed. The method, based on ultra fine colloidal grinding, was used to obtain phase pure indium-filled skutterudite nanoparticle powders, consisting mostly of particles with crystallite sizes of ≈ 20 nm. The phase composition and size distribution, ranging from 10 nm to 100 nm, were analyzed by X-ray powder diffraction and transmission electron microscopy. These nano powders are currently under further investigation to produce bulk-nano composite materials of identical composition, but with controlled grain sizes and grain boundary concentrations. The aim is to gain a deeper understanding on the influence of grain boundary scattering on the thermoelectric transport properties. With this the preparation of not only electronically optimized, but also phonon engineered skutterudite materials with superior thermoelectric properties should be possible in near future.

4

Tetragonal Tungsten Bronzes

This project was done in collaboration with [REDACTED] from the University of Oslo (Functional Energy Related Materials in Oslo, FERMiO). Project design, material synthesis and processing, chemical characterization and data analysis were conducted at the Johannes Gutenberg-University of Mainz. Powder consolidation was done at the German Aerospace Center (DLR). Thermogravimetric analyses and thermoelectric characterizations were conducted at the University of Oslo.

4.1. Motivation

Oxide thermoelectric materials exhibit great thermoelectric potential due to their high chemical and physical stability, low toxicity and often cheap, earth abundant chemical composition. So far, the only known oxide materials with competitive thermoelectric properties have been *p*-type materials. The ongoing search for suitable *n*-type materials has led to the Magnéli phases, which exhibit interesting thermoelectric properties, due to the complex structure, comprising crystallographic shear planes, giving rise to low thermal conductivity paired with a low resistivity. However, due to the limited compositional stability of the Magnéli phases, the optimization of the electronic properties by substitution or doping is severely restricted. Tetragonal tungsten bronzes (TTB) with composition $(\text{Nb}/\text{W})_{17}\text{O}_{47}$ are a series of compounds with a complex structure, closely related to the Magnéli phases. The large unit cell and the complex crystal structure is expected to induce low thermal conductivity. In

contrast to the Magnéli phases, the TTB are stable in a wide range of compositions ($\text{Nb}_{8-x}\text{W}_{9+x}\text{O}_{47}$, with $x = 0, \dots, 5$) and, thus, should allow control over the electronic properties by cation substitution. In addition, due to their structural similarity to the Magnéli phases, the occurrence of oxygen deficiencies or even CS planes might be possible, which would result in an additional way to tune the electronic and thermal properties. Although the tetragonal tungsten bronzes seem to have potential as *n*-type thermoelectric oxides, the thermoelectric properties have not yet been researched. Therefore, we decided to conduct a first assessment of the thermal stability, thermoelectric properties and possible optimization strategies of tetragonal tungsten bronzes.

4.2. Experimental Details and Methods

Synthesis Bulk samples of polycrystalline $\text{Nb}_{8-x}\text{W}_{9+x}\text{O}_{47}$ with compositions of $x = 0, 0.075, 0.1, 1$ were prepared by solid state reactions using powders of NbO_2 (Alfa Aesar, 99+%), Nb_2O_5 (ABCR, 99.5%), and WO_3 (Alfa Aesar, 99.8%). The phase purity of all starting materials was verified by X-ray diffraction. Annealing was performed in evacuated quartz ampoules, which were preheated at 1073 K under dynamic vacuum for 5 hours to ensure dry conditions. The stoichiometric amounts of the starting compounds were thoroughly ground, sealed in quartz ampoules, and annealed in a first step at 1173 K for 12 hours. In a second step, the harvested powders were ground again, re-sealed and re-annealed for 12 hours at 1173 K to ensure a homogeneous element distribution. Heating and cooling rates for all procedures in the horizontal tube furnaces were 5 K/min. The quartz ampoules were 10-12 cm in length and 11 mm in inner diameter with a maximum of 4 g starting materials per ampoule. The obtained powders of $\text{Nb}_{8-x}\text{W}_{9+x}\text{O}_{47}$ were hand ground, and phase purity was verified via powder X-ray diffraction prior to consolidation and characterization.

Powder Processing Batches of bulk powders with different substitution degree were used for consolidation into 1-1.5 mm thick, 12.7 mm diameter disks at 1173 K under vacuum and a pressure of 56 MPa by direct current-assisted short-time sintering utilizing a DSP ("Direktsinterpresse"). Boron nitride coated high density graphite was used as die material. In the first segment the pressure was applied, followed by a 6 min heating segment to 1173 K. After 10 min sinter time the pressure was released to 25 MPa and the sample was cooled down for 6 min. The resulting pellets had >95% theoretical density, as determined by the pellet mass and the archimedes method.

Characterization Details Room temperature powder X-ray diffraction measurements were performed on a Siemens D5000 powder diffractometer in transmission geometry with a Braun M50 position sensitive detector, Ge (220) monochromator and CuK_α radiation, with a step size of 0.0078° in 2Θ . The samples were mounted between two strips of scotch tape. Le Bail fits were performed of all diffraction data with TOPAS Academic V4.1 [155] applying the fundamental parameter approach using the crystallographic data from Craig and Stephenson as structure model. [151]

Thermal analysis was conducted using a CI Electronics MK2 microbalance. To distinguish between reversible reduction-oxidization reactions and irreversible sample decomposition the thermal stability was investigated under varying oxygen partial pressure. For this purpose the apparatus was connected to an in-house-built gas mixer, which has been described elsewhere. [181] Sample reduction and oxidization experiments were performed using the same microbalance. The sample and counterweight were attached to the arms of the balance with platinum wires. The sample was hanging in an alumina tube in a vertical tube furnace and the counterweight was hanging in a glass tube kept at room temperature. To ensure equilibrium, the weight was monitored isothermally at constant $p\text{O}_2$ values. Mixtures of O_2 and Ar were used to obtain a oxygen partial pressure between 10^{-5} and 1 atm, whereas lower oxygen partial pressures of up to 10^{-15} atm could be obtained by the use of CO ($\text{CO} + 1/2 \text{O}_2 \rightleftharpoons \text{CO}_2$). All thermogravimetric reductions and oxidizations were performed under conditions where the tetragonal tungsten bronzes are stable as confirmed by X-ray diffraction and all weight change can, therefore, be assigned to the oxygen non-stoichiometry. Equilibrium times increased with decreasing temperature and partial pressure of the reactive gas. Therefore, a reaction temperature of 1173 K was chosen as compromise between fast reaction kinetics and sample decomposition.

To measure the electrical conductivity and the Seebeck coefficient at high temperatures we used a custom-built assembly mounted into a NorECs ProboStat measurement cell as described elsewhere. [182] The gas atmosphere in the measurement cell was controlled by using a similar gas mixer as for the thermogravimetric investigation. The electronic measurements were performed under controlled atmosphere (room temperature - 773 K: $p\text{O}_2 \approx 10^{-5}$ atm; >773 K: $\approx 10^{-15}$ atm) and limited to a maximum temperature of 973 K to avoid sample oxidation. Thermal diffusivity was measured using a Netzsch laser flash diffusivity instrument (LFA micro flash 457). Heat capacity (C_p) was determined with the Pyroceram9606 standard from Netzsch. [183] All transport measurements were conducted up to 973 K, in order to prevent a change of the oxygen defect concentration during the measurements.

Scanning electron microscopy (SEM) images and energy dispersive X-ray spec-

troscopy (EDX) measurements of the as-synthesized powders and the sintered pellets were recorded using a FEI Nova NanoSEM600 equipped with an Everhart-Thornley detector (ETD) and a low voltage high contrast detector (vCD) in high vacuum mode. The acceleration voltage was chosen to be between 15-30 kV. The samples were mounted on an aluminium stub using adhesive conductive carbon tape. For energy dispersive X-ray spectroscopy, a built-in EDAX-Genesis detector was used. High-resolution transmission electron microscopy (HR-TEM) images were taken using a FEI Technai F20 with an acceleration voltage of 200 kV. Samples were either finely ground in an agate mortar or cut with a microtome into 1-10 nm thick slices, then dispersed in ethanol and drop casted on a carbon-Lacey grid.

4.3. Results and Discussion

4.3.1. Synthesis and Chemical Characterization

Starting from the binary oxides, the solid state synthesis of the complete series $\text{Nb}_{8-x}\text{W}_{9+x}\text{O}_{47}$ with $x = 0, \dots, 5$ is possible. The pseudo-binary phase diagram of Nb_2O_5 and WO_3 , postulated by Waring et al. reveals that the 4:9 phase ($\text{Nb}_8\text{W}_9\text{O}_{47}$) is stable above 1373 K and congruently melting at 1653 K (see supporting information C.1). However, screening of reaction parameters showed that the 4:9 phase and the complete series of tetragonal tungsten bronzes can be obtained at temperatures as low as 1173 K with short reaction times of 12 h and are stable at room temperature. To ensure a homogeneous cation distribution, all samples were subjected to a second annealing step at 1173 K for 12 h after the powder was thoroughly ground and resealed in an ampoule. Cation substituted, hence reduced, samples can be oxidized at high temperatures under structural changes, for example $\text{Nb}_7\text{W}_{10}\text{O}_{47} + 1/4 \text{O}_2 \rightarrow \text{Nb}_7\text{W}_{10}\text{O}_{47.5}$. Therefore, both annealing steps were conducted under vacuum to prevent the oxidation at higher temperatures. The unsubstituted end member $\text{Nb}_8\text{W}_9\text{O}_{47}$ exhibits a gray color, whereas all substituted samples are of a dark blue color. The dark color is a good indication for itinerant charge carriers, confirming that the cation substitution, indeed, increases the charge carrier concentration. The light gray color of the unsubstituted $\text{Nb}_8\text{W}_9\text{O}_{47}$ reveals the existence of some itinerant charge carriers. Considering the formal oxidation states of the cations no itinerant electrons should be present, therefore the gray color is a strong indication of oxygen deficiencies, which can be interpreted as self-doping. A possibility to circumvent the reduction during the synthesis under vacuum might be a synthesis conducted either under air or argon atmosphere.

Assuming that each substituted atom leads to an itinerant electron, a substitution degree of $x = 0.088$ was calculated to obtain a charge carrier concentration of 10^{20} per cm^3 . In addition, some itinerant electrons are already present, due to the small oxygen defect concentration after synthesis. Therefore, a series of samples with low substitution degree of nominal composition $\text{Nb}_{8-x}\text{W}_{9+x}\text{O}_{47}$, with $x = 0, 0.075, 0.1,$ and 1 , were prepared to investigate the thermal stability and thermoelectric transport properties. Due to the large unit cell, complex structure, and low symmetry of the tetragonal tungsten bronzes, Rietveld refinements of the laboratory X-ray diffraction data were not possible. Therefore, the computationally more simple Le Bail fits were used to match the diffraction data. The refined diffraction data can be seen in Figure 4.1 and in the supporting information C.1. All as-synthesized samples could

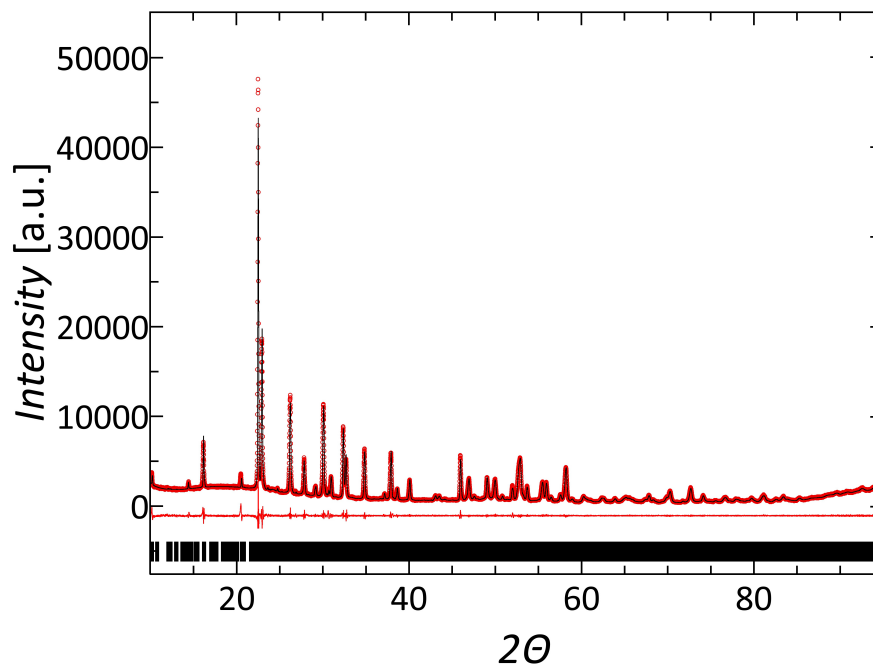


Figure (4.1) – Le Bail fit for the powder diffraction data of the $\text{Nb}_8\text{W}_9\text{O}_{47}$ sample (red dots), including profile fit (black solid line), and profile difference (red solid line). The refined peak positions are indicated by black tick marks.

be fitted using the crystallographic structure model of $\text{Nb}_8\text{W}_9\text{O}_{47}$ with R_{wp} values below 5%. In addition, data obtained from consolidated samples and pellets, which were subsequently reduced or oxidized (see Subsection 4.3.2) showed no significant difference within the resolution limit of the used diffractometer. However, many other structurally correlated compounds with slightly different compositions are known, for example $\text{Nb}_8\text{W}_7\text{O}_{41}$, $\text{Nb}_{12}\text{W}_{11}\text{O}_{63}$, $\text{Nb}_{18}\text{W}_{16}\text{O}_{93}$, or $\text{Nb}_{22}\text{W}_{20}\text{O}_{102}$. Therefore, it is difficult to confirm the actual crystal structure or phase composition using standard

laboratory diffraction data.

Consolidation experiments were conducted via current-assisted short-time sintering and uniaxial hot pressing. Uniaxial hot pressing of the samples had to be conducted for several hours at temperature above 1373 K to obtain high enough pellet densities. The use of short-time sintering allowed to reduce the consolidation temperature and time to few minutes at 1173 K. This allowed powder consolidation at temperatures where no significant sample degradation is expected (see subsection 4.3.2). The resulting short-time sintered pellets have densities above 95% and are, therefore, considered suitable for thermoelectric characterizations.

Scanning electron microscopy images were taken of the as-synthesized powders and consolidated pellets (see Figure 4.2). The obtained powders consist of anisotropic

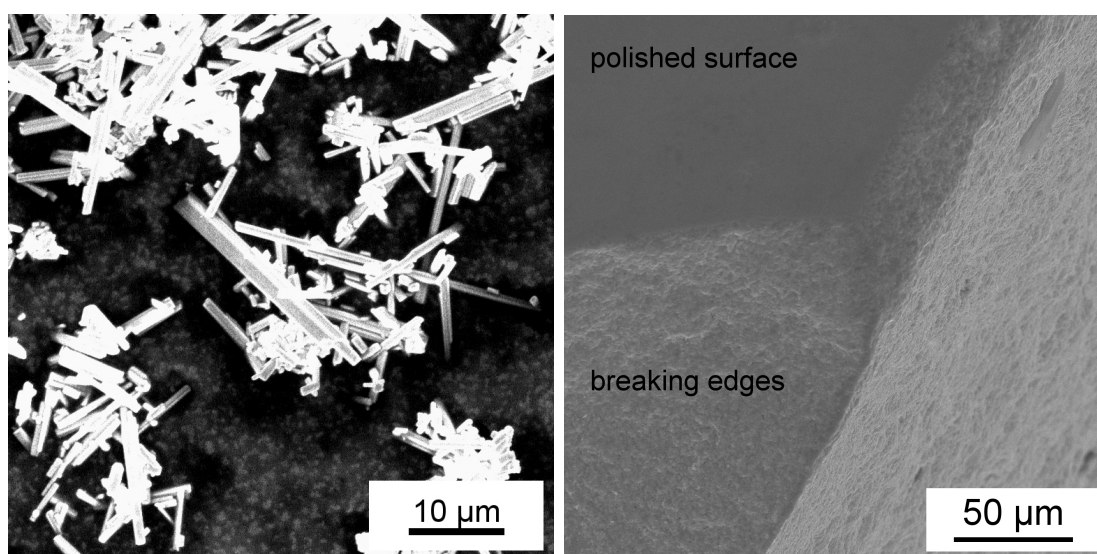


Figure (4.2) – *Scanning electron microscopy images of the as-synthesized powder (left) and the consolidated pellet (right).*

match-like crystals with prismatic crystal habit, few micrometer in diameter, but several micrometer in length. The consolidated pellets show high density with only few porous cavities visible at the breaking edge. The polished surface shows no signs contrast corroborating with a homogeneous elemental distribution. A zoomed-in image of the cavities can be seen in the supporting information Figure C.5. It is clearly visible that the sintering process did not lead to a preferred orientation of the prismatic crystals. In contrast a random orientation can be seen, similar to a compressed haystack. Therefore, no significant anisotropic contributions to the transport properties are expected.

A more in-depth investigation on the prevalent defects was obtained by high-resolution transmission electron microscopy imaging. As-synthesized pellets of composition $\text{Nb}_8\text{W}_9\text{O}_{47}$ and $\text{Nb}_7\text{W}_{10}\text{O}_{47}$ were analyzed to investigate the influence

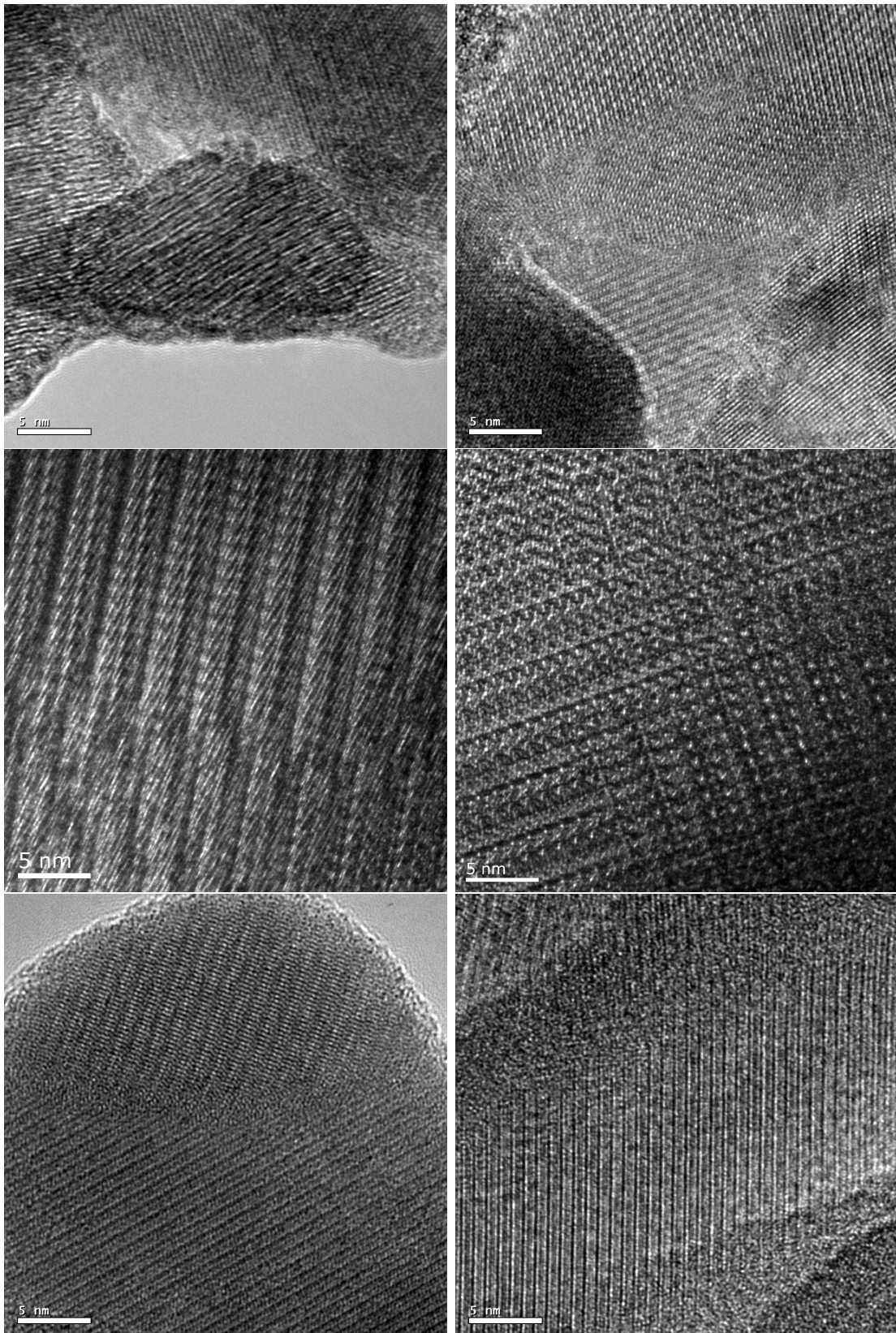


Figure (4.3) – *High resolution transmission electron microscopy images, illustrating the diversity of different grain sizes, Wadsley defects, and CS planes found in sintered samples of different substitution degree and varying oxygen deficiency.*

of cation substitution on the structure. Additionally, an as-synthesized pellet of composition $\text{Nb}_8\text{W}_9\text{O}_{47}$ was cut into two pieces, which were subsequently either oxidized or reduced (see subsection 4.3.2), to investigate the influence of oxygen deficiencies on the structure. An overview of the found defects and grain sizes are given in Figure 4.3, more images can be found in the supporting information section C.2. Interestingly, all investigated samples, including the fully oxidized one, exhibit a rich variety of defects, for example Wadsley defects and CS planes, which arise due to oxygen deficiencies. However, the yellow/white color of the oxidized sample indicates the absence of itinerant electrons. In conclusion, the additional few electrons in the conduction band, induced by defect formation, are trapped within the ionic cation potential, and therefore, are localized. However, at higher charge carrier concentrations (higher oxygen deficiency and/or higher cation substitution degree) the electrons become itinerant, which is reflected in the dark gray/blue color. Furthermore, the presence of defects in the fully oxidized sample might be an indication that the formation of Wadsley defects or even CS planes are driven by pressure during the sintering process. In addition to the different defects, a variety of grain sizes ranging from few to several hundred nanometers were found in all of the samples. The investigated TTB materials, thus, can be considered both, nanostructured and nanoscaled, due to the CS planes and grain sizes in the nanometer regime, respectively. As a consequence, the lattice thermal conductivity is expected to be low. However, a deep understanding of the structure and the origin of the defects will require further investigation (for example by detailed electron diffraction studies) and is well beyond the scope of this initial evaluation of the tetragonal tungsten bronzes for thermoelectric application.

4.3.2. Thermal Stability and Oxygen Deficiency

To obtain information on the thermal stability and the oxygen defect concentration at elevated temperatures, we conducted elaborated thermogravimetric analyses under controlled atmosphere. First of all, the thermal stability was investigated. Figure C.8 in the supporting information shows the entire TG run as function of time. An initial weight loss of 0.2% was encountered from room temperature up to 650 K. Some or all of this loss is probably associated to adsorbed water, but the possibility of oxygen non-stoichiometry at low temperatures, although improbable, can not be neglected. In Figure 4.4 zoomed-in plots of Figure C.8 are shown, emphasizing the high temperature behavior measured at $p\text{O}_2$ values of 10^{-5} atm (left) and 0.5 atm (right), respectively. The different oxygen partial pressures $p\text{O}_2$ were obtained by

diluting O_2 with Ar. An onset of an irreversible weight loss can be seen at ≈ 1373 K in both atmospheres and is probably associated to the volatilization of WO_3 . The rate of weight loss at 1520 K was determined to 0.10 and 0.13% per hour under high and low pO_2 conditions, respectively. No weight gain was observed while increasing pO_2 at 1273 K (see right image Figure 4.4), indicating no significant oxygen non-stoichiometry under these conditions. During the final cooling to room temperature, the pO_2 was again reduced to 10^{-5} atm at 920 K without observing any significant weight change. During this TG study, the sample color had changed from dark gray to white/slightly yellow. This indicates that the high temperature decomposition is superimposed with the healing of oxygen defects (oxidation) at elevated temperatures.

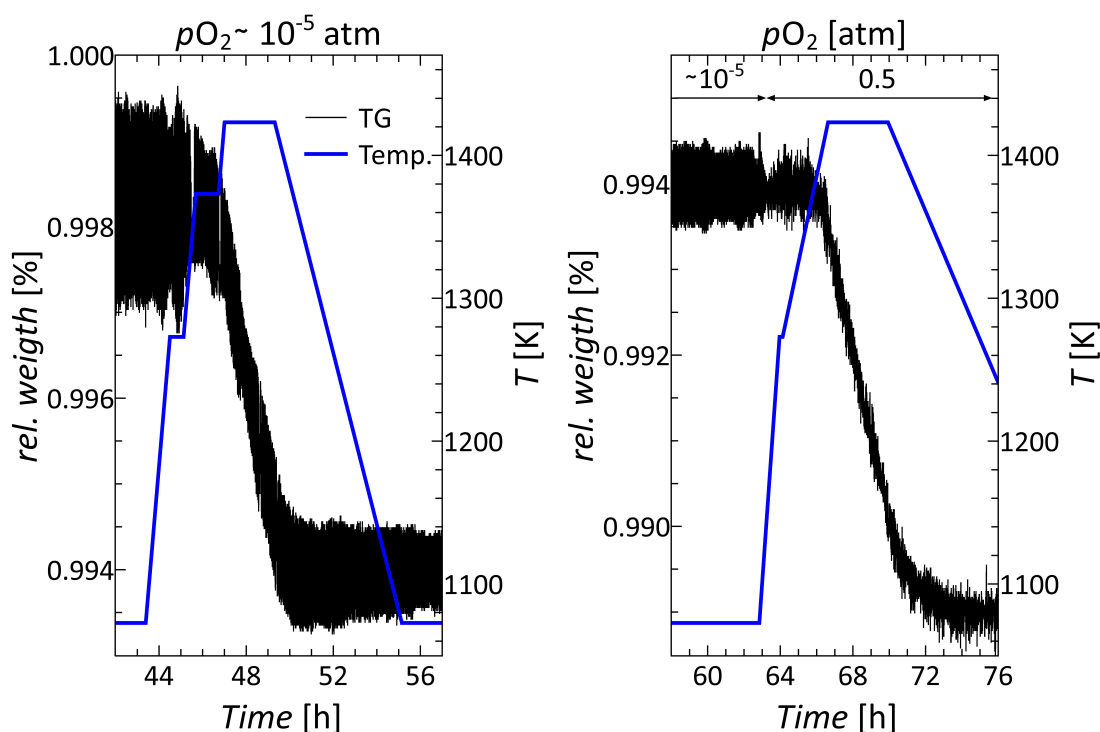


Figure (4.4) – Relative weight of $Nb_8W_9O_{47}$ as a function of time under different oxygen partial pressures. The weight loss above 1373 K indicates an irreversible decomposition at lower (left) and higher (right) oxygen partial pressures, probably correlated to the evaporation of WO_3 .

The reduction of the oxygen partial pressure by dilution with argon ($pO_2 \approx 10^{-5}$ atm), however, did not lead to oxygen partial pressures that were low enough to enable sample reduction. Therefore, reducing gases were investigated to obtain higher reduction potentials. The use of H_2 as a reductive gas ($pO_2 \approx 10^{-30}$ atm) did not lead to a reduction of $Nb_8W_9O_{47}$, but to sample decomposition, verified by X-ray diffraction. Therefore, milder reducing gas mixtures were tested, and indeed, a reduction of $Nb_8W_9O_{47}$ was possible with the use of a CO/Ar gas mixture. It was

found that for an effective reduction, a temperature of at least 1173 K is necessary for suitable kinetics. At 1173 K the used CO mixture corroborates with a p_{O_2} of $\approx 10^{-15}$ atm. Due to the correlated weight loss, the reduction can be monitored in the TG. After reduction, the color of the sample was dark blue and no significant structural change was observed by X-ray diffraction. Therefore, the weight loss has to be correlated to the formation of oxygen deficiencies. These defects give rise to only subtle structural changes, which could not be resolved by standard laboratory X-ray diffraction. It has to be noted that with each new oxygen defect two electrons are donated into the conduction band, and thus, the control of the defect concentration corroborates with the control of the charge carrier concentration. Figure 4.5 shows the reversible weight loss and gain, correlated to the reduction and oxidation of an as-synthesized $\text{Nb}_8\text{W}_9\text{O}_{47}$ sample. Both reduction and oxidation

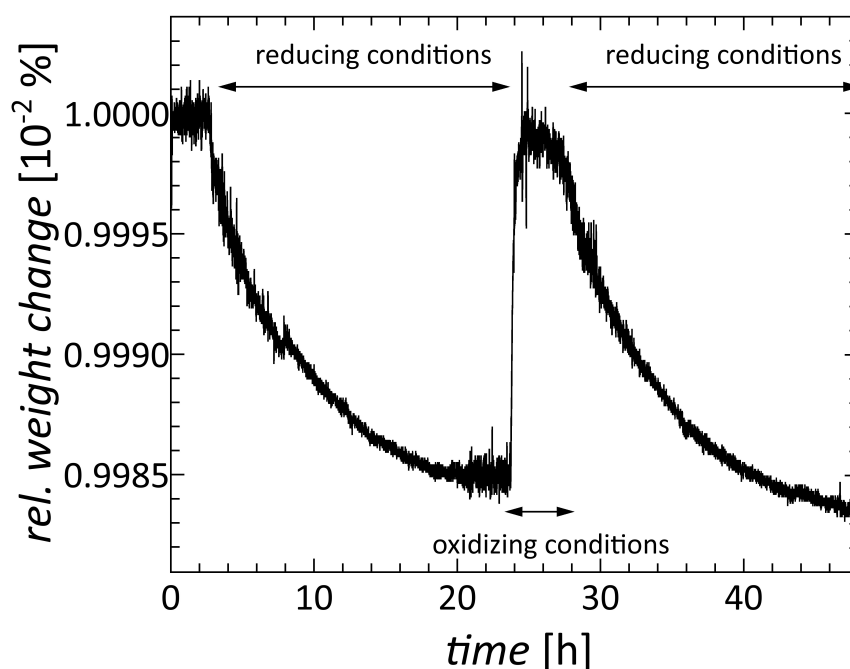


Figure (4.5) – Redox reaction of $\text{Nb}_8\text{W}_9\text{O}_{47-\delta}$ monitored by thermogravimetric analysis. The p_{O_2} was changed between $\approx 10^{-15}$ atm (reducing conditions) and 10^{-5} atm (oxidizing conditions) with the use of CO/Ar or O_2 /Ar gas mixtures at 1173 K. A maximum oxygen deficiency of $\delta = 0.35$ was calculated.

were conducted at 1173 K. For a reduction, the sample was heated in a gas mixture of CO and argon, which translates to an oxygen partial pressure of $\approx 10^{-15}$ atm at 1173 K. Despite the high temperature, the reduction process is rather slow and equilibrium was reached only after 24 h. After the reduction, the sample was re-oxidized by changing the atmosphere to a oxygen partial pressure of 10^{-5} atm. The oxidation reaction is much faster than the reduction, demonstrated by the rapid

weight gain at 24 h in Figure 4.5. After oxidation, the sample color has changed to white/slightly yellow again. The reduction-oxidation cycle, thus, is reversible and can be repeated without any sign of sample degradation. In conclusion, the control over the oxygen partial pressure at high temperatures enables to equilibrate the sample at a certain oxygen defect concentration corresponding to the oxygen partial pressure applied. By thermal quenching to room temperature, the defect concentration and the corresponding charge carrier concentrations can usually be preserved to the mid temperature range. [184] Assuming a complete oxidized sample before the reduction, the relative weight loss of 0.15% can be translated to a oxygen deficiency δ of 0.3 in $\text{Nb}_8\text{W}_9\text{O}_{47-\delta}$. In contrast to the substitution, each oxygen vacancy donates two electrons. Therefore, the maximum oxygen deficiency of 0.3 should be comparable to a substitution of $x = 0.6$.

4.3.3. Thermoelectric Transport Properties and Optimization Strategies

Starting from the unsubstituted, fully oxidized $\text{Nb}_8\text{W}_9\text{O}_{47}$, we aimed to increase the charge carrier concentration to enhance the thermoelectric properties. An increase of charge carriers can be obtained either by cation substitution or by an increase of oxygen defects, which are correlated to the reduction of the sample. To obtain a first assessment of the thermoelectric potential, a series of cation substituted compounds with composition $\text{Nb}_{8-x}\text{W}_{9+x}\text{O}_{47}$, $x = 0, 0.075, 0.1,$ and 1 , were investigated for their thermoelectric transport properties. To this end, measurements of the electrical conductivity, the Seebeck coefficient and the thermal conductivity were performed on as-synthesized pellets without preceding sample oxidization or reduction. Although the TTB were found to be stable up to 1373 K the characterization of the thermoelectric transport properties were conducted starting from room temperature up to 973 K to prevent a change in the oxygen defect concentration. Further, the electronic measurements were performed under controlled atmosphere (room temperature - 773 K: $p\text{O}_2 \approx 10^{-5}$ atm; >773 K: $\approx 10^{-15}$ atm) to ensure no sample oxidation during measurement. Thermal diffusivity measurements were conducted under N_2 , however, no signs of sample oxidation were found after the measurements. The results of the electronic transport measurements are plotted in Figure 4.6.

It can be seen that the electric conductivity of the investigated samples is very low, but increases with rising temperature. Additionally, an increasing substitution degree leads to a higher electric conductivity, reaching a value of 16 S/cm at 973 K for the

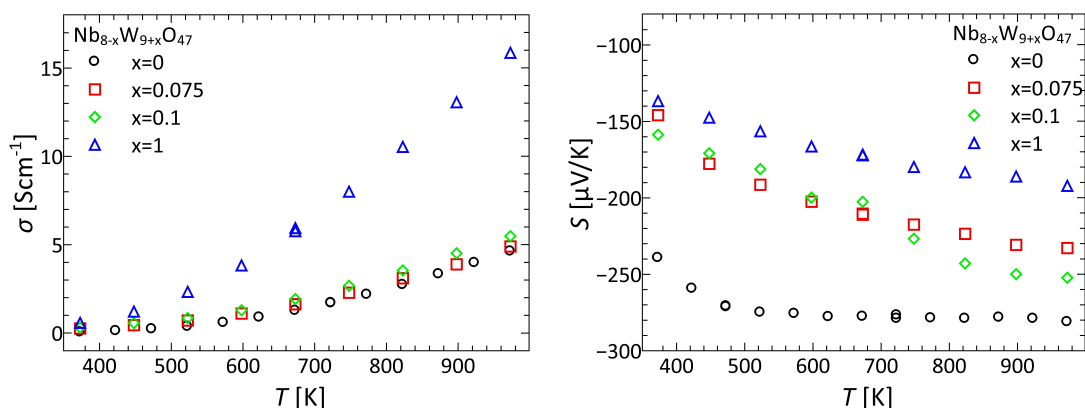


Figure (4.6) – Temperature dependence of the electronic transport properties from the cation substitution degree in tetragonal tungsten bronzes $\text{Nb}_{8-x}\text{W}_{9+x}\text{O}_{47}$ with $x = 0, 0.075, 0.1,$ and 1 , illustrating the trend of increasing charge carrier concentration with increasing substitution degree.

sample of composition $\text{Nb}_7\text{W}_{10}\text{O}_{47}$. Thus, the initial calculation of the substitution degree, to obtain materials with a charge carrier concentration around 10^{20} per cubic centimeter, has proven to be misleading, and higher substitution degrees are needed for a good electric conductivity. One possible reason for this might be that at low substitution degrees electrons are trapped in the local coulomb potential of the substituting tungsten atom. With increasing substitution degree, the distance between substituting atoms decreases and the electron "feels" not only the local potential of one, but an average potential of all neighboring substituting atoms. If the substitution degree is large enough for a complete delocalization of the coulomb potential, the electrons are able to move in an itinerant manner. In result, the mobility would have to scale with the charge carrier concentration. To prove this, further investigation of the charge carrier concentration and the electron mobility have to be conducted. Moreover, only minor changes in the electric conductivity were observed in the three samples with low substitution degree, which might be due to small variations of the oxygen defect concentration in those samples. At low substitution degrees, the additional charge carriers, due to oxygen defects, will have a larger influence on the transport properties than at higher substitution degrees.

In contrast to the electric conductivity, the measured Seebeck coefficients are rather large. At room temperature the Seebeck values range from $-240 \mu\text{V/K}$ to $-140 \mu\text{V/K}$ for samples of composition $\text{Nb}_8\text{W}_9\text{O}_{47}$ and $\text{Nb}_7\text{W}_{10}\text{O}_{47}$, respectively, and increase with increasing substitution degree. This corroborates with electrons as majority charge carriers and higher charge carrier concentration in higher substituted samples. All substituted samples showed a decreasing trend of the Seebeck coefficient dependent on the measurement temperature. The unsubstituted sample $\text{Nb}_8\text{W}_9\text{O}_{47}$,

however, showed a decrease in the Seebeck coefficient up to 480 K, which remains at a constant value around $-280 \mu\text{V}/\text{K}$ up to 973 K. Further investigation are needed to fully understand the underlying principles of the electronic transport properties of the tungsten bronzes, which, however, is beyond the scope of this principal investigation.

The measured thermal diffusivities and calculated thermal conductivities of the cation substituted series of tetragonal tungsten bronzes are shown in Figure 4.7. The

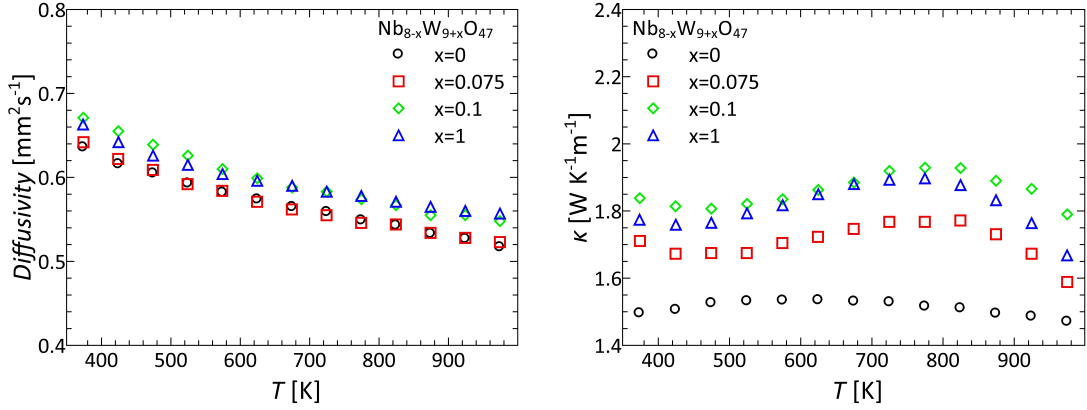


Figure (4.7) – Temperature dependence of the thermal diffusivity and conductivity in cation substituted tetragonal tungsten bronzes of composition $\text{Nb}_{8-x}\text{W}_{9+x}\text{O}_{47}$ with $x = 0, 0.075, 0.1, \text{ and } 1$.

thermal diffusivity values of all samples are very similar to each other. Beside a subtle increase upon substitution, no trend was observed. With increasing temperature, the thermal diffusivity slightly decreases, which leads to an almost temperature independent thermal conductivity. The wave-like temperature dependence of samples with $x > 0$ results from a small maximum in the measured C_p value (see supporting information Figure C.9) between 700 and 800 K. At elevated temperatures the measured C_p values of samples with $x > 0$ exceed the Dulong-Petit value, which can be attributed to anharmonic or electronic contributions. Those findings are similar to the results reported on misfit layered cobaltates. [185]

The obtained thermal conductivities are all quite low, with values ranging from $1.5 \text{ W K}^{-1}\text{m}^{-1}$ to $1.8 \text{ W K}^{-1}\text{m}^{-1}$ for the unsubstituted and substituted samples, respectively. These glass-like thermal conductivities can easily be explained by the nanosized grains and the complex disordered structure [146], and its similarities to silica, which is often found in complex tungsten niobates. [186] With increasing substitution degree, the structure of the TTB does not change, and in result no change in the lattice thermal conductivity was expected. However, the electrical conductivity increases upon substitution, which will result in an increase of the electronic contribution to the thermal conductivity. This explains the slightly higher thermal conductivity of samples with $x > 0$.

Using these initial measurements, the power factor and the thermoelectric figure of merit of the cation substituted series were calculated. The results are summarized in Figure 4.8. Due to the rather low electrical conductivity, the power factor is

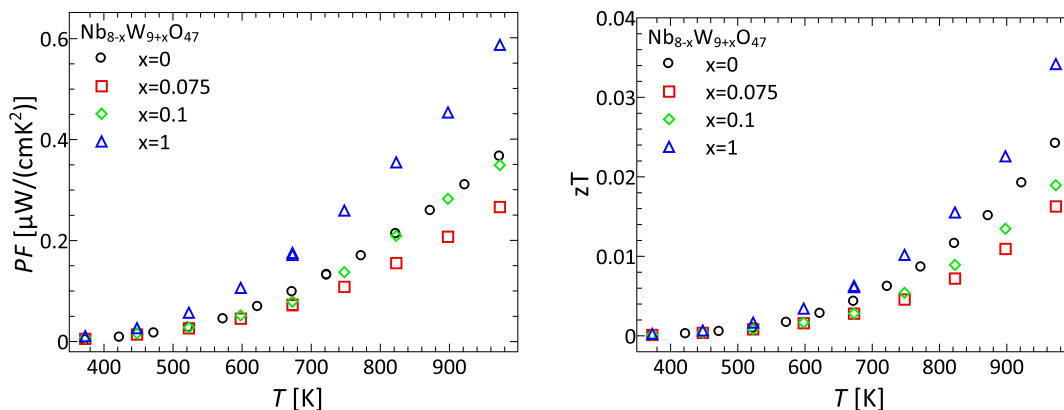


Figure (4.8) – Temperature dependence of the power factor (left) and the figure of merit (right) from the cation substitution degree in tetragonal tungsten bronzes $\text{Nb}_{8-x}\text{W}_{9+x}\text{O}_{47}$ with $x = 0, 0.075, 0.1,$ and 1 , illustrating the trend of increasing power factor and figure of merit with increasing substitution degree.

also not very large, but increases with rising temperature. No significant trend can be seen in samples with similar low substitution degree, which might be the result of a varying oxygen deficiencies in the as-synthesized samples. These findings underline the importance to control the oxygen defect content during the synthesis as well as during sample measurements. However, a substantial increase of the power factor to a value of $0.6 \mu\text{Wcm}^{-1}\text{K}^{-2}$ at 973 K could be obtained with the sample of composition $\text{Nb}_7\text{W}_{10}\text{O}_{47}$, with respect to lower substituted samples. This trend is also reflected in the thermoelectric figure of merit, and a value of 0.035 is obtained with the highest substituted sample ($x = 1$) at 973 K. In comparison to state of the art optimized n -type oxide thermoelectric materials, the figure of merit is ten times lower. Nevertheless, the Seebeck coefficients and the thermal conductivities exhibit comparable or better values. The lower figure of merit can be attributed to the low electric conductivity, which, in turn, has the highest optimization potential. Up to now, tetragonal tungsten bronzes with a maximal substitution level of $x = 1$ have been investigated, although a substitution level of up to $x = 5$ ($\text{Nb}_3\text{W}_{14}\text{O}_{47}$) is possible. With increasing substitution degree, the electric conductivity should be further improved, which will also result in an enhanced figure of merit.

Another optimization strategy to influence the charge carrier concentration is to control the oxygen deficiency. As previously shown, the oxygen deficiency can be reversibly varied at 1173 K by oxidization or reduction under controlled atmospheres (see Figure 4.5). Once equilibrated, the oxygen defect concentration can be con-

served by quenching to room temperature. To demonstrate that the control of the oxygen deficiency corroborates with the control of the electronic properties, a simple experiment was conducted. A sample of composition $\text{Nb}_8\text{W}_9\text{O}_{47}$ was repeatedly reduced and oxidized over three cycles under controlled conditions. The corresponding electronic properties were determined after each cycle. The reduction degree was monitored by using thermogravimetric analyses and the reduction was stopped after equilibrium had been reached to obtain similar oxygen defect concentrations. In the oxidized state the color was white/slightly yellow and the sample resistivity was too high for measurements in the used setup. The resistance of the sample was vaguely determined by a hand held multimeter to be higher than $1 \text{ M}\Omega$. In the reduced state, the sample was dark blue in color, and the results of the electronic transport measurements after each cycle are reported in Figure 4.9. Considering the simple

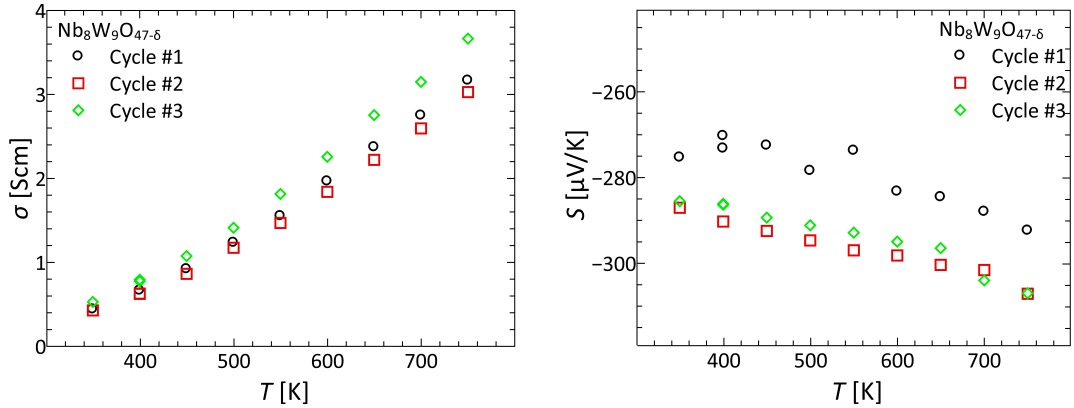


Figure (4.9) – *Electronic transport properties after controlled oxidization and reduction cycles. The measurements were performed in the reduced state, after the first, second and third redox cycle. The good reproducibility of the electronic properties illustrates the good control of the oxygen defect concentration, and hence the charge carrier concentration.*

experiment, and the substantial changes from the white, oxidized, isolating sample to the dark blue, reduced, semi-conducting sample, the measured electronic properties are very similar. The measured electric conductivities and the Seebeck coefficients in the three cycles are reproducible within a relative error of 17% and 7%, respectively. However, the reproducibility should be easily improved by a more elaborate sample preparation, for example by longer equilibration or faster quenching. The control of the oxygen non-stoichiometry, and in result the charge carrier concentration, thus is possible, and represents a further viable optimization strategy for tetragonal tungsten bronzes.

4.4. Conclusions and Outlook

A first assessment of the potential of tetragonal tungsten bronzes for thermoelectric energy conversion was conducted. These compounds of composition $\text{Nb}_{8-x}\text{W}_{9+x}\text{O}_{47-\delta}$ can be characterized by their infinitely adaptive structure and were chosen due to their structural complexity, and their possible electronic optimization by cation substitution x and oxygen deficiency δ . To this end, a series of compounds with low substitution degrees $x = 0, 0.075, 0.1, \text{ and } 1$, were synthesized and structurally characterized by X-ray diffraction and high-resolution transmission electron microscopy. To be able to conduct thermoelectric transport measurements, optimal sinter parameters, thermal stability and redox behavior at elevated temperatures were investigated. It was found that the materials have a more complex real-structure than initially thought. The simple synthesis under vacuum results in slightly oxygen deficient samples, which can easily be seen by the changing color of the obtained powders. Further, HR-TEM investigations of consolidated pellets with different substitution degree and different oxygen deficiency have shown varying grain sizes down to the lower nanometer regime and a variety of different Wadsley defects and crystallographic shear planes. Thermogravimetric analyses have shown an irreversible decomposition at 1323 K, possibly due to the evaporation of WO_3 .

The oxygen deficiency could be reversibly altered by reduction or oxidation reactions at 1173 K depending on the applied atmosphere. The reduction was conducted with a CO/Ar gas mixture corresponding to a $p\text{O}_2$ value around 10^{-15} atm. To reach equilibrium conditions, the samples had to be reduced for 24 h. In contrast, the oxidation process was proved to be faster and could easily be performed with an O_2/Ar mixture at a $p\text{O}_2$ around 10^{-5} atm. Due to the reversible generation or healing of oxygen defects at elevated temperatures, the oxygen content and, in result, the electronic properties could be tuned in a limited range. The relative weight gain or loss, correlated to the oxidation or reduction, was monitored gravimetrically, which allowed to reproducibly vary the oxygen deficiency and produce materials with a specific oxygen defect concentration and corresponding electronic properties. A maximum oxygen deficiency of $\delta = 0.3$ was determined for $\text{Nb}_8\text{Nb}_9\text{O}_{47-\delta}$. In contrast to the substitution, each oxygen vacancy donates two electrons. Therefore, the maximum oxygen deficiency of 0.3 should be comparable to a substitution of $x = 0.6$.

Thermoelectric transport measurements were conducted up to 973 K under controlled atmosphere to prevent a change of the oxygen stoichiometry during measurements. All samples exhibited a rather low electric conductivity between 1 and

16 S/cm and high negative Seebeck coefficients ranging from -280 to -140 $\mu\text{V}/\text{K}$, indicating *n*-type conduction. With an increasing substitution degree, more charge carriers are introduced into the conduction band, which results in an increase of the electric conductivity and smaller negative Seebeck coefficients. However, further investigation on the charge carrier concentration and mobility are needed to gain in-depth understanding on the electronic transport and the conduction mechanism in the tetragonal tungsten bronzes. The complex structure, composed of nano-sized grains, and a high concentration of Wadsley defects and crystallographic shear planes results in glass-like, temperature independent thermal conductivities ranging from 1.5 to 1.8 $\text{WK}^{-1}\mu\text{m}^{-1}$. Due to the infinitely adaptive nature of the crystal structure, cation substitution is not effectively affecting the thermal conductivity. However, higher substituted samples exhibit a slightly larger thermal conductivity, probably due to a more significant contribution of the electronic thermal conductivity. The power factor and the figure of merit were calculated from the measured transport properties. Due to the rather low electric conductivity the power factor and thermoelectric figure of merit of the investigated tetragonal tungsten bronzes were small. The highest power factor and zT were obtained for the highest substituted sample ($\text{Nb}_7\text{W}_{10}\text{O}_{47}$) with values of $0.6 \mu\text{Wcm}^{-1}\text{K}^{-2}$ and 0.035 at 973 K, respectively. Although the obtained figure of merit is lower than in state of the art optimized *n*-type materials, the high Seebeck coefficient paired with the low, glass-like thermal conductivity demonstrates the potential of tetragonal tungsten bronzes for thermoelectric applications. Both investigated optimization strategies, the cation substitution and the controlled oxygen deficiency have proven to be suitable to affect the electronic properties. Therefore, further optimization of the figure of merit is to be expected, which makes the initial value of 0.035 promising.

After this initial assessment of the thermoelectric properties and optimization strategies, more detailed investigation are currently envisaged to obtain a better understanding of the charge transport in these complex oxide materials. This includes the investigation of higher substituted samples, which should exhibit higher electric conductivity. To be able to properly separate the contributions of the oxygen deficiency from the cation substitution, we plan to investigate samples without significant oxygen defects after synthesis. To do so, the influence of the atmosphere during synthesis has to be investigated. A synthesis under high argon pressure or an argon/air mixture is expected to yield tetragonal tungsten bronzes with less oxygen defects. Moreover, Hall and XPS measurements of these, better defined materials will probably provide very useful information on the nature of the conduction mechanism. Additionally, the influence of the sintering process on the

oxygen deficiency, the real structure and the corresponding effect on the electronic properties could also be investigated. To conclude, the electronic optimization by controlled oxygen deficiencies could be further refined to obtain and characterize materials with different, well defined oxygen defect concentrations. This optimization strategy might also be applied to higher substituted samples, although special care will be necessary under oxidizing conditions in order not to oxidize the substituted materials to an extent where the structure is changed irreversibly.

A

Quaternary Chalcogenides

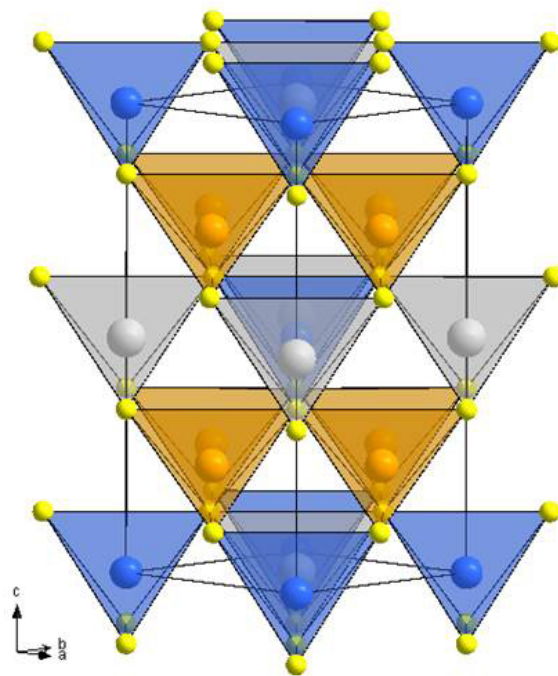


Figure (A.1) – Crystal structure of the stannite type $\text{Cu}_2\text{ZnGeSe}_{4-x}\text{S}_x$. Cu atoms are indicated by orange, Ge atoms are indicated by gray, Zn atoms are indicated by blue, and Se/S atoms are indicated by yellow spheres, with the tetrahedral coordination of the elements indicated. Note the difference in the ordering of the metal cations. While Zn and Ge share a plane in this structure, Cu resides on the 4d-Wyckoff position $(0, 1/2, 1/4)$ alone, forming slabs of Cu–Se/S-tetrahedra.

A.1. Refined X-ray Diffraction Data

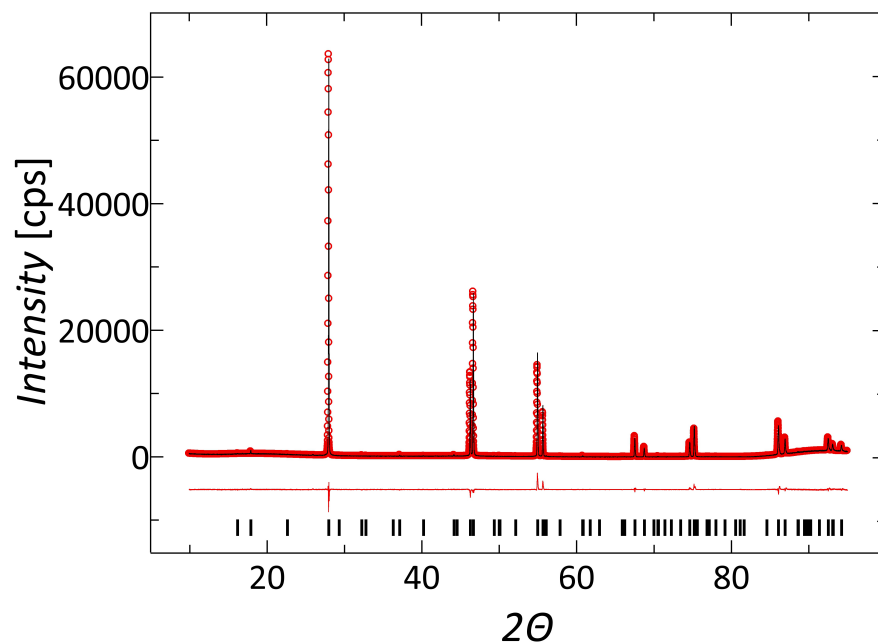


Figure (A.2) – Refined powder diffraction data of $\text{Cu}_2\text{ZnGeSe}_3\text{S}$, including profile fit (black solid line), and profile difference (red solid line). The refined peak positions are indicated by black tick marks.

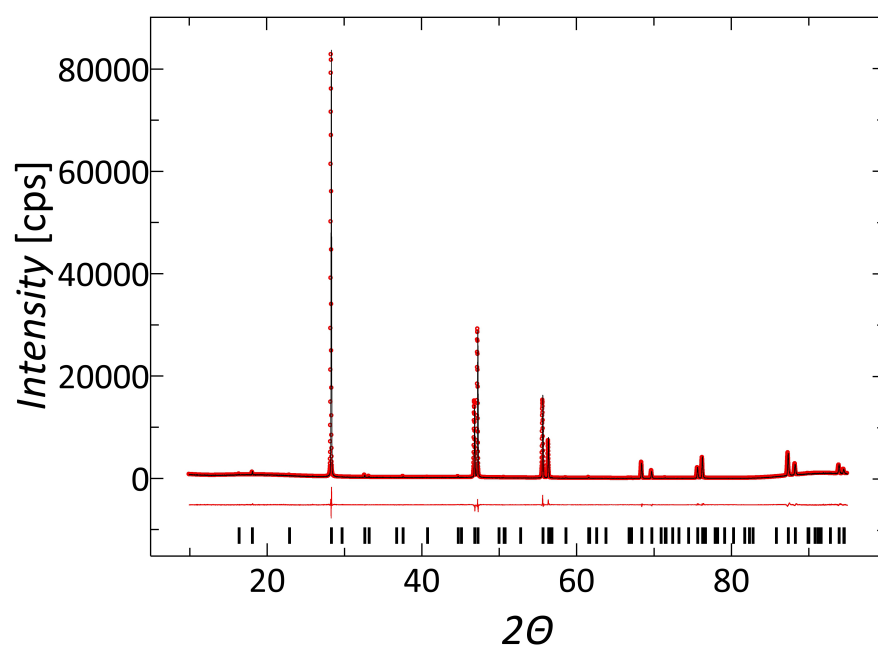


Figure (A.3) – Refined powder diffraction data of $\text{Cu}_2\text{ZnGeSe}_2\text{S}_2$, including profile fit (black solid line), and profile difference (red solid line). The refined peak positions are indicated by black tick marks.

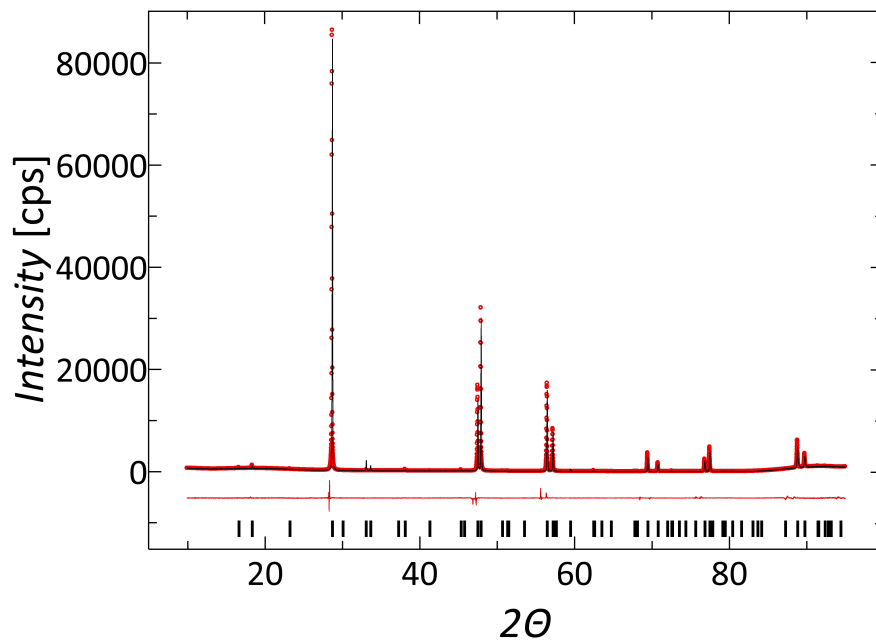


Figure (A.4) – Refined powder diffraction data of $\text{Cu}_2\text{ZnGeSe}_3$, including profile fit (black solid line), and profile difference (red solid line). The refined peak positions are indicated by black tick marks.

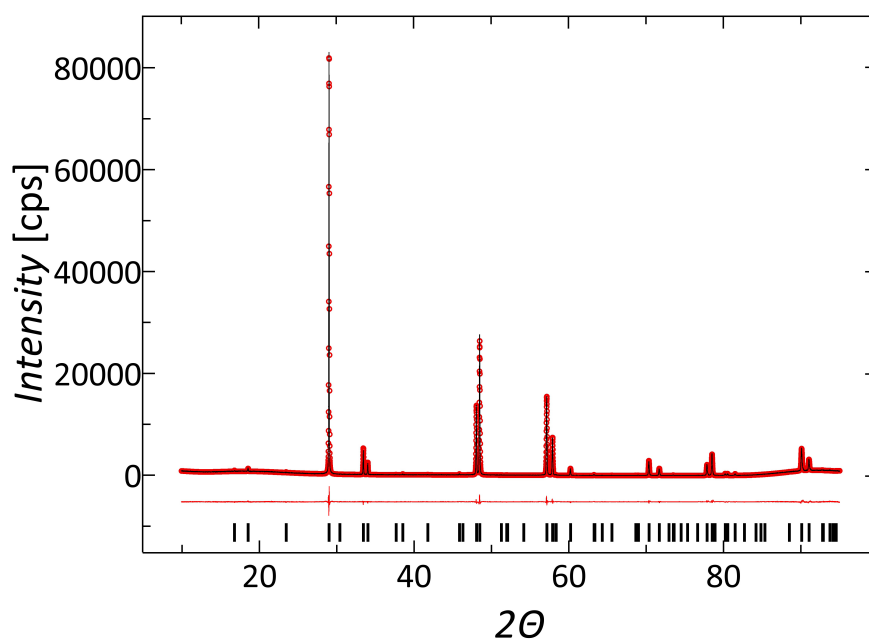


Figure (A.5) – Refined powder diffraction data of $\text{Cu}_2\text{ZnGeS}_4$, including profile fit (black solid line), and profile difference (red solid line). The refined peak positions are indicated by black tick marks.

A.2. Differential Scanning Calorimetry

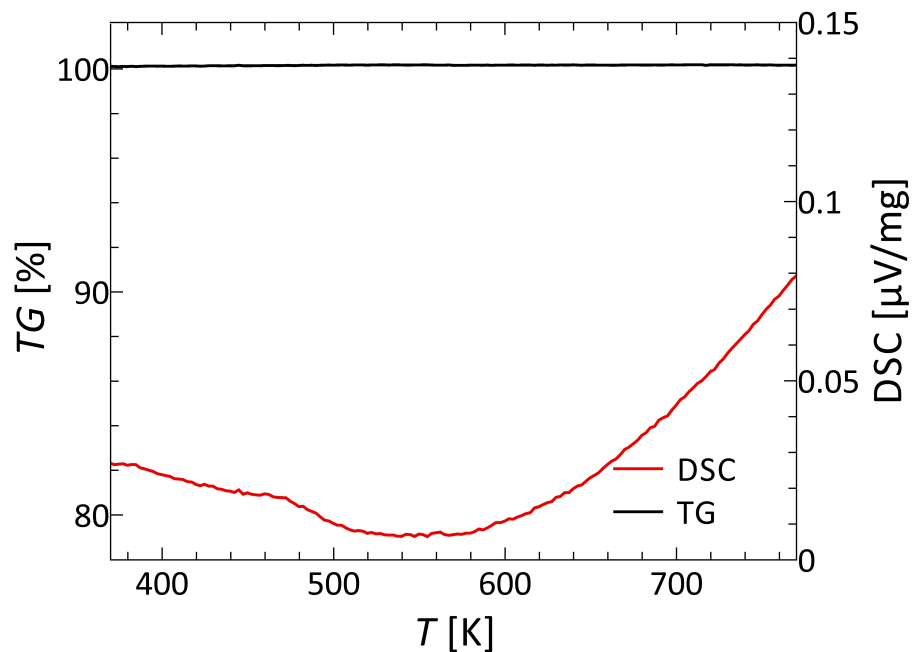


Figure (A.6) – DSC/TG measurements of $\text{Cu}_2\text{ZnGeSe}_3\text{S}$. DSC signal (red line) showing a subtle phase transition around 480 K; TGA (black line) illustrating the thermal stability.

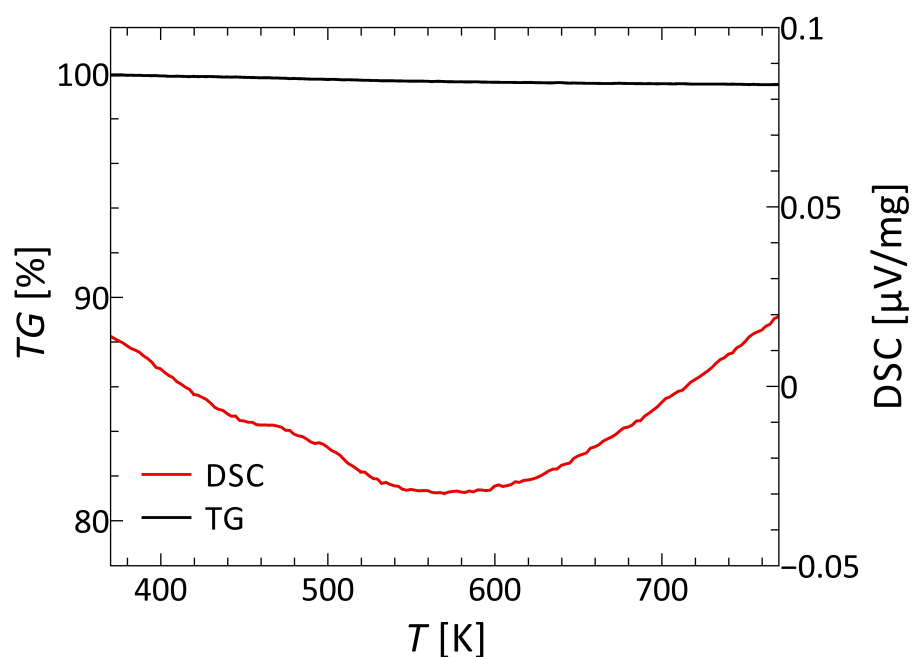


Figure (A.7) – DSC/TG measurement of $\text{Cu}_2\text{ZnGeSe}_2\text{S}_2$. DSC signal (red line) showing a subtle phase transition around 500 K; TGA (black line) illustrating the thermal stability.

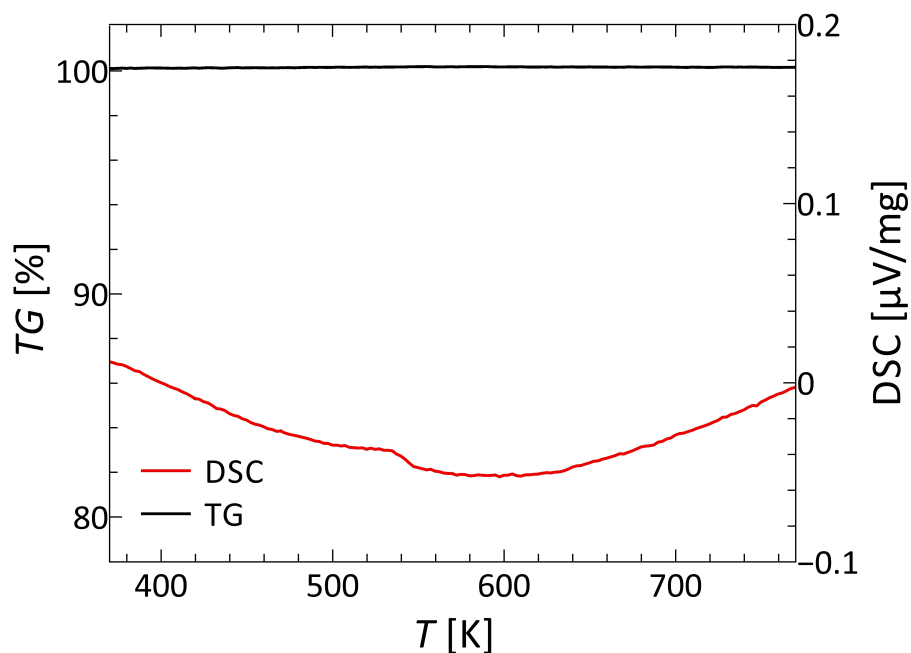


Figure (A.8) – DSC/TG measurement of $\text{Cu}_2\text{ZnGeSe}_3$. DSC signal (red line) showing a subtle phase transition around 540 K; TGA (black line) illustrating the thermal stability.

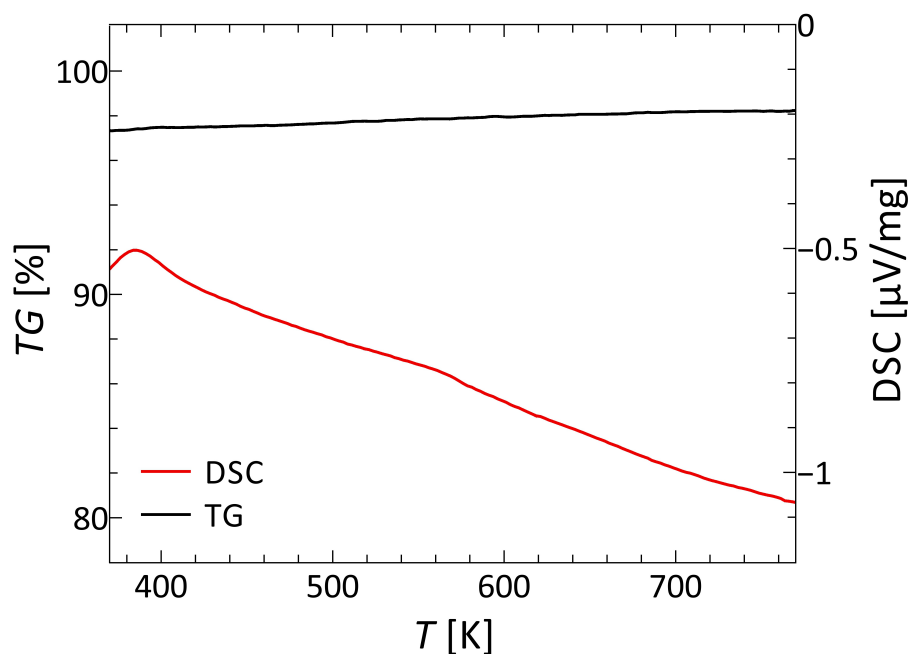


Figure (A.9) – DSC/TG measurement of $\text{Cu}_2\text{ZnGeS}_4$. DSC signal (red line) showing a subtle phase transition around 560 K; TGA (black line) illustrating the thermal stability.

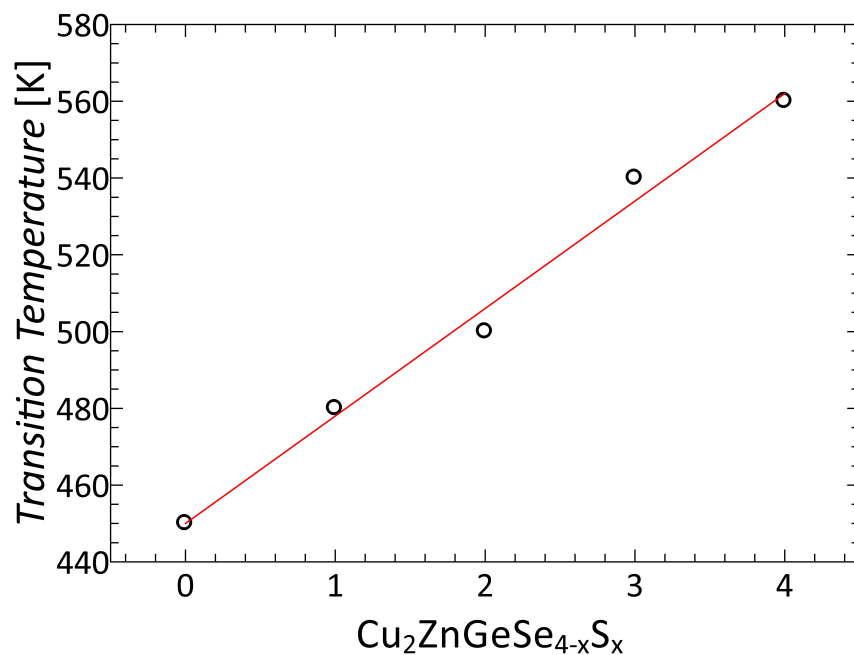


Figure (A.10) – Superionic phase transition temperatures in dependence of the substitution degree. $\text{Cu}_2\text{ZnGeSe}_4$ data from [76]

A.3. UV-Vis Data

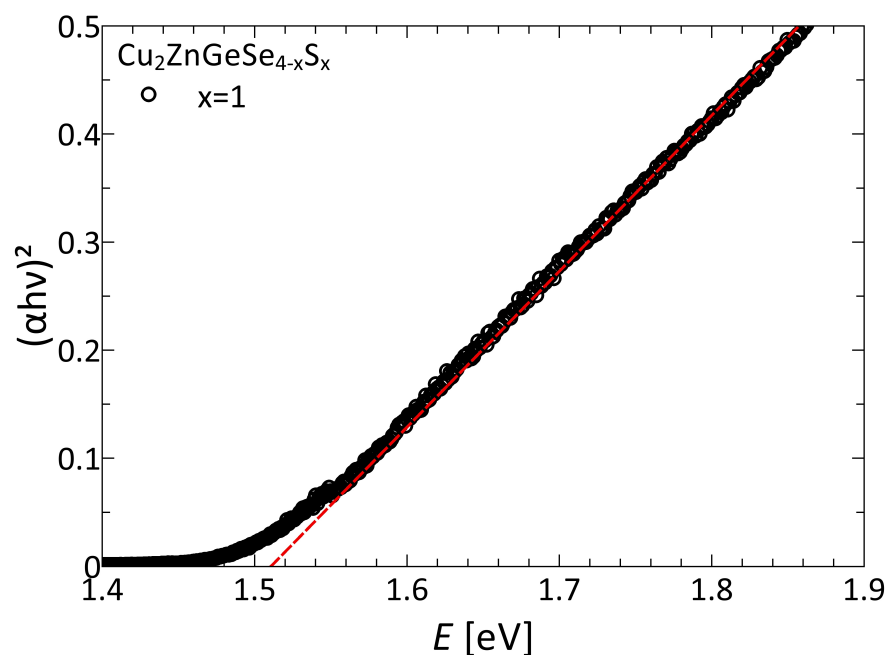


Figure (A.11) – Kubelka-Munk function of $\text{Cu}_2\text{ZnGeSe}_3\text{S}$ with an extrapolated band gap energy of 1.5 eV.

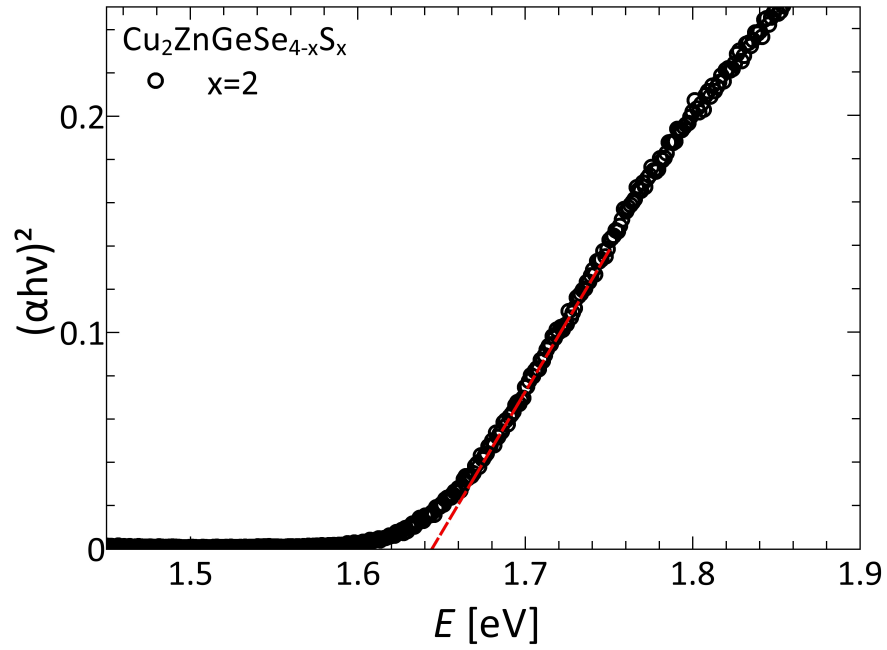


Figure (A.12) – Kubelka-Munk function of $\text{Cu}_2\text{ZnGeSe}_2\text{S}_2$ with an extrapolated band gap energy of 1.6 eV.

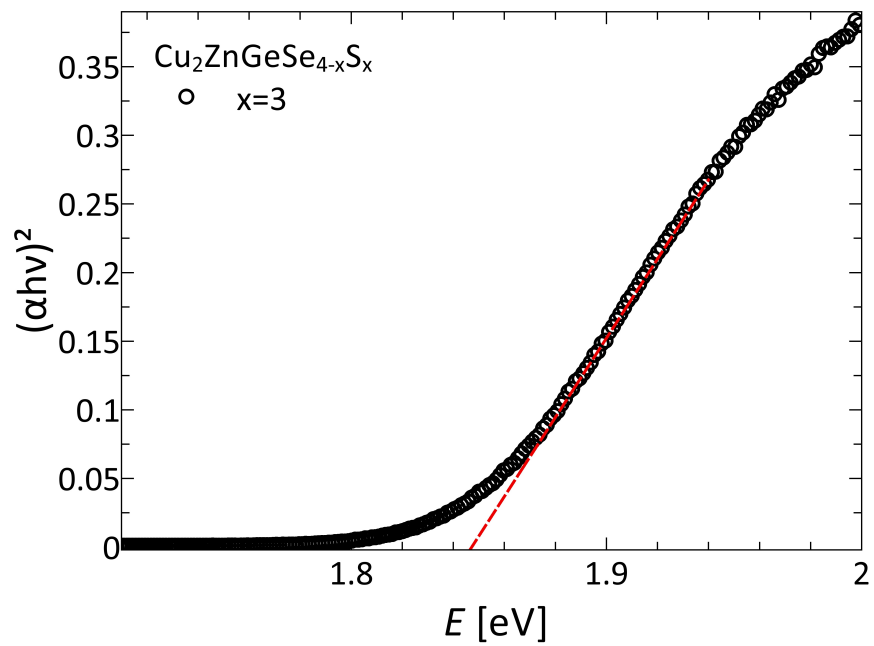


Figure (A.13) – Kubelka-Munk function of $\text{Cu}_2\text{ZnGeSeS}_3$ with an extrapolated band gap energy of 1.8 eV.

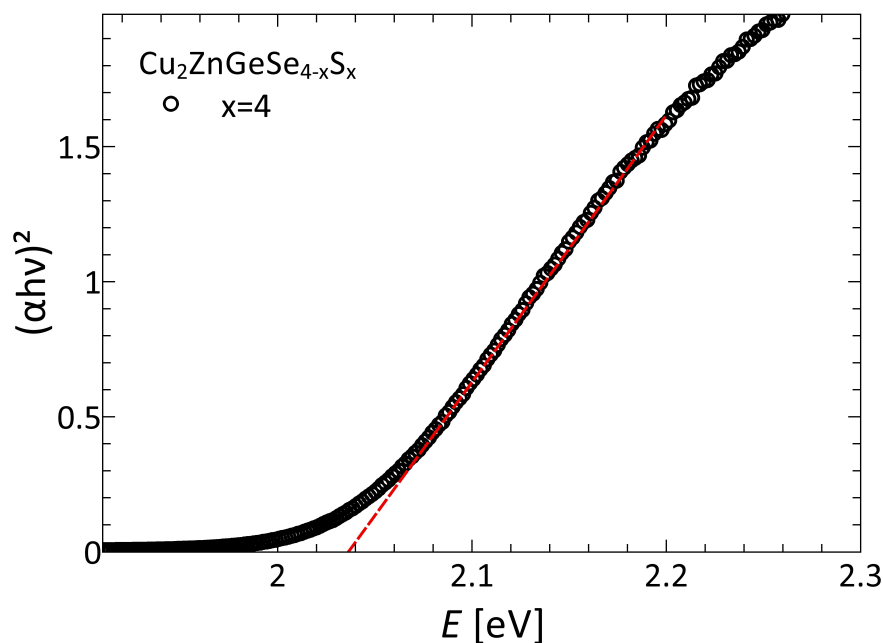


Figure (A.14) – Kubelka-Munk function of $\text{Cu}_2\text{ZnGeSe}_4$ with an extrapolated band gap energy of 2.0 eV.

A.4. Thermal Conductivity Data

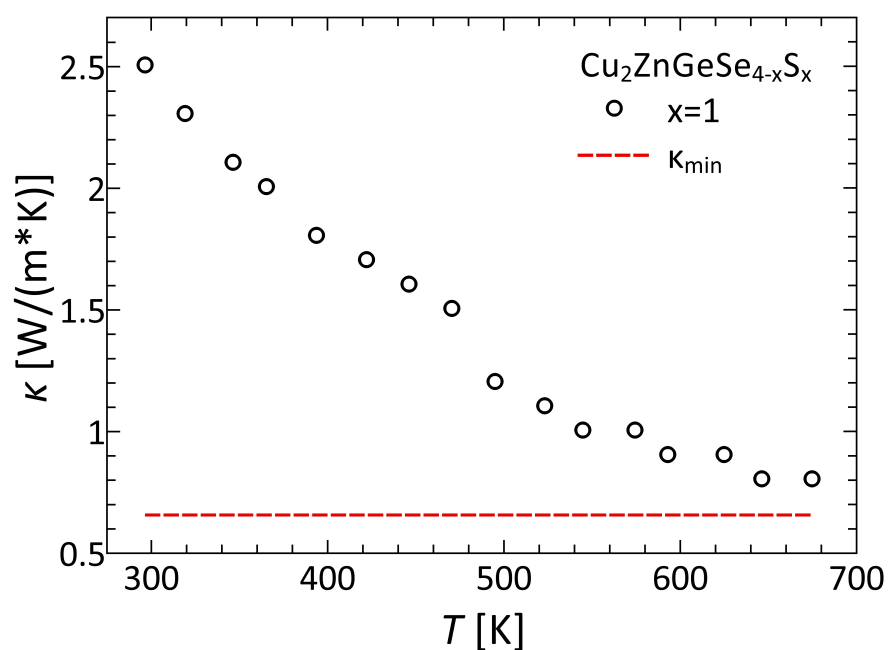


Figure (A.15) – Thermal conductivity data of $\text{Cu}_2\text{ZnGeSe}_3\text{S}$ showing the phase transition around 480 K; red dashed line represents the calculated minimal lattice thermal conductivity.

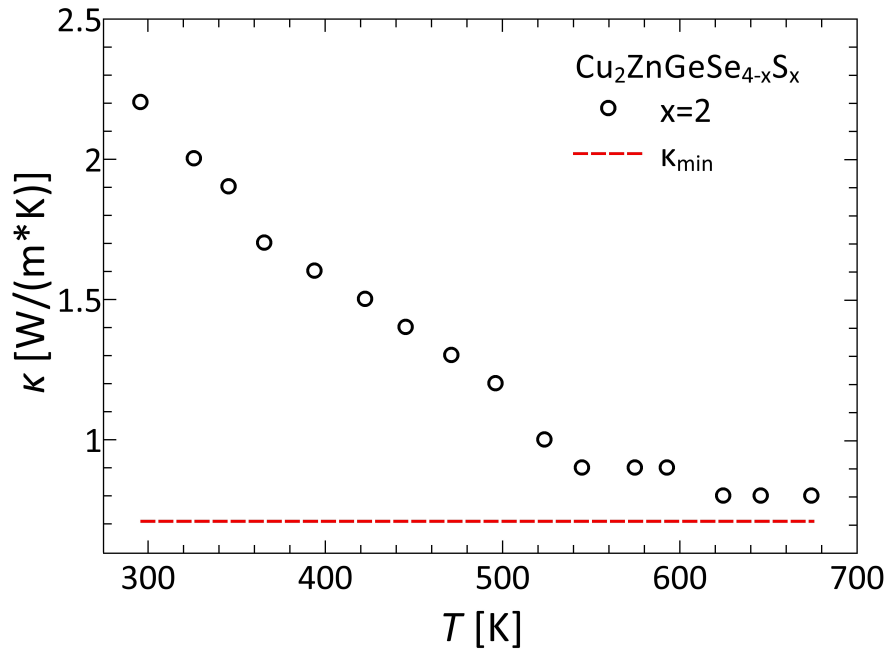


Figure (A.16) – Thermal conductivity data of $\text{Cu}_2\text{ZnGeSe}_2\text{S}_2$ showing the phase transition around 500 K; red dashed line represents the calculated minimal lattice thermal conductivity.

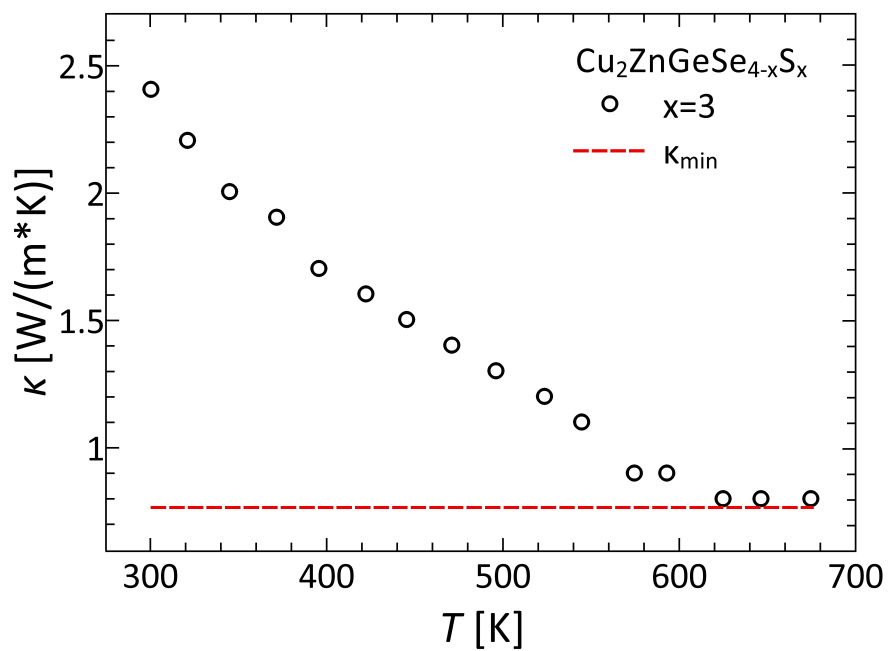


Figure (A.17) – Thermal conductivity data of $\text{Cu}_2\text{ZnGeSe}_3\text{S}_3$ showing the phase transition around 540 K; red dashed line represents the calculated minimal lattice thermal conductivity.

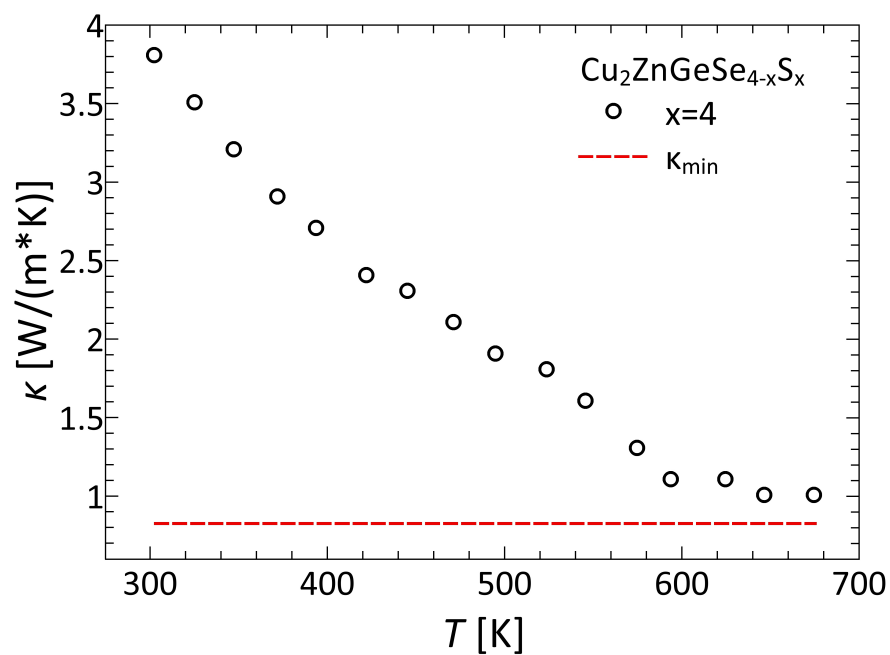


Figure (A.18) – Thermal conductivity data of $\text{Cu}_2\text{ZnGeS}_4$ showing the phase transition around 560 K; red dashed line represents the calculated minimal lattice thermal conductivity.

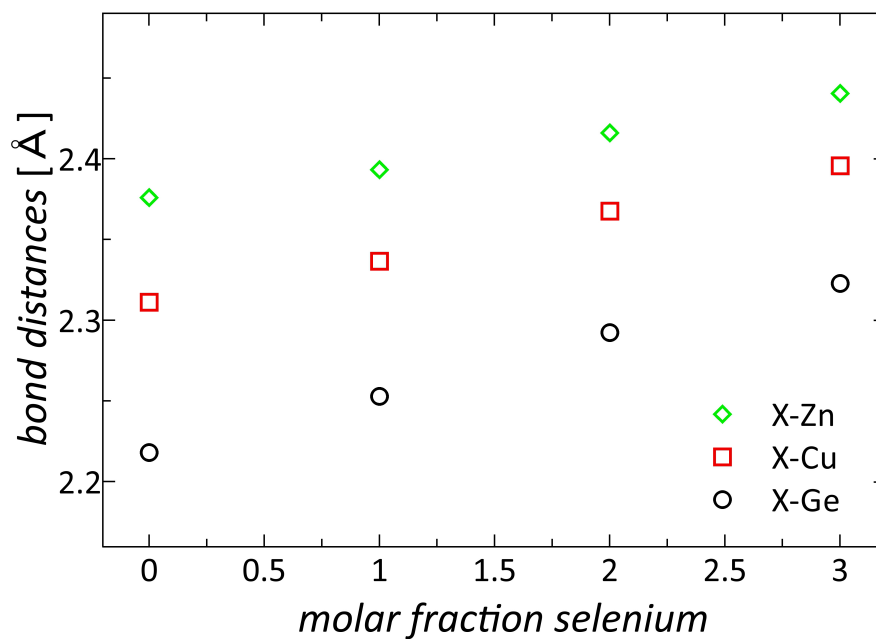


Figure (A.19) – Refined metal-chalcogen bond distances of the solid solution series $\text{Cu}_2\text{ZnGeSe}_{4-x}\text{S}_x$ with $x = 1, 2, 3, 4$ showing a linear trend of increasing bond distances with increasing molar fraction of selenium.

B

Indium-filled Skutterudites

B.1. EDX & PSM

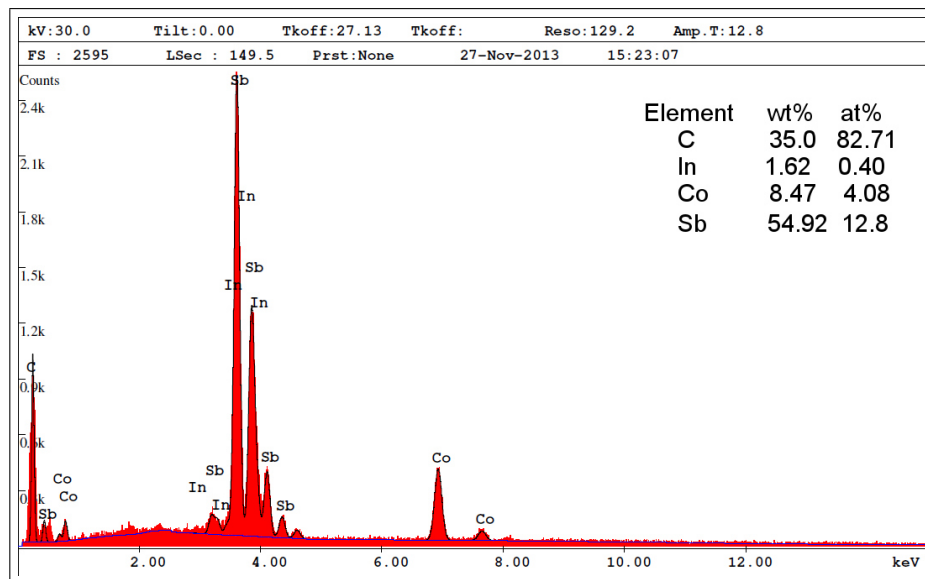


Figure (B.1) – EDX measurement of the $In_xCo_4Sb_{12}$ powder seen on Figure 3.3 left.

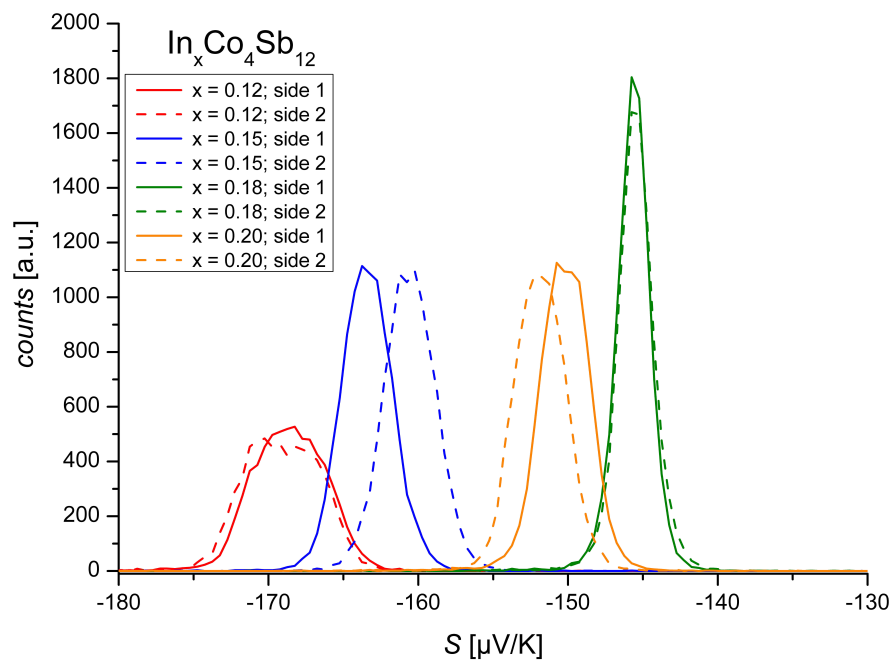


Figure (B.2) – PSM Histogram of measured Seebeck coefficients. Full and dashed lines represent measurements conducted on opposite sides of the pellet. The narrow distribution of Seebeck values corroborates with a homogeneous sample composition.

B.2. Refined Synchrotron Data

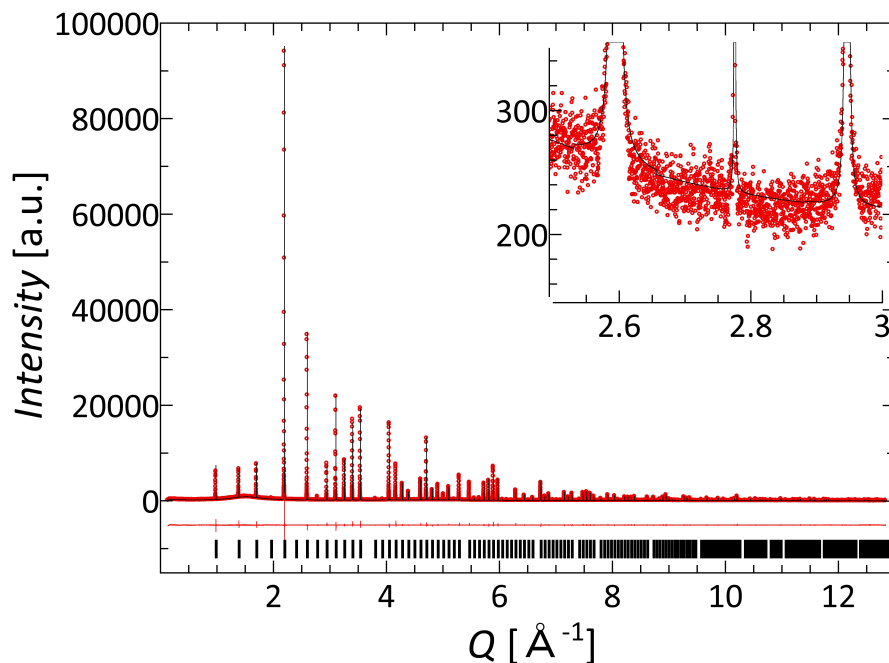


Figure (B.3) – Refined powder diffraction data for $\text{In}_{0.12}\text{Co}_4\text{Sb}_{12}$ sample (red dots), including profile fit (black solid line), and profile difference (red solid line). The refined peak positions are indicated by black tick marks.

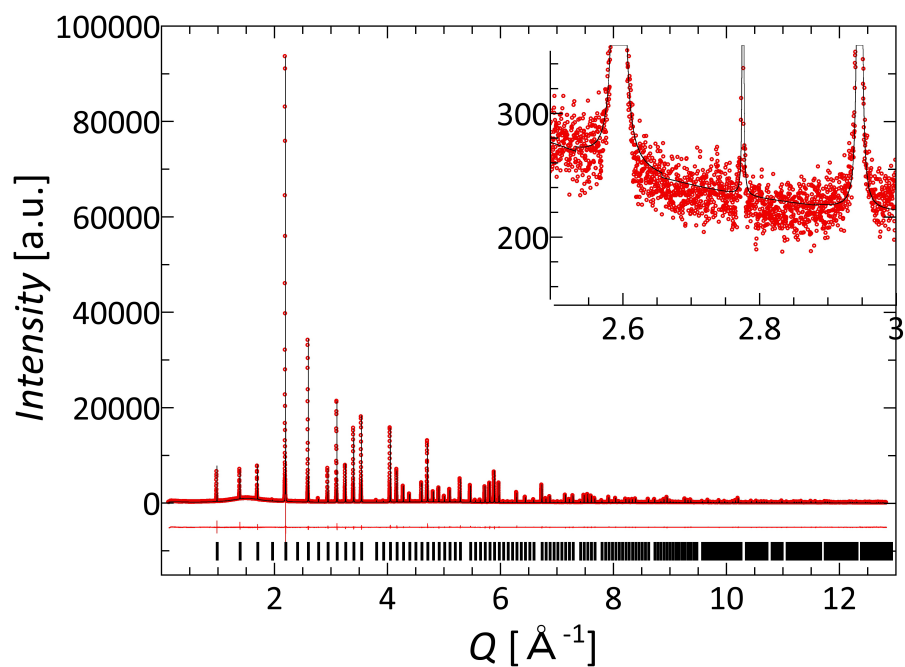


Figure (B.4) – Refined powder diffraction data for sintered $\text{In}_{0.12}\text{Co}_4\text{Sb}_{12}$ sample (red dots), including profile fit (black solid line), and profile difference (red solid line). The refined peak positions are indicated by black tick marks.

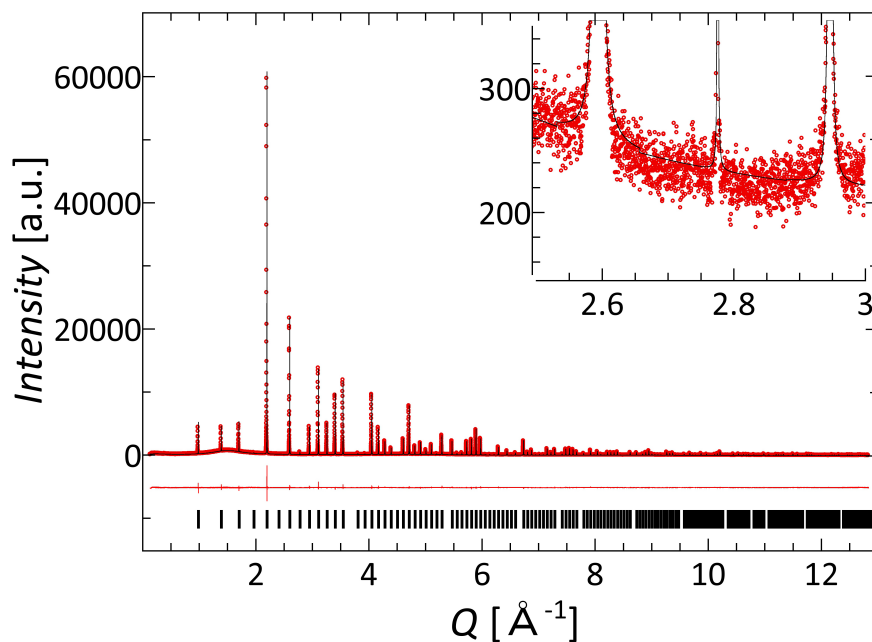


Figure (B.5) – Refined powder diffraction data for $\text{In}_{0.12}\text{Co}_4\text{Sb}_{12}$ sample (red dots) after the first thermoelectric characterization cycle, including profile fit (black solid line), and profile difference (red solid line). The refined peak positions are indicated by black tick marks.

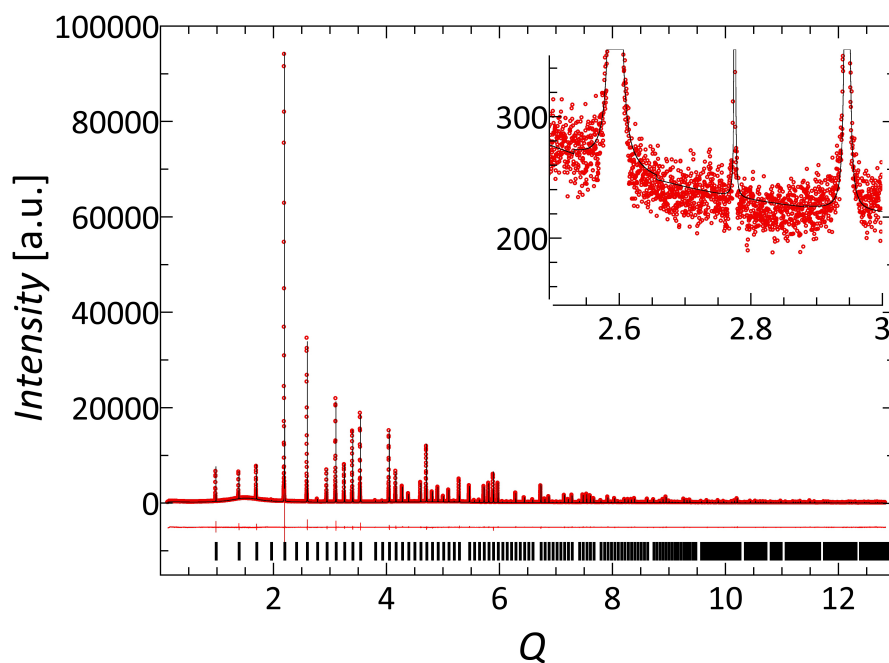


Figure (B.6) – Refined powder diffraction data for $\text{In}_{0.12}\text{Co}_4\text{Sb}_{12}$ sample (red dots) after the second thermoelectric characterization cycle, including profile fit (black solid line), and profile difference (red solid line). The refined peak positions are indicated by black tick marks.

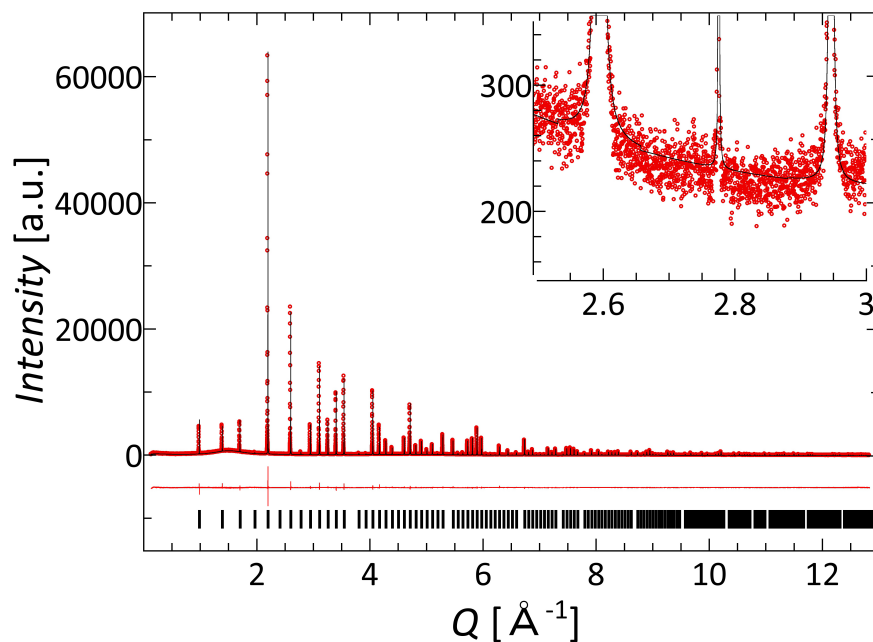


Figure (B.7) – Refined powder diffraction data for $\text{In}_{0.12}\text{Co}_4\text{Sb}_{12}$ sample (red dots) after the third thermoelectric characterization cycle, including profile fit (black solid line), and profile difference (red solid line). The refined peak positions are indicated by black tick marks.

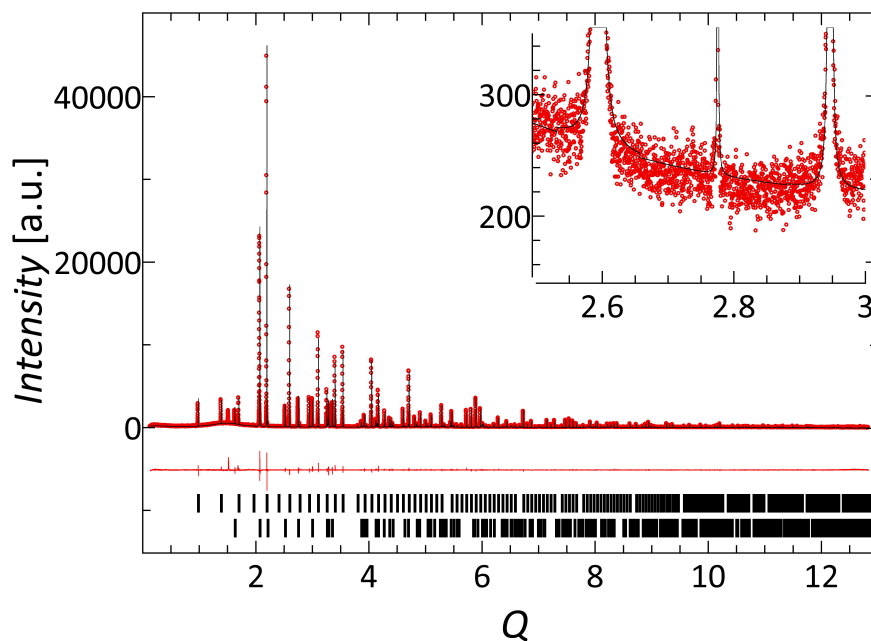


Figure (B.8) – Refined powder diffraction data for $\text{In}_{0.15}\text{Co}_4\text{Sb}_{12}$ sample (red dots), including profile fit (black solid line), and profile difference (red solid line). The refined peak positions are indicated by black tick marks.

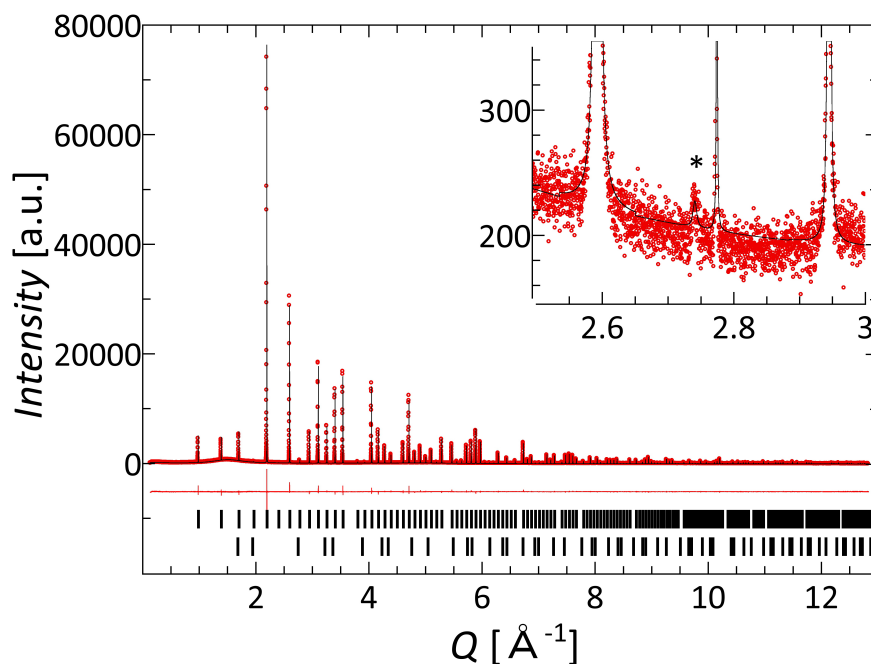


Figure (B.9) – Refined powder diffraction data for $\text{In}_{0.18}\text{Co}_4\text{Sb}_{12}$ sample (red dots), including profile fit (black solid line), and profile difference (red solid line). The refined peak positions are indicated by black tick marks (top $\text{In}_{0.18}\text{Co}_4\text{Sb}_{12}$, bottom InSb). Zoomed in image illustrates the presence of a small InSb side phase marked with an asterisk. Note the large difference in peak intensities between the skutterudite phase and the InSb side phase.

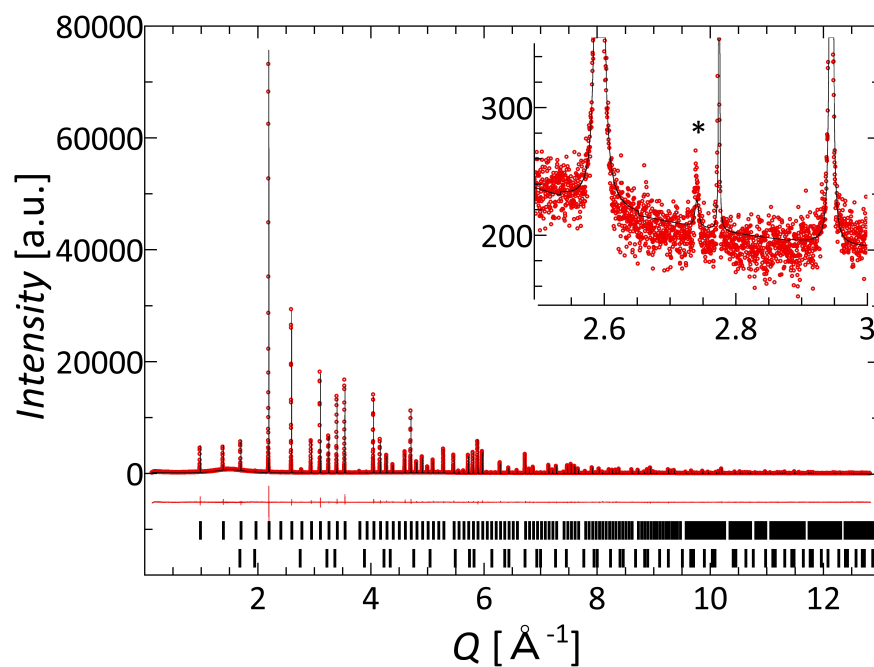


Figure (B.10) – Refined powder diffraction data for $\text{In}_{0.20}\text{Co}_4\text{Sb}_{12}$ sample (red dots), including profile fit (black solid line), and profile difference (red solid line). The refined peak positions are indicated by black tick marks (top $\text{In}_{0.20}\text{Co}_4\text{Sb}_{12}$, bottom InSb). Zoomed in image illustrates the presence of a small InSb side phase marked with an asterisk. Note the large difference in peak intensities between the skutterudite phase and the InSb side phase.

B.3. ^{121}Sb -Mössbauer Spectra

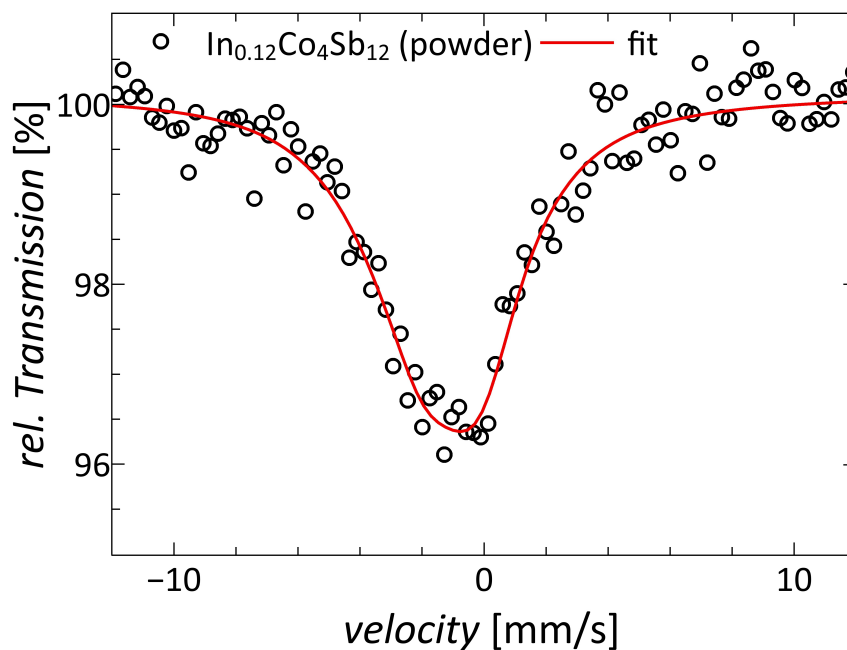


Figure (B.11) – ^{121}Sb Mössbauer spectrum of $\text{In}_{0.12}\text{Co}_4\text{Sb}_{12}$ powder before consolidation and thermal cycling.

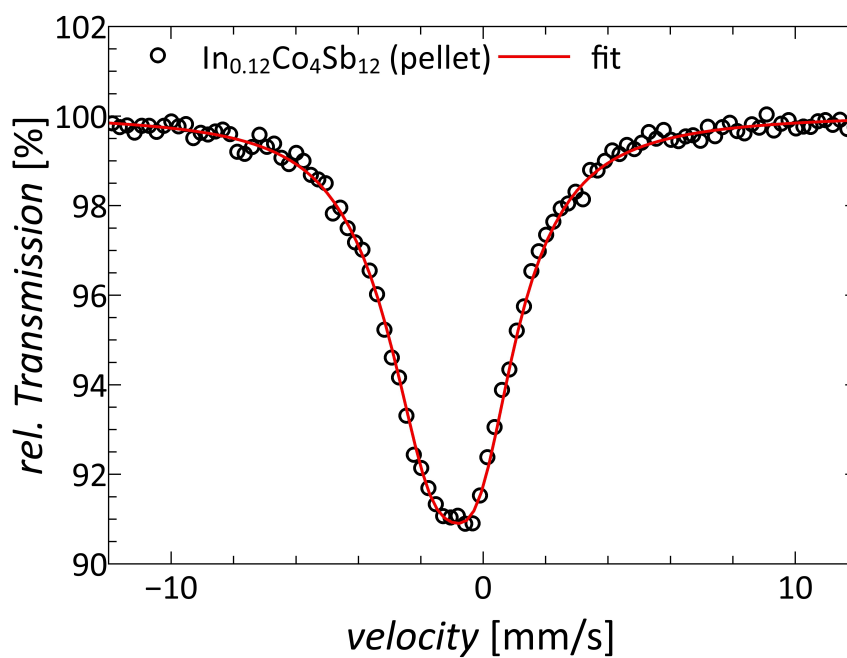


Figure (B.12) – ^{121}Sb Mössbauer spectrum of the $\text{In}_{0.12}\text{Co}_4\text{Sb}_{12}$ pellet after consolidation and thermal cycling.

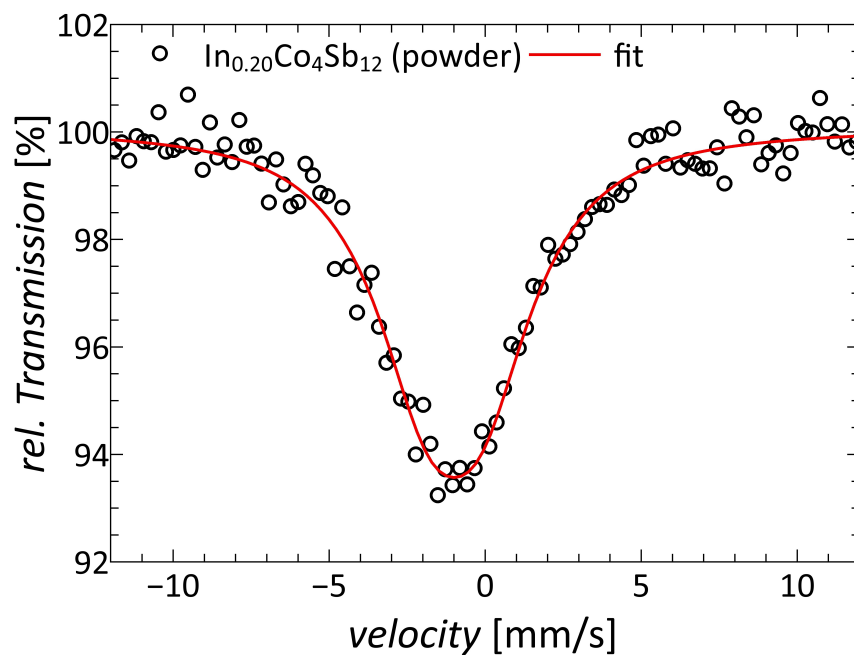


Figure (B.13) – ^{121}Sb Mößbauer spectrum of $\text{In}_{0.20}\text{Co}_4\text{Sb}_{12}$ powder before consolidation and thermal cycling.

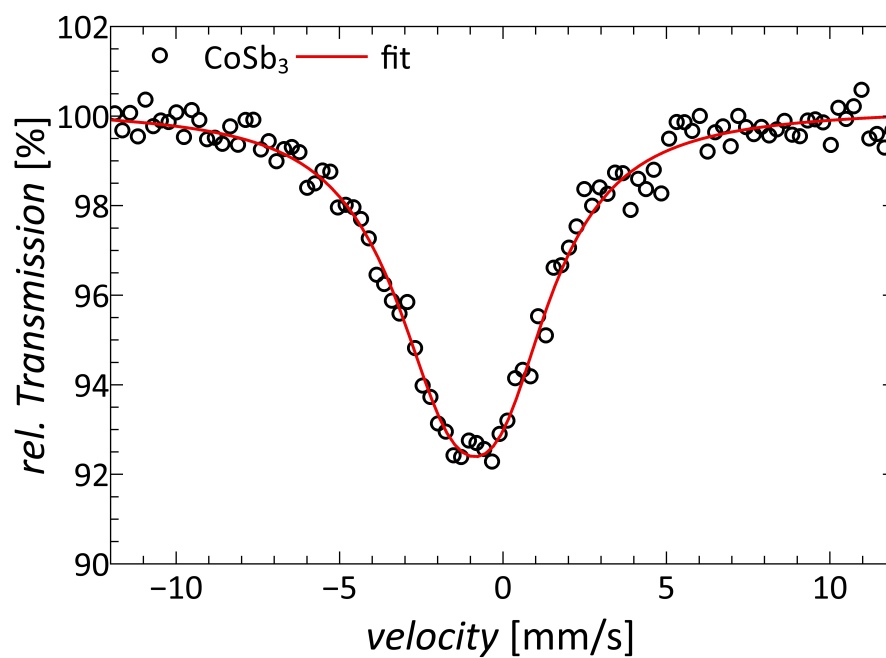


Figure (B.14) – ^{121}Sb Mößbauer spectrum of CoSb_3 before consolidation and thermal cycling.

B.4. Thermoelectric Transport Data

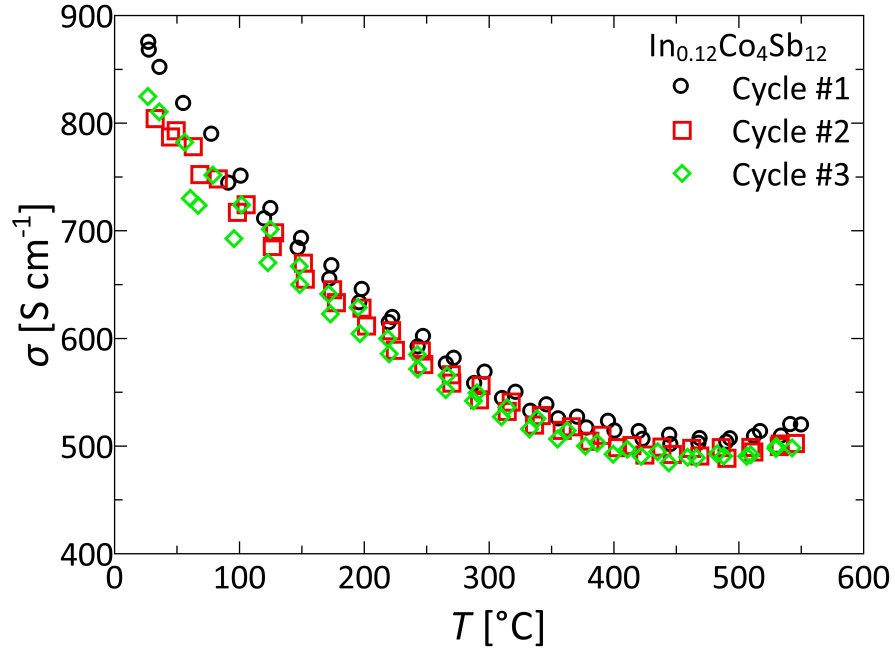


Figure (B.15) – Temperature dependence of subsequent electrical conductivity measurement cycles of the sample with nominal composition $\text{In}_{0.12}\text{Co}_4\text{Sb}_{12}$, illustrating a subtle degradation of the electric conductivity with increasing number of thermal cycles.

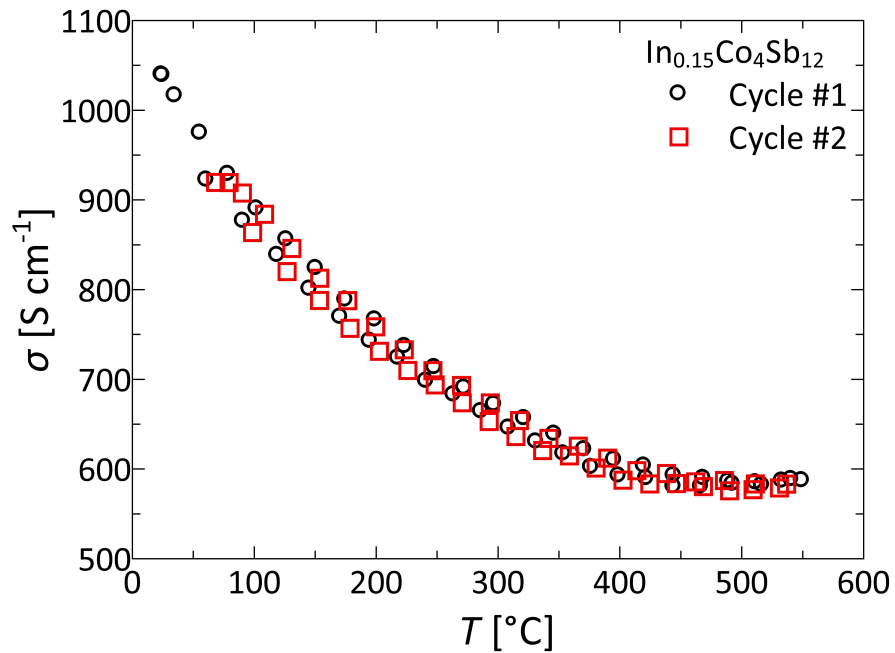


Figure (B.16) – Temperature dependence of subsequent electrical conductivity measurement cycles of the sample with nominal composition $\text{In}_{0.15}\text{Co}_4\text{Sb}_{12}$, illustrating a subtle degradation of the electric conductivity with increasing number of thermal cycles.

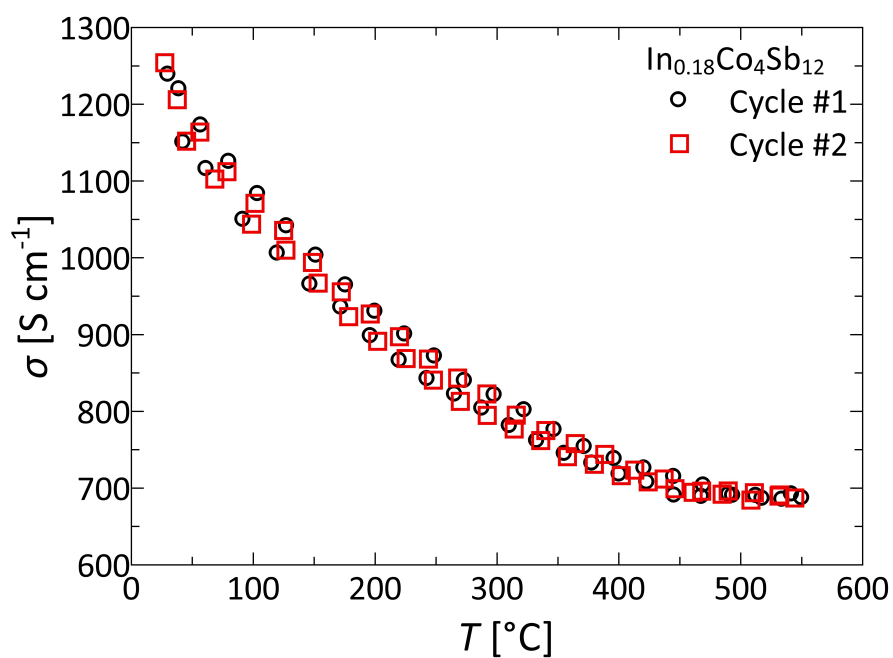


Figure (B.17) – Temperature dependence of subsequent electrical conductivity measurement cycles of the sample with nominal composition $\text{In}_{0.18}\text{Co}_4\text{Sb}_{12}$, illustrating a subtle degradation of the electric conductivity with increasing number of thermal cycles.

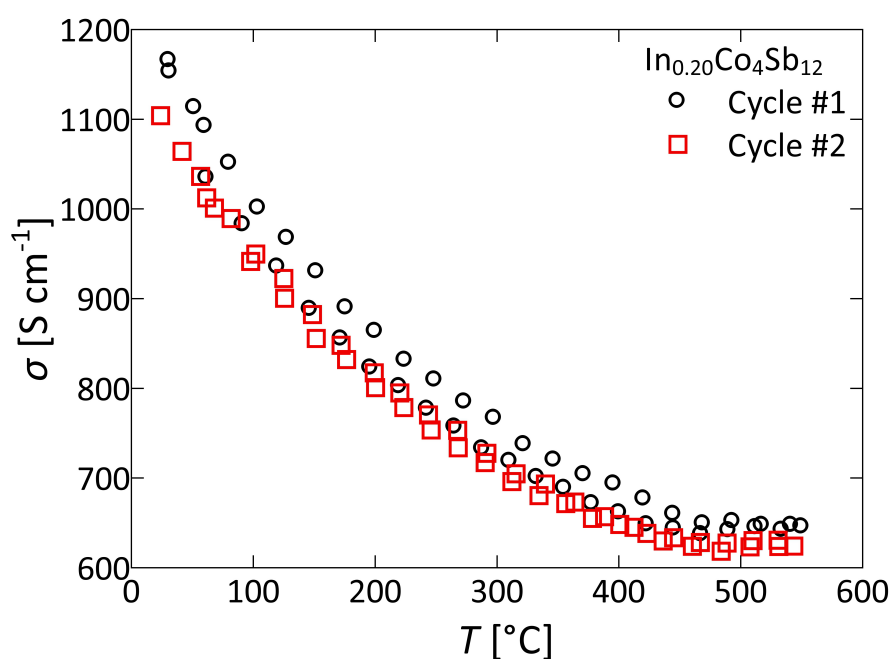


Figure (B.18) – Temperature dependence of subsequent electrical conductivity measurement cycles of the sample with nominal composition $\text{In}_{0.20}\text{Co}_4\text{Sb}_{12}$, illustrating a subtle degradation of the electric conductivity with increasing number of thermal cycles.

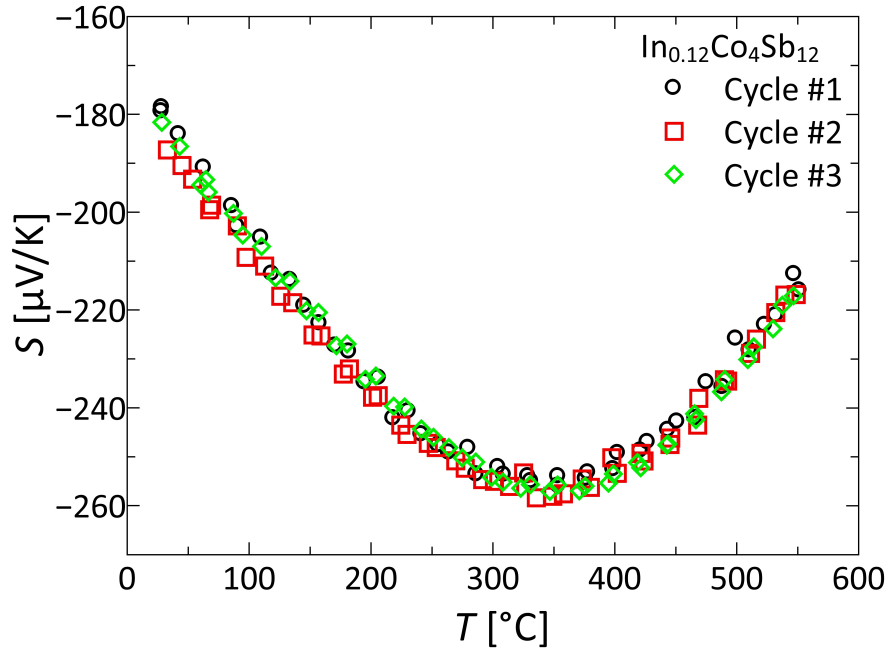


Figure (B.19) – Temperature dependence of subsequent Seebeck coefficient measurement cycles of $\text{In}_{0.12}\text{Co}_4\text{Sb}_{12}$. With increasing thermal cycling a subtle deterioration of the Seebeck coefficients can be seen.

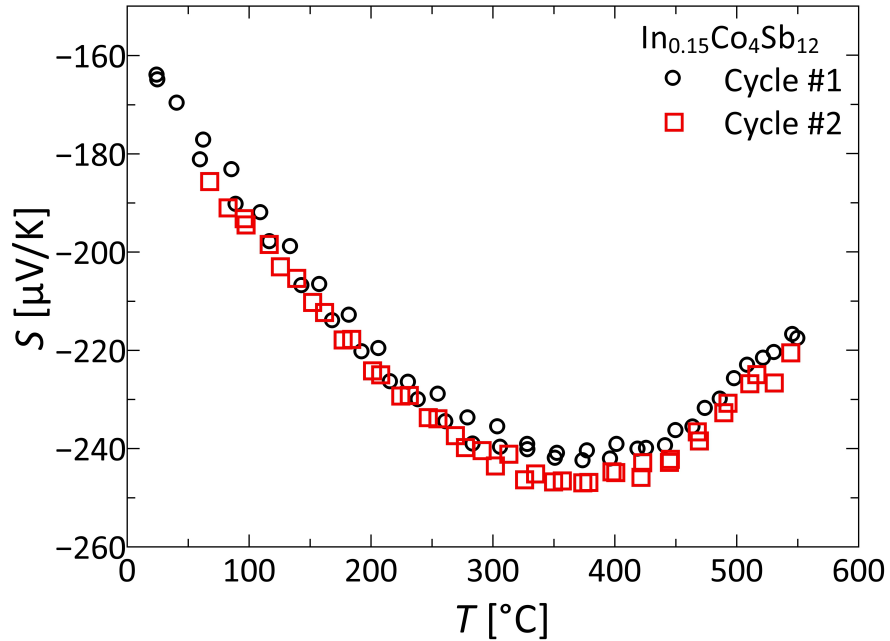


Figure (B.20) – Temperature dependence of subsequent Seebeck coefficient measurement cycles of $\text{In}_{0.15}\text{Co}_4\text{Sb}_{12}$. With increasing thermal cycling a subtle deterioration of the Seebeck coefficients can be seen.

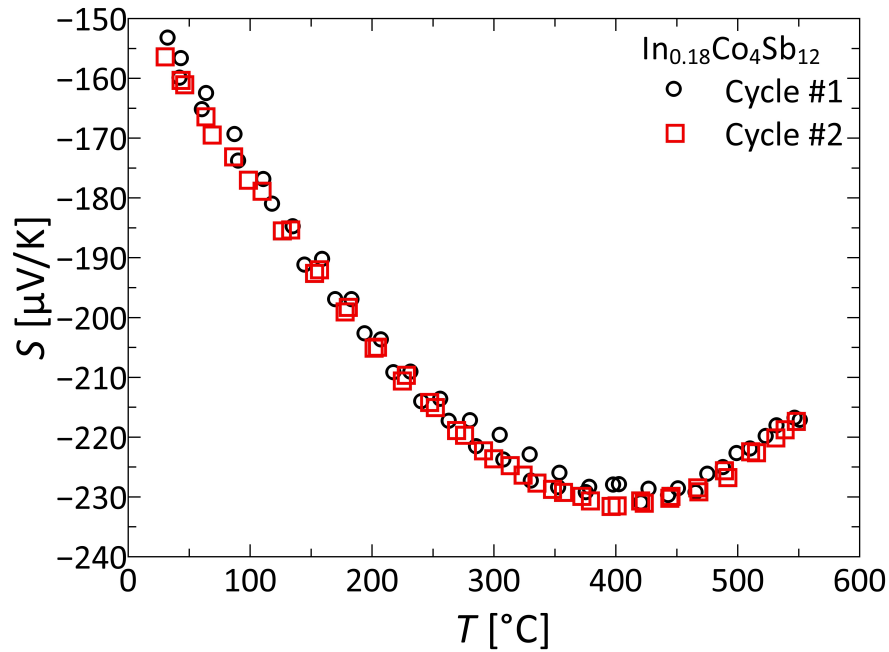


Figure (B.21) – Temperature dependence of subsequent Seebeck coefficient measurement cycles of $\text{In}_{0.18}\text{Co}_4\text{Sb}_{12}$. With increasing thermal cycling a subtle deterioration of the Seebeck coefficients can be seen.

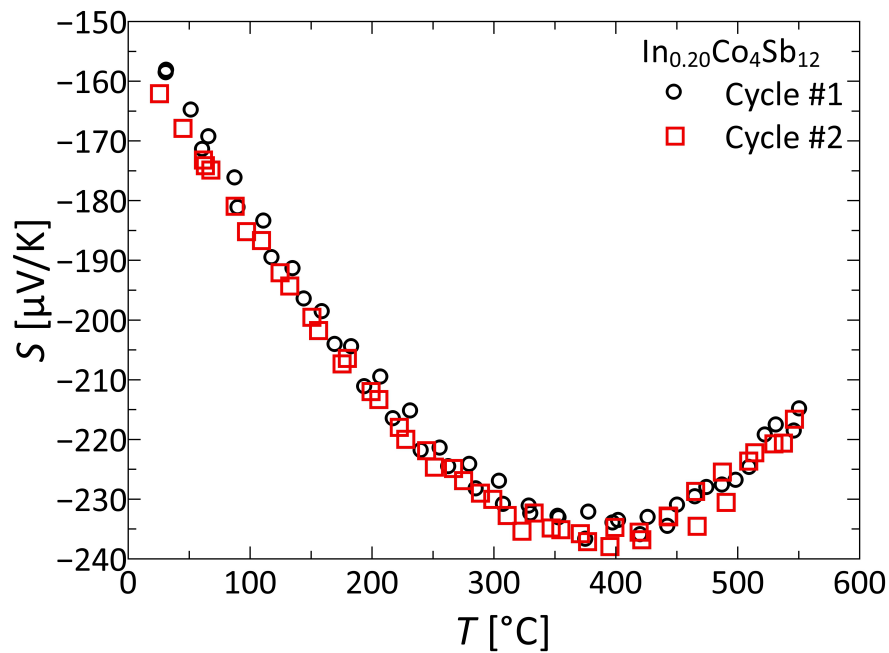


Figure (B.22) – Temperature dependence of subsequent Seebeck coefficient measurement cycles of $\text{In}_{0.20}\text{Co}_4\text{Sb}_{12}$. With increasing thermal cycling a subtle deterioration of the Seebeck coefficients can be seen.

B.5. Nanoparticle Synthesis

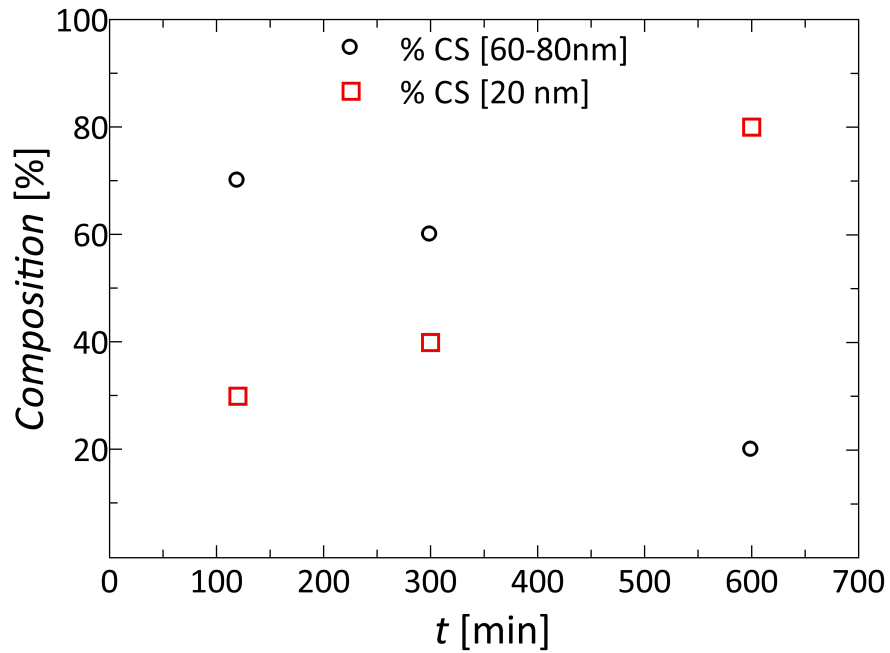


Figure (B.23) – Refined crystallite size distribution in dependence of the milling time. After 2, 5, and 10 h milling time powder samples were taken for X-ray diffraction. Two different crystallite sizes were used in the Rietveld refinement to obtain an approximation of the crystallite size distribution. The first crystallite size converged to 20 nm, whereas the second crystallite size converged to sizes between 60-80 nm.

C.1. Refined X-ray Diffraction Data

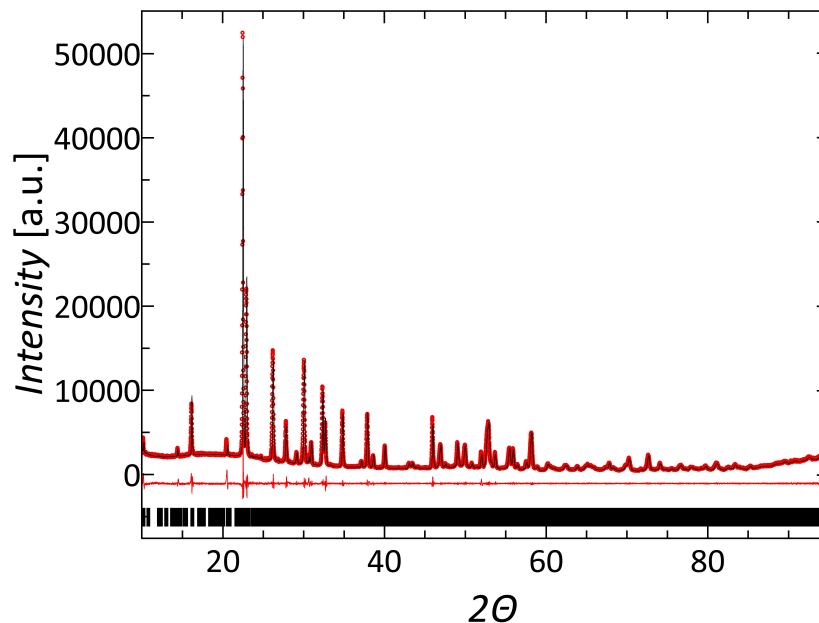


Figure (C.2) – Le Bail fit for the powder diffraction data of $Nb_{7.925}W_{9.075}O_{47}$ (red dots), including profile fit (black solid line), and profile difference (red solid line). The refined peak positions are indicated by black tick marks.

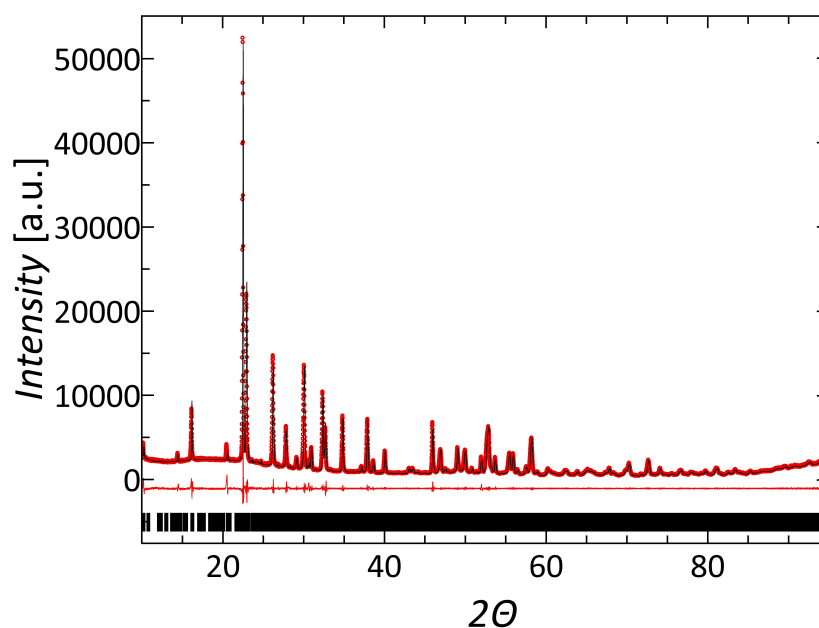


Figure (C.3) – Le Bail fit for the powder diffraction data of $Nb_{7.9}W_{9.1}O_{47}$ (red dots), including profile fit (black solid line), and profile difference (red solid line). The refined peak positions are indicated by black tick marks.

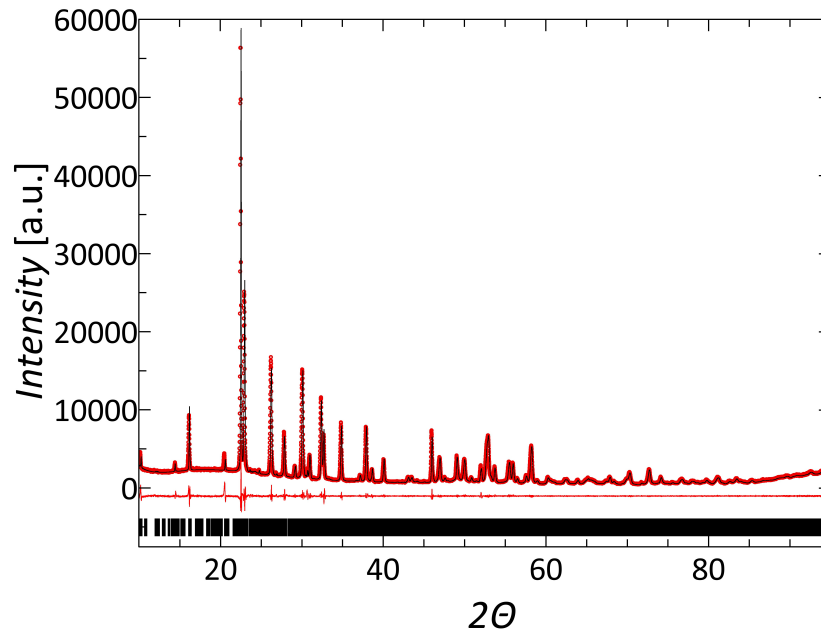


Figure (C.4) – Le Bail fit for the powder diffraction data of $\text{Nb}_7\text{W}_{10}\text{O}_{47}$ (red dots), including profile fit (black solid line), and profile difference (red solid line). The refined peak positions are indicated by black tick marks.

C.2. SEM and HR-TEM Images

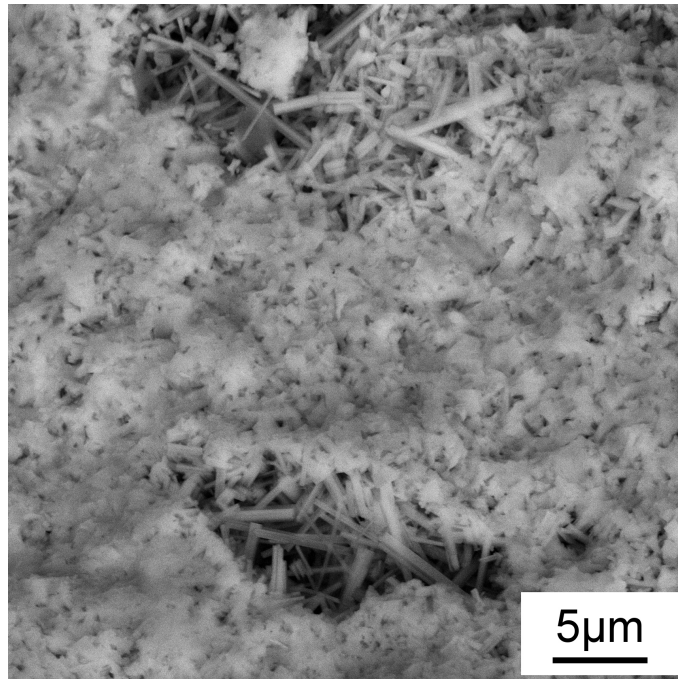


Figure (C.5) – Zoomed-in SEM image of cavities in shot-time sintered tetragonal tungsten bronzes. The sintering process lead to a random orientation of the prismatic crystals similar to a compressed haystack.

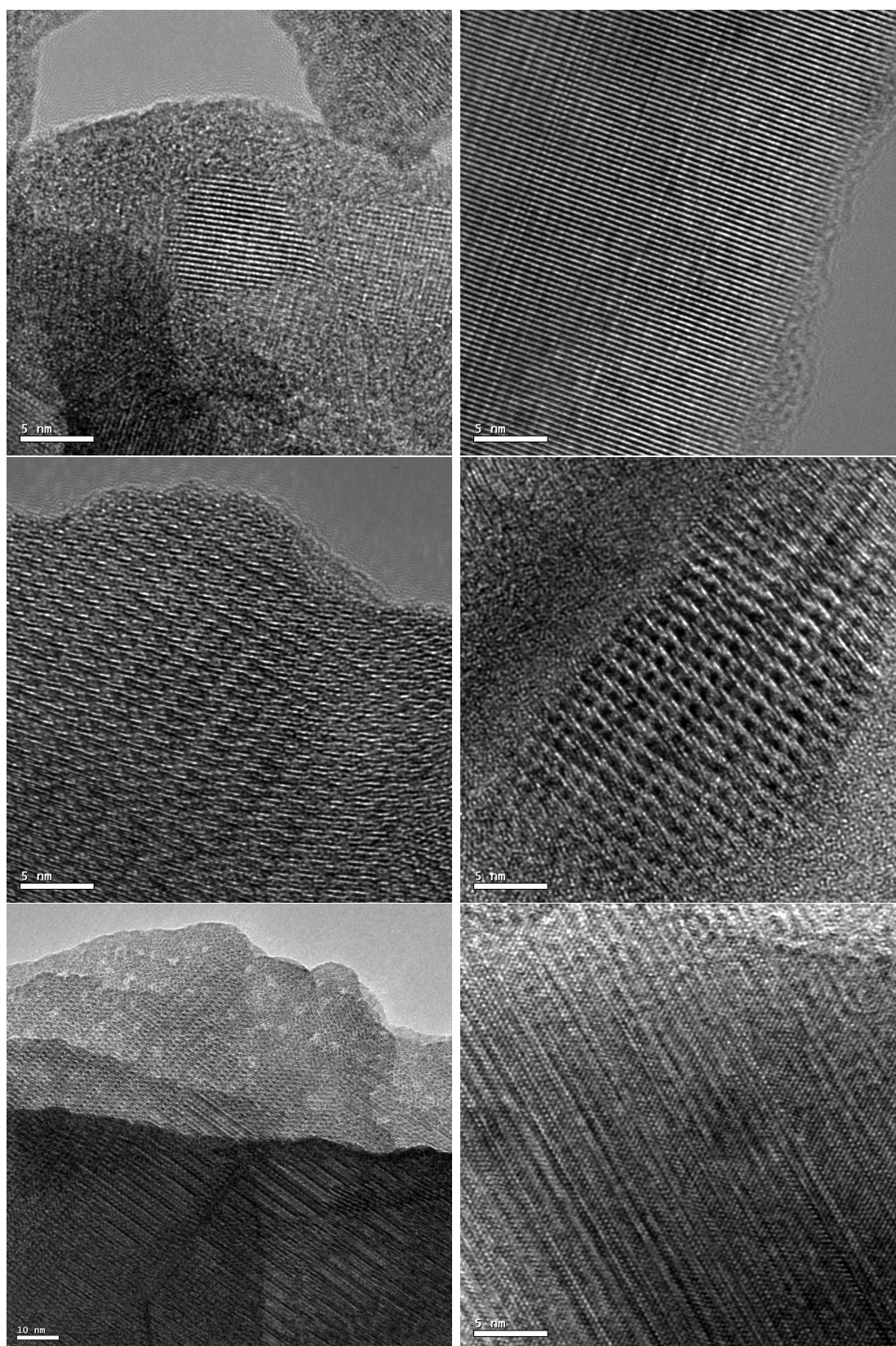


Figure (C.6) – High resolution transmission electron microscopy images, illustrating the diversity of different Wadsley defects, CS planes, and grain sizes found in the sintered TTB samples.

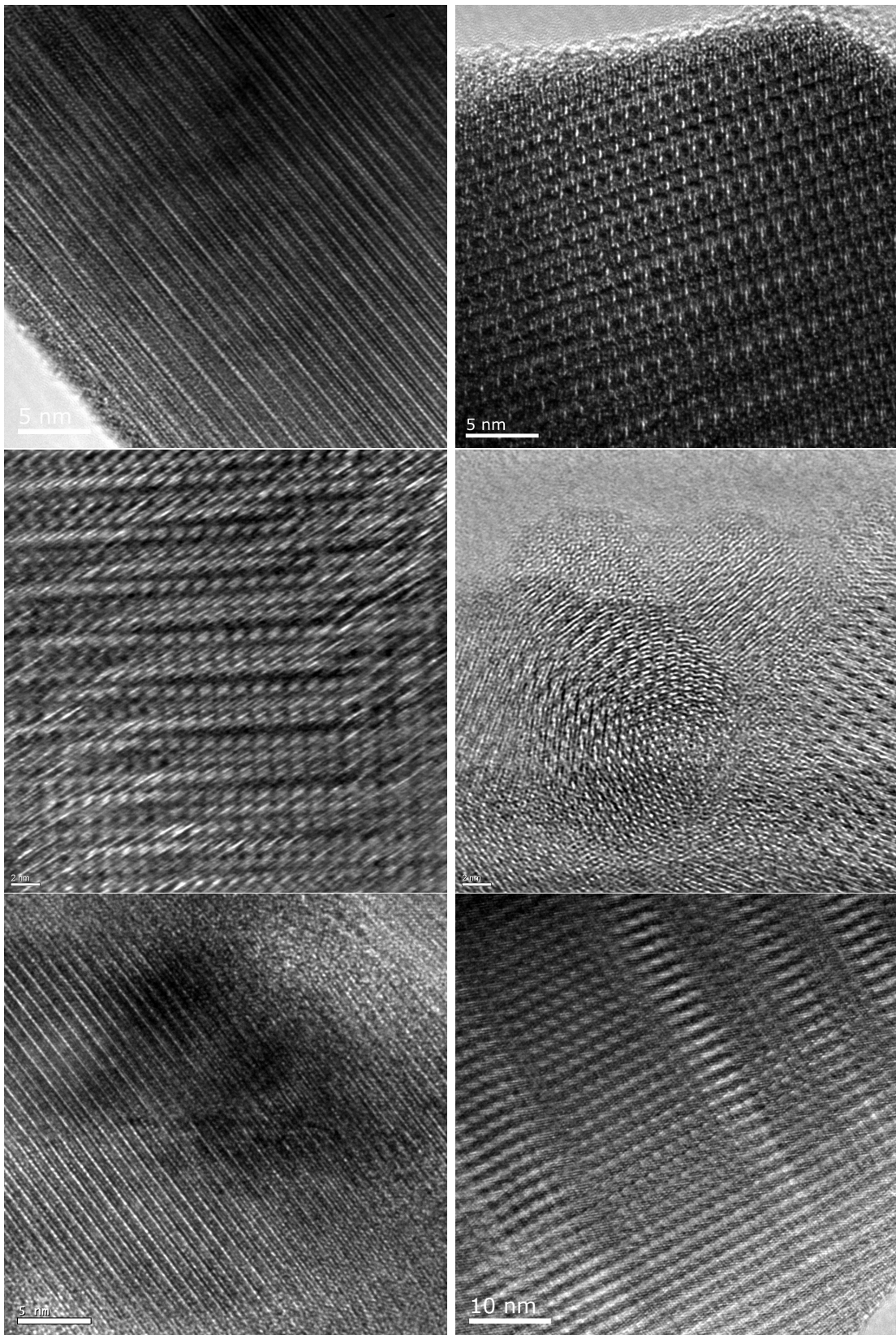


Figure (C.7) – High resolution transmission electron microscopy images, illustrating the diversity of different Wadsley defects, CS planes, and grain sizes found in the sintered TTB samples.

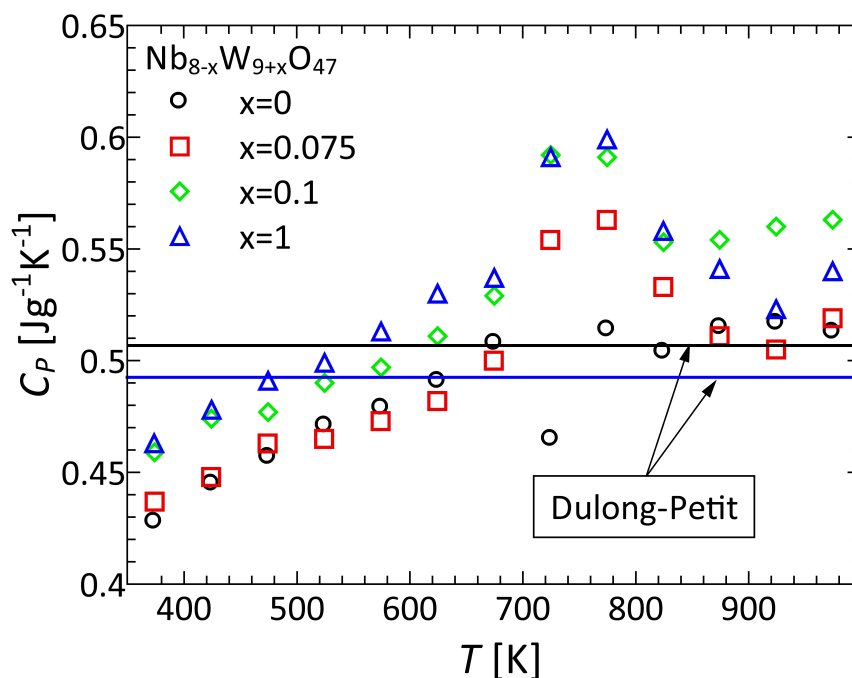


Figure (C.9) – Temperature dependent heat capacity (C_p) of $Nb_{8-x}W_{9+x}O_{47}$ with $x = 0, 0.075, 0.1,$ and 1 . Strait lines represent the calculated Dulong-Petit approximation.

C.3. Thermal Stability and TE Properties

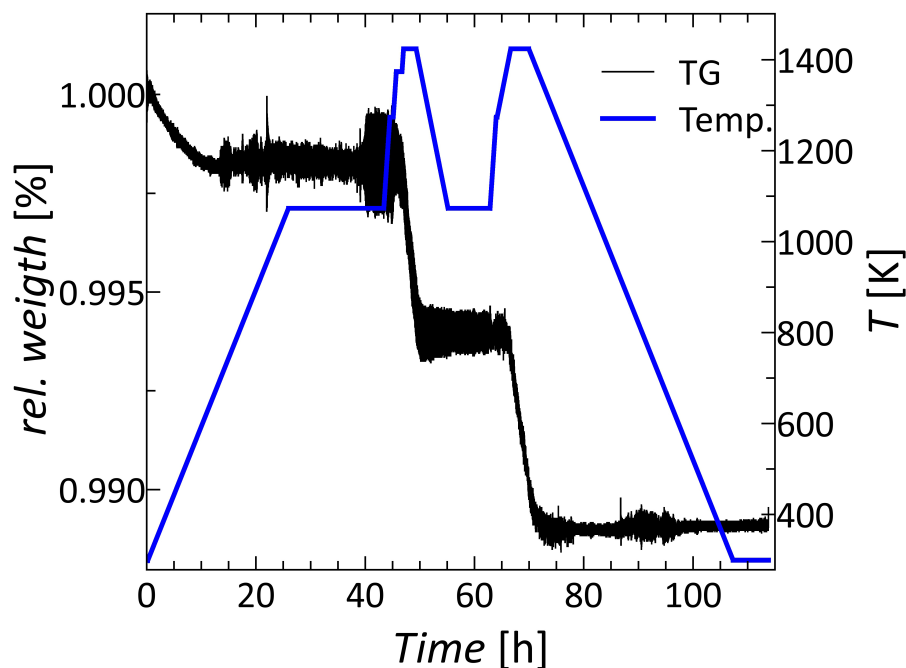


Figure (C.8) – Thermal stability of $Nb_8W_9O_{47}$ under varying pO_2 . Relative weight of $Nb_8W_9O_{47}$ as a function of time with corresponding temperature profile.

Bibliography

- [1] DiSalvo, F. J. *Science* **1999**, *285*, 703–706.
- [2] Bell, L. E. *Science* **2008**, *321*, 1457–61.
- [3] Snyder, G.; Toberer, E. S. *Nature Materials* **2008**, *7*, 105–114.
- [4] Tritt, T. M.; Subramanian, M. A. *MRS Bulletin* **2011**, *31*, 188–198.
- [5] Abelson, R. *CRC Thermoelectrics Handbook - Macro to Nano (Chapter 56)*, 2nd ed.; Taylor & Francis: London, 2006.
- [6] MacDonald, D. *Thermoelectricity - An Introduction to the Principles*; Dover Publications: London, 2006.
- [7] Seebeck, T. J. *Annalen der Physik* **1826**, *82*, 253–286.
- [8] Wood, C. *Reports on progress in physics* **1988**, *51*, 459–539.
- [9] Goldsmid, H. J. *Application of Thermoelectricity*; Butler & Tanner Ltd: London, 1960.
- [10] Goldsmid, H. J. *Thermoelectric Refrigeration*; Plenum Press: New York, 1964.
- [11] Rowe, D. *Thermoelectrics Handbook - Macro to Nano*, 2nd ed.; CRC Press, Boca Raton, 2006; pp 1–954.
- [12] Peltier, J. C. A. *Annales de Chimie et de Physique* **1834**, LVI:371–387.
- [13] Thomson, W. *Proceedings of the Royal Society of Edinburgh* **1851**, III:91–98.
- [14] Ashcroft, N.; Mermin, N. *Solid State Physics*; Thomson Learning Inc.: United States of America, 1976.
- [15] Göpel, W.; Wiemhöfer, H.-D. *Statistische Thermodynamik*; Spektrum Akademischer Verlag: Heidelberg, 2000.
- [16] May, A. F. Ph.D. thesis, California Institute of Technology, 2010.
- [17] Cox, P. *The electronic structure and properties of solids*; Oxford University Press: New York, 1987.

Bibliography

- [18] Fistul, V. *Heavily Doped Semiconductors*; Plenum Press: New York, 1969.
- [19] Sootsman, J. R.; Chung, D. Y.; Kanatzidis, M. G. *Angewandte Chemie* **2009**, *48*, 8616–39.
- [20] Franz, R.; Wiedemann, G. *Annalen der Physik und Chemie* **1853**, *165*, 497–531.
- [21] Goldsmid, H. J. *Introduction to Thermoelectricity*; Springer Berlin Heidelberg: Berlin, Heidelberg, 2010; Vol. 121.
- [22] Lorenz, L. *Annalen der Physik und Chemie* **1872**, *223*, 429–452.
- [23] Tritt, T. *Thermal Conductivity. Theory, Properties and Applications*; Kluwer Academic: New York, 2004.
- [24] Kittel, C. *Einführung in die Festkörperphysik*, 14th ed.; John Wiley & Sons: New York, 2005.
- [25] Slack, G. *CRC Handbook of Thermoelectrics*; CRC Press: Boca Raton, 1995; p 407.
- [26] Toberer, E. S.; Zevalkink, A.; Snyder, G. J. *Journal of Materials Chemistry* **2011**, *21*, 15843.
- [27] Elliott, S. *The Physics and Chemistry of Solids*; John Wiley & Sons: Chichester, 1998.
- [28] Steigmeier, E.; Abeles, B. *Physical Review* **1964**, *136*, A1149–A1155.
- [29] Soma, T. *Solid State Communications* **1980**, *34*, year.
- [30] Venkatasubramanian, R.; Siivola, E.; Colpitts, T.; O’Quinn, B. *Nature* **2001**, *413*, 597–602.
- [31] Hsu, K. F.; Loo, S.; Guo, F.; Chen, W.; Dyck, J. S.; Uher, C.; Hogan, T.; Polychroniadis, E. K.; Kanatzidis, M. G. *Science* **2004**, *303*, 818–21.
- [32] Biswas, K.; He, J.; Blum, I. D.; Wu, C.-I.; Hogan, T. P.; Seidman, D. N.; Dravid, V. P.; Kanatzidis, M. G. *Nature* **2012**, *489*, 414–8.
- [33] Goldsmid, H.; Penn, A. *Physics Letters A* **1968**, *27*, 523–524.
- [34] Chen, N.; Gascoin, F.; Snyder, G.; Müller, E.; Karpinski, G.; Stiewe, C. *Applied Physics Letters* **2005**, *87*, 171903.

- [35] Yang, J.; Meisner, G. P.; Chen, L. *Applied Physics Letters* **2004**, *85*, 1140.
- [36] Meisner, G.; Morelli, D.; Hu, S.; Yang, J.; Uher, C. *Physical Review Letters* **1998**, *80*, 3551–3554.
- [37] Zhou, Z.; Uher, C.; Jewell, A.; Caillat, T. *Physical Review B* **2005**, *71*, 235209.
- [38] Alekseeva, G.; Efimova, B.; Ostrovsk, L. M.; Serebrya, O. S.; Tsy-pin, M. *Sov. Phys. Semicond.* **1971**, *4*, 1122.
- [39] Abeles, B. *Physical Review* **1963**, *131*, 1906–1911.
- [40] Heinrich, C. P.; Day, T. W.; Zeier, W.; Snyder, G.; Tremel, W. *Journal of the American Chemical Society* **2014**, *136*, 442–8.
- [41] Wang, H.; LaLonde, A. D.; Pei, Y.; Snyder, G. *Advanced Functional Materials* **2013**, *23*, 1586–1596.
- [42] Callaway, J.; von Baeyer, H. *Physical Review* **1960**, *120*, 1149–1154.
- [43] Cahill, D. G.; Watson, S.; Pohl, R. *Physical Review B* **1992**, *46*, 6131–6140.
- [44] Altenkirch, E. *Physikalische Zeitschrift* **1909**, *20*, 560–568.
- [45] Altenkirch, E. *Physikalische Zeitschrift* **1911**, *12*, 920–924.
- [46] LaLonde, A. D.; Pei, Y.; Wang, H.; Jeffrey Snyder, G. *Materials Today* **2011**, *14*, 526–532.
- [47] Snyder, G.; Ursell, T. *Physical Review Letters* **2003**, *91*, 1–4.
- [48] Toberer, E. S.; May, A. F.; Snyder, G. *Chemistry of Materials* **2010**, *22*, 624–634.
- [49] Hamid Elsheikh, M.; Shnawah, D. A.; Sabri, M. F. M.; Said, S. B. M.; Haji Hassan, M.; Ali Bashir, M. B.; Mohamad, M. *Renewable and Sustainable Energy Reviews* **2014**, *30*, 337–355.
- [50] Mahan, G. D.; Sofo, J. O. *Proceedings of the National Academy of Sciences of the United States of America* **1996**, *93*, 7436–9.
- [51] Wang, H.; Pei, Y.; LaLonde, A. D.; Snyder, G. J. *Proceedings of the National Academy of Sciences of the United States of America* **2012**, *109*, 9705–9.

Bibliography

- [52] Pei, Y.; Heinz, N. a.; LaLonde, A.; Snyder, G. J. *Energy & Environmental Science* **2011**, *4*, 3640.
- [53] Pei, Y.; LaLonde, A. D.; Wang, H.; Snyder, G. *Energy & Environmental Science* **2012**, *5*, 7963.
- [54] Heremans, J.; Wiendlocha, B.; Chamoire, A. M. *Energy & Environmental Science* **2012**, *5*, 5510.
- [55] Zeier, W.; Day, T.; Schechtel, E.; Snyder, G.; Tremel, W. *Functional Materials Letters* **2013**, *06*, 1340010.
- [56] Heremans, J.; Jovovic, V.; Toberer, E. S.; Saramat, A.; Kurosaki, K.; Charoenphakdee, A.; Yamanaka, S.; Snyder, G. J. *Science (New York, N.Y.)* **2008**, *321*, 554–7.
- [57] Pei, Y.; Wang, H.; Snyder, G. J. *Advanced Materials* **2012**, *24*, 6125–35.
- [58] Pei, Y.; Shi, X.; LaLonde, A.; Wang, H.; Chen, L.; Snyder, G. *Nature* **2011**, *473*, 66–69.
- [59] Medlin, D.; Snyder, G. *Current Opinion in Colloid & Interface Science* **2009**, *14*, 226–235.
- [60] Pichanusakorn, P.; Bandaru, P. *Materials Science and Engineering R* **2010**, *67*, 19–63.
- [61] Zeier, W. G.; Heinrich, C. P.; Day, T.; Panithipongwut, C.; Kieslich, G.; Brunklaus, G.; Snyder, G. J.; Tremel, W. *Journal of Materials Chemistry A* **2014**.
- [62] Porras, G.; Quintero, M. *Physica Status Solidi B* **1999**, *215*, 1067–1074.
- [63] Guen, L.; Glaunsinger, W.; Wold, A. *Materials Research Bulletin* **1979**, *14*, 463–467.
- [64] Matsushita, H.; Maeda, T.; Katsui, A.; Takizawa, T. *Journal of Crystal Growth* **2000**, *208*, 416–422.
- [65] Guen, L.; Glaunsinger, W. *Journal of Solid State Chemistry* **1980**, *35*, 10–21.
- [66] Quintero, M.; Morocoima, M.; Quintero, E. *Revista Mexicana de Fisica* **2007**, *53*, 154–157.

- [67] Wang, H. *International Journal of Photoenergy* **2011**, *2011*, 1–10.
- [68] Wang, K.; Shin, B.; Reuter, K. B.; Todorov, T.; Mitzi, D. B.; Guha, S. *Applied Physics Letters* **2011**, *98*, 051912.
- [69] Fan, F.-J.; Wu, L.; Yu, S.-H. *Energy & Environmental Science* **2014**, *7*, 190.
- [70] Todorov, T. K.; Reuter, K. B.; Mitzi, D. B. *Advanced Materials* **2010**, *22*, E156–E159.
- [71] Barkhouse, D. A. R.; Gunawan, O.; Gokmen, T.; Todorov, T. K.; Mitzi, D. B. *Progress in Photovoltaics: Research and Applications* **2012**, *20*, 6–11.
- [72] Shi, X. Y.; Huang, F. Q.; Liu, M. L.; Chen, L. D. *Applied Physics Letters* **2009**, *94*, 122103.
- [73] Liu, M. L.; Chen, I.-W.; Huang, F.-Q.; Chen, L.-D. *Advanced Materials* **2009**, *21*, 3808–3812.
- [74] Liu, M. L.; Huang, F.-Q.; Chen, L.-D.; Chen, I.-W. *Applied Physics Letters* **2009**, *94*, 202103.
- [75] Sevik, C.; Cagin, T. *Applied Physics Letters* **2009**, *95*, 112105.
- [76] Zeier, W. G. W.; LaLonde, A.; Gibbs, Z. M.; Heinrich, C. P.; Panthöfer, M.; Snyder, G. J.; Tremel, W. *Journal of the American Chemical Society* **2012**, *134*, 7147–54.
- [77] Zeier, W.; Pei, Y.; Pomrehn, G.; Day, T.; Heinz, N.; Heinrich, C. P.; Snyder, G.; Tremel, W. *Journal of the American Chemical Society* **2013**, *135*, 726–32.
- [78] Schäfer, W.; Nitsche, R. *Materials Research Bulletin* **1974**, *9*, 645–654.
- [79] Hall, S. R.; Szymanski, J. T.; Stewart, J. M. *The Canadian Mineralogist* **1978**, *16*, 131–137.
- [80] Schorr, S.; Hoebler, H.-J.; Tovar, M. *European Journal of Mineralogy* **2007**, *19*, 65–73.
- [81] Li, Y.; Meng, Q.; Deng, Y.; Zhou, H.; Gao, Y.; Li, Y.; Yang, J.; Cui, J. *Applied Physics Letters* **2012**, *100*, 231903.
- [82] Parker, D.; Singh, D. J. *Physical Review B* **2012**, *85*, 125209.

Bibliography

- [83] Kosuga, A.; Plirdpring, T.; Higashine, R.; Matsuzawa, M.; Kurosaki, K.; Yamanaka, S. *Applied Physics Letters* **2012**, *100*, 042108.
- [84] Liu, H.; Shi, X.; Xu, F.; Zhang, L.; Zhang, W.; Chen, L.; Li, Q.; Uher, C.; Day, T.; Snyder, G. *Nature Materials* **2012**, *11*, 422–5.
- [85] Plirdpring, T.; Kurosaki, K.; Kosuga, A.; Day, T.; Firdosy, S.; Ravi, V.; Snyder, G.; Harnwungmoung, A.; Sugahara, T.; Ohishi, Y.; Muta, H.; Yamanaka, S. *Advanced Materials* **2012**, *24*, 3622–6.
- [86] Shavel, A.; Arbiol, J.; Cabot, A. *Journal of the American Chemical Society* **2010**, *132*, 4514–4515.
- [87] Shin, S. W.; Han, J. H.; Park, C. Y.; Moholkar, A. V.; Lee, J. Y.; Kim, J. H. *Journal of Alloys and Compounds* **2012**, *516*, 96–101.
- [88] Shavel, A.; Cadavid, D.; Ibáñez, M.; Carrete, A.; Cabot, A. *Journal of the American Chemical Society* **2012**, *134*, 1438–41.
- [89] Ibáñez, M.; Zamani, R.; Li, W.; Shavel, A.; Arbiol, J.; Morante, J. R.; Cabot, A. *Crystal Growth & Design* **2012**, *12*, 1085–1090.
- [90] Yang, H.; Jauregui, L. a.; Zhang, G.; Chen, Y. P.; Wu, Y. *Nano Letters* **2012**, *12*, 540–5.
- [91] Ibáñez, M.; Cadavid, D.; Zamani, R.; García-Castelló, N.; Izquierdo-Roca, V.; Li, W.; Fairbrother, A.; Prades, J. D.; Shavel, A.; Arbiol, J.; Pérez-Rodríguez, A.; Morante, J. R.; Cabot, A.; Garc, N.; Pe, A. *Chemistry of Materials* **2012**, *24*, 562–570.
- [92] Li, W.; Ibáñez, M.; Zamani, R. R.; García-Castelló, N.; Gorsse, S.; Cadavid, D.; Prades, J. D.; Arbiol, J.; Cabot, A. *CrystEngComm* **2013**, *15*, 8966.
- [93] Boyce, J.; Huberman, B. *Physics Reports* **1979**, *51*, 189–265.
- [94] Jeitschko, W.; Braun, D. *Acta Crystallographica B* **1977**, *33*, 3401–3406.
- [95] Morelli, D. T.; Meisner, G. P. *Journal of Applied Physics* **1995**, *77*, 3777.
- [96] Sales, B.; Mandrus, D.; Williams, R. *Science* **1996**, *272*, 1325–8.
- [97] Koza, M. M.; Johnson, M. R.; Viennois, R.; Mutka, H.; Girard, L.; Ravot, D. *Nature Materials* **2008**, *7*, 805–10.

- [98] Keppens, V.; Mandrus, D.; Sales, B. *Nature* **1998**, *395*, 876–878.
- [99] Shi, X.; Zhang, W.; Chen, L.; Yang, J. *Physical Review Letters* **2005**, *95*, 185503.
- [100] Ballikaya, S.; Wang, G.; Sun, K.; Uher, C. *Journal of Electronic Materials* **2010**, *40*, 570–576.
- [101] He, T.; Chen, J.; Rosenfeld, H. D.; Subramanian, M. A. *Chemistry of Materials* **2006**, *18*, 759–762.
- [102] Park, K.-H.; Kim, I.-H. *Journal of Electronic Materials* **2010**, *40*, 493–498.
- [103] Graff, J.; Zhu, S.; Holgate, T.; Peng, J.; He, J.; Tritt, T. M. *Journal of Electronic Materials* **2011**, *40*, 696–701.
- [104] Mallik, R. C.; Stiewe, C.; Karpinski, G.; Hassdorf, R.; Müller, E. *Journal of Electronic Materials* **2009**, *38*, 1337–1343.
- [105] Ballikaya, S.; Uzar, N.; Yildirim, S.; Chi, H.; Su, X.; Tan, G.; Tang, X.; Uher, C. *Journal of Electronic Materials* **2012**, *42*, 1622–1627.
- [106] Shi, X.; Yang, J.; Salvador, J. R.; Chi, M.; Cho, J. Y.; Wang, H.; Bai, S.; Yang, J.; Zhang, W.; Chen, L. *Journal of the American Chemical Society* **2011**, *133*, 7837–46.
- [107] Sales, B.; Mandrus, D.; Chakoumakos, B.; Keppens, V.; Thompson, J. *Physical Review B* **1997**, *56*, 15081–15089.
- [108] Tang, G. D.; Wang, Z. H.; Xu, X. N.; He, Y.; Qiu, L.; Du, Y. W. *Journal of Electronic Materials* **2011**, *40*, 611–614.
- [109] Hermann, R.; Jin, R.; Schweika, W.; Grandjean, F.; Mandrus, D.; Sales, B.; Long, G. *Physical Review Letters* **2003**, *90*, 135505.
- [110] Toprak, M. S.; Stiewe, C.; Platzek, D.; Williams, S.; Bertini, L.; Müller, E.; Gatti, C.; Zhang, Y.; Rowe, M.; Muhammed, M. *Advanced Functional Materials* **2004**, *14*, 1189–1196.
- [111] MI, J.-L.; Tu, J.-P. *Journal of Inorganic Materials* **2008**, *23*, 715.
- [112] Guo, Q.-S.; Li, H.; Su, X.-L.; Tang, X.-F. *Acta Physica Sinica* **2010**, *59*, 6666.
- [113] Li, H.; Tang, X.; Su, X.; Zhang, Q. *Applied Physics Letters* **2008**, *92*, 202114.

Bibliography

- [114] Li, H.; Tang, X.; Zhang, Q. *Journal of Electronic Materials* **2009**, *38*, 1224–1228.
- [115] Zhang, L. Ph.D. thesis, Universität Wien, 2009.
- [116] Li, H.; Tang, X.; Zhang, Q.; Uher, C. *Applied Physics Letters* **2009**, *94*, 102114.
- [117] Du, Y.; Cai, K. F.; Chen, S.; Qin, Z.; Shen, S. Z. *Journal of Electronic Materials* **2011**, *40*, 1215–1220.
- [118] Li, G.; Kurosaki, K.; Ohishi, Y.; Muta, H.; Yamanaka, S. *Journal of Electronic Materials* **2012**, *42*, 1463–1468.
- [119] Sesselmann, A.; Dasgupta, T.; Kelm, K.; Müller, E.; Perlt, S.; Zastrow, S. *Journal of Materials Research* **2011**, *26*, 1820–1826.
- [120] Biswas, K.; Muir, S.; Subramanian, M. *Materials Research Bulletin* **2011**, *46*, 2288–2290.
- [121] Grytsiv, A.; Rogl, P.; Michor, H.; Bauer, E.; Giester, G. *Journal of Electronic Materials* **2013**, *42*, 2940–2952.
- [122] Leszczynski, J.; Dauscher, A.; Masschelein, P.; Lenoir, B. *Journal of Electronic Materials* **2010**, *39*, 1764–1768.
- [123] Tang, Y.; Qiu, Y.; Xi, L.; Shi, X.; Zhang, W.; Chen, L.; Tseng, S.-M.; Chen, S.-W.; Snyder, G. *Energy & Environmental Science* **2014**.
- [124] Koumoto, K.; Wang, Y.; Zhang, R.; Kosuga, A.; Funahashi, R. *Annual Review of Materials Research* **2010**, *40*, 363–394.
- [125] Bruce, D.; O'Hare, D.; Walton, R. *Functional Oxides*; John Wiley & Sons: West Sussex, 2010; p 318.
- [126] Terasaki, I.; Sasago, Y.; Uchinokura, K. *Physical Review B* **1997**, *56*, R12685–R12687.
- [127] Yamauchi, H.; Karvonen, L.; Egashira, T.; Tanaka, Y.; Karppinen, M. *Journal of Solid State Chemistry* **2011**, *184*, 64–69.
- [128] Limelette, P.; Hardy, V.; Auban-Senzier, P.; Jérôme, D.; Flahaut, D.; Hébert, S.; Frésard, R.; Simon, C.; Noudem, J.; Maignan, A. *Physical Review B* **2005**, *71*, 233108.

- [129] He, J.; Liu, Y.; Funahashi, R. *Journal of Materials Research* **2011**, *26*, 1762–1772.
- [130] Li, F.; Wei, T.-R.; Kang, F.; Li, J.-F. *Journal of Materials Chemistry A* **2013**, *1*, 11942.
- [131] Tsubota, T.; Ohtaki, M.; Eguchi, K.; Arai, H. *Journal of Materials Chemistry* **1997**, *7*, 85–90.
- [132] Guilmeau, E.; Bérardan, D.; Simon, C.; Maignan, A.; Raveau, B.; Ovono, D. O.; Delorme, F. *Journal of Applied Physics* **2009**, *106*, 053715.
- [133] Kieslich, G. Ph.D. thesis, Johannes Gutenberg-Universität Mainz, 2013.
- [134] Magnéli, A.; Virtanen, A. I.; Laaksonen, T.; Hakala, M. *Acta Chemica Scandinavica* **1949**, *3*, 88–89.
- [135] Magnéli, A.; Oughton, B. M.; Holtermann, H.; Sørensen, J. S.; Sørensen, N. A. *Acta Chemica Scandinavica* **1951**, *5*, 581–584.
- [136] Magnéli, A.; Blomberg, B.; Holtermann, H.; Sørensen, J. S.; Sørensen, N. A. *Acta Chemica Scandinavica* **1951**, *5*, 585–589.
- [137] Magnéli, A.; Blomberg-Hansson, B.; Kihlberg, L.; Sundkvist, G. *Acta Chemica Scandinavica* **1955**, *9*, 1382–1390.
- [138] Andersson, S.; Sundholm, A.; Magnéli, A.; Högberg, B.; Kneip, P.; Palmstierna, H. *Acta Chemica Scandinavica* **1959**, *13*, 989–997.
- [139] Gadó, P.; Magnéli, A.; Niklasson, R. J. V.; Brunvoll, J.; Hinton, M. *Acta Chemica Scandinavica* **1965**, *19*, 1514–1515.
- [140] Gadó, P.; Holmberg, B.; Magnéli, A.; Kallner, A. *Acta Chemica Scandinavica* **1965**, *19*, 2010–2011.
- [141] Kieslich, G.; Veremchuk, I.; Antonyshyn, I.; Zeier, W. G.; Birkel, C. S.; Weldert, K.; Heinrich, C. P.; Visnow, E.; Panthöfer, M.; Burkhardt, U.; Grin, Y.; Tremel, W. *Physical chemistry chemical physics : PCCP* **2013**, *15*, 15399–403.
- [142] Anderson, J. S. *Journal of the Chemical Society, Dalton Transactions* **1973**, 1107.
- [143] Krumeich, F. *Zeitschrift für Kristallographie* **1997**, *212*, 708–711.

Bibliography

- [144] Krumeich, F.; Hussain, A.; Bartsch, C.; Gruehn, R. *Zeitschrift für anorganische und allgemeine Chemie* **1995**, *621*, 799–806.
- [145] Krumeich, F.; Bartsch, C.; Gruehn, R. *Journal of Solid State Chemistry* **1995**, *427*, 268–274.
- [146] Krumeich, F. *Acta Crystallographica B* **1998**, *54*, 240–249.
- [147] Roth, R.; Waring, J. *Journal of Research of the National Bureau of Standards* **1966**, *l*, year.
- [148] England, P.; Booth, J.; Tilley, R.; Ekström, T. *Journal of Solid State Chemistry* **1982**, *44*, 60–74.
- [149] Heurung, G.; Gruehn, R. *Journal of the Less Common Metals* **1980**, *76*, 17–32.
- [150] Sleight, A. W.; Sletten, E.; Sletten, J.; Kulonen, E.; Brunvoll, J.; Bunnenberg, E.; Djerassi, C.; Records, R. *Acta Chemica Scandinavica* **1966**, *20*, 1102–1112.
- [151] Craig, D. C.; Stephenson, N. C. *Acta Crystallographica B* **1969**, *25*, 2071–2083.
- [152] Binnewies, M.; Glaum, R.; Schmidt, P.; Schmidt, M. *Chemische Transportreaktionen*; De Gruyter, 2011.
- [153] Doverspike, K.; Dwight, K.; Wold, A. *Chemistry of Materials* **1990**, *2*, 194–197.
- [154] LaLonde, A. D.; Ikeda, T.; Snyder, G. *The Review of scientific instruments* **2011**, *82*, 025104.
- [155] Coelho, A. *TOPAS Academic V4.1*; Cohelo Software: Brisbane, Australia, 2004.
- [156] Pankove, J. I. *Optical Processes in Semiconductors*; Dover Publications: New York, 1975.
- [157] Iwanaga, S.; Toberer, E. S.; LaLonde, A.; Snyder, G. *The Review of scientific instruments* **2011**, *82*, 063905.
- [158] Borup, K. A.; Toberer, E. S.; Zoltan, L. D.; Nakatsukasa, G.; Errico, M.; Fleurial, J.-P.; Iversen, B. B.; Snyder, G. J. *The Review of scientific instruments* **2012**, *83*, 123902.
- [159] Vegard, L. *Zeitschrift für Physik* **1921**, *5*, 17–26.

- [160] Matsushita, H.; Ichikawa, T.; Katsui, A. *Journal of Materials Science* **2005**, *40*, 2003–2005.
- [161] Haight, R.; Barkhouse, A.; Gunawan, O.; Shin, B.; Copel, M.; Hopstaken, M.; Mitzi, D. B. *Applied Physics Letters* **2011**, *98*, 253502.
- [162] Tanaka, K.; Fukui, Y.; Moritake, N.; Uchiki, H. *Solar Energy Materials and Solar Cells* **2011**, *95*, 838–842.
- [163] Sesselmann, A. J. Ph.D. thesis, Universität Augsburg, 2012.
- [164] Boor, J.; Stiewe, C.; Ziolkowski, P.; Dasgupta, T.; Karpinski, G.; Lenz, E.; Edler, F.; Müller, E. *Journal of Electronic Materials* **2013**, *42*, 1711–1718.
- [165] Ishida, K.; Nishizawa, T. *Journal of Phase Equilibria* **1990**, *11*, 22–26.
- [166] Biswas, K.; Muir, S.; Subramanian, M. *Materials Research Bulletin* **2011**, *46*, 2288–2290.
- [167] Platzek, D.; Karpinski, G.; Drasar, C.; Müller, E. *Materials Science Forum* **2005**, *492-493*, 587–592.
- [168] Jeitschko, W.; Foecker, A. J.; Paschke, D.; Dewalsky, M. V.; Evers, C. B. H.; Künnen, B.; Lang, A.; Kotzyba, G.; Rodewald, U. C.; Möller, M. H. *Zeitschrift für anorganische und allgemeine Chemie* **2000**, *626*, 1112–1120.
- [169] Kjekshus, A.; Nicholson, D. G.; Rakke, T.; Jalonen, H.; Lüning, B.; Swahn, C.-G. *Acta Chemica Scandinavica* **1973**, *27*, 1315–1320.
- [170] Devos, I.; Womes, M.; Heilemann, M.; Olivier-Fourcade, J.; Jumas, J.-C.; Tirado, J. L. *Journal of Materials Chemistry* **2004**, *14*, 1759.
- [171] Lefebvre-Devos, I.; Lassalle, M.; Wallart, X.; Olivier-Fourcade, J.; Monconduit, L.; Jumas, J. *Physical Review B* **2001**, *63*, 125110.
- [172] Olivier-Fourcade, J.; Ibanez, A.; Jumas, J.; Maurin, M.; Lefebvre, I.; Lippens, P.; Lannoo, M.; Allan, G. *Journal of Solid State Chemistry* **1990**, *87*, 366–377.
- [173] Sharma, R. C.; Ngai, T. L.; Chang, Y. A. *Bulletin of Alloy Phase Diagrams* **1989**, *10*, 657–664.
- [174] Zhao, X. Y.; Shi, X.; Chen, L. D.; Zhang, W. Q.; Zhang, W. B.; Pei, Y. Z. *Journal of Applied Physics* **2006**, *99*, 053711.

Bibliography

- [175] Dyck, J. S.; Chen, W.; Uher, C.; Chen, L.; Tang, X.; Hirai, T. *Journal of Applied Physics* **2002**, *91*, 3698.
- [176] Mallik, R. C.; Stiewe, C.; Karpinski, G.; Hassdorf, R.; Müller, E. *Journal of Electronic Materials* **2009**, *38*, 1337–1343.
- [177] Birkel, C. S.; Kieslich, G.; Bessas, D.; Claudio, T.; Branscheid, R.; Kolb, U.; Panthöfer, M.; Hermann, R. P.; Tremel, W. *Inorganic Chemistry* **2011**, *50*, 11807–12.
- [178] Birkel, C. S.; Mugnaioli, E.; Gorelik, T.; Kolb, U.; Panthöfer, M.; Tremel, W. *Journal of the American Chemical Society* **2010**, *132*, 9881–9.
- [179] Birkel, C. Ph.D. thesis, Johannes Gutenberg-Universität Mainz, 2010.
- [180] Kieslich, G.; Birkel, C. S.; Stewart, A.; Kolb, U.; Tremel, W. *Inorganic Chemistry* **2011**, *50*, 6938–43.
- [181] Norby, T. *Solid State Ionics* **1988**, *28-30*, 1586–1591.
- [182] Schrade, M.; Fjeld, H.; Finstad, T. G.; Norby, T. *The Journal of Physical Chemistry C* **2014**, *118*, 2908–2918.
- [183] Salmon, D. R.; Tye, R. P. *International Journal of Thermophysics* **2010**, *31*, 338–354.
- [184] Schrade, M.; Kabir, R.; Li, S.; Norby, T.; Finstad, T. G. *Journal of Applied Physics* **2014**, *115*, 103705.
- [185] Saucke, G.; Populoh, S.; Vogel-Schäuble, N.; Sagarna, L.; Mogare, K.; Karvonen, L.; Weidenkaff, A. *MRS Proceedings* **2013**, *1543*, 83–92.
- [186] Winter, M. R.; Clarke, D. R. *Journal of the American Ceramic Society* **2007**, *90*, 533–540.

Curriculum Vitae

Persönliche Daten:

Name	Heinrich
Vorname	Christophe Paul
Geburtstag	30.08.1984
Geburtsort	Berlin
Staatsangehörigkeit	Deutsch



Ausbildung:

ab 2011 bis 2014	Promotion im Fachbereich Chemie Johannes Gutenberg-Universität Mainz
ab 2005 bis 2010	Studium der Chemie (Diplom) Johannes Gutenberg-Universität Mainz
ab 1995 bis 2004	Staatliches Gymnasium Saarburg

Wissenschaftlicher Lebenslauf:

24/05/2014	Abschluss der Promotion an der Johannes Gutenberg-Universität Mainz Betreuer: [REDACTED] und [REDACTED]
01/2013 bis 04/2013	Forschungsaufenthalt an der University of Waterloo, Kanada; Betreuer: [REDACTED]
01/2011 bis 12/2014	Forschung im Rahmen der Promotion an der Johannes Gutenberg-Universität, Mainz in Kollaboration mit: [REDACTED] (CalTech, USA) [REDACTED] (DLR, Köln) [REDACTED] (University of Oslo, Norwegen) [REDACTED] (University of Waterloo, Kanada)
01/2011 bis 05/2014	Kollegiat der Graduate School of Excellence MAINZ
09/2009	Forschungsaufenthalt an der University of Cornell, Ithaca, USA; Betreuer: [REDACTED]
09/2008 bis 04/2009	Research Scholar an der University of Toledo, USA Betreuer: [REDACTED]